NASA/TM–20240015600

BOLT-2 Roughness Side Flight Data
Results and Analysis

Scott A. Berry and Casey J. Broslawski
Langley Research Center, Hampton, Virginia

Bradley M. Wheaton
Johns Hopkins University Applied Physics Laboratory, Laurel, Maryland

David W. Adamczak
Air Force Research Laboratory, Wright-Patterson Air Force Base, Ohio

Rodney Bowersox
Texas A&M University, College Station, Texas

Aaron T. Dufrene
CUBRC Inc., Buffalo, New York

December 2024

NASA STI Program Report Series

The NASA STI Program collects, organizes, provides for archiving, and disseminates NASA's STI. The NASA STI program provides access to the NTRS Registered and its public interface, the NASA Technical Reports Server, thus providing one of the largest collections of aeronautical and space science STI in the world. Results are published in both non-NASA channels and by NASA in the NASA STI Report Series, which includes the following report types:

- TECHNICAL PUBLICATION. Reports of completed research or a major significant phase of research that present the results of NASA Programs and include extensive data or theoretical analysis. Includes compilations of significant scientific and technical data and information deemed to be of continuing reference value. NASA counterpart of peer-reviewed formal professional papers but has less stringent limitations on manuscript length and extent of graphic presentations.

- TECHNICAL MEMORANDUM. Scientific and technical findings that are preliminary or of specialized interest, e.g., quick release reports, working papers, and bibliographies that contain minimal annotation. Does not contain extensive analysis.

- CONTRACTOR REPORT. Scientific and technical findings by NASA-sponsored contractors and grantees.

- CONFERENCE PUBLICATION. Collected papers from scientific and technical conferences, symposia, seminars, or other meetings sponsored or co-sponsored by NASA.

- SPECIAL PUBLICATION. Scientific, technical, or historical information from NASA programs, projects, and missions, often concerned with subjects having substantial public interest.

- TECHNICAL TRANSLATION. English-language translations of foreign scientific and technical material pertinent to NASA's mission.

Specialized services also include organizing and publishing research results, distributing specialized research announcements and feeds, providing information desk and personal search support, and enabling data exchange services.

For more information about the NASA STI program, see the following:

- Access the NASA STI program home page at http://www.sti.nasa.gov

- Help desk contact information:

https://www.sti.nasa.gov/sti-contact-form/
and select the "General" help request type.

NASA/TM–20240015600

BOLT-2 Roughness Side Flight Data

Results and Analysis

Scott A. Berry and Casey J. Broslawski
Langley Research Center, Hampton, Virginia

Bradley M. Wheaton
Johns Hopkins University Applied Physics Laboratory, Laurel, Maryland

David W. Adamczak
U.S. Air Force Research Laboratory, Wright-Patterson Air Force Base. Ohio

Rodney Bowersox
Texas A&M University, College Station, Texas

Aaron T. Dufrene
CUBRC Inc., Buffalo, New York

National Aeronautics and
Space Administration

Langley Research Center
Hampton, VA 23681

December 2024

Acknowledgments

The BOLT flight project, which includes multiple flights to date, was originally initiated by Ivett Leyva, formerly a Program Manager (PM) of the Air Force Office of Scientific Research (AFOSR), and then later managed by Sarah Popkin, also formerly of AFOSR. The successful BOLT-2 flight could not have happened without their advocacy and dedication. Also, BOLT heavily leveraged knowledge and technologies gained from the HIFiRE series of sounding rocket flights, which was proposed and managed by Doug Dolvin, of the Air Force Research Laboratory (AFRL). Design and fabrication of the BOLT-2 flight hardware occurred at CUBRC, with support from Tim Wadhams, Vince Smith, Chris Halt, and Will Winter, and many others. Mike Holden was an original co-PI for this flight before he passed away. This flight was named in honor of his memory (see statement below). The flight data computers were provided by Rob Pietsch of the Australian Defense Sciences Technology group (DSTG) thru a collaborative effort with AFRL. Much of the success of the BOLT-2 flight must be attributed to the dedicated and seasoned Wallops flight support team, which included Jim Lanzi, Ted Gass, David Kilcoyne, to name a few. The post flight analysis of the trajectory data was also supported with atmospheric analysis completed by Mary Bedrick, of the Air Force Weather Agency (AFWA). Supplemental atmospheric measurements were also conducted by the Hypersonic Flight in the Turbulent Stratosphere team (HYFLITS) team. Finally, Chris Yam, formerly of Purdue University, Brett Bathel and Andrew Leidy, of NASA LaRC, and Greg McKiernan and Cam Butler, of JHU/APL, supported the pre-flight measurements of the nose-joint steps.

A plaque placed on the vehicle contained the following statement:

> This flight experiment, AFOSR's Boundary Layer Turbulence II (BOLT II), is in memory and honor of Dr. Michael "Mike" Holden, also known as "Mr. Hypersonics". Mike is a founding father of our hypersonics community, and taught us to always think higher and faster, constantly pushing the envelope of what is possible in hypersonic flow physics, flight systems, and ground testing. Mike would have succeeded at anything he put his mind to, but he chose the higher and faster path. His 60+ years of work and monumental contributions to hypersonics will outlive all of us.

This report is available in electronic form at
http://

Table of Contents

List of Figures

Summary

This report provides an in-depth review of the flight data obtained from Side B, also known as the roughness side, of BOLT-2, which was developed and designed to measure the effectiveness of boundary layer trips at hypersonic conditions. Three discrete-roughness trips were implemented on Side B at specific locations, with the necessary sensor layout, to investigate the flight conditions at which they no longer maintained turbulence behind them. All three trips were the same type that were scaled and sized based on predictions of local boundary layer thicknesses to provide the same level of effectiveness. One trip was on the vehicle centerline, where the boundary layer is relatively thick, while the other two were symmetrically located outboard where the boundary layer is much thinner. The relative difference in boundary layer thickness between these locations was roughly on the order of 3-to-1, thus the centerline trip was geometrically about three times larger than the outboard trips. A first order assessment of the Side B flight results is indicated by these three trips forcing transition onset at the same time during flight. The enclosed flight data shows that the performance of each individual trip was nearly identical, with allowances for minor variations attributed to measurement accuracy.

Introduction

The Air Force Office of Scientific Research (AFOSR) established a basic research flight test program to study boundary layer transition and/or turbulence (BOLT) on a sounding rocket at hypersonic Mach numbers. The primary objective of this flight program is to obtain boundary layer transition or turbulence data for comparison against current techniques for analyzing and predicting boundary layer behavior. Two flights were initially funded and flown. BOLT-1 was flown out of Esrange, Sweden, during May of 2021, but was unsuccessful due to an unforeseen dynamic instability (pitch-roll coupling) that occurred shortly after first-stage separation. John Hopkins University Applied Physics Laboratory (JHU/APL) was the prime contractor for the first flight with the German Aerospace Center (DLR) Mobile Rocket Base (MORABA) providing launch services. A recent review of the first BOLT flight campaign is provided in [1]. BOLT-2 was successfully flown out of the NASA Wallops Flight Facility (WFF) in Virginia during March of 2022. The prime contractor for this flight was a group led by Texas A&M University (TAMU) and CUBRC. References [2] and [3] provide recent reviews of the overall BOLT-2 effort. Recently, the decision was made to fund a second attempt at the first flight, with the original team for lead and launch. This third flight (called BOLT-1B) has very recently had a successful launch in September of 2024.

As shown in Fig. 1, the BOLT geometry provides a low-curvature concave surface with swept leading edges that is representative of a generic hypersonic configuration, including pressure gradients and wall temperature effects. BOLT was intended as a continuance of the Hypersonic International Flight Research and Experimentation (HIFiRE) boundary layer transition series [4], except on a non-axisymmetric hypersonic configuration. With HIFiRE focused largely on canonical shapes (simple and elliptic cones), BOLT was specifically derived to be three-dimensional with swept leading edges (LE) and concave surfaces (like a waverider configuration). Computations on BOLT have revealed a complex flow field that includes a center region whose boundary layer is relatively thick and stable, while the outer sections exhibit a much thinner boundary layer with a mixture of instability modes (for example, see [5]). There are two identical sides of BOLT separated by gutters, allowing for both smooth-wall and roughness experiments to be flown at the same time. The primary focus of these research flights is to provide smooth-wall data on the boundary layer transition process and resultant turbulence under hypersonic conditions [6]. For the roughness side experiments, these flights also provide an opportunity to examine various roughness types under hypersonic boundary layer conditions. The research objective of the roughness experiments flown on the alternate side (Side B) is to improve knowledge regarding roughness effects on boundary layer transition and turbulence on a realistic hypersonic vehicle. A sounding rocket flight test program provides the means to study boundary layer transition and turbulence in low disturbance environments that typically cannot be obtained in ground-based facilities. Conventional facilities can provide the proper freestream Reynolds numbers, but with added freestream noise (disturbances that alter the boundary layer instabilities), while quiet facilities can provide less noise but usually not at matching conditions for a typical flight program. For the roughness side experiment on the BOLT-1 flight, the focus was two-dimensional nose-joint steps (see [7]). For BOLT-2, the focus of the roughness side experiment was discrete roughness elements, which are also often referred to as boundary layer (BL) trips. As described in [8], a combined experimental and computational effort was established to inform decisions for placing and sizing these BL trips and laying out the sensor suite for flight. Wind tunnel data were provided by the United States Air Force Academy (USAFA) Mach 6 Ludwieg tube (M6LT) [9]. Computational mean flow solutions at wind tunnel and flight conditions were completed by TAMU to track streamlines for sensor placement and boundary layer information for scaling to flight.

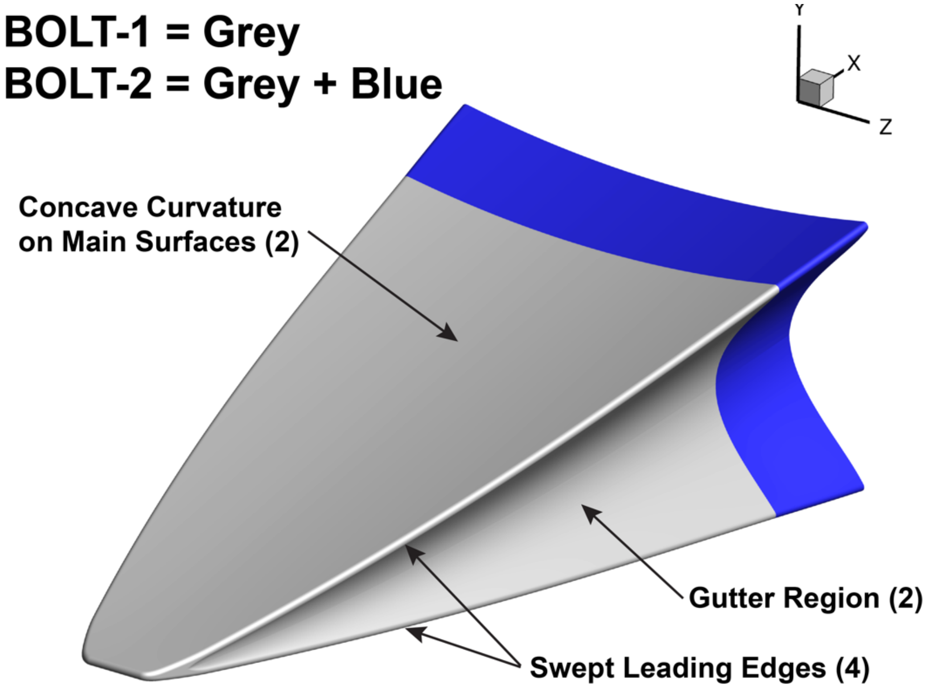

Figure 1. Sketch of BOLT vs. BOLT-2.

While AFOSR has primarily sponsored the BOLT campaigns as university-led projects to foster the next generation of researchers in hypersonic boundary layer transition and turbulence, NASA has also been involved with both efforts as a contributing partner with support from the Aeronautics Research Mission Directorate (ARMD), Advanced Air Vehicle Program (AAVP), Hypersonic Technologies Project (HTP). The initial set of wind tunnel aeroheating data was obtained in the LaRC 20-Inch Mach 6 Air Tunnel on the BOLT geometry and presented at the kick-off meeting [10], providing an early assessment of the transition fronts and behavior. That data, along with subsequent results obtained in other tunnels (including quiet facilities), provided benchmark information for comparison against computational analysis being done by the broader team. For both flights, NASA was tasked with leading the definition of the roughness side experiments, focusing on the effect of nose-joint steps for BOLT-1 and BL trips for BOLT-2. The current paper provides a review of the measurements obtained during the BOLT-2 flight.

As mentioned above, the BOLT-2 Side B roughness experiment was designed to investigate the effectiveness of BL trips in flight. For hypersonic vehicles, especially, the BL state, whether laminar or turbulent, has a significant impact on the convective heating to the body, with a turbulent BL providing for heating many times greater than when laminar. Normally, the desire is to maintain laminar flow for as long as possible, so that surface heating, and resulting internal conduction, is minimized. However, there are times when a turbulent BL is preferred, such as ahead of engine inlets, as a laminar BL is more suspectable to flow separation and can lead to engine unstart. Thus, BL trips are typically used to force turbulence when needed. For instance, with the Hyper-X program, an extensive ground test campaign was implemented to design and size BL trips for the program, whose performance was confirmed after the successful flights. Reference [11] provides a review of the Hyper-X ground-test campaign that was conducted, while [12] reviews the flight data that was obtained as part of that program. The Hyper-X ground-test effort included comparing several trip types and eventually selected an array of truncated swept ramps as the tripping mechanism. One of the other trip types examined was a diamond shaped protuberance that had been the original baseline going in based on previous wind tunnel studies. The diamond trip originated from earlier Shuttle tripping studies, where the thermal protection system (TPS) tiles were simulated as a protrusions that were square tiles oriented at a 45° to the mean flow direction (see [13], for instance). From the Hyper-X testing, the diamond trip appeared to be on equal footing as a vortex-generating device that enhances transition onset. But, it was not selected, ultimately, due to concerns about its integrity during flight from excessive heating to its front face, especially at the higher sustained Mach number conditions of the Hyper-X flights (Mach 7 and 10). The selected swept ramp trips were expected to have lesser issues with thermal loading and ultimately were proven to have performed as expected. Swept ramp tripping devices have subsequently been used on other flight test programs, such as the X-51 program. The BOLT-2 flight represented an opportunity to obtain flight performance data on the BL trip type not chosen during the Hyper-X program, allowing further investigation into consistency in trends between wind tunnel and flight. With BOLT-2 being a sounding rocket flight experiment, with a ballistic trajectory into suborbital space, the heating profile is not as severe as the previous Hyper-X flights that flew much longer at sustained hypersonic conditions. The diamond-shaped trip has been part of previous flight testing, such as on the HIFiRE-1 [14] and HyBOLT [15] vehicles, but those flights had varying levels of success.

The present paper is intended as a final review of the BOLT-2 roughness side flight data, allowing an assessment of the ground-based methodology used to select and size the BL trips for flight. All the Side B data will be presented, but the primary focus will be to determine the conditions during ascent and descent when the trips no longer were able to sustain turbulent flow, which is referred to here as determining the time of transition onset. Limited comparisons against smooth-wall computational fluid dynamic (CFD) predictions will anchor the flight measurements, allowing easier determination of times of laminar and turbulent flow. Transition onset maps for both ascent and descent conditions will then be developed and presented, from which incipient and effective conditions can be extracted. The incipient condition refers to the time at which the BL trip just begins to induce non-laminar behavior in the far field, while the effective condition represents the time at which turbulence is forced just behind the trip. The incipient and effective conditions can then be used to calculate BL properties for eventual comparison to similar ground-test computations. The present paper stops at the reporting of the appropriate freestream conditions for the incipient and effective cases for both ascent and descent from the flight data review. Computational comparisons of the methodology for scaling from wind tunnel to flight are left for a subsequent report.

Symbols

b	Trip width (mm)
D	Trip diagonal (mm)
k	Trip height (mm)
M	Mach number
Re	unit Reynolds number (1/m)
Re_L	Reynolds number based on vehicle length
t	Time from liftoff (s)
X	Lengthwise distance from the nose (m)
Y	Height above vehicle centerline (m)
Z	Spanwise distance from vehicle centerline (m)
L	Vehicle reference length from nose to end of body (m)
α	Vehicle angle of attack (deg)
β	Vehicle angle of sideslip/yaw (deg)
δ	Boundary layer thickness (mm)

Experimental Method

Flight Vehicle

The BOLT-2 configuration, shown in Fig. 1, is 1.0m long, comprised of a blunt, cylindrical leading edge (nose radius of 5mm), followed by four swept leading edges with two main concave surfaces on opposite sides (designated as Side A and Side B), with two gutter regions intended to isolate the main surfaces from each other. Note, the concavity for BOLT is only implemented in the spanwise direction, the surface in streamline direction is flat. Side A is dedicated to studying smooth surface boundary layer transition and turbulence [2, 3] while Side B is focused on roughness effects. The flight vehicle was designed by CUBRC with a nickel 201 nose and stainless steel 410 body (further details can be found in [16]). The nose-to-body joint is located at 0.186m from the nose. Preflight thermal analysis revealed that a notionally flush nose joint would become a small rear-facing step due to vehicle aeroheating during hypersonic flight, with the expectation that this step would be sufficiently small not to influence the transition behavior on either side. Measurements of the steps around the circumference of the nose-joint were taken preflight and those results are provided in [17]. Figure 2 provides a photo of part of the launch stack as the vehicle was being prepared for launch. Shown in the photo are the flight geometry, the transition section covered in cork, and the payload section that include the data acquisition and telemetry systems. Reference [2] contains additional details on the overall BOLT-2 vehicle design, including all the sensor details, and layouts for both sides. Additional photos that capture other relevant details for the Side B roughness experiment can be found in Appendix A.

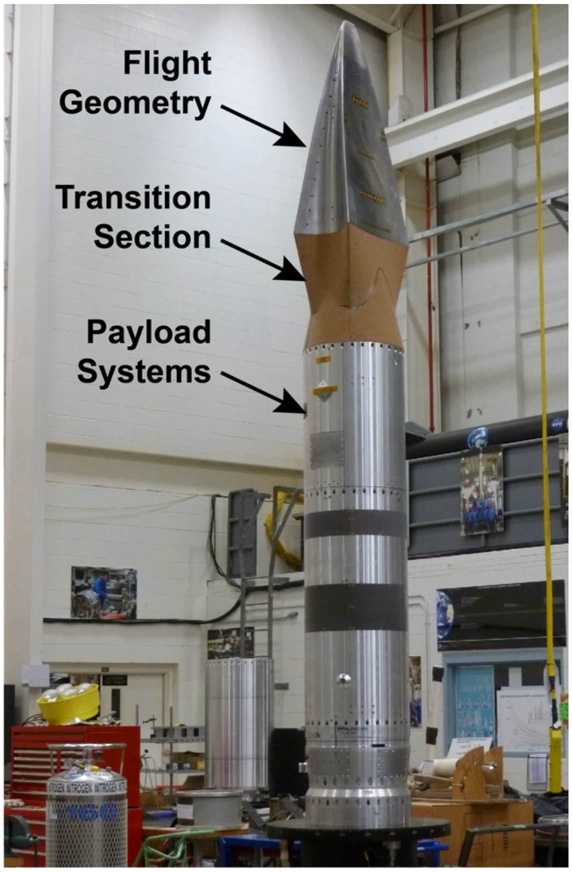

Figure 2. BOLT-2 flight vehicle being prepared for launch at Wallops Flight Facility.

As mentioned above and discussed in [8], the Side B experiment for BOLT-2 was focused on the effect of discrete roughness elements, specifically due to diamond-shaped vortex generators, also sometimes referred to as “pizza box” trips. These trips have been studied extensively over the years in ground-based testing and proven to be an efficient tripping device. The heritage of the diamond shape trips came from previous test campaigns using Space Shuttle Orbiter models [13] and were tested as part of the Hyper-X program [11].

For BOLT-2, the approach taken for the roughness experiment was to utilize three discrete trips based on the diamond shape, with one on centerline (designated as the CL Trip) and two others that were identical near the swept leading edges (designated as LE-19 and LE-81 Trips). Figure 3 provides two sketches: a) shows the trip locations on BOLT-2 in relation to other important features, including the sensor array locations, and b) indicates the key trip dimensions and orientation. The height (k) of each trip are based on 70% of the predicted local boundary layer height for a flight Reynolds number of 2.5 million during descent, with the width (b) being three times larger than the height [8]. Note, all three trips are expected to cause transition onset at the same time during flight. Table 1 specifies the chosen locations and dimensions of the three BOLT-2 trips. Surface impression molds were taken of the trips before flight and subsequent analysis indicates the trips to be within 1.2% of the desired height [17]. Figure 4 provides photos of all three trips showing some of the local sensors (on or near the trips). The view orientation for these photos is always looking aft in the downstream direction.

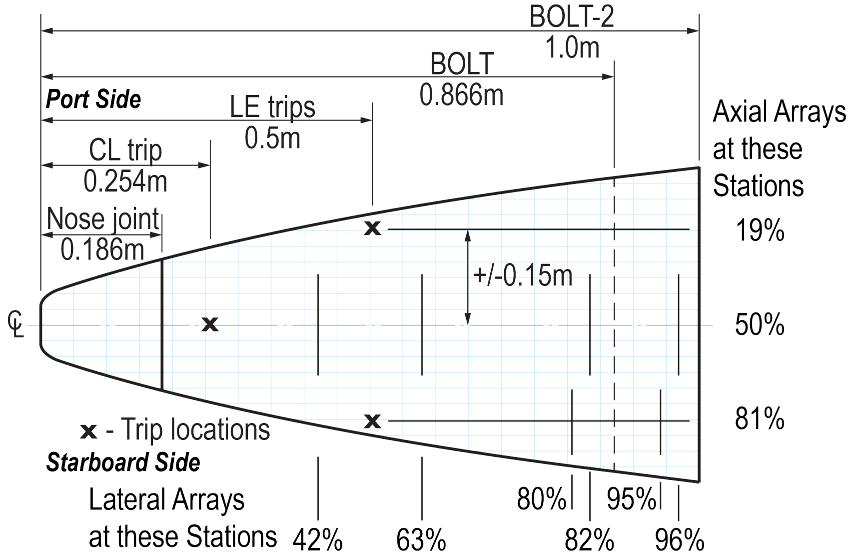

a) Trip locations in relation to sensor arrays

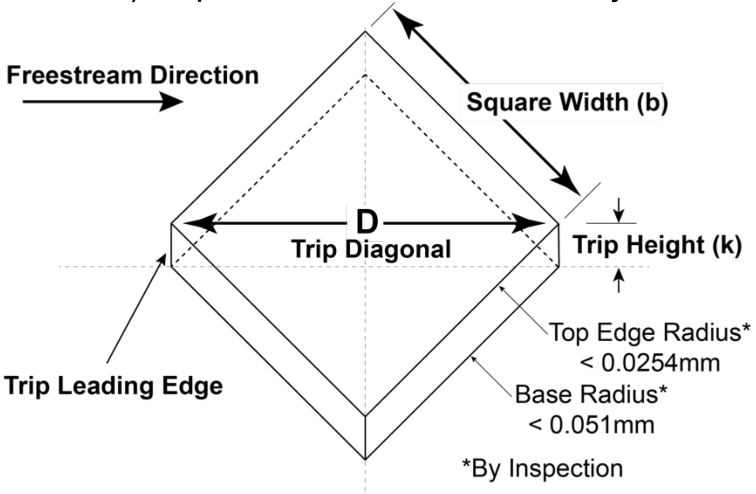

b) Key dimension of the diamond trips

Figure 3. Sketches showing locations and dimensions of the BOLT-2 trips.

Table 1. Key dimensions for Side B trips.

Side B Trips	X (m)	Z (m)	Height (mm)	Width (mm)
CL	0.254	0.000	2.625	7.875
LE-19	0.500	0.146	0.903	2.709
LE-81	0.500	-0.146	0.903	2.709

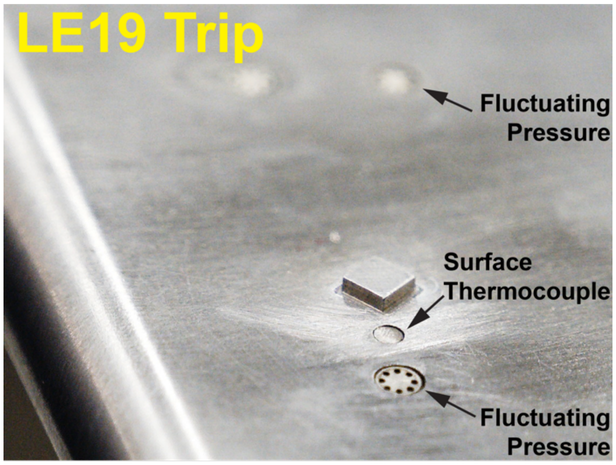

a) **LE-19 trip**

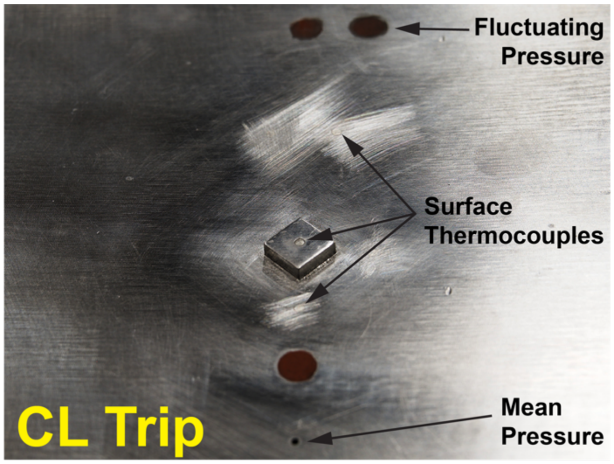

b) **CL trip**

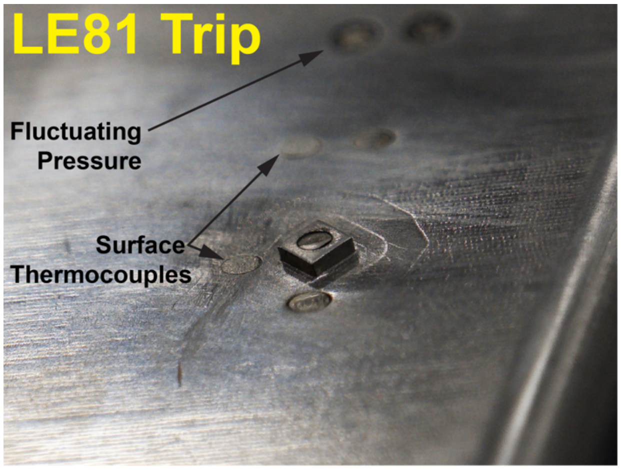

c) **LE-81 trip**

Figure 4. Photos (looking downstream) showing the trips and local sensors.

Flight Instrumentation

Overall, BOLT-2 telemetered down over 400 channels of data covering both sides of the vehicle, as well as the gutter regions. Table 2 provides a complete list of sensor types and counts, while Fig. 5 provides a sensor layout specifically for Side B. The naming convention utilized for sensors on Side B only include an initial set of letters designating the sensor type, followed by the vehicle side (A or B), and a unique numerical shorthand for the location. The Side B sensor types include Medtherm thermocouples (MT), Vatell thermogages (TG), CUBRC thin-films (TF), Honeywell© pressure gages (HWP), high-frequency PCB® sensors (PCB), and Kulite® pressure gages (KUL). As shown in Fig. 3a, the sensor arrays were laid out in a grid pattern, at specific longitudinal and spanwise positions in percentages of the distance (down or across the body) from 0 to 100. For instance, the sensor listed in Fig. 5 as MT-B-70-19 is a Side B thermocouple located 70% down the body and 19% of the vehicle span. The 76 Side B thermocouple channels correspond to 38 locations. All thermocouples are dual sensors (providing both a front and back face temperature), suitable for direct conversion to heat transfer, if desired. Measurements from the front side sensors are designated at the end of sensor identifier with an "F" for front face reading, while in-depth measurements would have a "B" for back face. For the present report, only the front side (or surface) data have been analyzed. More than half of the Side B thermocouples were distributed along three longitudinal stations behind each trip (at 19%, 50%, and 81% of the vehicle span), as depicted in Fig. 3a. Twelve thermocouples were distributed in two spanwise arrays behind the LE-81 trip (at 80% and 95% down the vehicle), to measure the width of the turbulent wedge as it develops in time. The 12 TG sensors on Side B were distributed across two spanwise arrays behind the CL trip (at 42% and 82% down the vehicle). Side B also had 12 of custom-made TF sensors, and these provided two additional spanwise arrays behind the CL trip (at 63% and 96% down the vehicle). On Side B, there were four locations with mean pressure measurements identified with "HWP" and a total of 12 sensors for measuring pressure fluctuations, designated with either "PCB" or "KUL." Note that despite Side B being set up with the naming convention based on location within a grid pattern, a spreadsheet error led to the movement of one thermocouple (MT-B-80-19) from its intended location of 80% lengthwise and 19% spanwise to an incorrect location at 80% lengthwise and 70% spanwise. A second non-conformity was later found, likely due to an installation error, when it was determined that MT-B-50-79 and MT-B-50-81 had been switched. All other sensors were installed in the correct location to its Side B designation, as can be seen by a close inspection of Fig. 5. Additional details of the BOLT-2 flight instrumentation can be found in Ref. [3]. Also, specific locations and other details for all Side B sensors can be found in Appendix B.

Table 2. Flight instrumentation types and designations.

Total # Channels	Type / Designation	Vendor & Model#	Side B only
192	Thermocouple (MT)	Medtherms Type E Dual TCS-061-EE	76
57	Heat Transfer (TG)	Vatell TG-2000	12
50	Thin-Film (TF)	CUBRC custom design	12
39	Mean Pressure (HWP)	Honeywell 19C – 15 psia	4
19	Fluctuating Pressure (PCB)	PCB-112B05,	7
5	Fluctuating Pressure (KUL)	Kulite XCE-093-5psid	5
4	High Frequency Pressure	PCB-132B	0
14	Skin Friction	Ahmic	0
5	Accelerometer	Endevco ±100g	0
11	Internal Payload	Various	0

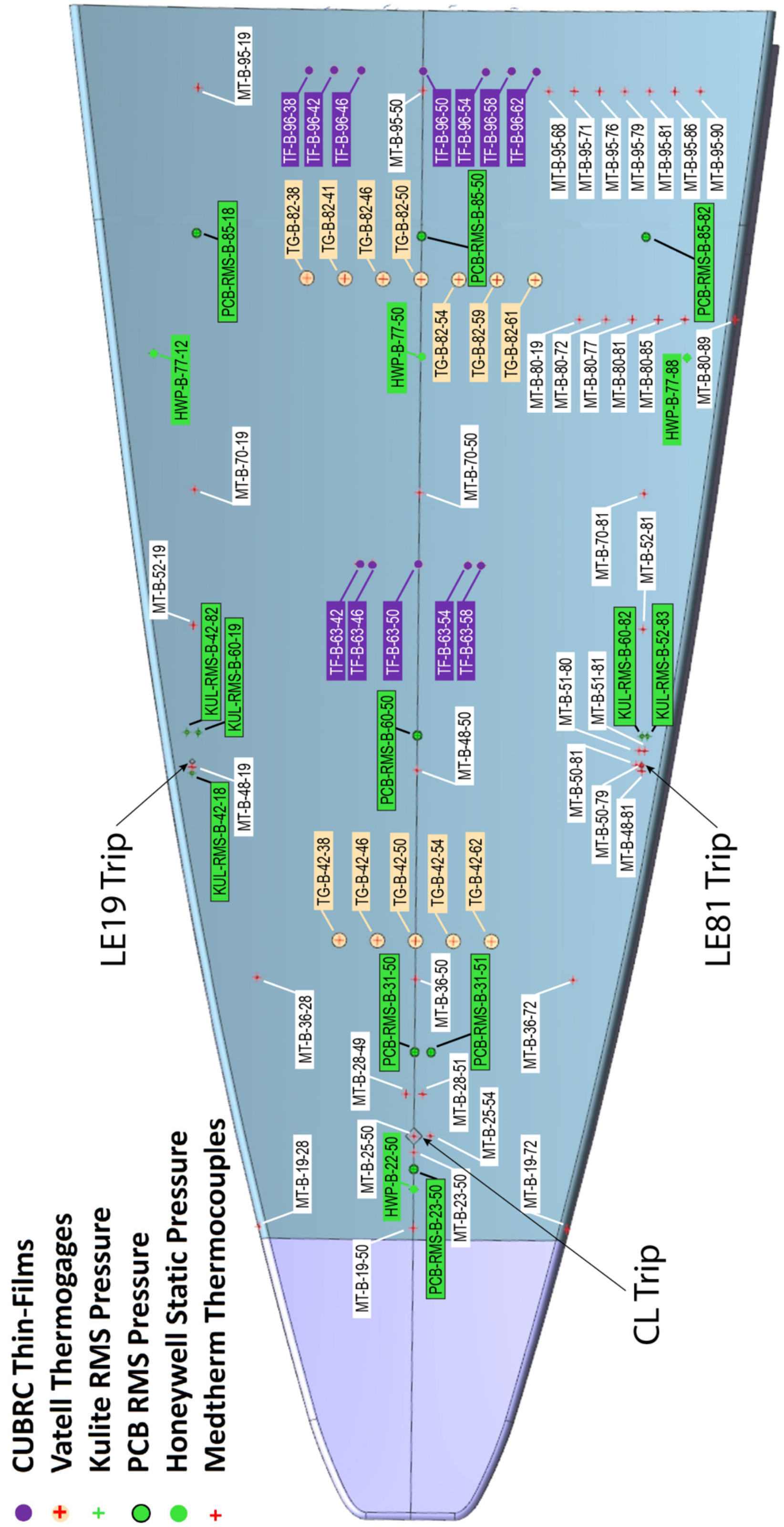

Figure 5. Side B instrumentation map.

Data Acquisition & Telemetry System

The data acquisition system for BOLT-2 was derived from the system used under the Hypersonic International Flight Research (HIFiRE) program conducted by the Australian Defense Sciences Technology Group (DSTG) and the Air Force Research Laboratory. Data acquisition utilized a distributed flight computer system can accommodate 32 analog input data channels, 16 digital outputs, 8 digital inputs, and 3 serial data ports per “node”. The serial data ports can be used for devices like global positioning system receivers, inertial measuring units, or any device that can output a serial data stream. The telemetry is distributed as a high-speed serial telemetry bus on the flight computers to the transmitters.

The flight computers are programmed utilizing a custom real time C operating system. Additional software driver modules are utilized for specialized devices flown on payloads such as inertial measuring units, high speed data acquisition units, GPS devices etc. A library of drivers has been developed over the years and new drivers are added for new devices on flights. To date more than 15 hypersonic flight tests have flown with these systems by AFRL and/or DSTG.

Thirteen flight computers were utilized for BOLT-2 divided into three telemetry (TM) data streams for a total of 416 analog data channels. The flight computers were setup to generate three TM streams with four nodes on streams 1 and 2, and then five nodes on stream 3. Each TM stream was run at 15 million bits per second (Mbps) to allow the maximum telemetry to be transmitted to ground stations during flight. This gave a total of 45Mbps for the experimental sensors and payload systems data. With the chosen frame length (20,736 bits) a base sample rate of 723.3796Hz was utilized for most sensors. Sensors desiring a higher sample rate were then a multiple of the base sample rate.

The BOLT-2 flight computer system used a 24-bit analog-to-digital (A/D) converter for all sensors providing a nominal ±2.5V maximum input range with overrange capability to ±2.7V. Analog sensors were grouped into sets of 16 assigned to specific collection boards, which provided sensor power (if needed), sensor amplification, and filtering. BOLT-2 utilized four different types of sensor collection boards to handle the variety of sensors (to be discussed in next section) and then one additional board to handle the payload systems. The 416 sensor channels on BOLT-2 required a total of 26 collection boards.

The sensor collection boards had been previously calibrated prior to installation utilizing a Fluke model 753 calibrator to generate input signals. Depending on the sensor type, a discrete set of voltages was sent to each sensor input of the collection board and then recorded by the flight computer system as a 24-bit word versus the input voltage. From the collected data, either linear or cubic curve fits were generated. Cubic curve fits were used for thermocouple sensors. Most other sensors were very linear, so a linear fit was utilized.

Sensor Boards

BOLT-2 had a variety of sensors for measurements in flight, such as thermocouples, pressure sensors, heat-flux sensors, thin-films, and skin-friction sensors. Depending on the type of sensor, a specialized input circuit was required for the different sensor collection boards. The boards utilized three input circuit types to condition and amplify the sensor input signal.

Thermocouple (TC) inputs were amplified and filtered with a circuit utilizing a thermocouple amplifier integrated circuit (IC). The TC IC amplifier also handled the cold junction reference offset internally. A total gain of 50.028 was used for all Type E TC channels, thus allowing a measurement range of 0 to 650°C (1202°F). An initial low-pass filter with a cutoff frequency of 107Hz was also used in front of the TC amplified circuit, providing for anti-aliasing and a -3dB point at the filter frequency with a -20dB/decade roll-off. Type K thermocouples (for internal temperatures) utilized the same IC amplifier with a total gain of 122.4.

A second circuit type was utilized for the mean pressures, thin films, heat flux and skin friction sensors. This circuit utilized an instrumentation amplifier to both power each sensor (if needed) and provide amplification with a gain to the sensor output. Additional amplification and filtering were utilized (as needed) after the instrumentation amplifier providing additional gain and low-pass filtering for anti-aliasing (-3dB point at the filter frequency with a -20dB/decade roll-off). The gains and filter frequencies were set depending on the sensor type.

The third type of sensor input circuit was used for the PCB sensors. This circuit type provided a constant current power supply for the sensor and output amplification and filtering. The PCB sensors were powered at 24 volts with a 4-milliamp constant current source. The output was then fed to an anti-aliasing low-pass filter of 34.3kHz and then amplified with a gain of 4.17 before routing to the A/D system.

Initial sensor calibrations

During assembly and integration of the sensors and flight data acquisition into the flight vehicle, each sensor input was initially calibrated to provide for the engineering unit conversion factors from the flight system 24bit digital outputs of the A/D conversion system. Each sensor type had a different calibration procedure, as described below.

For the thermocouples, the sensor collection boards, and corresponding flight computers, were calibrated prior to installation utilizing a simulated type E thermocouple input from 0 to 700°C (1292°F). This allowed the full data system, from sensor input to A/D output, to be calibrated directly. A cubic curve fit was utilized for the MT sensors and applied post flight to derive the engineering unit output data. The standard quoted accuracy for a Type E thermocouple is ±1.7°C or 0.5%. A few thermocouples were Type K and were calibrated from 0 to 500°C (932°F).

Initial Honeywell pressure sensors calibrations were completed using a direct voltage input to the sensor collection board. An input range of 0 to 100mV was used to determine the response curves. The calibration data was post processed to produce a calibration of mV/count, which was then combined with a nominal output of (units of psi/mV) to compute the final engineering unit conversion of psi/Counts. The nominal output sensor was utilized at this stage as no calibration for each sensor was provided from the manufacturer. Additional calibrations will be discussed later as used during ground and flight-testing phases.

The TG sensor inputs for each channel were calibrated from 0-10mV direct input to the sensor collection board. The calibration data was post processed to produce a calibration of mV/count, which was then combined with the factory calibration curves provided by Vatell (units of (W/cm^2)/mV) to compute the final engineering unit conversion of (W/cm^2)/Counts. The Vatell factory calibration data was also used for pre-flight checkouts and during flight.

The calibration procedure for the TF gauges was similar to the TG sensors in that a simulated input voltage range was input to the sensor collection board and then recorded on the flight computer after A/D conversion. A voltage range of -0.1 to 0.6 volts was utilized for the TF simulated inputs. The calibration curves for temperature to sensor output were provided by CUBRC (deg K/volt). These were used with the voltage calibration inputs to derive the final engineering unit linear curve fits (deg K/count).

Ahmic skin friction and temperature calibrations were like above. An input range of -10 to +10mV was used on the skin friction input and a range of -0.1 to 0.6 volts was used on the temperature measurement input. These were combined with the Ahmic provided calibrations for each channel for final output units of Pa and deg C.

Calibration of the Kulites and PCB sensors were done differently than all other sensors and relied on the calculated gain value form the sensor collection board. The actual gain could not be measure directly as the filtering used removed the mean values from the output (high pass filter). A calibration was done on a direct input to the A/D inputs of the flight computers of -2.5 to 2.5V. This was then combined with the calculated gain and the manufacturers calibrations. This caused more error on the sensor collection boards as the actual gains on the amplification stages were not calibrated for. Engineering output of pressure is in units of psi.

Thermocouples

The largest group of sensors utilized on BOLT-2 were the Medtherm Type E Dual coaxial thermocouples (model TCS-061-EE, designated MT). Each MT instrument consisted of a front-face and back-face type E thermocouple (TC) in a cylindrical body that are slightly longer than the wall thickness that they penetrate. Each TC was bonded into a slip fit hole utilizing a high temperature adhesive. The front face sensor of each TC was then filed and sanded to provide the proper contour of the vehicle surface. The front surface TC junction is thus formed during the sanding process, where filaments of the sanded material form the connection of the outer conductor sleeve to the inner conductor wire of the thermocouple.

For Side B of BOLT-2, the 38 MT sensors utilized 76 analog channels. The MT sensors were all sampled at the base sample rate (723.4Hz). There were also four Omega Type K thermocouples utilized for internal temperatures on flight systems, these were also sampled at the base sample rate. These were the self-adhesive type.

Mean Pressures

The surface mean pressures were obtained utilizing Honeywell 19C – 15 psia rated sensors, which were designated as HWP in the data files. The HWP sensors were intended for recording the surface static pressure over time. They were mounted internally using a manifold with stainless steel tubing (typical length of 2-3 ft) run to the desired surface locations. The pressure tubes were bonded into place on the surface with the same high temperature adhesive. The HWP sensors were sampled at the base sample rate (723.4Hz). On Side B, the HWP sensors were primarily intended to be part of the flush air data system (FADS) that includes the Side A and gutter pressures.

During ground testing and flight, it was possible to calculate additional calibration curves for the HWP sensors using specific points collected over time. During the full-scale flight vehicle ground test in the CUBRC LENS 2 shock tunnel runs [16], the test chamber was pumped down to a near vacuum in steps. Correspondingly, a similar procedure was done using two points during flight. The pre-flight pressures at the launch pad representing the highest pressures and the apogee measurements for the lowest pressures were utilized to again provide a pressure-to-TM counts conversion. This allowed calibrations as near to the test events to minimize drifting from the factory calibrations and to try to remove the effect of thermal shift. Measurement uncertainty with these pressure sensors should be on the order of <1% over the measurement range for this flight.

Thermogages

A limited number of Vatell TG-2000 thermogages were utilized during the BOLT-2 flight, with the intention of allowing comparison of derived heating rates (from the thermocouples) to directly measured heating provided by the TG sensors. These sensors had not been previously used in flight, and the hope was to gain insight into their operational viability in a flight environment. The TG sensors had a desired sample rate of 2000Hz but due to the telemetry rate and frame size, a rate of 2170.14 Hz was obtained (super-commutated to the base sample rate x3). The TG sensors were bonded in place using the same high temperature adhesive.

To minimize sensor drift over time, an additional step was included to compute the zero offsets corresponding to known points with zero heat flux as an input. This was done pre-flight and then also post flight using the flight data. The pre-flight zero offsets were used for sensor checkouts pre-flight during integration and testing. These sensors exhibited drifting of the zeroes over time as the payload was powered on at different times.

Post flight zeros were computed at two points in time for the flight. The first set of zeros were computed from just before T=0 (launch time). This set of offsets was then used for the TG sensors data during the ascent window. The second set of TG zeros was then calculated during the exo-atmospheric phase of flight. These offsets were used for the TG sensor data during the reentry window. Utilizing this approach for zeroing the TG sensors provided a more consistent dataset that eliminated some of the heating effects on the sensors themselves. The stated accuracy of the TG-2000 sensors is ±3% for short duration applications (where the total amount of heat absorbed by the gauge does not raise its temperature above 392°F). Due to the longer duration test times for this flight case, the uncertainty with these sensors should be somewhat higher than quoted.

Thin Films

Another smaller set of sensors employed for BOLT-2 was the thin-film (TF) sensors, again to gain operational experience with them under flight conditions. The TF sensors were custom built by CUBRC and connected to a custom sensor collection board. These sensors are based on the design approach outlined by [18]. They utilize a fast-response platinum resistance temperature measurement representing the model surface. The sensor material properties are well characterized, and thickness is selected so that a semi-infinite solid assumption can be used in short duration tests to calculate heat transfer from the measured surface temperature rise. Standard practice was used by CUBRC utilizing a high-temperature plaster to secure these sensors into place.

However, these assumptions are not valid for a long-duration flight test, but the surface temperature data are still valid, although qualitative in nature due to the sensor materials differing from the surrounding stainless-steel body. Two TFs with back-face instruments were included on Side A for this flight, but, unfortunately, the back-face data was not acquired. A more in-depth analysis, based on internal temperatures from some other source (such as a combination of CFD conjugate heat transfer analysis, finite element analysis, or utilization of surrounding thermocouple and heat transfer data) could potentially be used to turn these temperature traces into a heat flux approximation, but to date no such analysis has been completed. Additionally, transition onset in most locations happened very quickly due to the parabolic flight trajectory, so turbulent spikes often seen in ground tests at transitional Reynolds numbers were not readily observed. The TF sensors were all sampled at a rate of 10127.3Hz (x14 samples per TM frame), well above the Nyquist rate. With the sensor substrate material (quartz) being less thermally conductive than the surrounding SS surface, the resulting measurements should be somewhat higher than the actual surface temperatures. For this reason, we do not have a stated accuracy for the TF results. Again, these measurements are intended for comparison only.

Fluctuating Pressures

For pressure fluctuation measurements on Side B, both Kulite XCE-093-5psid (KUL) and PCB 112B05 were utilized. These sensors were sampled at 50.6kHz which was slightly lower than the desired rate of 57kHz due to fitting all the telemetry into the available bandwidth. All the PCB and Kulite pressure sensors utilized a bandpass filter (combining low-pass and high-pass filters) to capture only AC signals, thus allowing only pressure oscillations to be recorded while removing the mean pressure. The PCB sensors were screwed into threaded holes in the model and then secured with a high temperature adhesive.

The PCB sensors utilized a constant current driver with a 24V power source to power the sensors and included a high pass filter. The output was then low-pass filtered at 17.5kHz and then amplified with a gain of 4.17. The manufacturer gains for the PCB's were then utilized with a direct input calibration to the A/D system of -2.5 to 2.5V. This was then combined to derive the engineering unit curve fits to produce an output in psi. As mentioned previously, this caused more error as the actual gains on the sensor boards were not measured. Since these measurements are intended primarily for the fluctuating component of pressure, the absolute value of measurement is less important and thus no there is no implied accuracy.

Side B Instrumentation Summary

The previous subsections provide insight into the BOLT-2 data acquisition system, sensor types, and calibration procedures that were used for conversion of the raw signals to engineering units. As conveyed in Table 2, Side B had a total of 116 sensors associated with the external vehicle surface, with a predominance of them being thermocouples. Table 3 summarizes the BOLT-2 Side B sensor types along with the applied gains, filters, and sampling rates (discussed above).

Table 3. BOLT-2 Side B sensor gain settings, filters, and sample rates.

Sensor Type	Total Gain	1st Stage Gain	2nd Stage Gain	Low Pass Filter (Hz)	High Pass Filter (Hz)	Sample Rate (Hz)
Type E TC	50.028	90.35	0.5537	107		723.4
Type K TC	122.4	122.4	1	107		723.4
Honeywell 19C	24.408	24.408	1	250		723.4
Heat flux	247.5	10	24.75	500		2170.1
Thin Film	4.0	4	1	5000		10127.3
Skin Friction	247.5	10	24.75	500		1446.8
Skin Friction Temps	4.0	4	1	100		723.4
PCB Fluctuations	4.17	1	4.17	34300	100.7	50636.6
Kulite Pressure	247.5	10	24.75	28300	100.7	50636.6

Flight Trajectory

A two-stage (Terrier Mark 70 - Improved Malemute) sounding rocket was used for the successful BOLT-2 flight from WFF on March 21, 2022. Figure 6 provides some of the flight performance data based on the current best estimated trajectory (BET), which had two science windows during ascent and descent. The BET utilized for the present analysis was generated in two steps. First was to develop a best estimated atmosphere (BEA) with updated atmospheric properties, specifically the pressure, temperature, density, and winds aloft as a function of latitude, longitude, and geometric altitude. This process utilized the original GPS-generated trajectory file along with updated atmospheric information using the Goddard Earth Observing System Model, Version 5 (GEOS-FP), and day-of-flight radiosonde data provided by WFF and LIDAR data provided by the GB-HALAS group [19]. The BEA was calculated from ground level to approximately 77.3 km for the ascent and descent portions of the experimental test windows. The second step was to modify the trajectory file based on the new atmospheric properties of the BEA and the Inertial Measuring Unit (IMU) data and the global positioning system (GPS) data. The IMU dataset contained the vehicle attitude data in the IMU frame for roll, pitch and yaw versus trajectory time. Both the computed IMU yaw, pitch, and roll as well as the Euler direction cosine matrix (DCM) were included. The IMU data was output in time at a rate of 50 Hz (0.02 sec timesteps). The GPS data set contained the vehicle position and velocity versus time. The GPS dataset also contained the individual satellite information as received. The GPS output the vehicle position and velocity in an earth centered earth fixed frame (ECEF). The position was also output

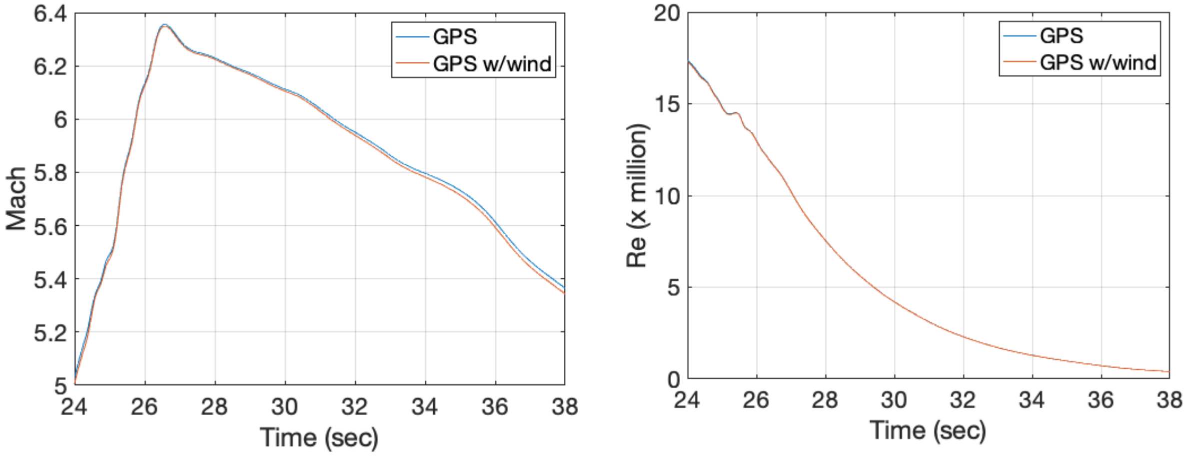

a) Mach number during ascent **b) Unit Reynolds number during ascent**

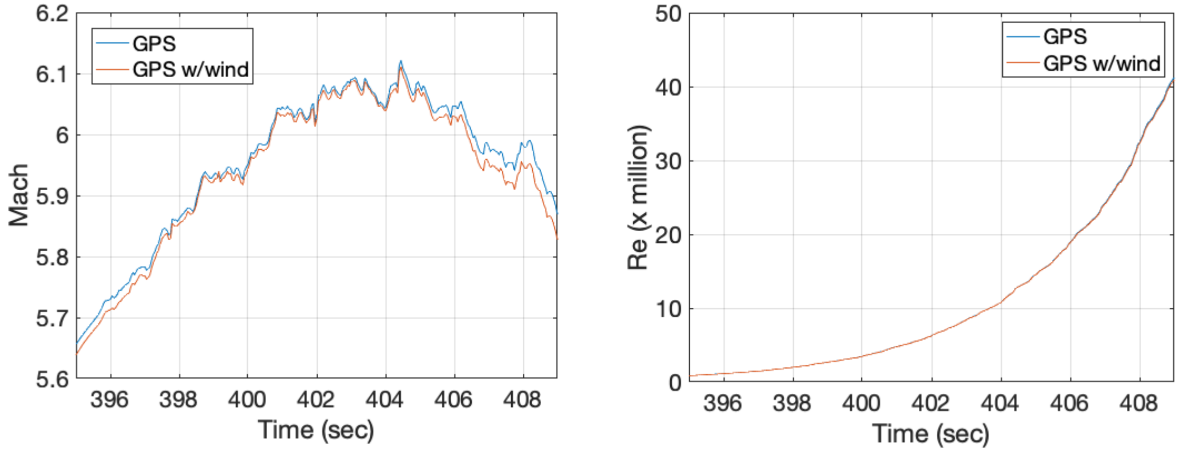

c) Mach number during descent **d) Unit Reynolds number during descent**

Figure 6. BOLT-2 flight performance during ascent and descent.

in a latitude, longitude, altitude geodetic frame. The GPS data was output in time at a rate of 20 Hz, or 0.05 sec timesteps. The BEA, IMU, and GPS data were combined to calculate and finalize the BET based on vehicle attitudes in the wind axis aerodynamic frame for the as flown trajectory. The GPS timesteps of 20 Hz data was chosen to compute the new parameters. The FADS data have not been used at this point to further refine the attitude information.

An unusual result to note for this flight is the vehicle flew higher and further than preflight predictions, an overperformance outside of the typical 2-σ probability bounds assigned preflight. Based on a postflight review of events, the following were contributing factors to this anomalous result: a pitch-down event at rail exit accounted for nearly 50% of the impact location miss, while thrust dispersions accounted for around 20%, and drag dispersions contributed 7%. The remaining error was attributed to an unfortunate stack up of acceptable misalignments with the fins, nose, and center-of-gravity (CG) offset. [20]

The plotted trajectory data in Fig. 6 include both with and without accounting for winds aloft showing that atmospheric winds did not have a strong impact on the derived BET results. The designated test windows during ascent and descent were based on Mach numbers (M) greater than 5 and freestream Reynolds numbers (Re_L) greater than 0.3 million. Based on these criteria applied to the as-flown trajectory, the science windows correspond to 24 to 38 seconds during ascent and 395 to 409 seconds during descent. The M and Re during the ascent science window are provided in Figs. 6a and 6b, while Figs. 6c and 6d provide these parameters during the descent science window. Note, in the data analysis plots to be shown later, the ascent window has been extended to cover from 10 to 35 seconds, as a few of the observed transition onset times occur prior to 24 seconds.

Figure 7 provides the vehicle attitude during these same science windows based on an assessment of both GPS and IMU data separately, with and without corrections for atmospheric winds. Again, the differences seen using different approaches for deriving the vehicle attitude during flight has only minor impact on the plotted results. As shown by Fig. 7, the vehicle angle of attack (α) and sideslip (β) were generally small. During the entire ascent window, mean alpha was found to be -0.53°, and mean beta was -0.02°, while during descent, mean alpha was -0.21° and mean beta was -0.24°. These values are consistent with those reported previously [3]. However, if the window of interest is restricted to only the times corresponding to times of transition movement due to the BL trips, then these mean values shift to values generally smaller. Based on the ascent and descent times of interest (to be discussed subsequently), the mean values of α and β was closer to -0.3° and 0.15°, respectively, during ascent, and -0.15° and -0.1° during descent. Figure 8 provides the reference system utilized for BOLT-2 and introduces the concept of the four quadrants around the periphery of the nose-joint step. The quadrants were assigned based on clockwise direction around the vehicle when at the nose looking aft. Side A has quadrants 1 and 4 (subsequently called Q1 and Q4), while Side B has Q2 and Q3. Thus, based on Fig. 8, a negative angle of attack corresponds to Side A being windward, or conversely, Side B being leeward. The negative sideslip corresponds to the vehicle pointing nose right (meaning Q1 and Q2 would be slightly windward).

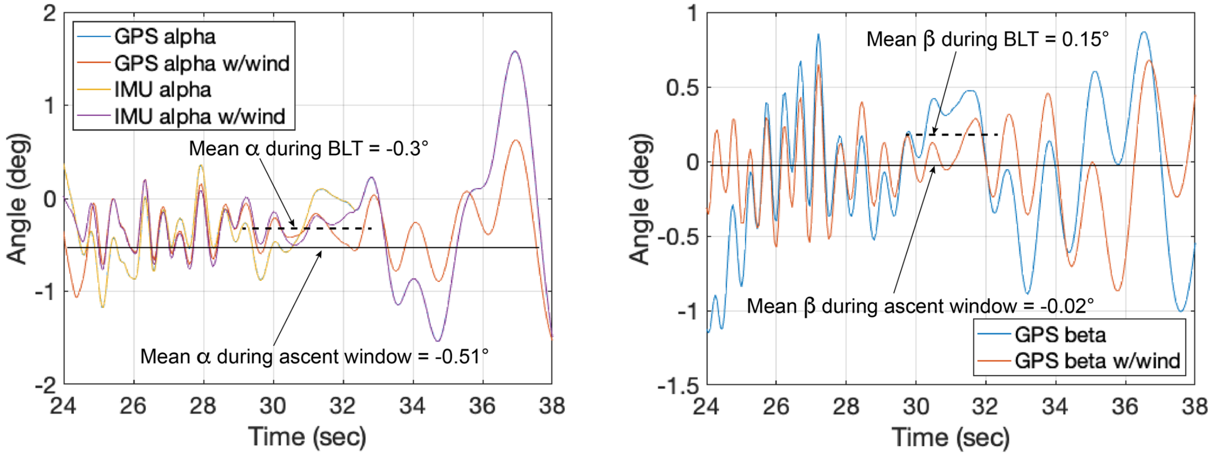

a) Angle of attack during ascent **b) Angle of sideslip during ascent**

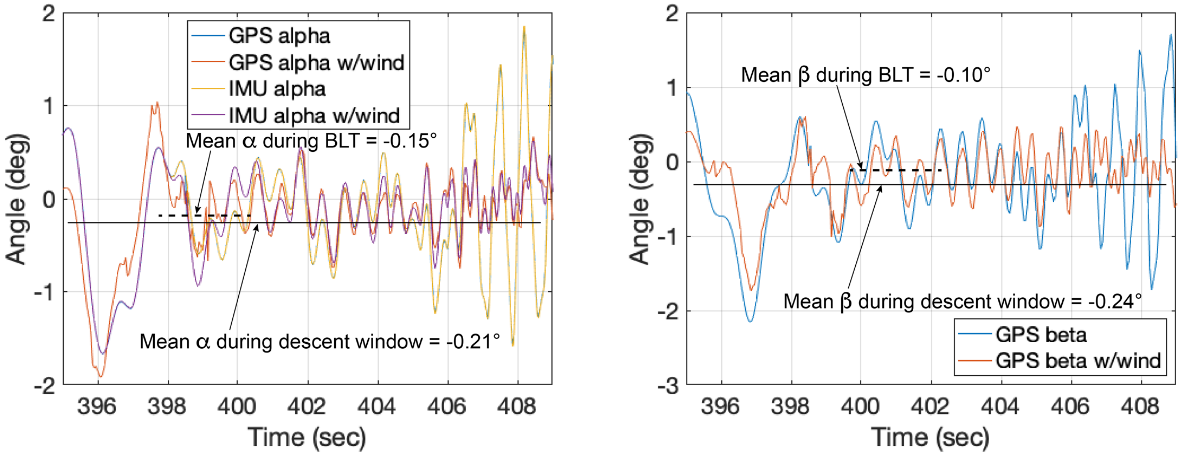

c) Angle of attack during descent **d) Angle of sideslip during descent**

Figure 7. BOLT-2 vehicle attitude during ascent and descent.

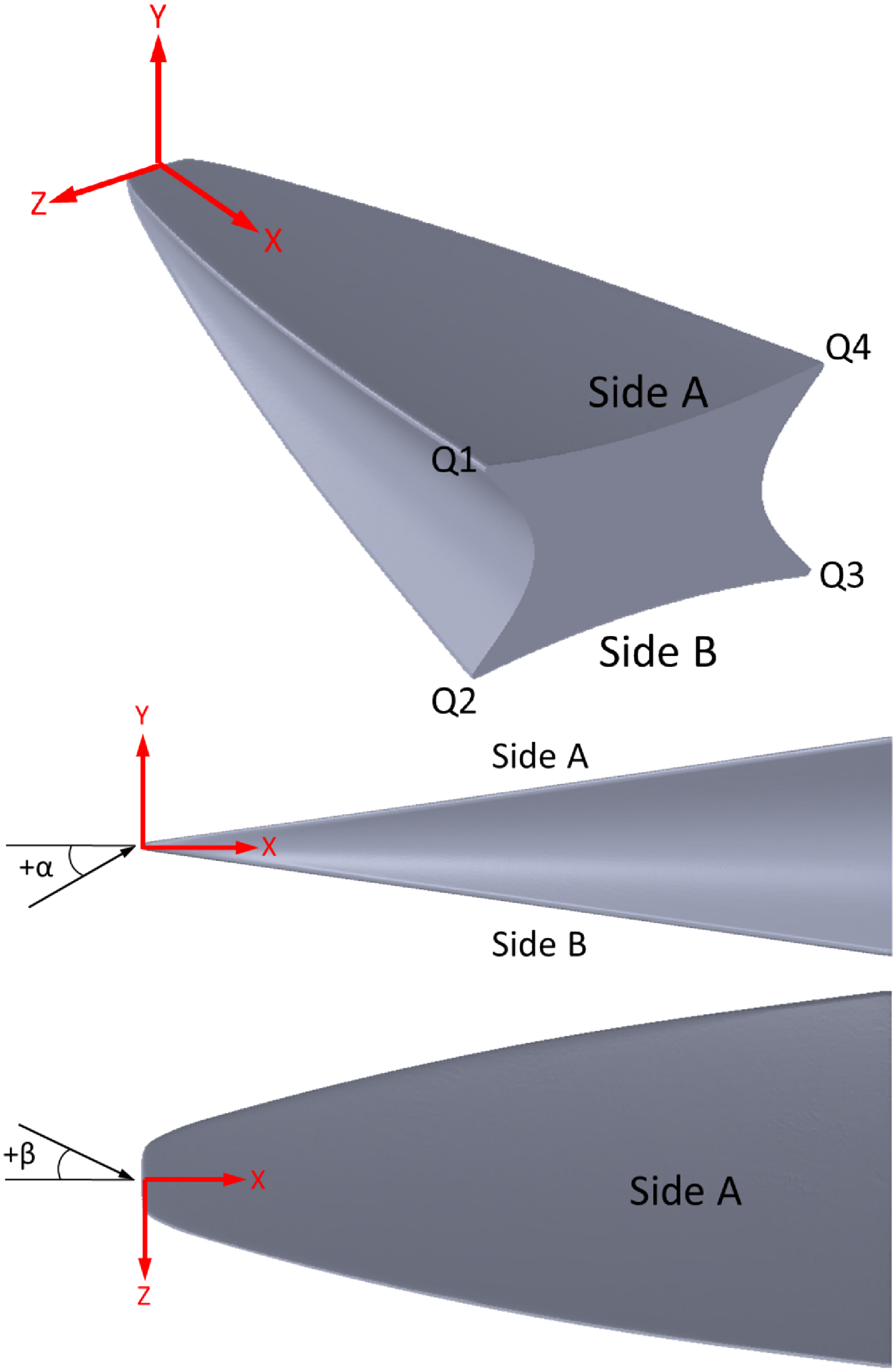

Figure 8. BOLT-2 coordinate system and inertial reference.

Standard practice for unguided sounding rocket flights is to utilize spin stabilization to minimize trajectory dispersions. For the BOLT-2 mission, the desired spin rate was achieved utilizing canted fins on both stages of the booster. In addition, a set of spin motors was utilized on the first stage motor to provide an initial spin once clear of the launch rail. This was done to further aid in dispersion reduction for the trajectory downrange.

Figure 9 depicts the actual roll rates during the ascent and descent windows. Initially, during ascent window (shown in Fig. 9a), the roll rate is initially positive and increasing to nearly 100 degrees/s (or under 0.3 Hz) but then starts to slow down. Later during ascent, the spin has reversed to a rate of -100 degrees/s (or just under -0.3 Hz). This roll-reversal was not expected, as the selected fin cant angles were selected to provide for a slightly positive rate. It is theorized that the cause of the spin rate mismatch with pre-flight expectations was due to manufacturing asymmetries coupled with the difficulty in setting all four fins precisely. During the time outside of the atmosphere, from ~75sec to 390sec of flight, the attitude control system (ACS) controlled spin rate to be near zero. This was part of the turn-over maneuver for the second stage to re-orient to a nose down attitude prior to re-entry. During descent, as shown in Fig. 9b, the spin rate again returned to the slightly negative value of -100deg/s, consistent with the end of ascent. Later, as the vehicle continues deeper into the atmosphere, the negative spin rate increases further. This again re-enforces the issues of asymmetries and the difficulty in setting precise fin angles. Some oscillations are observed starting at around 402sec, where the spin rate decreased and then increased sharply. These oscillations are likely due to changes in the fin shape or cant angle caused by heating effects during reentry.

Early during project formulation, there was a desire to keep the roll rate low (under ±5 Hz), to minimize the impact of vehicle dynamics on post-flight interpretation of the data. For most of both test windows, the roll rate was well under ±1 Hz, even though the vehicle ended up spinning in a direction not expected. Another stated goal of the flight was to maintain “incidence and yaw angles to within 2 degrees,” which was also accomplished. Having very small angles of attack and sideslip coupled with the low vehicle spin minimized the vehicle dynamics which greatly simplified the analysis utilized for this document.

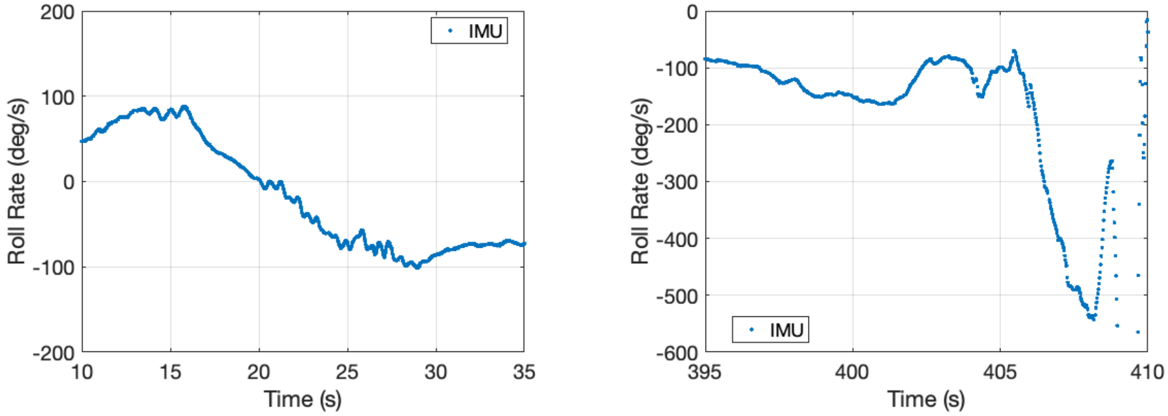

a) ***Ascent*** b) ***Descent***

Figure 9. BOLT-2 flight roll rate during science windows.

Post-Flight Analysis

The primary goal for the present analysis of trip performance during flight is to track the movement of transition by developing transition onset maps from all relevant sensors on Side B. The global footprint of the transition process will address both the incipient condition, which will be based on transition onset first showing up in the far-stream sensors, as well as the effective condition, which reflects when transition onset is as close to the trip location as can be measured. Note that transition movement during ascent occurs when the boundary layer (BL) is initially turbulent, so movement is tracked by when each sensor location indicates a re-laminarization as freestream conditions change (primarily as Reynolds number decreases). Meanwhile during descent the opposite occurs, the boundary layer switches in a more traditional sense, going from laminar to turbulent conditions (as the Re increases). To identify the point of departure from one BL state to the other, the thermocouple data will be converted from surface temperatures to heat transfer. This will allow quantitative comparisons against a database of laminar and turbulent computations, building confidence with the extraction of the onset times. The thermocouple data represents a significant proportion of the Side B data and will be used to anchor the present analysis. The remaining thermogage and thin-film results, which is a much smaller percentage of the overall data set, are considered qualitative pending further analysis.

The thermocouple data were analyzed using the Cook-Felderman method [21-22] to derive the heat transfer rates at each sensor location as a function of time. This method assumes semi-infinite one-dimensional heat conduction, which is an acceptable approach for most locations except for the swept leading edges. Reference [23] provides a more in-depth discussion of the methodology and equations used. Filtering of the thermocouple data was done during heat flux calculations to reduce noise, by using a 5-point moving average of the data. This down-sampling helped to improve both processing time and resulting file size of the final figures. During the ascent window, an initial reference time (where heat flux is near zero) of 0.001s was assumed. During descent, this reference time was selected as 370s. These flight-derived heat-flux results were then plotted against the database of predicted laminar and turbulent heating rates developed as part of a postflight thermal analysis of BOLT-2 vehicle using the BET. Comparisons of the measured heating to predicted laminar and turbulent bounds helps to distinguish, for each body point (or measurement location), the times along the flight trajectory that the boundary layer switches from one extreme to the other, thereby identifying the transition onset time. Reference [3] examined other approaches, such as multidimensional analysis, to arrive at heat flux from the thermocouple data. For the sake of the present paper, the transition onset times are defined as: (a) during ascent, the departure time of the measured heating away from the turbulent trend, or (b) during descent, the arrival time to the turbulent trend. Thus, onset times here refer to the time at which each sensor location starts or stops matching fully turbulent heating predictions. Times derived in this manner matched remarkably well with an earlier qualitative assessment of onset time results based purely on identifying the slope change in the temperature-time traces. As noted previously, the present analysis only looks at the front face thermocouple data.

The database of laminar and turbulent solutions was derived from postflight simulations, based on BET-derived flight conditions utilizing the Metacomp CFD++ code, to provide cold-wall heat flux and recovery temperatures at set points along the trajectory. These simulations utilized a quarter symmetry grid with 29M cells, but with only 2nd-order fluxes. As such, these simulations are not expected to be fully grid converged for the center region where lifted vortex structures are located, and thus minor heating differences could be seen in this region. The use of symmetry indicates the included solutions are for a flight attitude of zero alpha and beta, even though the flight vehicle is experiencing small, but nonzero angles of attack and yaw. All CFD solutions were completed at altitudes below 33km to avoid rarefied flow regimes and capture portions of the trajectory where heating is more severe, which overlaps the research test windows during ascent and descent. The cold-wall solutions were completed with a 300K isothermal boundary condition.

Results and Discussion

This section will be organized and presented by sensor type, first starting with the thermocouple data, after conversion to heat transfer, followed by the directly measured heat transfer data, then the thin-film results, and finally the pressure data. Within each subsection, the data will be further organized by select groupings to help identify the systematic nature of transition movement during both the ascent and descent test windows. The goal will be to capture the onset times on ascent and descent maps indicating the transient nature of BL transition process. The transition onset maps will then be used to identify the key trajectory points that represent the incipient and effective conditions from the flight data. In reference to Fig. 8, the Side B data will be presented with vehicle orientation rolled, thus Q2 will be the upper half and Q3 the bottom half of the layouts shown. Some of the results captured herein were originally published in a preliminary conference report [24], however the present document represents a more complete and final review of all the BOLT-2 Side B flight data.

Thermocouple Results

Roughly half of the Side B thermocouples were purposefully placed in replicate locations to Side A, to allow direct comparisons. Table 4 provides a complete list of these 19 sensor pairs. In the plots and discussion to follow, comparisons of the converted heat transfer rates from the measured thermocouple data for replicate sensors from both sides (when available) are provided to quantify tripping effects from the smooth side results. All Side B traces will be plotted with black lines, while any Side A results will be shown with grey lines for easy distinction. Plotting the two sides together, in comparison to nominal computational solutions with α and β fixed at zero, should illuminate any vehicle maneuvering influence, specifically pitch and yaw effects. Note that data shown for Q2 of Side B will be compared against Q1 of Side A, while Q3 is in comparison to Q4. In all the heat transfer plots, the point of departure from the turbulent heating levels (if it can be determined) are identified as the time of BL transition onset for each sensor location. This was done for consistency between the ascent and descent cases. In many of the upcoming plots, the onset times are obvious. Occasionally, the onset times are harder to determine, which requires a degree of "in family" assessment to help inform onset time selection.

Table 4. Replicate sensors from the two sides.

Side A Sensor	X (m)	Y (m)	Z (m)	Side B Sensor
MT-A-1-1	0.193	±0.029	0.103	MT-B-19-28
MT-A-1-3	0.193	±0.028	0.0	MT-B-19-50
MT-A-1-5	0.193	±0.029	-0.103	MT-B-19-72
MT-A-2-2	0.358	±0.053	0.106	MT-B-36-28
MT-A-2-5	0.358	±0.048	0.000	MT-B-36-50
MT-A-2-13	0.358	±0.053	-0.106	MT-B-36-72
MT-A-4-10	0.796	±0.105	-0.106	MT-B-80-19
MT-A-4-11	0.796	±0.107	-0.124	MT-B-80-72
MT-A-4-12	0.796	±0.109	-0.141	MT-B-80-77
MT-A-4-13	0.796	±0.111	-0.159	MT-B-80-81
MT-A-4-14	0.796	±0.113	-0.177	MT-B-80-85
MT-A-4-15	0.796	±0.116	-0.210	MT-B-80-89
MT-A-6-5	0.947	±0.119	0.000	MT-B-95-50
MT-A-6-10	0.947	±0.122	-0.084	MT-B-95-68
MT-A-6-11	0.947	±0.123	-0.101	MT-B-95-71
MT-A-6-12	0.947	±0.124	-0.118	MT-B-95-76
MT-A-6-13	0.947	±0.126	-0.135	MT-B-95-79
MT-A-6-14	0.947	±0.128	-0.152	MT-B-95-81
MT-A-6-16	0.947	±0.122	-0.186	MT-B-95-90

Sensors Near to Joint Step

Figure 10 provides a sketch showing four Side B thermocouples in near vicinity to the nose-joint steps: two on the leading edge just behind the step (MT-B-19-28 and MT-B-19-72) and two directly downstream but slightly inboard, away from the LE (MT-B-36-28 and MT-B-36-72). These four will be used to assess the step effect behavior during ascent and descent. Note that MT-B-19-28 and MT-B-36-28 are part of Q2, while MT-B-19-72 and MT-B-36-72 are on Q3.

Figures 11 -14 present the converted heat transfer results from these four thermocouples in comparison to computed laminar and turbulent heating values during ascent. Both Figs. 11 and 12 suggest that the leading edges behaved as if they remained laminar during the entire ascent test window. On the other hand, Figs. 13 and 14 would suggest that downstream of these steps on Side B, both sensors were initially turbulent and indicated consistent transition onset times at about 24 seconds during the ascent window. Figure 13 also indicates that two sides (Side A to Side B, thus Q2 to Q1) were consistent with a transition onset time of roughly 24 seconds, while Fig. 14 indicates that transition onset on Side B was a few seconds earlier (Q3 was earlier than Q4). An initial observation from the above is the quadrant that has the latest indication of transition onset during ascent could be indicative of a possible influence from roughness effects, perhaps from either surface roughness or steps.

Figures 15 - 18 provide the converted heat transfer traces for the same four thermocouples during the descent test window in comparison to the computed laminar and turbulent heating. Again, the leading-edge traces in Figs. 15 and 16 indicate laminar behavior during descent, all the way to end of flight at 409.0 seconds. The thermocouples downstream both indicate transition onset at about the same time, at 406.0 seconds. Consistent with the ascent results, one quadrant, shown in Fig. 17, indicates that Q2 has the same transition onset time as Q1 (Side A), while the other, shown in Fig. 18, indicates transition onset roughly 2 seconds earlier for Q4 (Side A). With consistent results during ascent and descent and considering that vehicle attitude is relatively steady throughout the test windows, provides further evidence that Q4 of Side A was likely the "rougher" quadrant throughout flight. Towards the end of this document, once all the data has been presented, a recap of possible step effects from the BOLT-2 flight data will be discussed.

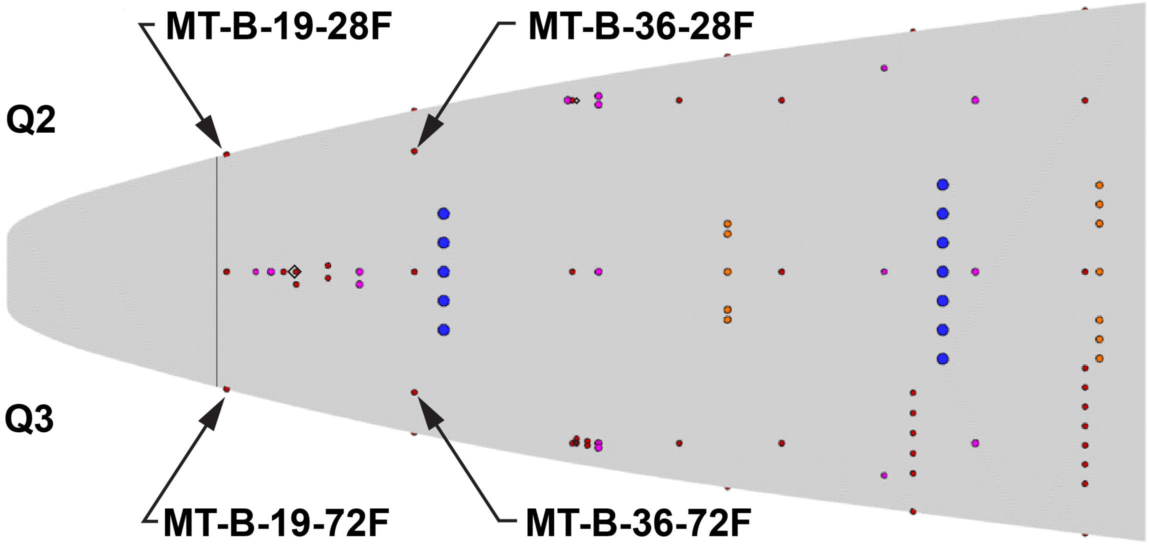

Figure 10. Thermocouples in near vicinity to the nose-joint step.

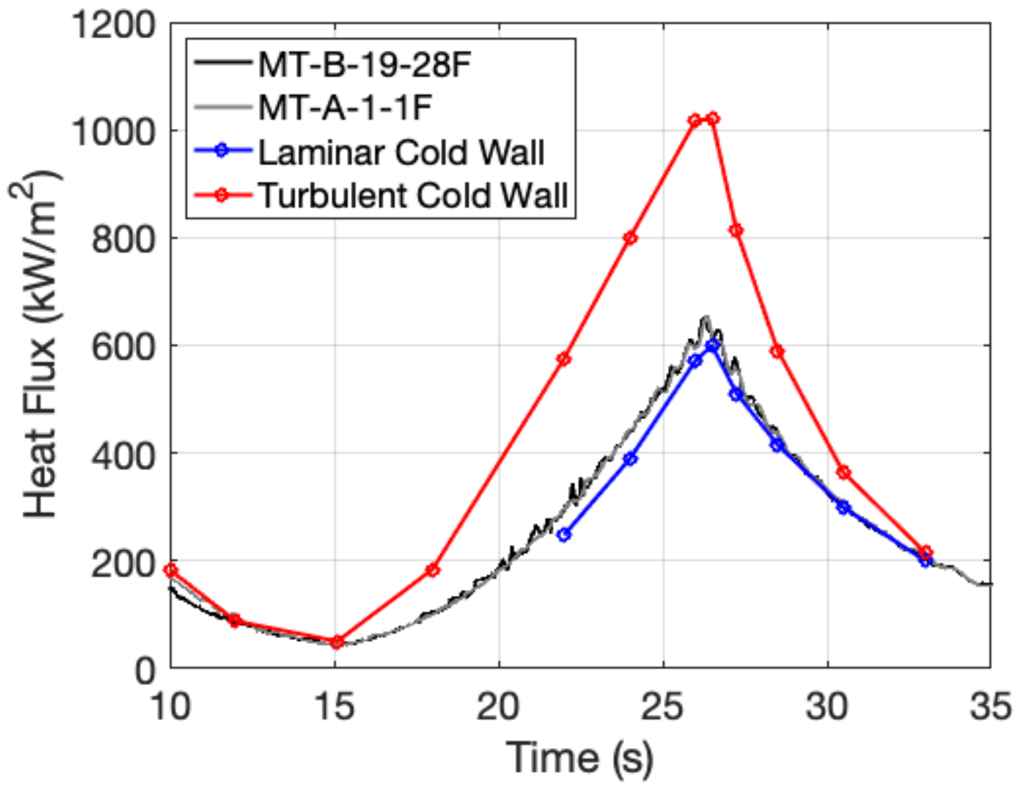

Figure 11. Calculated heat transfer during ascent from sensor MT-B-19-28

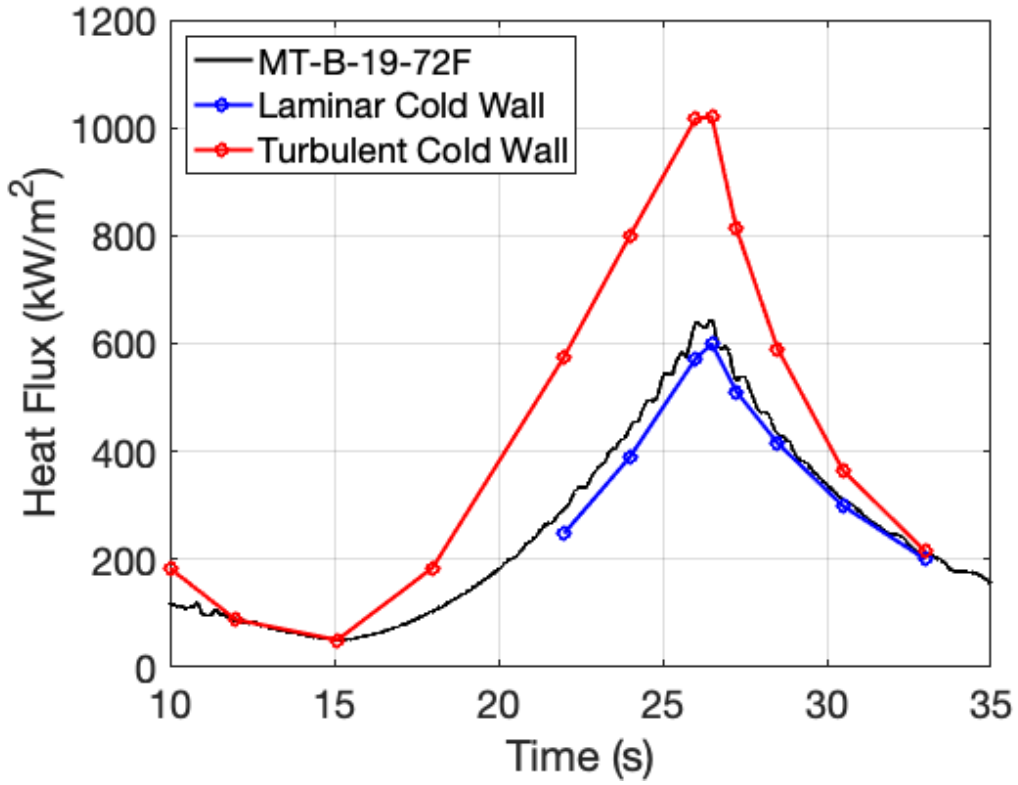

Figure 12. Calculated heat transfer during ascent from sensor MT-B-19-72

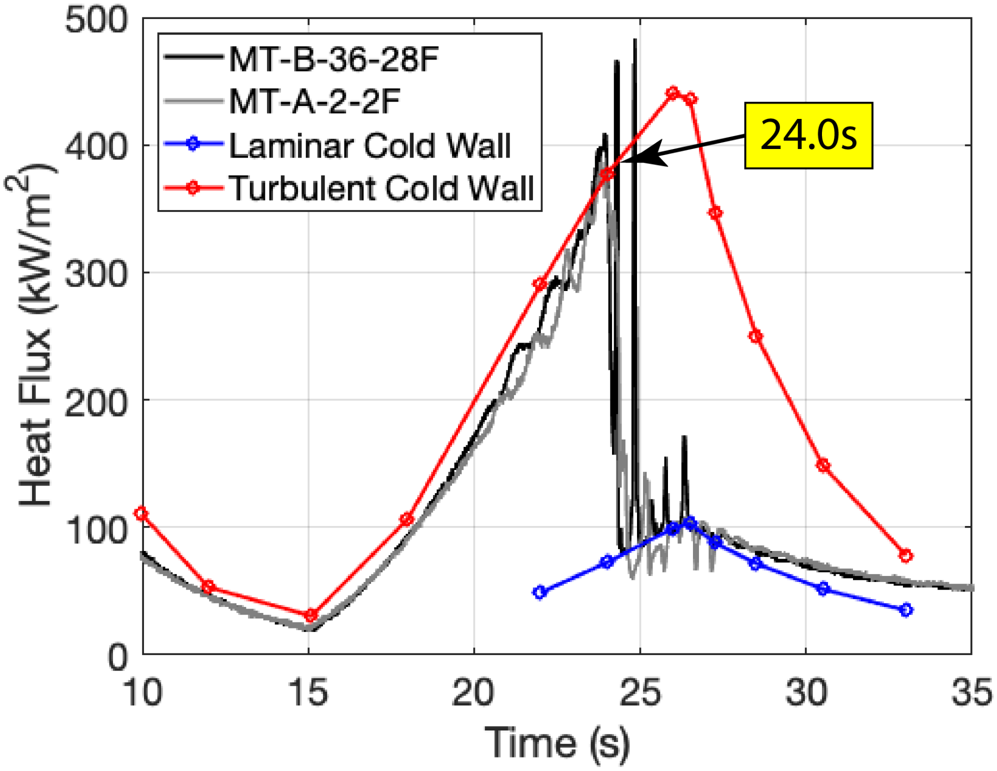

Figure 13. Calculated heat transfer during ascent from sensor MT-B-36-28

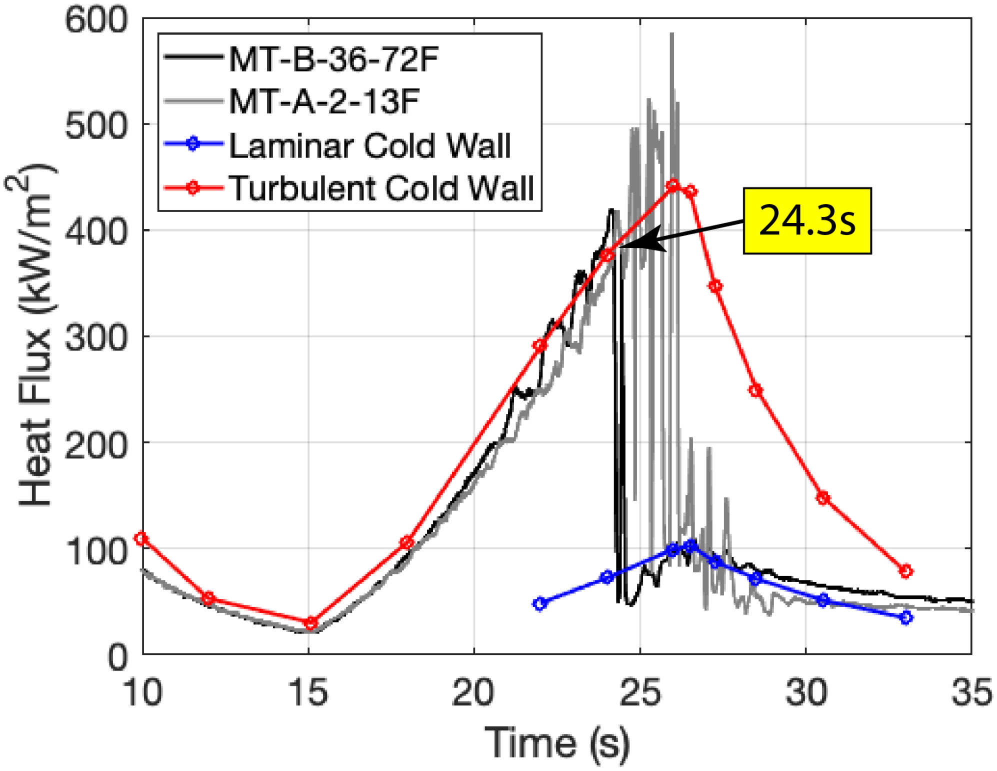

Figure 14. Calculated heat transfer during ascent from sensor MT-B-36-72

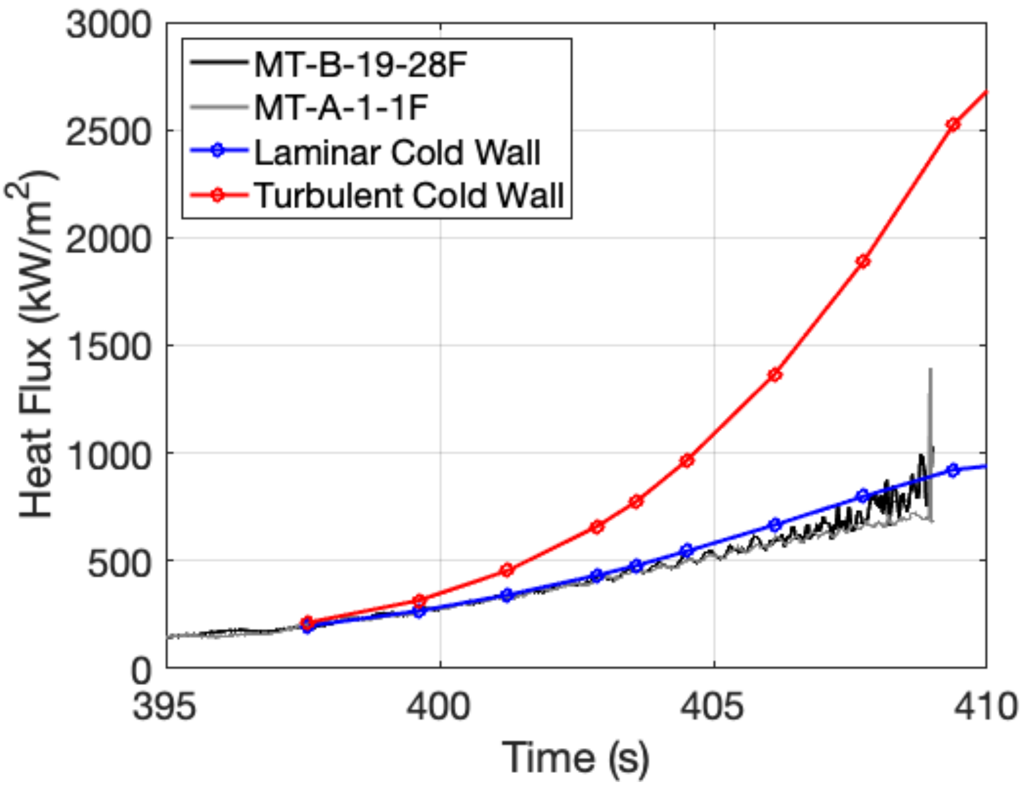

Figure 15. Calculated heat transfer during descent from sensor MT-B-19-28

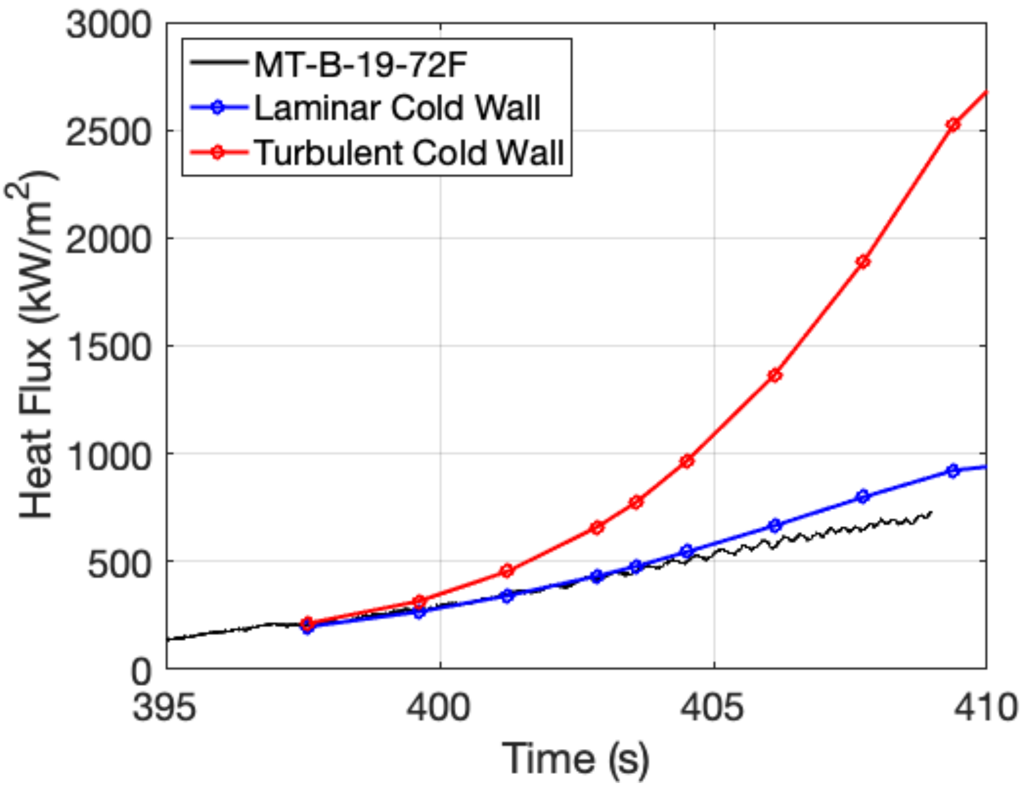

Figure 16. Calculated heat transfer during descent from sensor MT-B-19-72

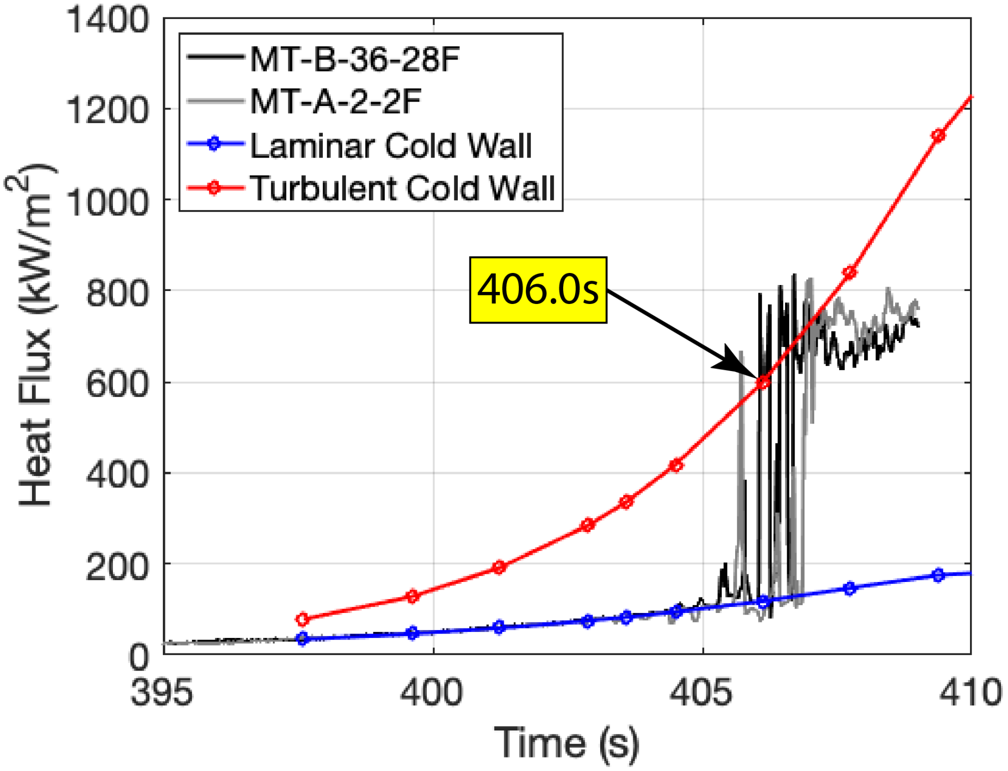

Figure 17. Calculated heat transfer during descent from sensor MT-B-36-28

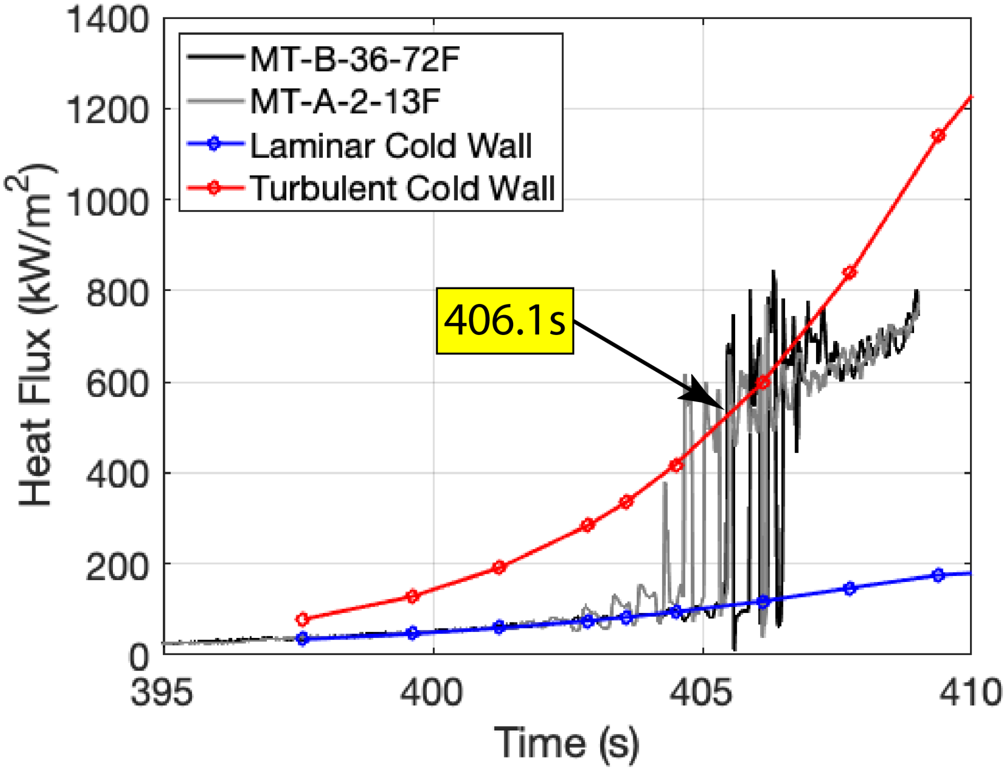

Figure 18. Calculated heat transfer during descent from sensor MT-B-36-72

Array In line with CL Trip

Figure 19 provides a sketch showing five Side B thermocouples that span the centerline of the vehicle, starting with MT-B-19-50 just behind the nose-joint, followed by several downstream of the CL trip (MT-B-36-50, MT-B-48-50, MT-B-70-50, and MT-B-95-50). These five will be used to determine the incipient and effective transition onset times associated with the CL trip during ascent and descent.

Downstream of the centerline (CL) trip, transition onset is demonstrated to progressively move down the body during ascent, as defined by the points of departure from the turbulent heating levels shown in Figs. 20 - 24, starting at 29.9s with the sensor nearest the trip (MT-B-36-50F), next at 30.7s (MT-B-48-50F), then at 31.6s (MT-B-70-50F), and finally at 33.1s (MT-B-95-50F). Note that in most cases the point of departure is easy to observe in the heating vs. time traces. But in rare cases subjectivity is required, such as in Fig. 21 where a transition onset time of 29.9s was selected based on consideration of the other locations in this group. A comparison between the sides at the end of the body is presented in Fig. 24, indicating that the CL trip was responsible for an additional 4-5 seconds of turbulence, as Side A was nearly all laminar at 28 seconds. Thus, the CL trip is demonstrated to have influenced transition behavior during ascent, with incipient transition (the point at which the trip first is detected in the far field) at 33.1s, while 29.9s would be considered the effective condition (when transition onset is at close to the trip as possible). A second comparison between the sides is presented in Fig. 20, which is for the sensor in front of the CL trip (MT-B-19-50F). In this case, the comparison suggests that, just downstream of the joint, Side B had the earlier transition onset time at 15.6s while Side A was slightly delayed (at ~18s). This observation could be related to the results previously discussed, with Side A showing slightly delayed transition onset during ascent in comparison to Side B. Additional discussion about possible steps effects from this sensor grouping will be deferred to later in this document.

During descent, transition onset from the CL trip starts at the rear of the vehicle and moves up the body, as shown in Fig 25 - 29, per expectations: beginning at 397.6s (MT-B-95-50); next at 398.7s (MT-B-7-50); then at 399.3s (MT-B-48-50); and finally at 399.6s (MT-B-36-50). Thus, during descent, the incipient point would be 397.7s and the effective condition would be 399.6s. The side-to-side comparison at the end of the vehicle (Fig. 29) shows the CL trip resulted in transition onset roughly 5 seconds before being seen on the smooth side, while in front of the trip both sides stayed laminar past the test window (at 409.5s) on descent.

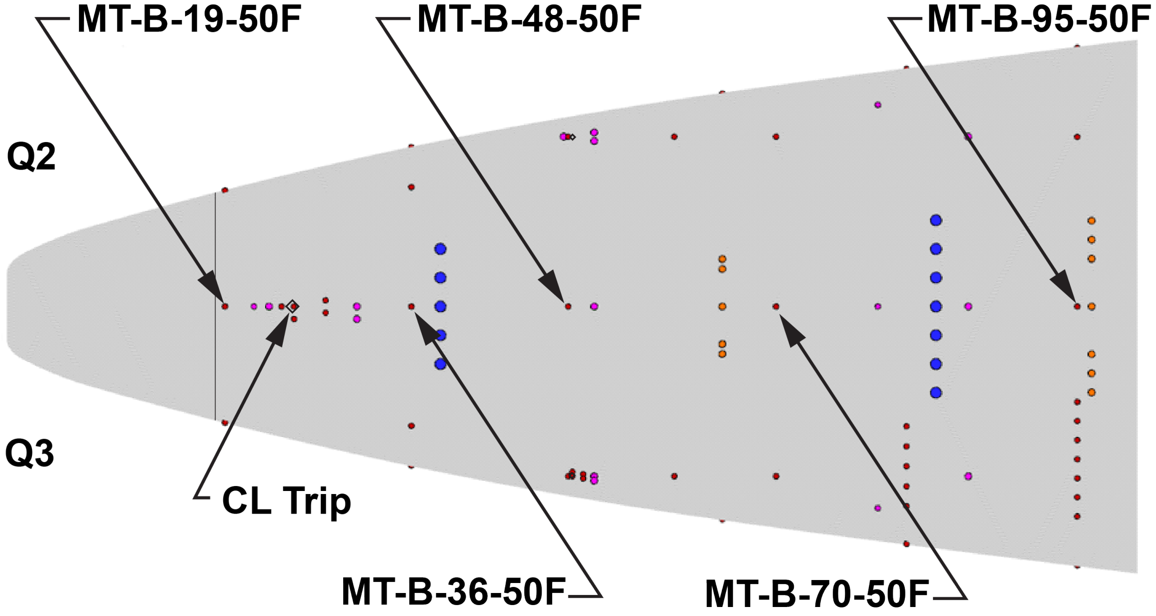

Figure 19. Thermocouples along Side B centerline

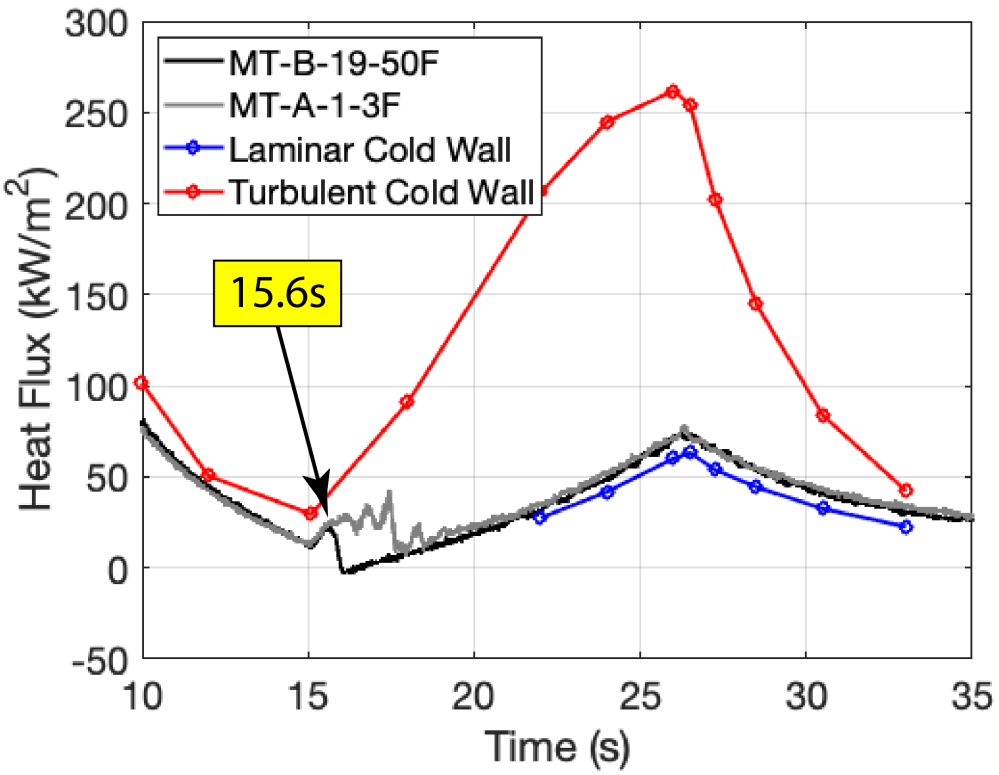

Figure 20. Calculated heat transfer during ascent from sensor MT-B-19-50F

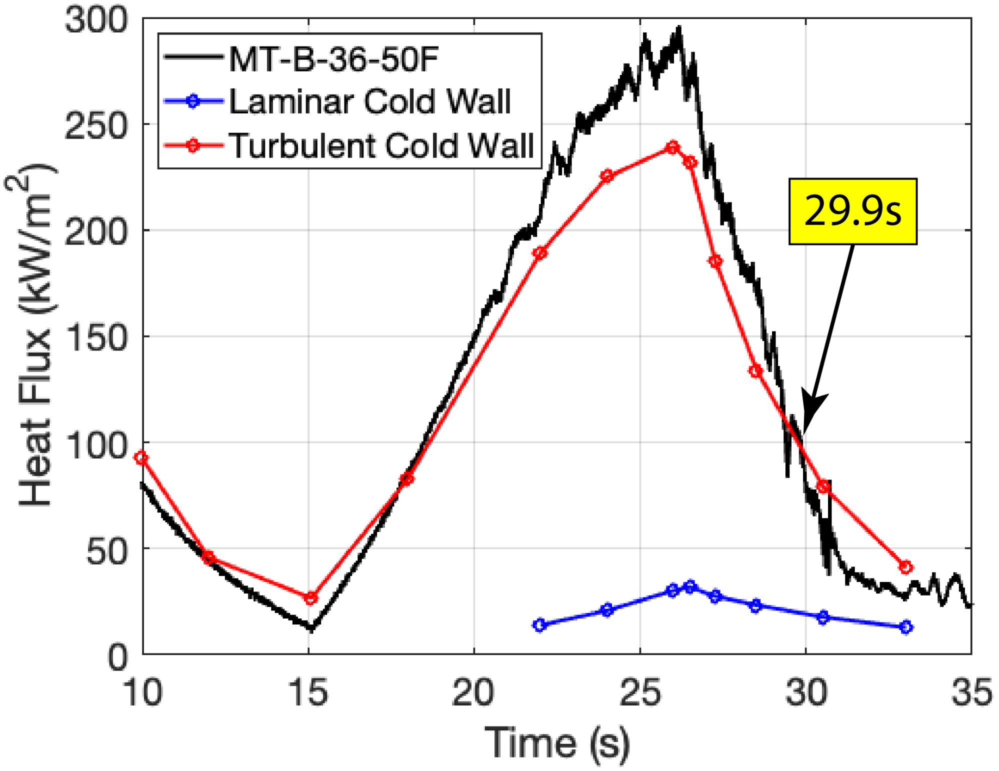

Figure 21. Calculated heat transfer during ascent from sensor MT-B-36-50F

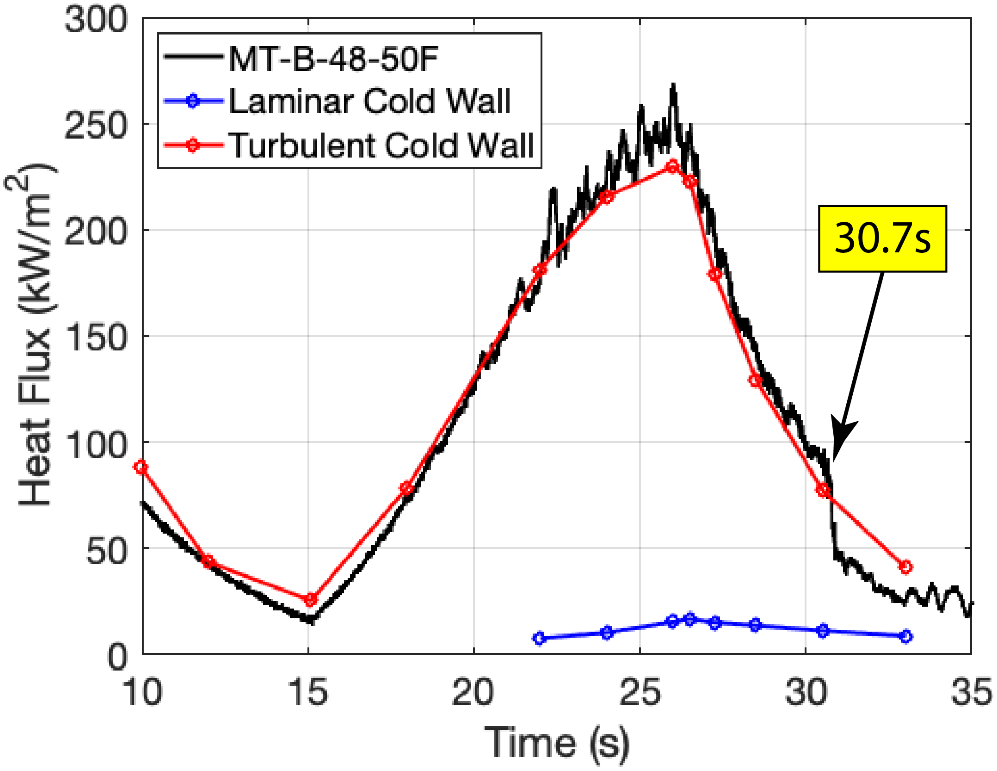

Figure 22. Calculated heat transfer during ascent from sensor MT-B-48-50F

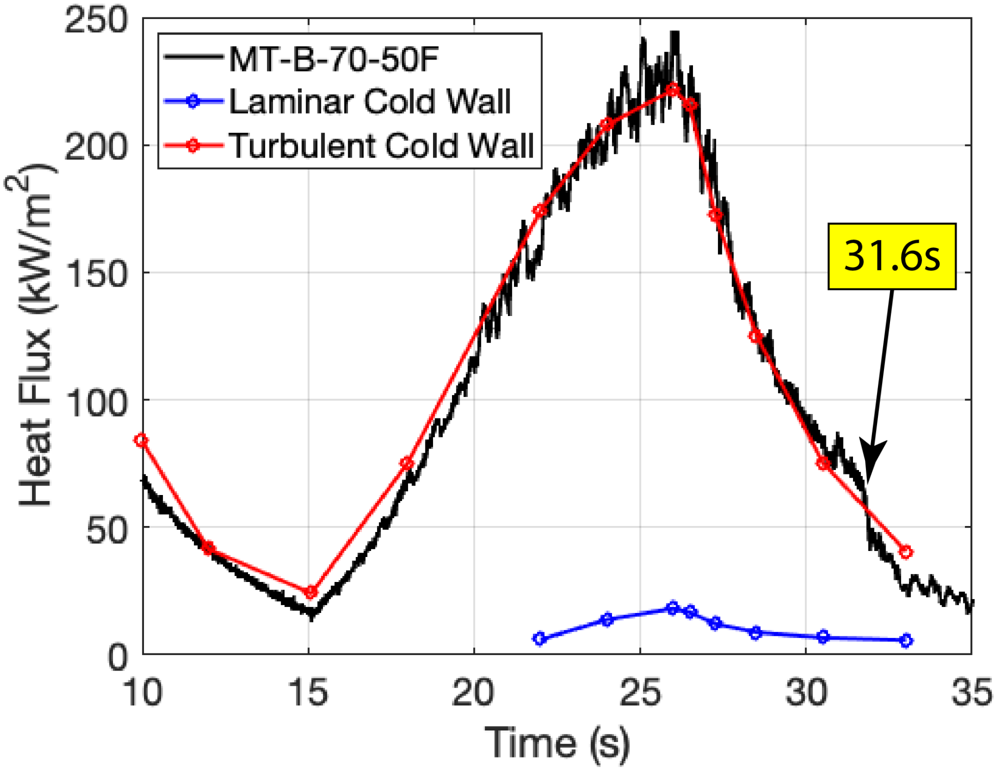

Figure 23. Calculated heat transfer during ascent from sensor MT-B-70-50F

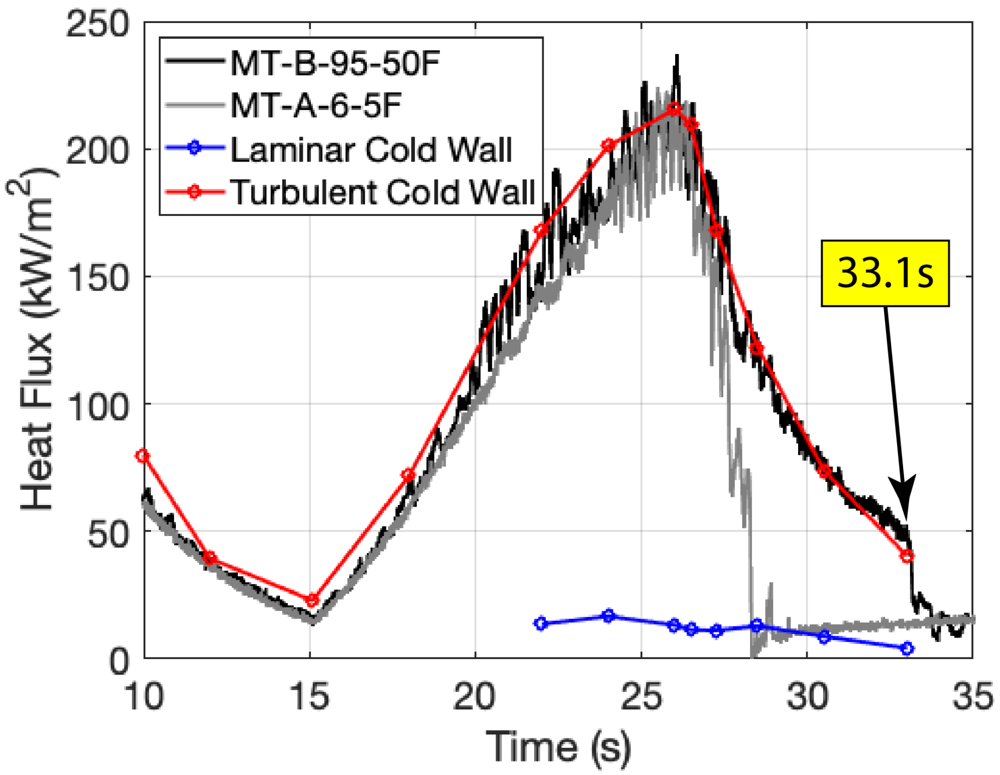

Figure 24. Calculated heat transfer during ascent from sensor MT-B-95-50F

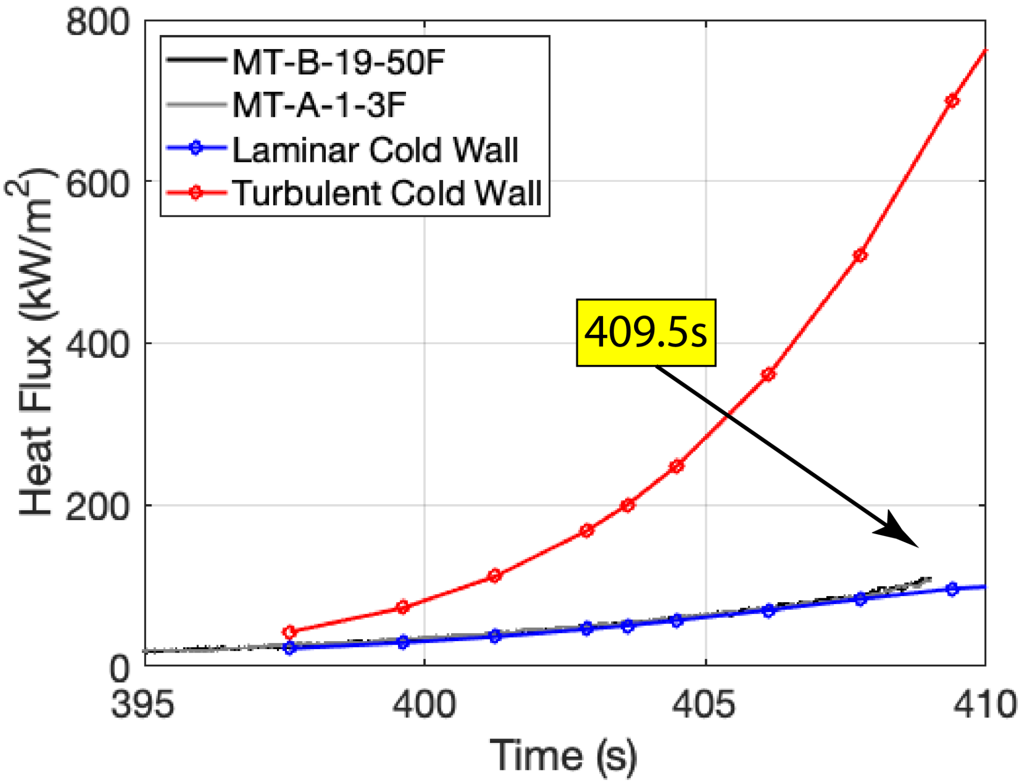

Figure 25. Calculated heat transfer during descent from sensor MT-B-19-50F

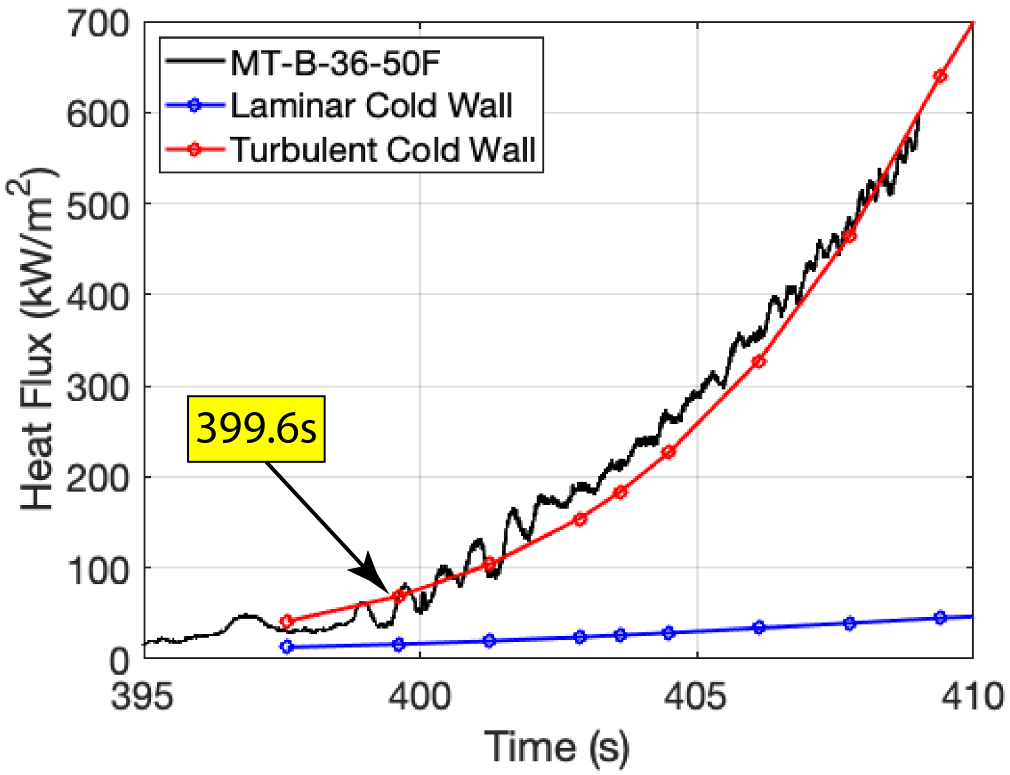

Figure 26. Calculated heat transfer during descent from sensor MT-B-36-50F

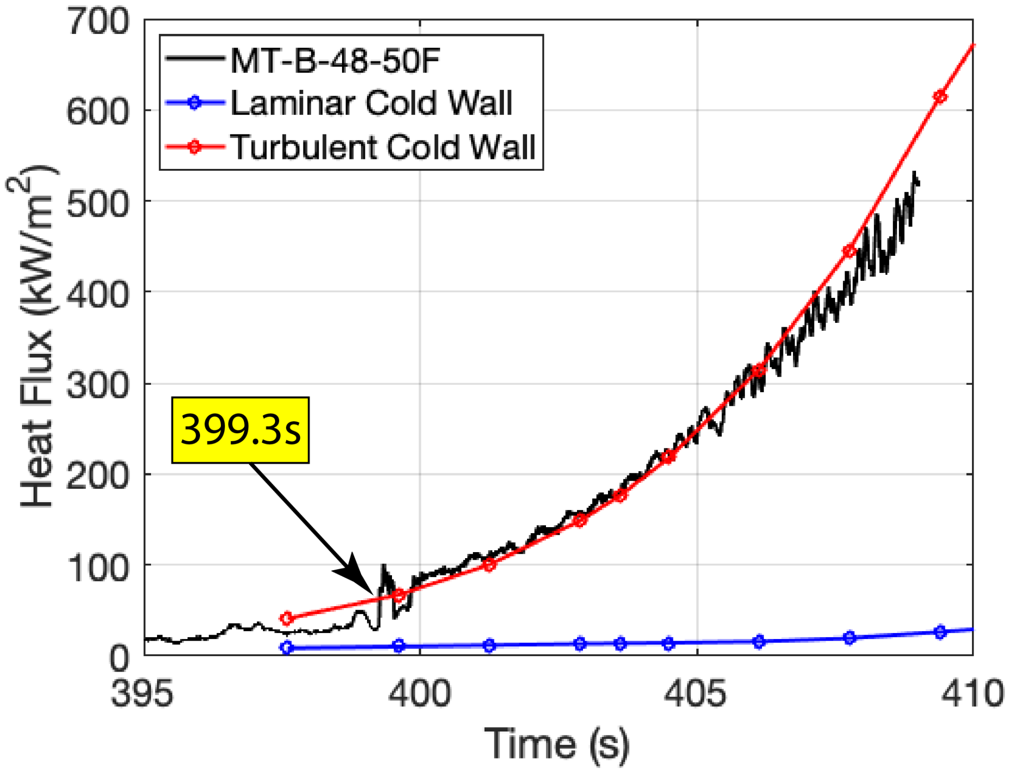

Figure 27. Calculated heat transfer during descent from sensor MT-B-48-50F

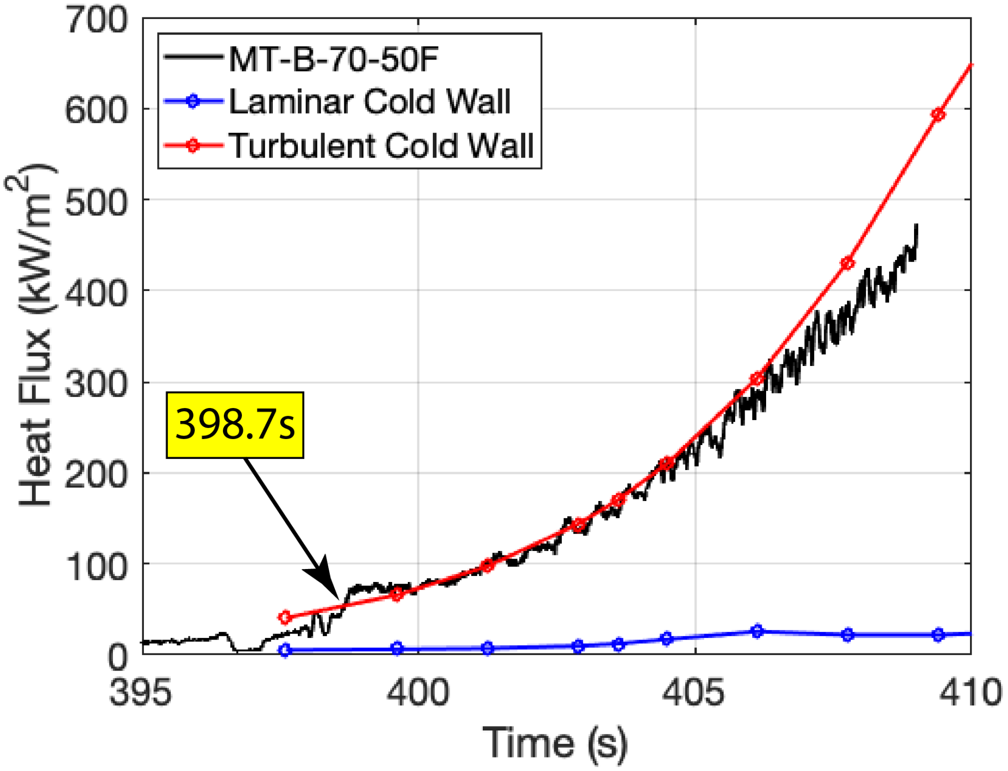

Figure 28. Calculated heat transfer during descent from sensor MT-B-70-50F

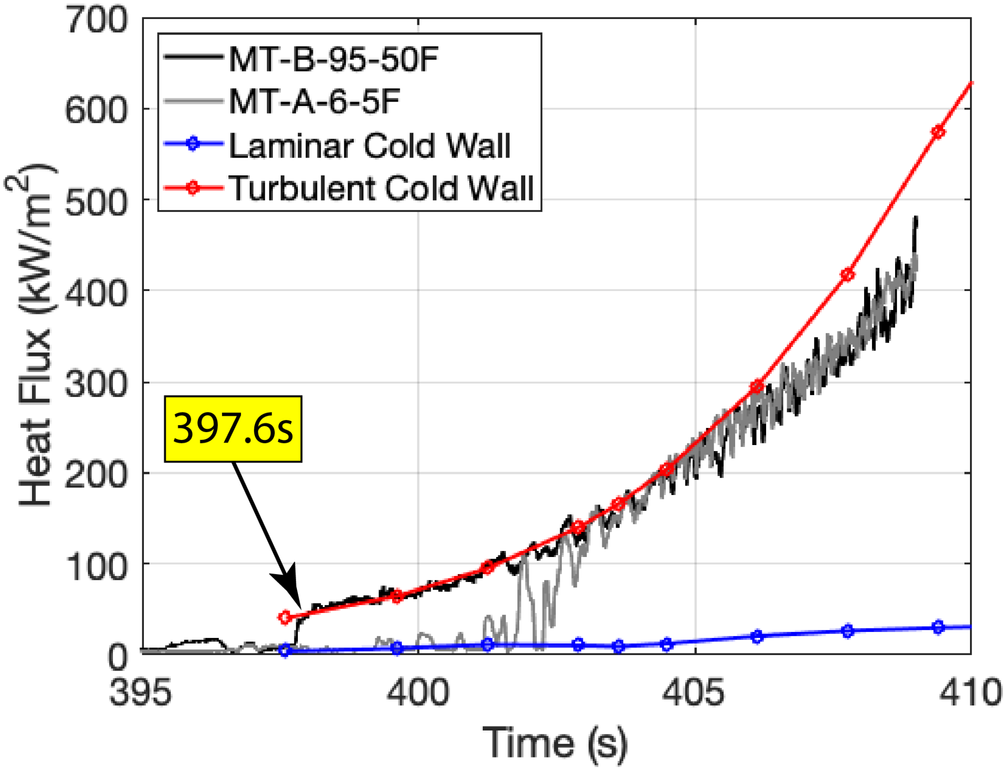

Figure 29. Calculated heat transfer during descent from sensor MT-B-95-50F

Sensors Near to CL Trip

Figures 30 and 31 provide sketches of the notional sensor map from both a global perspective and a zoomed-in view, respectively, showing the five Side B thermocouples that are near the centerline trip, starting with MT-B-23-50 which is just in front of the trip, MT-B-25-50 on top, MT-B-25-54 to the starboard side, and MT-B-28-49 and MT-B-28-51 that trail and straddle the trip. These five sensors are intended to illuminate the local heating associated with any vortex rollup (sometimes commonly referred to as a horseshoe shaped heating pattern) forming around the trip during flight. It is important to note that within the heating plots to come in this section, the CFD results are from smooth body solutions (no trips included) and are intended to reveal trip related deviations in heating.

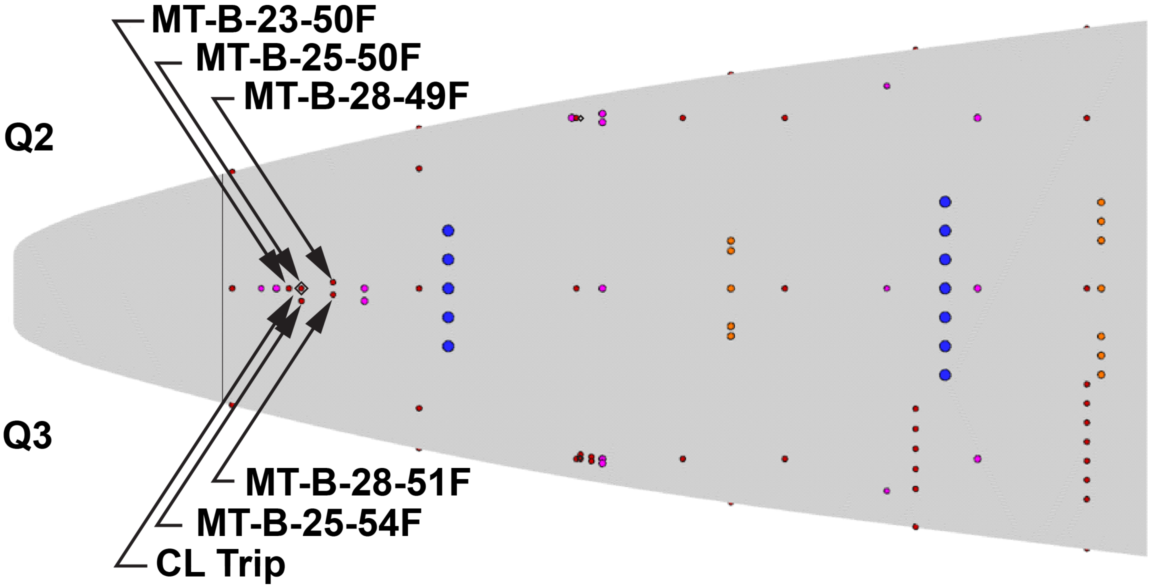

Figure 30. Thermocouples in near vicinity to Side B CL trip

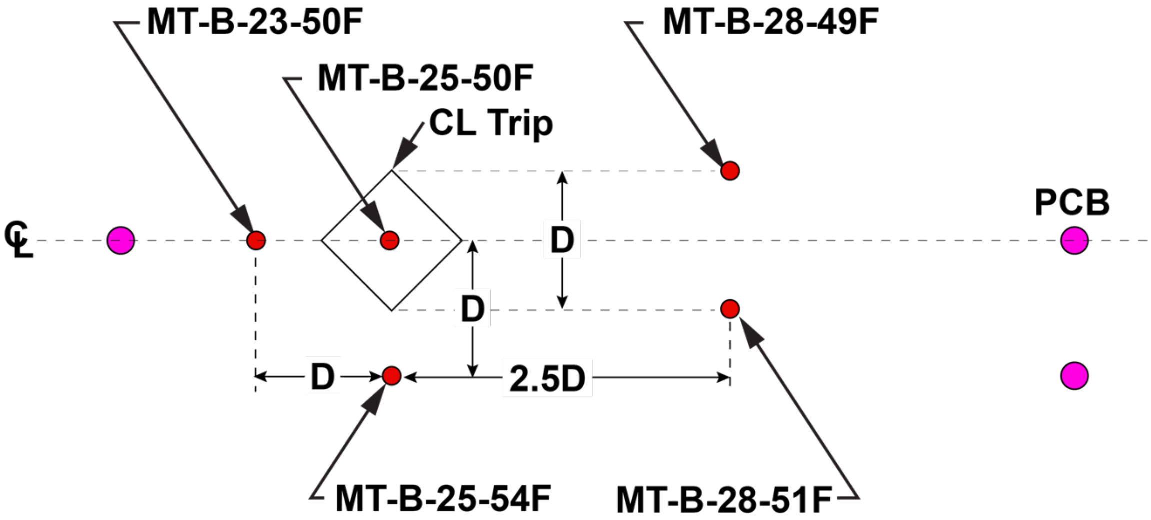

Figure 31. Close-up sketch of near CL trip thermocouples with relative spacing

The heating traces in vicinity to the CL trip during ascent are shown in Figs. 32 - 36, allowing an assessment of the local heating behavior, such as from the trip-induced heating pattern (that wraps around the trip in a horseshoe-like footprint), as a function of time. For instance, in front of the trip, MT-B-23-50 (Fig. 32) is shown to behave as if there is no trip, in line with the smooth wall turbulent heating values, until about 18s, which is interpreted as the time when the local BL becomes laminar, and the horseshoe vortex quickly changes to expand over this sensor location. After t=18s, measured heating levels follow a trend that falls between the laminar and turbulent smooth wall predictions, which could be indicative of the local augmentation resulting from the horseshoe heating induced by the trip under laminar conditions. Please refer to Appendix C for an in-depth discussion of flow around the trips as interpreted from looking at surface streamlines from an oil-flow image on a similar configuration. Figure 33 provides the heating for MT-B-25-50, which is located on top of the trip and therefore does not behave at any point like the smooth wall computations, nor should it be expected to. In this case, a sensor on top of the trip is likely being influenced by heating from multiple dimensions, so the one-dimensional and semi-infinite accounting of the present heating analysis should not be expected to provide a meaningful result. As a point of possible interest as a boundary condition for future computations, the peak measured temperature from this sensor during ascent was 270°C (or 518°F) at around 27s. Figure 34 (MT-B-25-54) provides the local heating to one side of the trip, which initially tracks along with the smooth wall turbulent heating predictions until (again) about t=18s, when the measured heating starts to rise significantly above (~2x) the smooth-wall turbulent predictions. A similar result is seen downstream of the trip, in Fig. 36 (MT-B-28-51), which initially tracks with the smooth wall turbulent trends until about 18s, at which point the measured trace moves above the predicted turbulent levels. The trace shown for MT-B-28-49 (Fig. 35) appears to indicate this sensor as being faulty or otherwise unreliable, perhaps due to an intermittent short circuit or wiring fault. Considering the transition onset times during ascent from other nearby thermocouples, with MT-B-19-50 (near the nose-joint step) showing 15.6s and MT-B-36-28 and MT-B-36-72 (a little further downstream but away from the trip) showing 24.0s and 24.3s, respectively, a transition onset time of 18s near the CL trip seems appropriate.

During descent, the trends seen in Figs. 37 - 41 are consistent with above, except that now the vehicle starts out entirely laminar. For instance, Fig. 37 (MT-B-23-50) indicates that the measured trace follows the smooth-body laminar prediction until about 401s, when the measured heating starts to rise, but not to the smooth wall turbulent levels. Both the sensor to the one side (MT-B-25-54) and trailing the trip (MT-B-28-51) start off following the laminar trace until about 395s, at which point they both trend slightly higher than the predicted smooth-wall turbulent heating. During descent, the other nearby thermocouples indicate either no transition onset (see Fig. 25 for MT-B-19-50) or onset at roughly 406s just downstream of the trip location (see Fig. 17 for MT-B-36-28 and Fig. 18 for MT-B-36-72). The peak temperature on top of the trip during descent was 355°C (671°F) near the end of flight (407s).

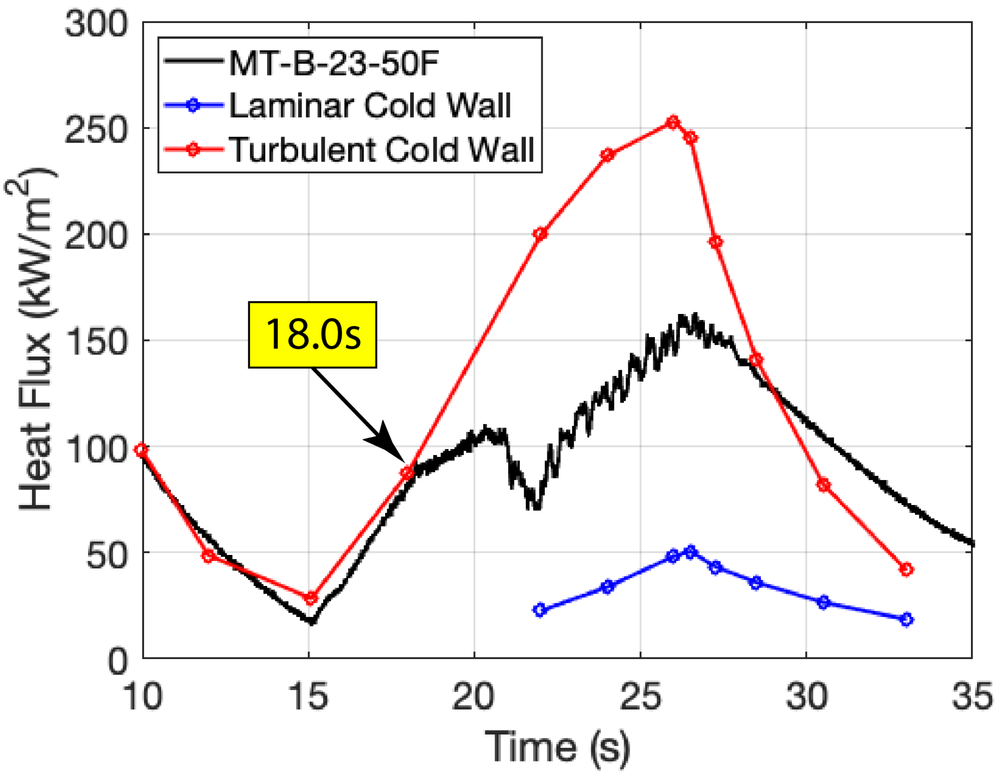

Figure 32. Calculated heat transfer during ascent from sensor MT-B-23-50F

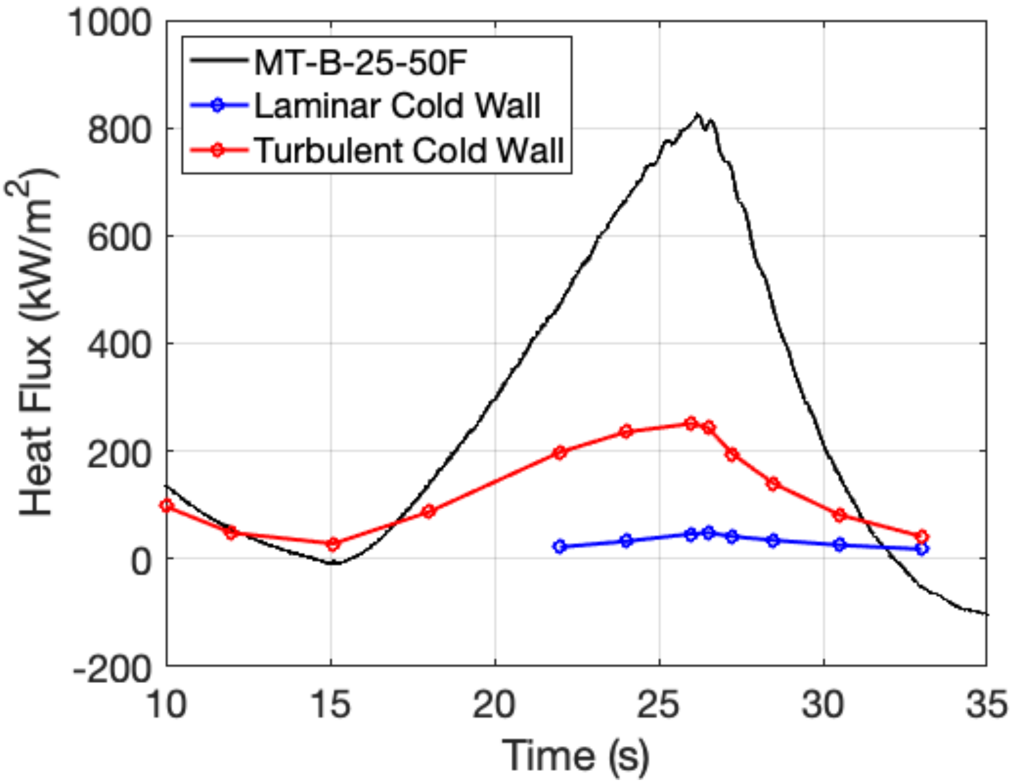

Figure 33. Calculated heat transfer during ascent from sensor MT-B-25-50F

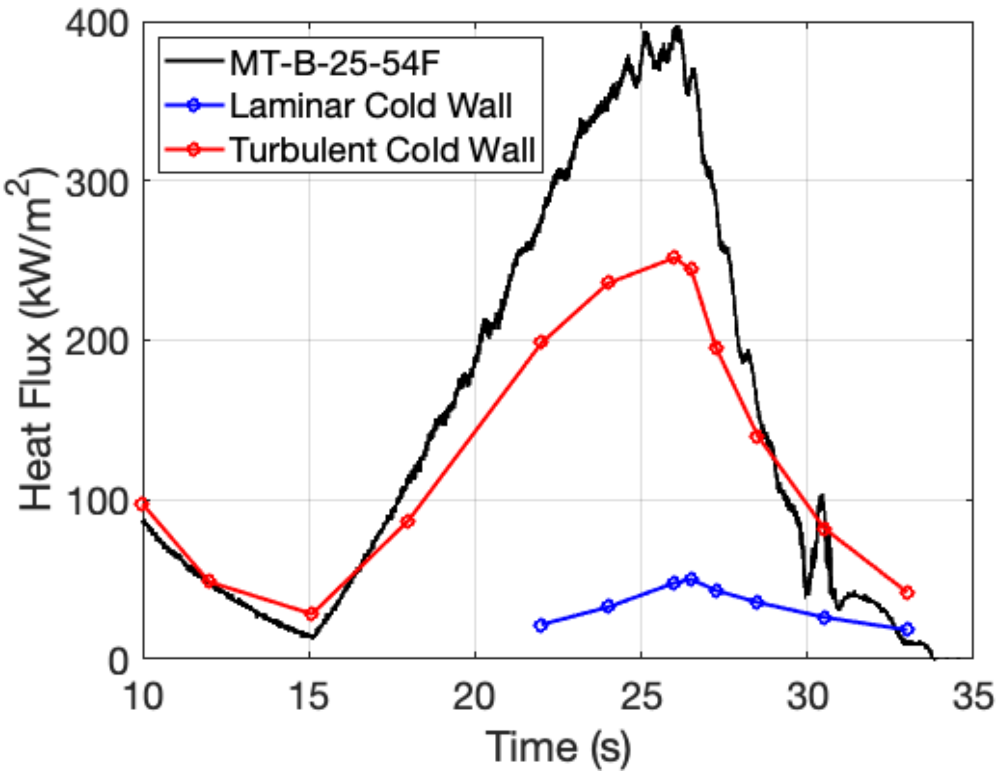

Figure 34. Calculated heat transfer during ascent from sensor MT-B-25-54F

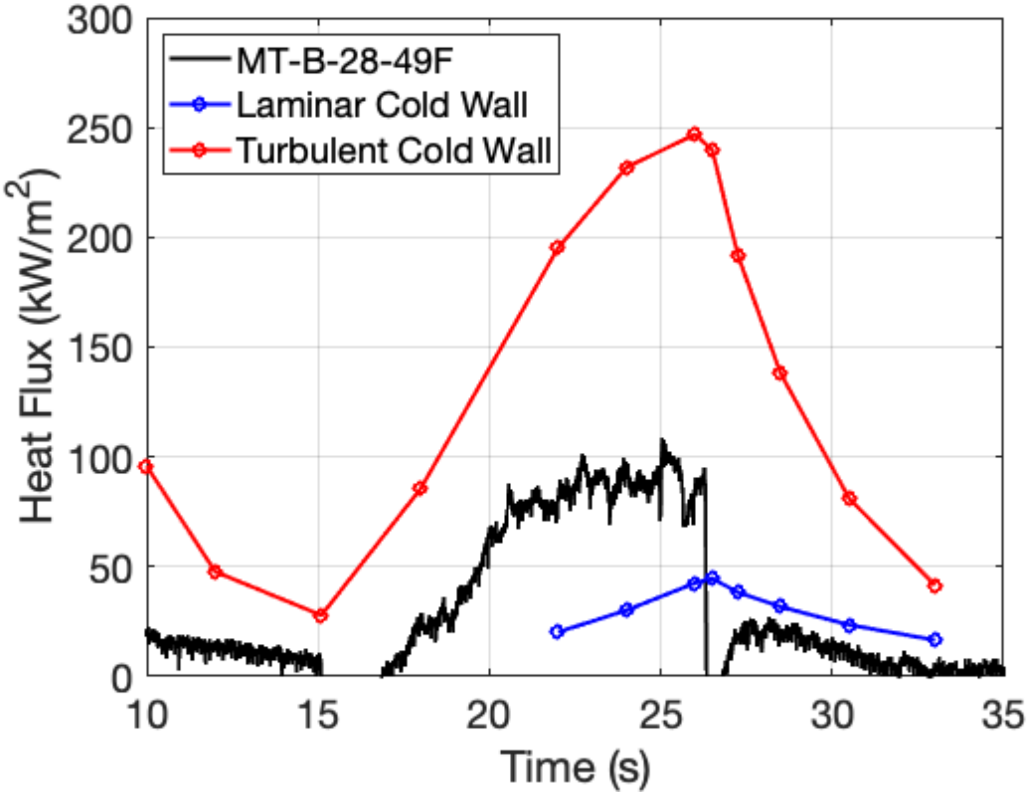

Figure 35. Calculated heat transfer during ascent from sensor MT-B-28-49

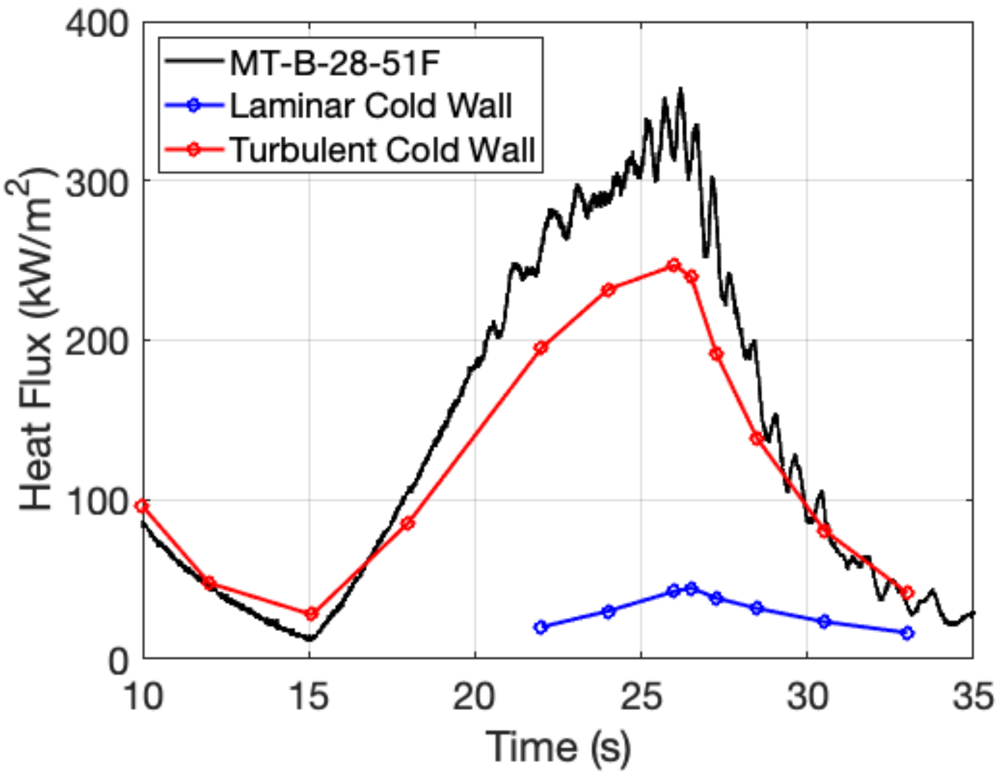

Figure 36. Calculated heat transfer during ascent from sensor MT-B-28-51

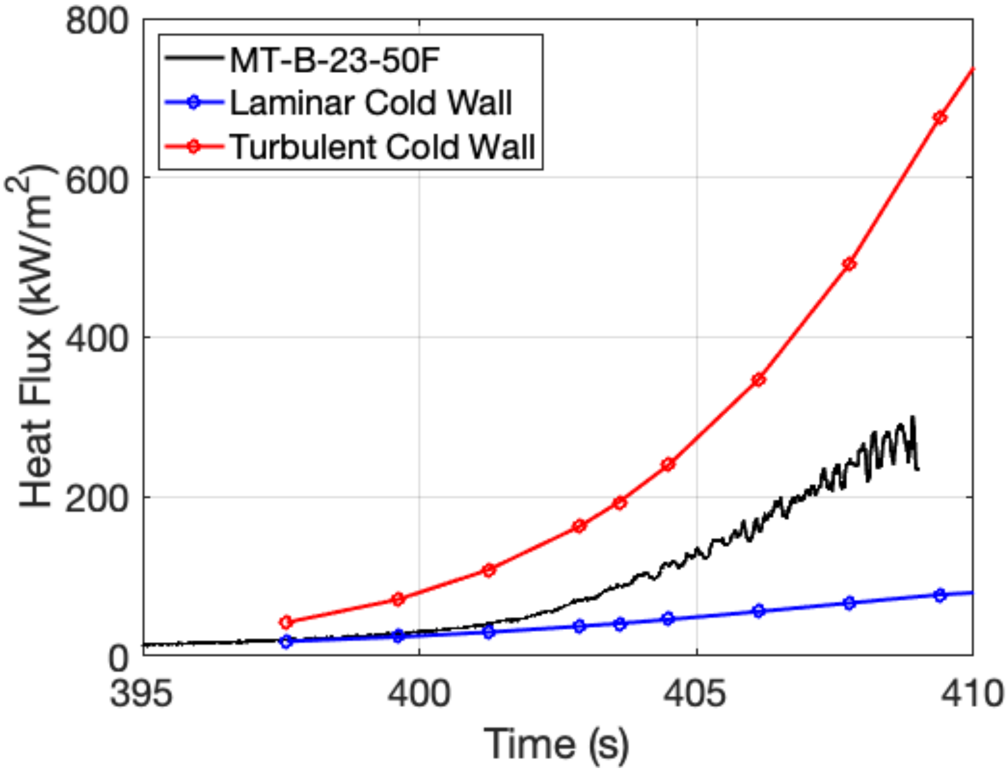

Figure 37. Calculated heat transfer during descent from sensor MT-B-23-50F

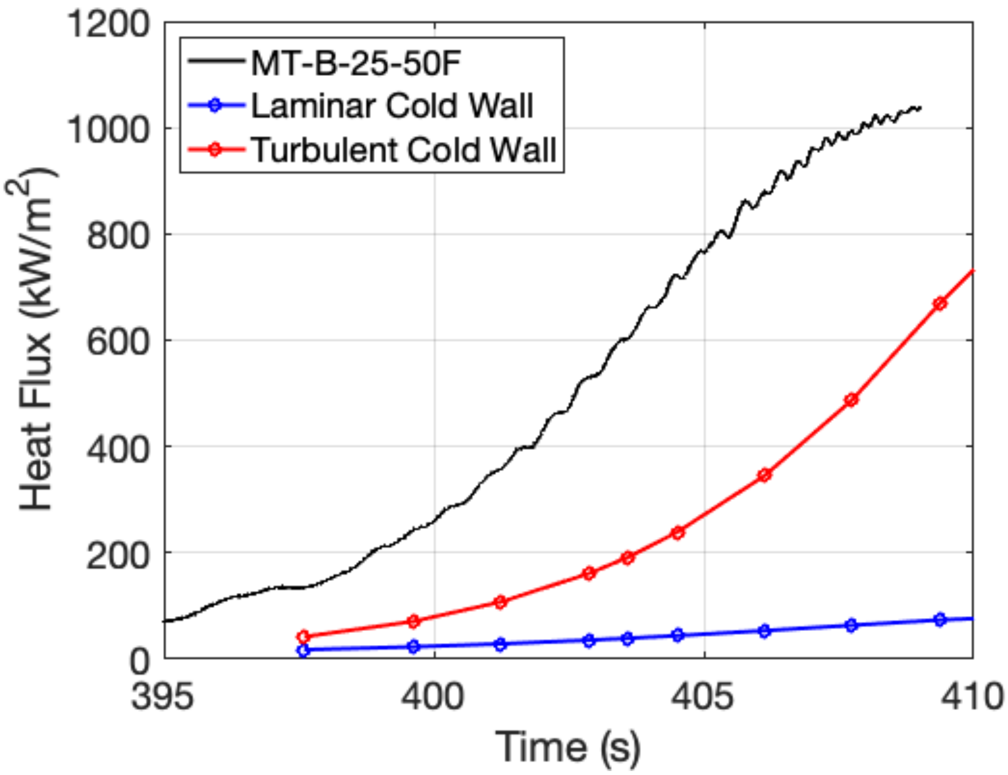

Figure 38. Calculated heat transfer during descent from sensor MT-B-25-50F

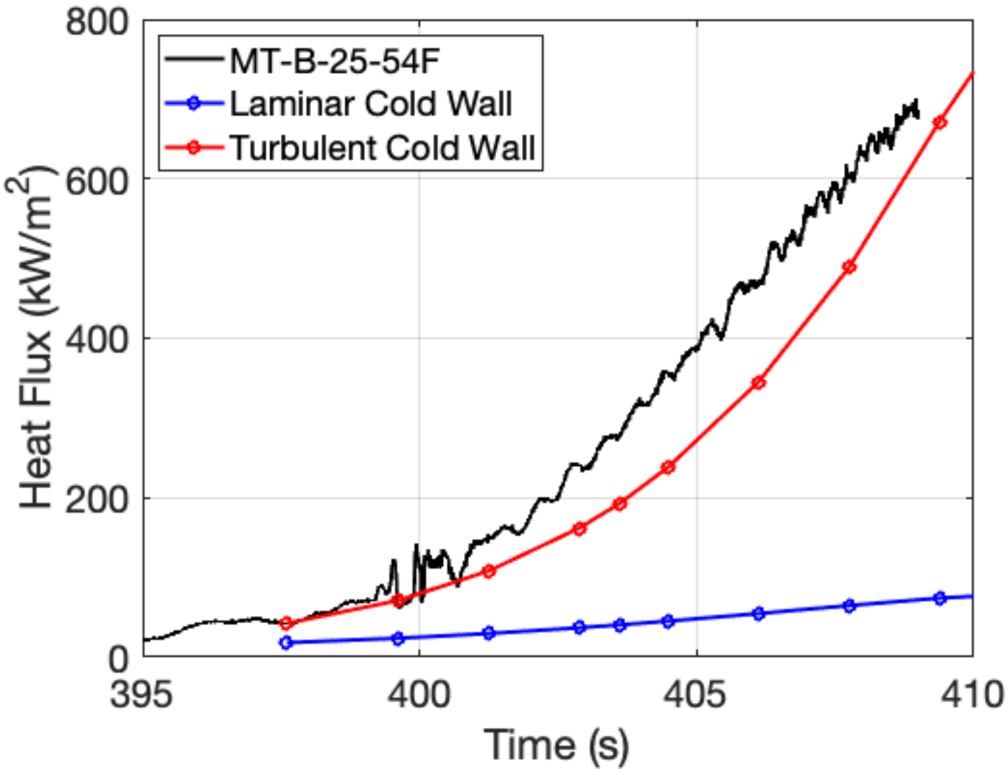

Figure 39. Calculated heat transfer during descent from sensor MT-B-25-54F

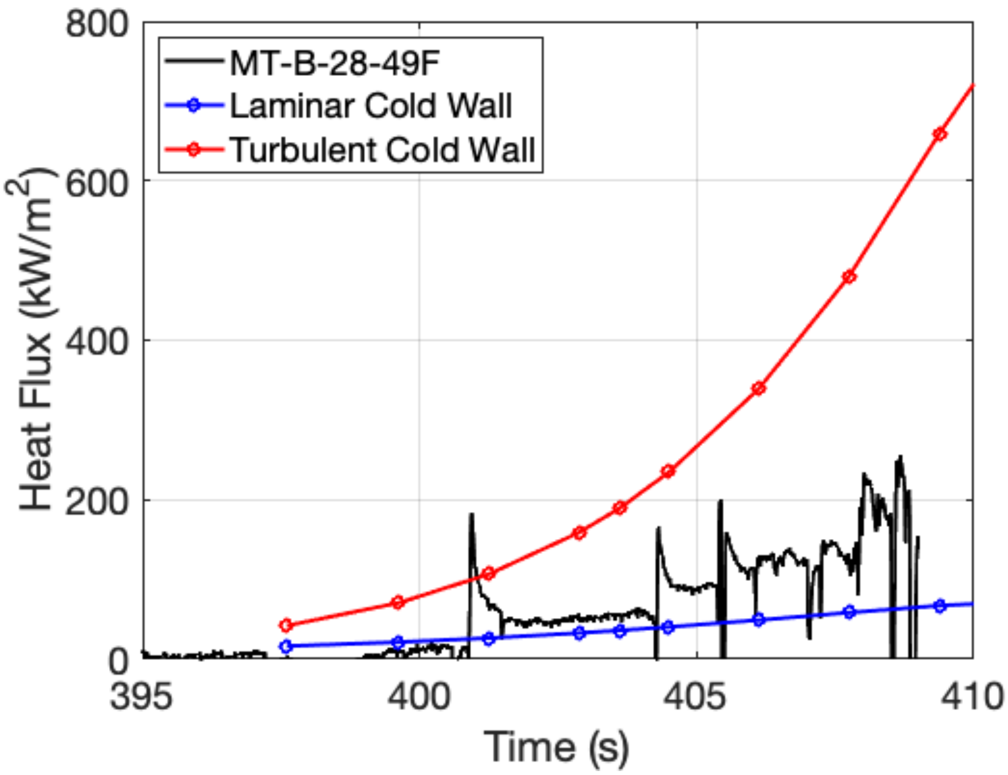

Figure 40. Calculated heat transfer during descent from sensor MT-B-28-49

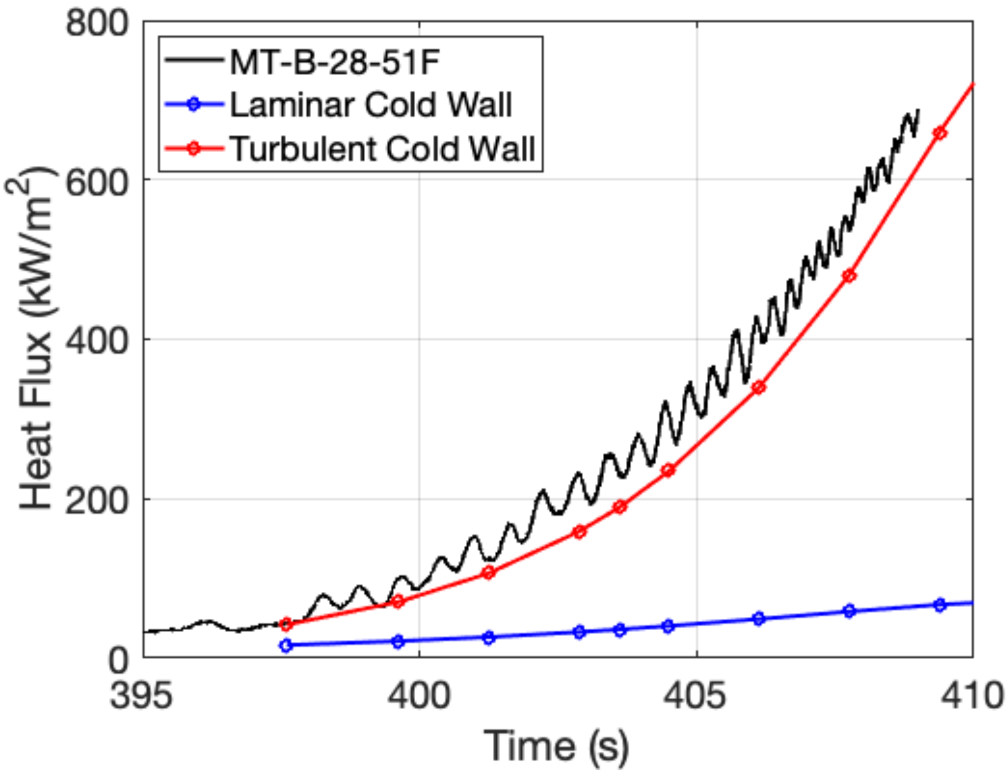

Figure 41. Calculated heat transfer during descent from sensor MT-B-28-51F

Array In line with LE-19 Trip

Figure 42 provides a sketch showing four Side B thermocouples that are aligned along the length of the port side leading edge trip (LE-19), starting with MT-B-48-19 in front of the trip, followed by MT-B-52-19, MT-B-70-19, and MT-B-95-19 behind the trip. These four will be used to determine the incipient and effective transition onset times associated with the LE-19 trip during ascent and descent.

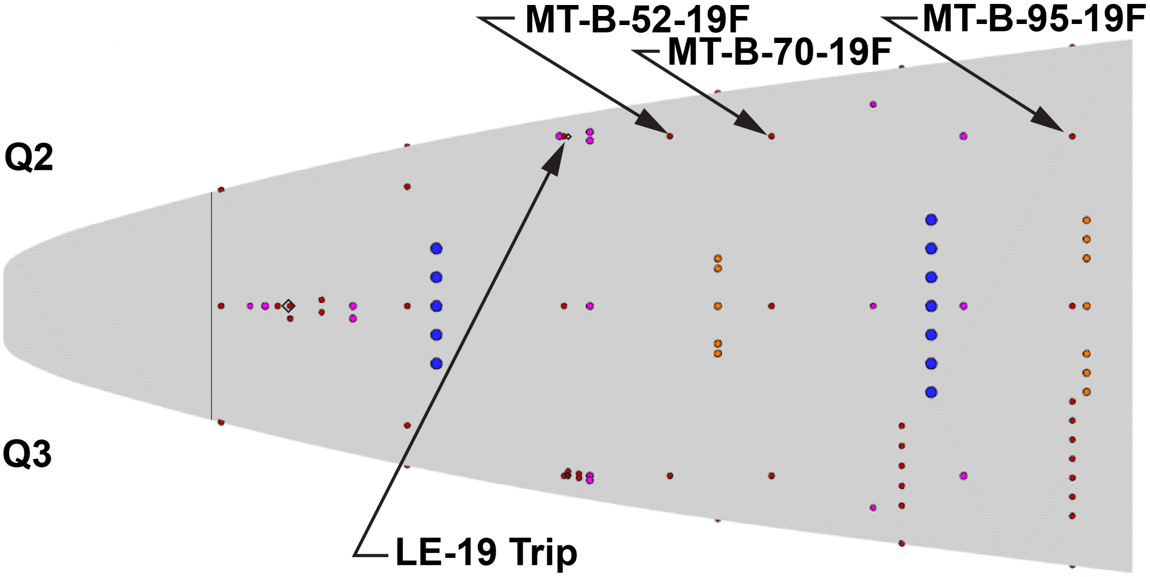

Figure 42. Thermocouples aligned with the Side B LE-19 trip

Figures 43 - 46 provides the measured heating traces during ascent for the thermocouples in line with the LE-19 trip. In front of the trip, at MT-B-48-19 (Fig. 43), the measured heating follows the smooth-wall turbulent predicted values until about 23s, at which time it then falls between the laminar and turbulent predictions. The behavior here is comparable to that observed in front of the CL trip at MT-B-23-50, except since this location is further down the vehicle, the observed onset time is more in agreement with the t=22s measured at MT-B-36-28 (which is just a little upstream of this trip). Downstream of the LE-19 trip, the inferred transition onset times during ascent are shown in Figs. 44 - 46, which shows well-behaved and systematic movement of transition with this sensor array, starting with 29.1s at MT-B-52-19F (Fig. 44), then 29.8s at MT-B-70-19F (Fig. 45), and 29.9s at MT-B-95-19F (Fig. 46). Thus, incipient transition during ascent for LE-19 would correspond to 29.9s, while effective transition would be at 29.1s. There are no comparisons between Sides A and B with any of these four sensors, nor are there spanwise arrays of thermocouples behind the LE-19 trip.

Figures 47 - 50 provides the measured heating traces for the same thermocouples in line with the LE-19 trip during descent. Figure 47 provides the measured heating for MT-B-48-19, just in front of the trip, and indicates heating consistent with the predicted laminar values initially until around 396s, which then rises to a level in between laminar and turbulent until about 406s where it jumps above the predicted turbulent levels. The initial measurements from 396s to 406s could be due to the influence of the horseshoe rollup around the LE-19 trip under an initially laminar incoming boundary layer. After 406s the incoming boundary layer then switches to a turbulent condition. Downstream of the LE-19 trip, the inferred transition onset times during descent quickly moves up the body, as expected, first starting at 400.7s at MT-B-95-19, followed by MT-B-70-19 at 400.8s, and finally 401.2s at MT-B-52-19. Incipient transition for LE-19 would correspond to 400.7s, while effective transition is at 401.2s during descent. Again, there are no comparison data from Side A nor data from spanwise arrays.

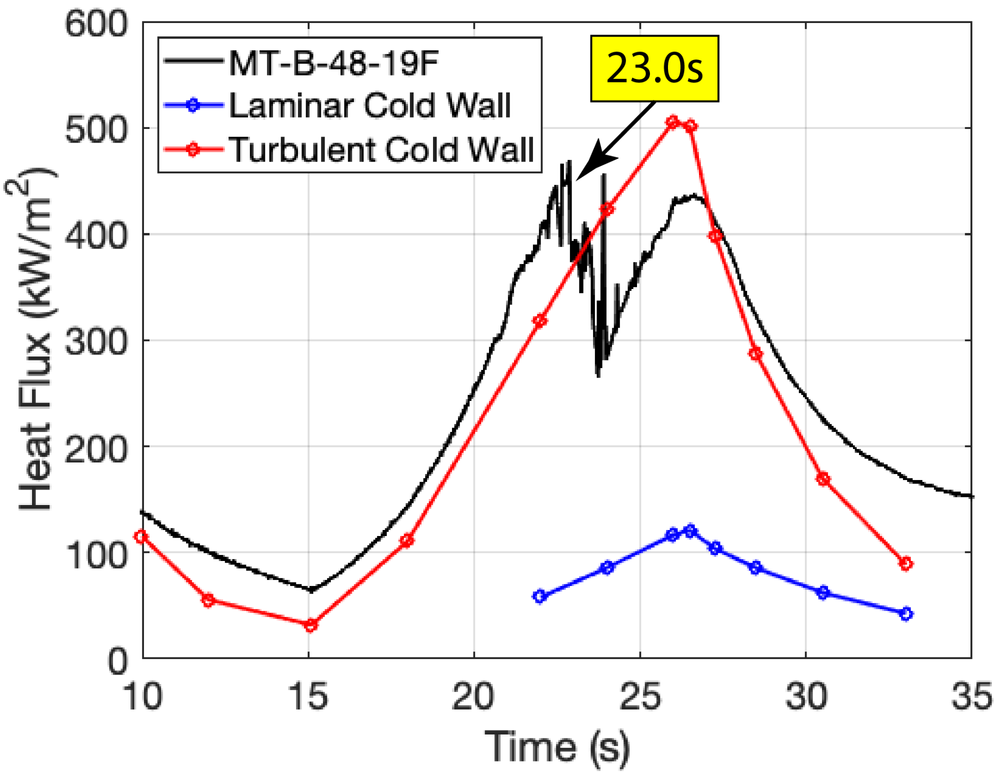

Figure 43. Calculated heat transfer during ascent from sensor MT-B-48-19

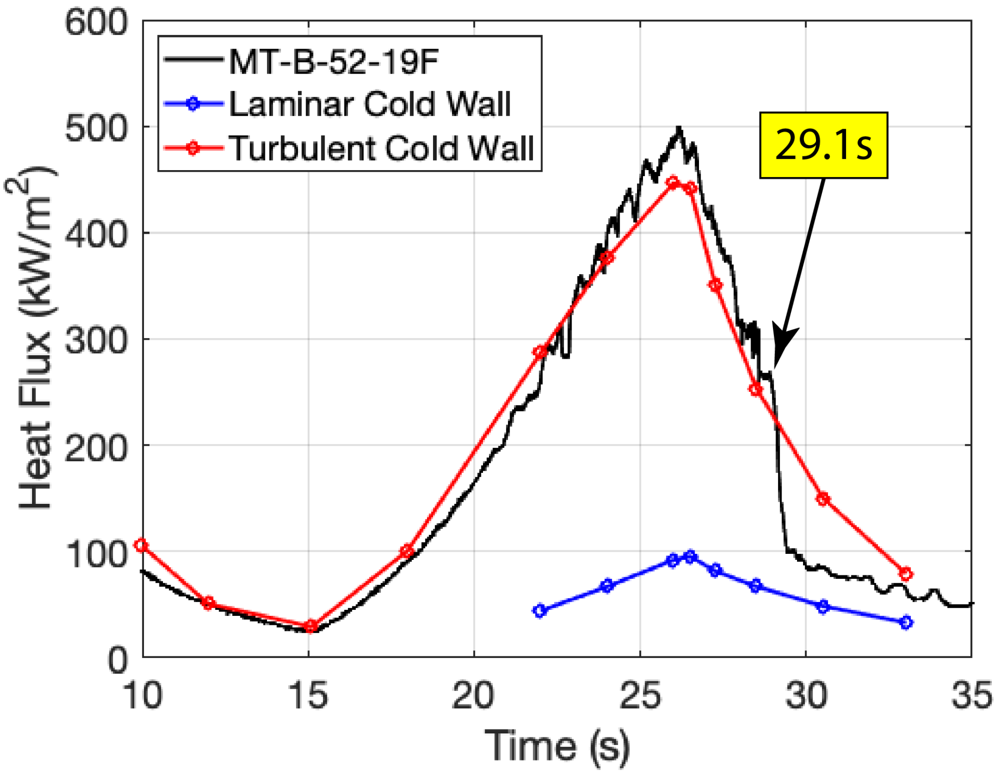

Figure 44. Calculated heat transfer during ascent from sensor MT-B-52-19

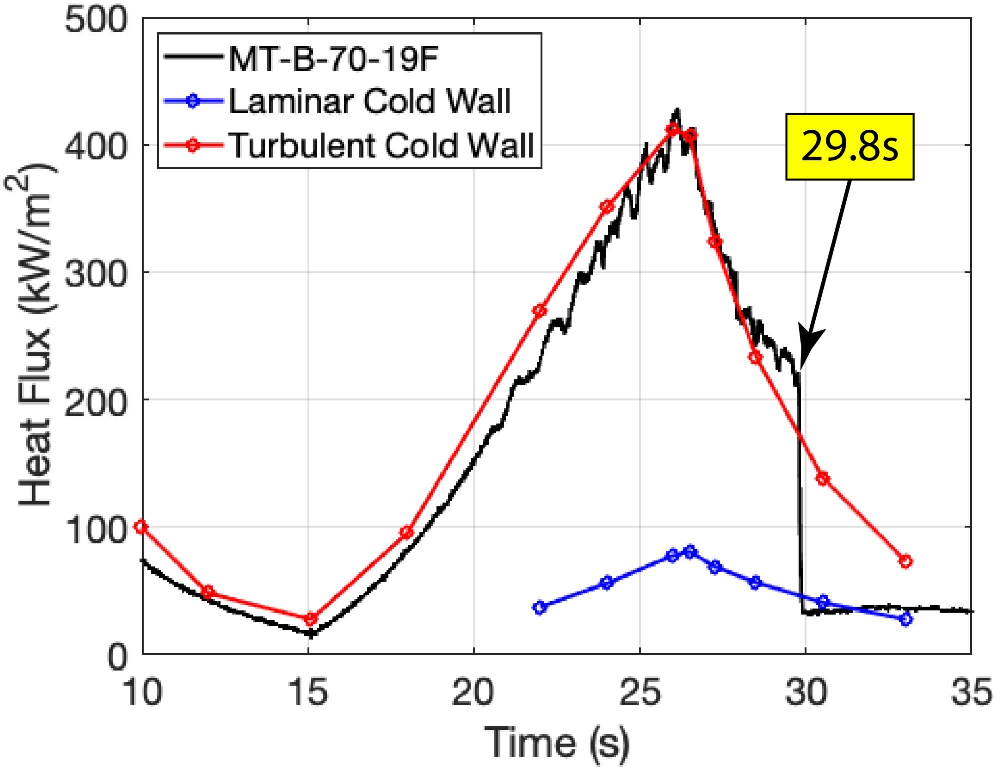

Figure 45. Calculated heat transfer during ascent from sensor MT-B-70-19

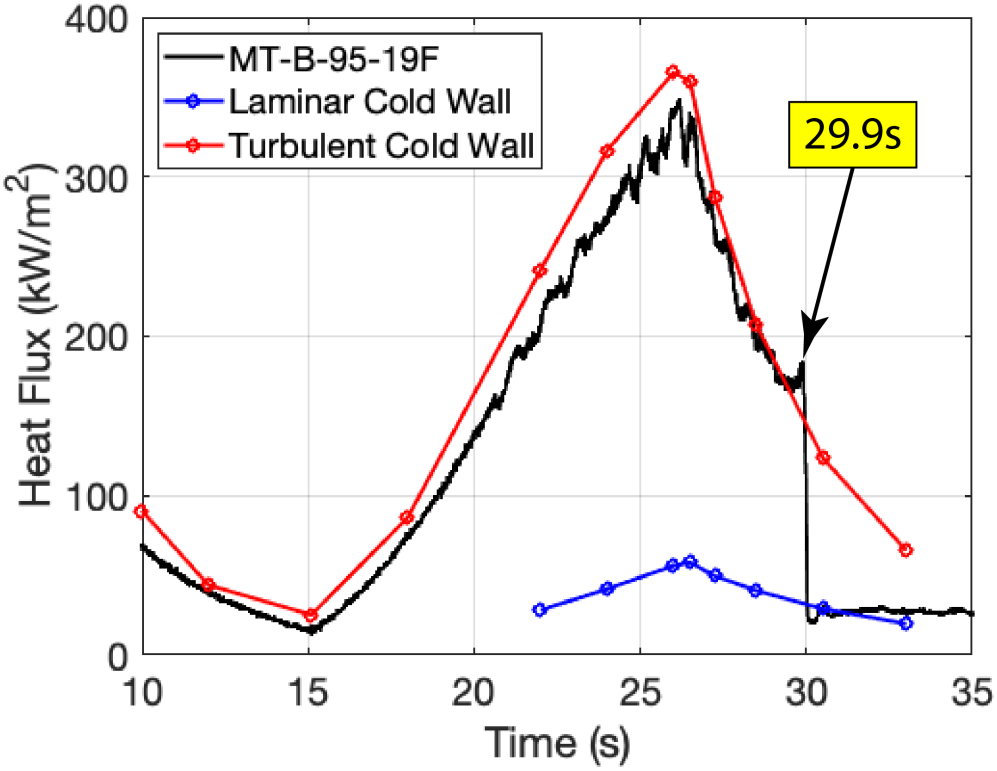

Figure 46. Calculated heat transfer during ascent from sensor MT-B-95-19

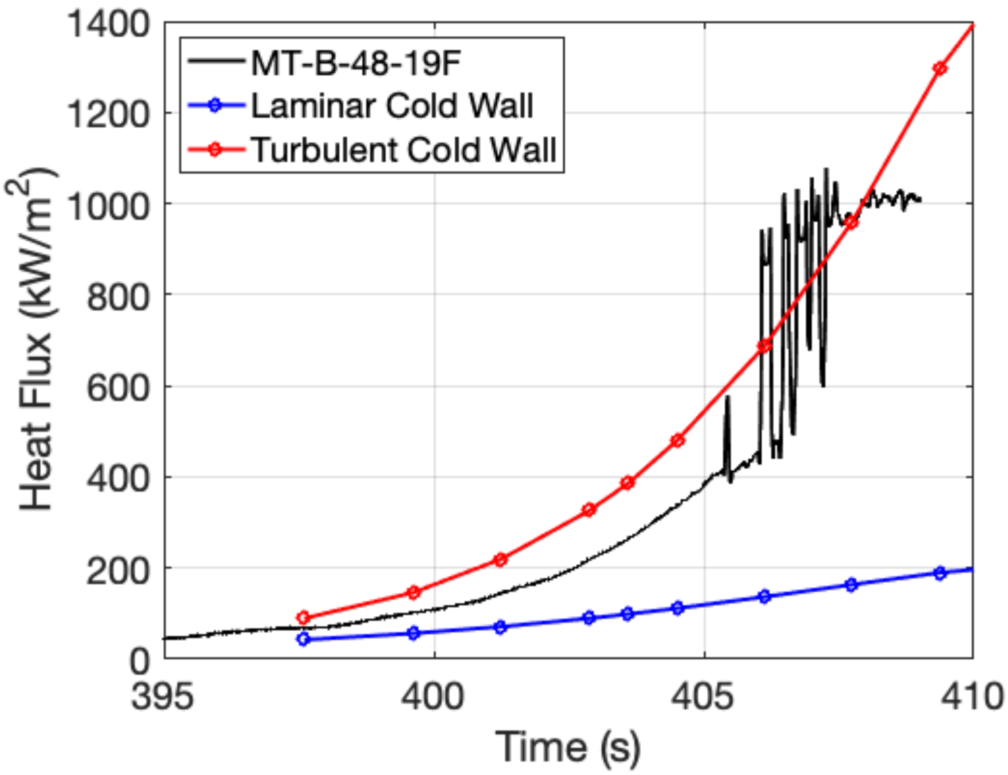

Figure 47. Calculated heat transfer during descent from sensor MT-B-48-19

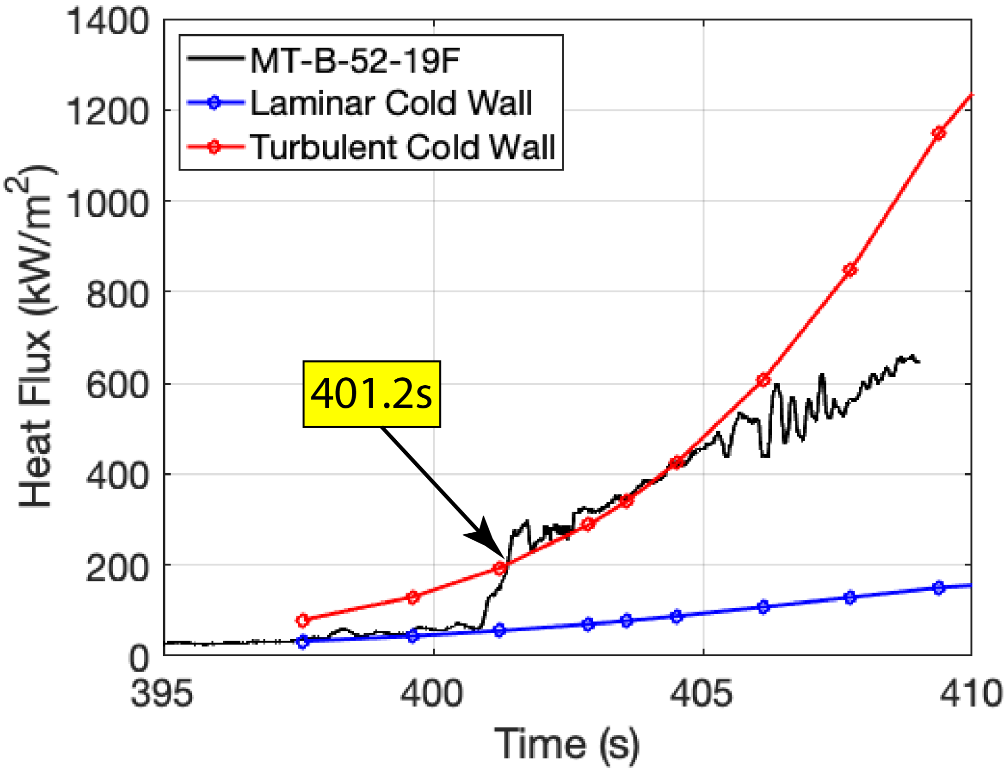

Figure 48. Calculated heat transfer during descent from sensor MT-B-52-19

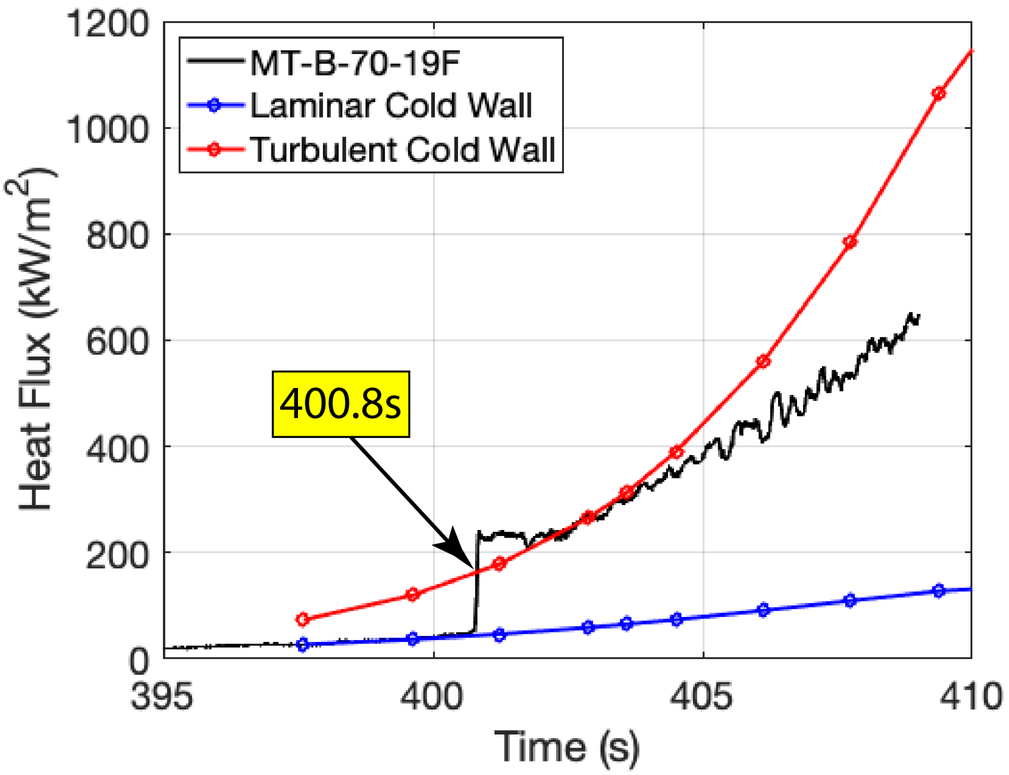

Figure 49. Calculated heat transfer during descent from sensor MT-B-70-19

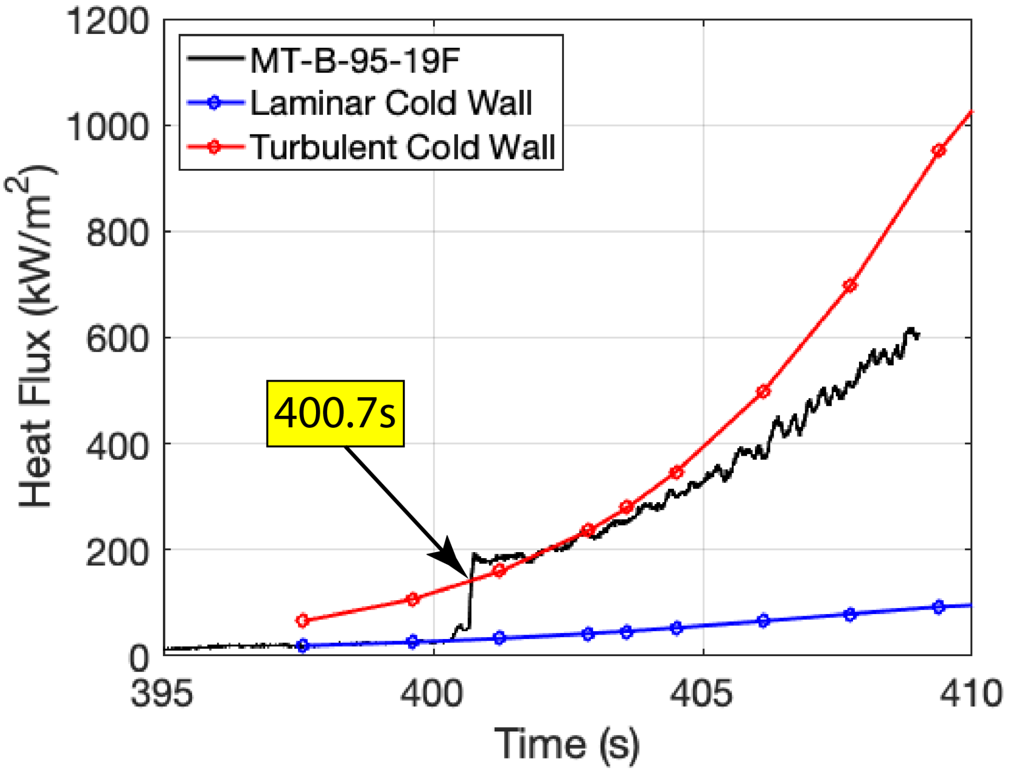

Figure 50. Calculated heat transfer during descent from sensor MT-B-95-19

Sensors Near to LE-81 Trip

Figures 51 - 52 provide sketches of the notional sensor map from both a global perspective and a zoomed-in view, respectively, showing five Side B thermocouples that are near the LE-81 trip, starting with MT-B-48-81 just in front of the trip, MT-B-50-79 on top, MT-B-50-81 to the port side, and MT-B-51-80 and MT-B-51-81 that trail and straddle the trip. Note that two trip sensor locations (MT-B-50-81 and MT-B-50-79) had inadvertently gotten swapped during fabrication, thus the sensor alignment does not strictly match the planned layout. These five sensors are intended to illuminate the local heating associated with flow structures that forms around the trip during flight. As mentioned previously, the heating plots in this section utilize CFD results from smooth body solutions (no trips included) and are intended to reveal trip related deviations in heating.

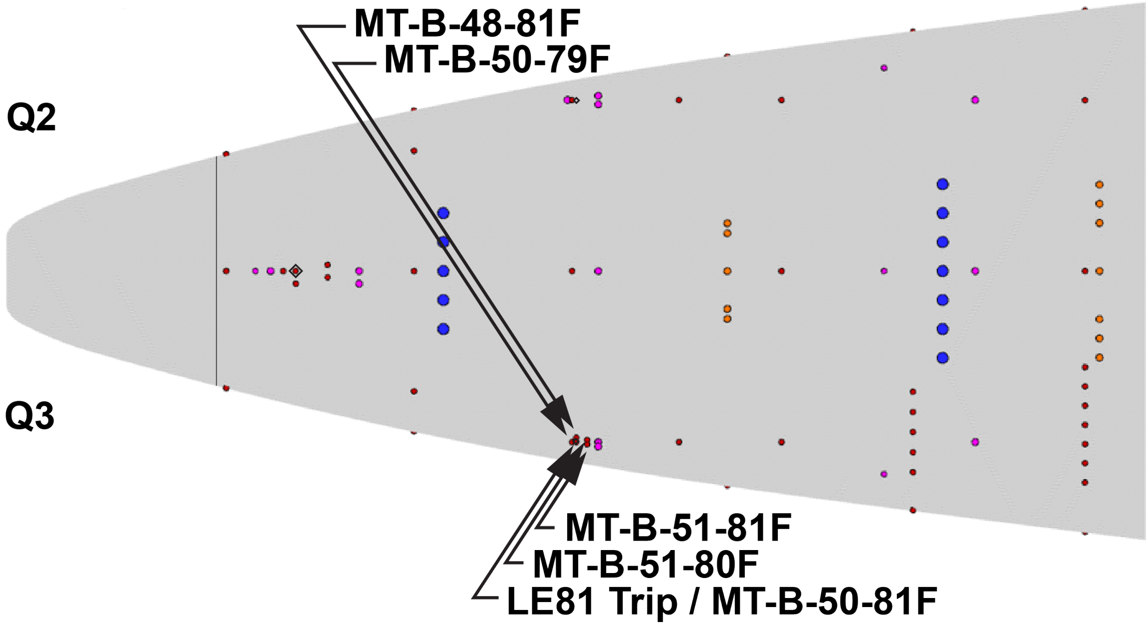

Figure 51. Thermocouples in near vicinity to Side B LE-81 trip

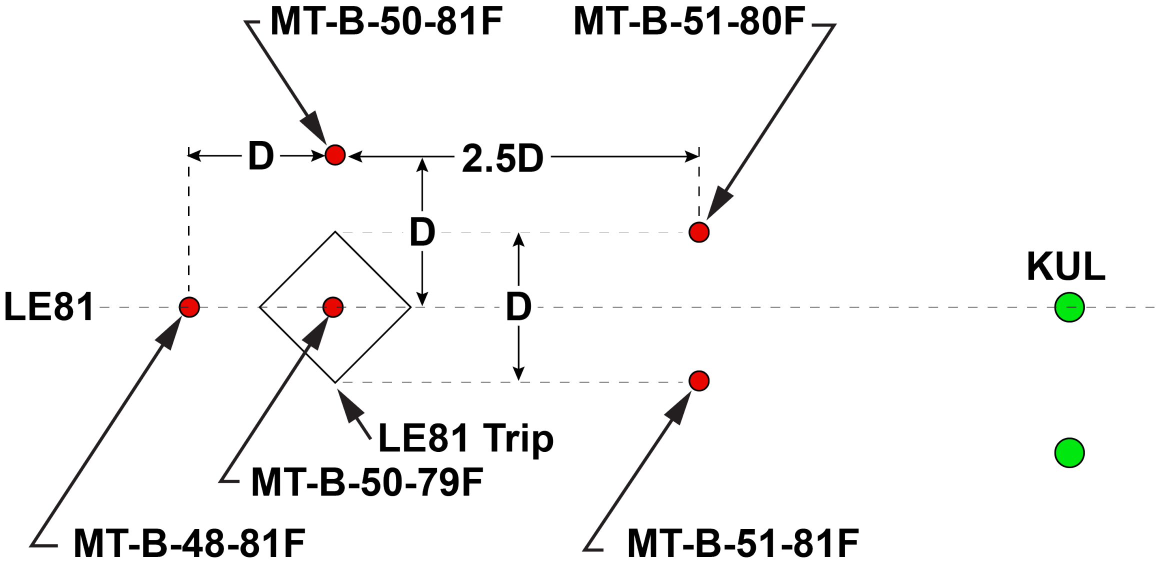

Figure 52. Close-up sketch showing spacing of thermocouples near LE-81 trip

Figures 53 - 57 provide the heating traces during ascent for the thermocouples in near vicinity to the LE-81 trip. In front of the trip, at MT-B-48-81 (Fig. 53), the derived heating mostly aligns with the smooth-wall turbulent predictions until about 23s, at which time the heating level drops to a level between the laminar and turbulent predictions. The measured trace resembles the observations from in front of the other LE trip at MT-B-48-19 (Fig. 43), although with some slightly bigger intermittency behavior from 22s to 24s. Figure 54 provides the measured heating trace from on top of the LE-81 trip (MT-B-50-79), which does not behave at any point like the smooth wall computations, nor should it be expected to. As mentioned before, a sensor on top of the trip is likely being influenced by heating from multiple dimensions, so the one-dimensional and semi-infinite accounting of the present heating analysis should not be expected to provide a meaningful result. The character of this trace also leads one to conclude that it might be defective. The trace to the port side of the LE-81 trip (MT-B-50-81), shown in Fig. 55, also does not follow either the laminar or turbulent prediction in a similar way to any other trace, thus suggesting that this could also be a defective sensor. Downstream of LE-81 trip, the measured heating traces for MT-B-51-80 and MT-B-51-81are shown in Figs. 56 & 57, respectively. Both traces initially follow the smooth-wall turbulent heating prediction until about 21.0s and 20.8s, at which point they both jump higher the smooth-wall turbulent result. It is hard to speculate about heating levels in the higher shear zones of the trip wake without some supporting computations.

During descent, the trends are similar except that the vehicle starts off completely laminar, as shown in Figs. 58 – 62. For instance, Fig. 58 (MT-B-48-81) indicates that the measured trace follows the smooth-body laminar prediction until roughly 400s, at which point heating begins to rise, but stays below smooth-wall turbulent levels until about 405.4s. The time between 400s and 405.4s is assumed to be when MT-B-48-81 senses the vortex-augmented heating while still under laminar conditions. Both the sensor to the side (Fig. 60) and on top of the trip (Fig. 61) continue to provide results that seem unreliable (same as during ascent). The two sensors downstream of the LE-81 trip (Figs. 61 and 62) track along the turbulent predictions starting at about 396s.

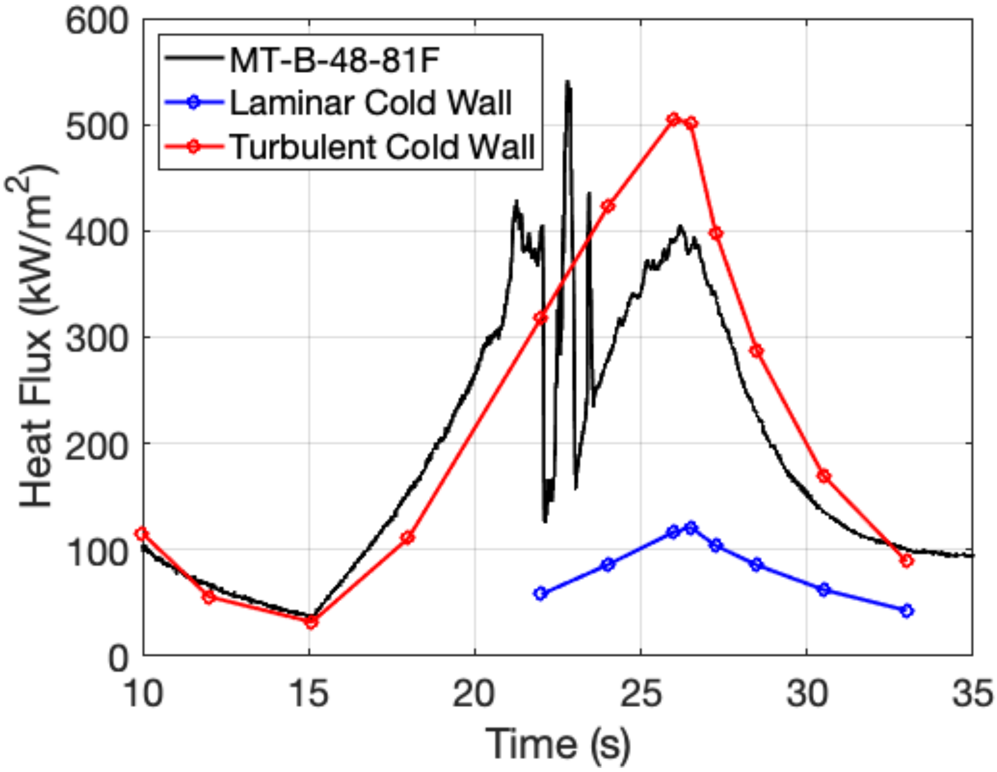

Figure 53. Calculated heat transfer during ascent from sensor MT-B-48-81

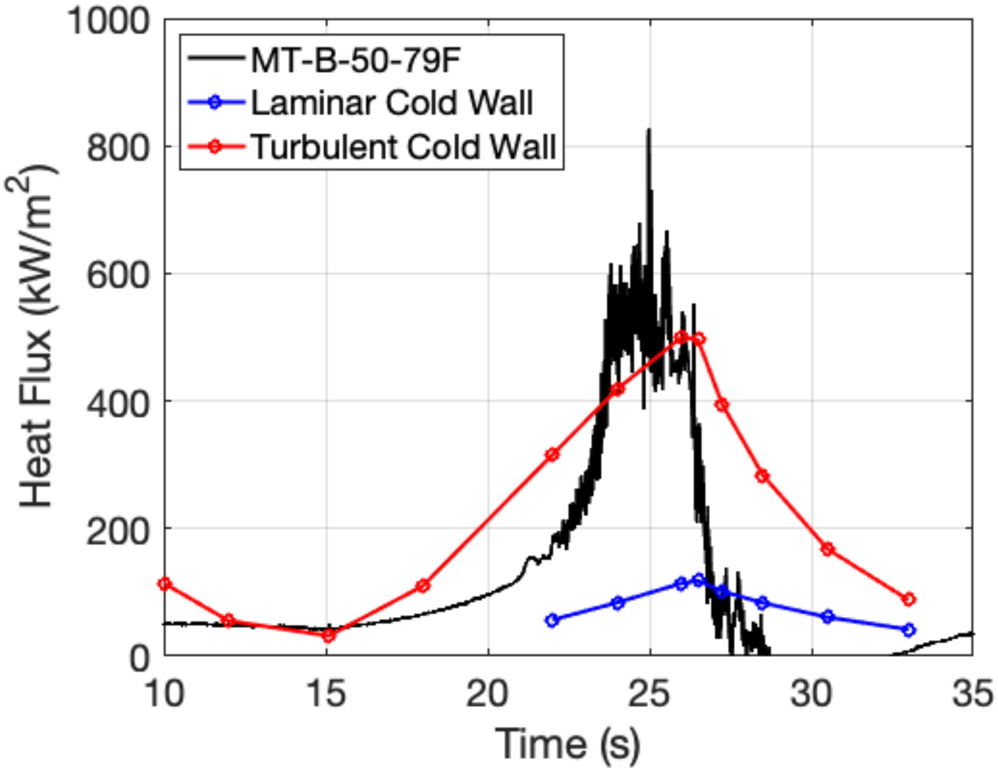

Figure 54. Calculated heat transfer during ascent from sensor MT-B-50-79

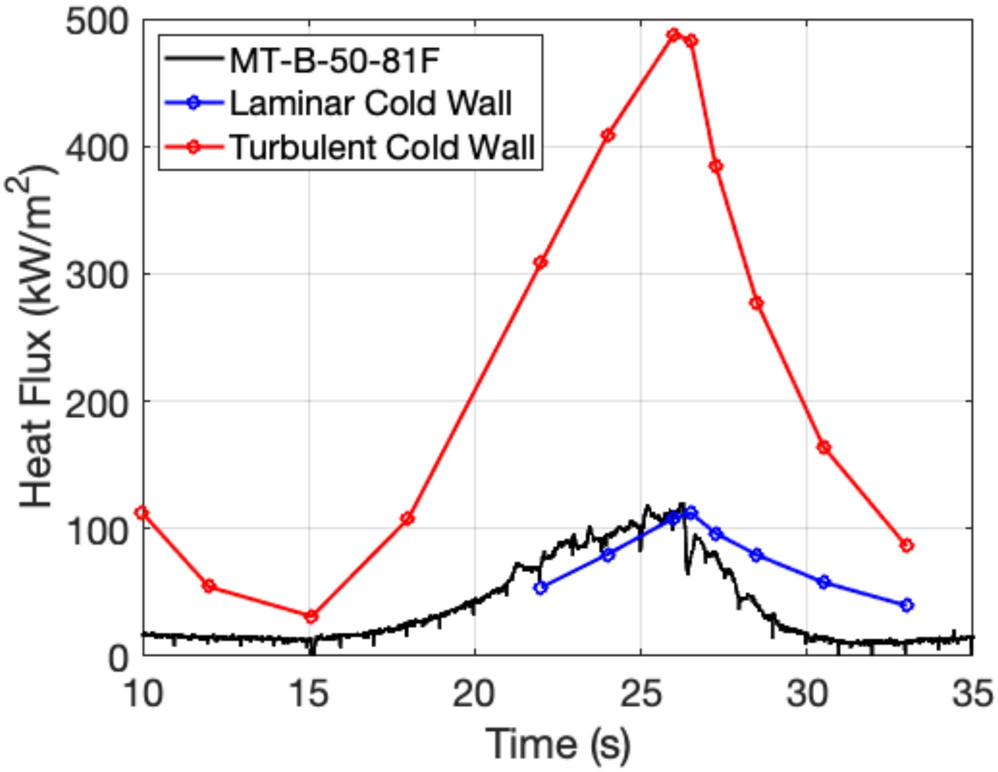

Figure 55. Calculated heat transfer during ascent from sensor MT-B-50-81

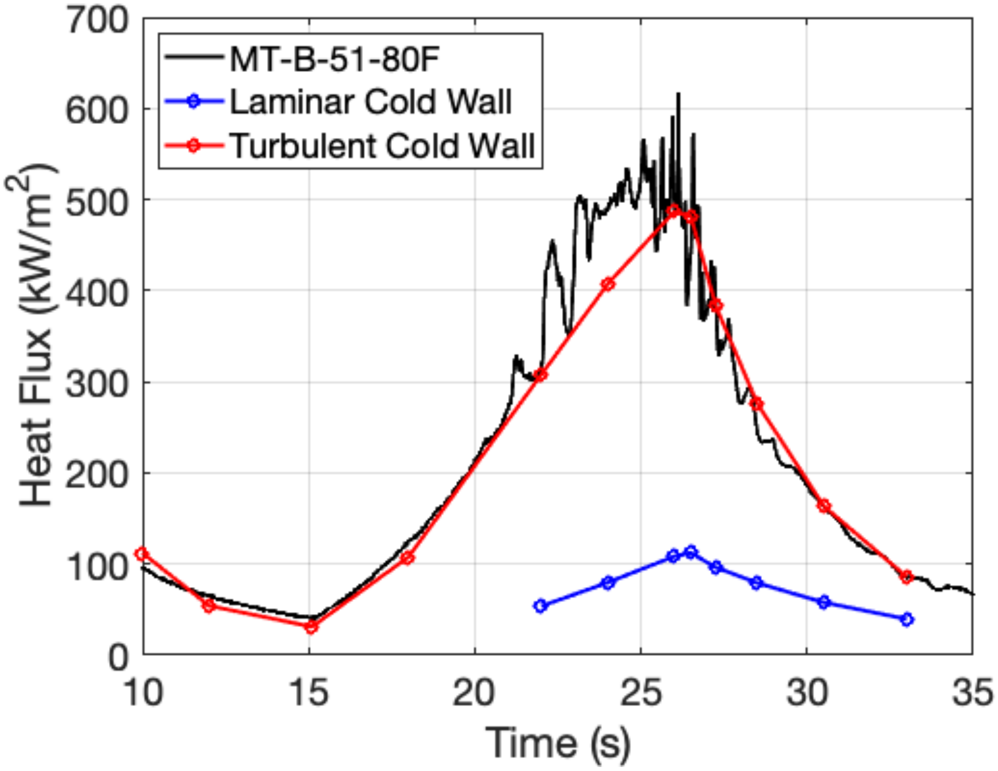

Figure 56. Calculated heat transfer during ascent from sensor MT-B-51-80

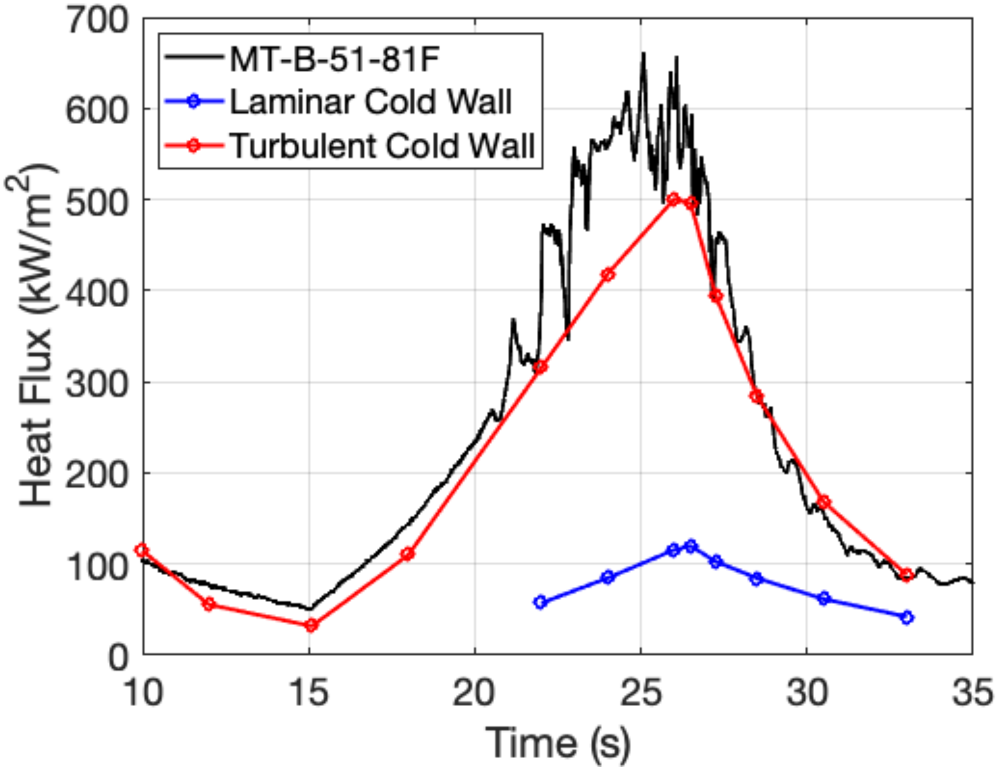

Figure 57. Calculated heat transfer during ascent from sensor MT-B-51-81

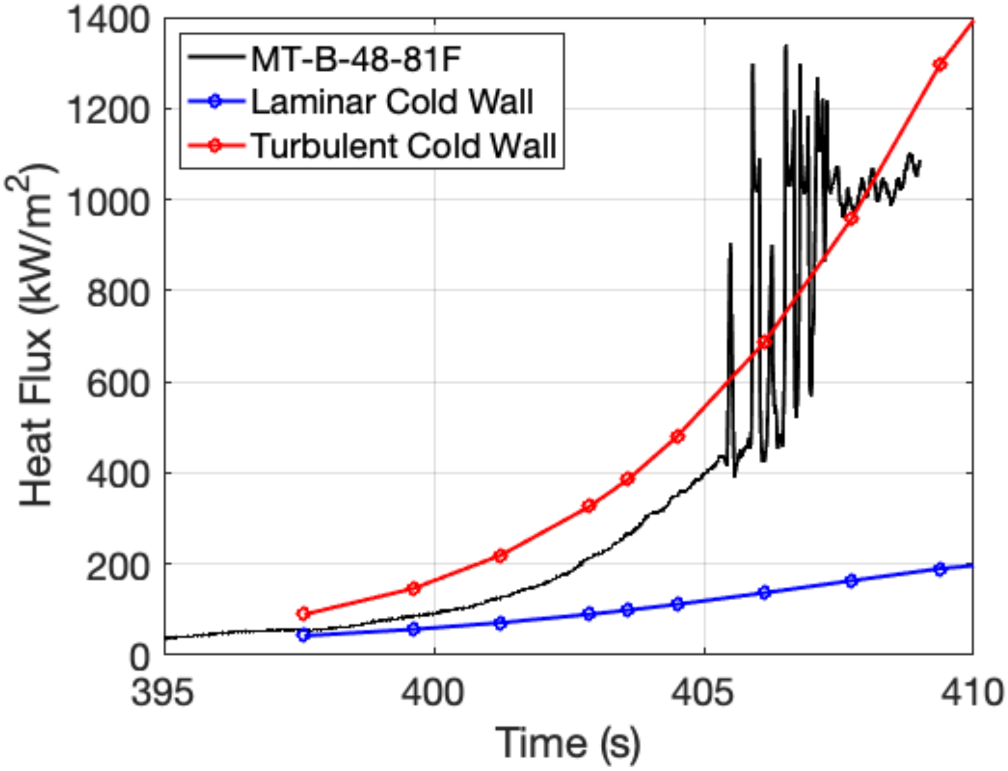

Figure 58. Calculated heat transfer during descent from sensor MT-B-48-81

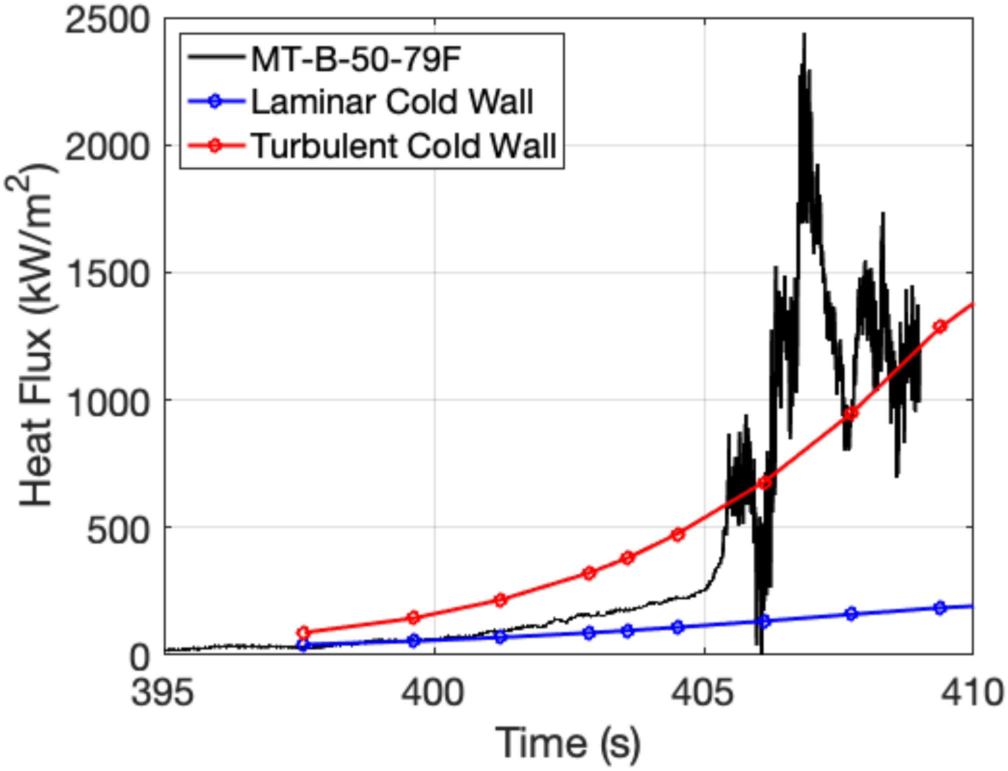

Figure 59. Calculated heat transfer during descent from sensor MT-B-50-79

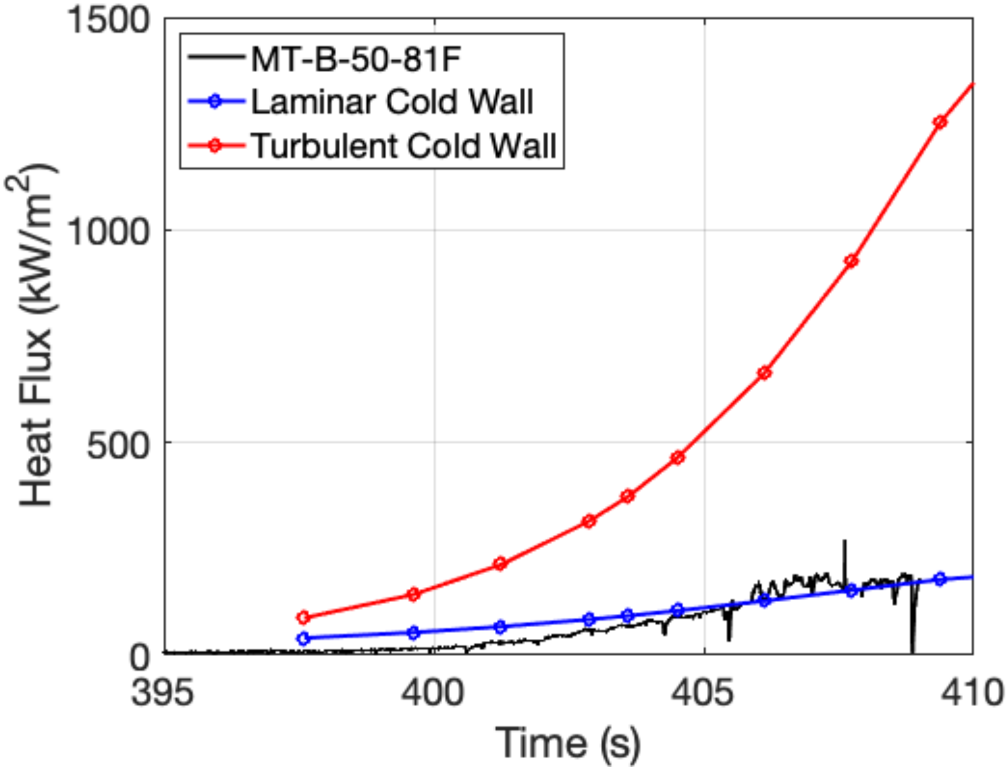

Figure 60. Calculated heat transfer during descent from sensor MT-B-50-81

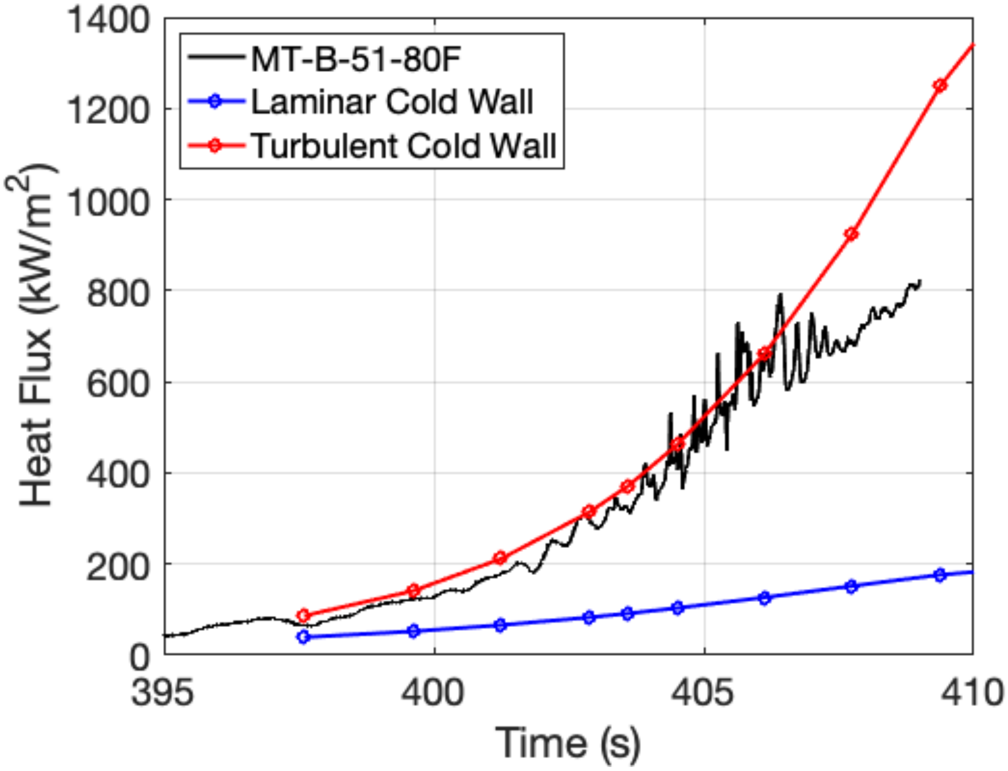

Figure 61. Calculated heat transfer during descent from sensor MT-B-51-80

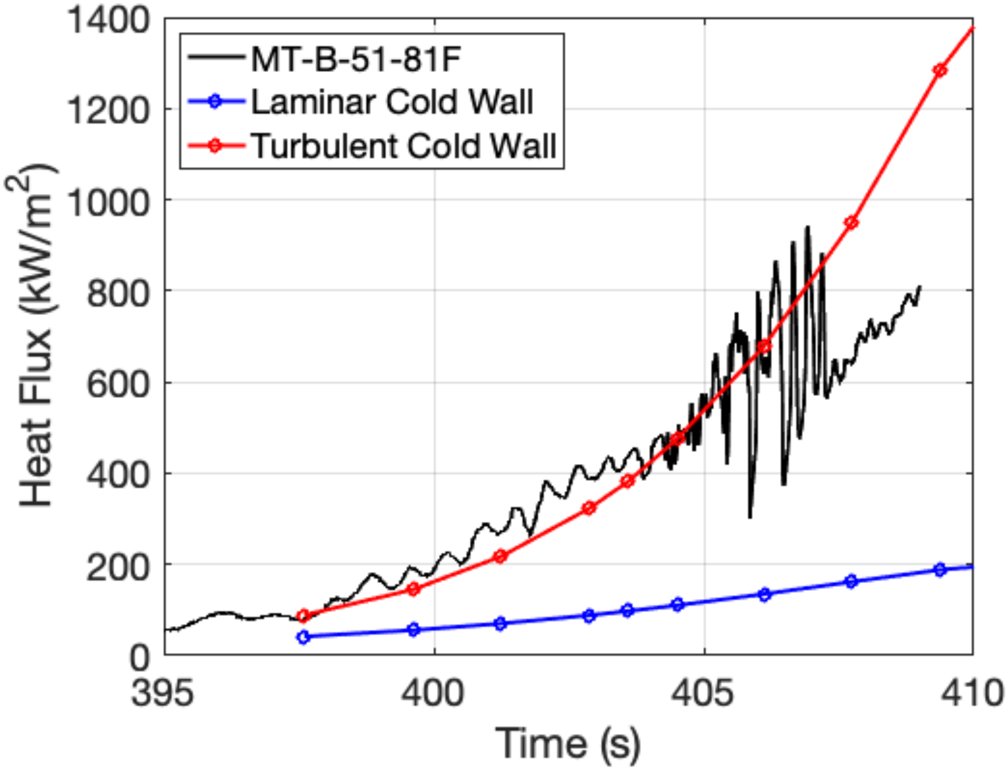

Figure 62. Calculated heat transfer during descent from sensor MT-B-51-81

Array In Line with LE-81 Trip

Figure 63 provides a sketch showing three Side B thermocouples that are aligned downstream of the LE-81 trip, starting with MT-B-70-81, followed by MT-B-80-81, and MT-B-95-81. These three will be used to determine the incipient and effective transition onset times associated with the LE-81 trip during ascent and descent. Note that MT-B-52-81 was flagged as a bad sensor prior to flight and could not be revived. Since this sensor is the one closest behind the LE-81 trip, its loss will contribute to a mismatch in interpretation of effective onset times between the two LE trips.

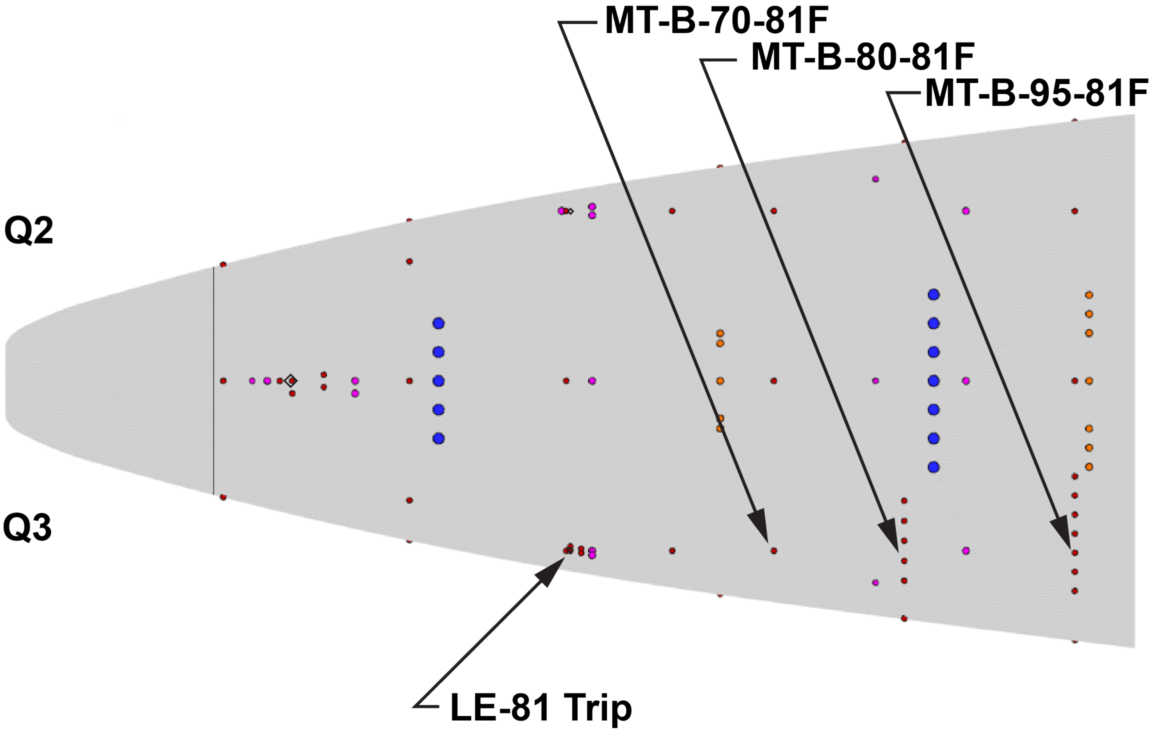

Figure 63. Thermocouples aligned downstream of the Side B LE-81 trip

Figures 64 - 66 provide the transition onset times as inferred during ascent from the converted heat transfer traces from the surface thermocouples behind the LE-81 trip. The time at which each sensor deviates from the turbulent heat transfer rates is well behaved and consistent with the previous ascent times (both CL and LE-19), as expected. As mentioned, the TC closest to the LE-81 trip (MT-B-52-81F) was not working prior to flight. The next closest one to the LE-81 trip (MT-B-70-81F) is the first to depart from turbulent heating levels at 29.5s (Fig. 64), followed in quick succession with 29.9s at MT-B-80-81F (Fig. 65) and 30.0s at MT-B-95-81F (Fig. 66). Thus, incipient transition for LE-81 would correspond to 30.0s, with an effective result at 29.5s during ascent. Although, as noted, the effective time here is not directly comparable to the effective time at LE-19 due to the different sensor locations. Comparisons between two sides, shown in Figs. 65 & 66, indicate that the LE-81 trip provided forced transition on Side B for roughly 2 seconds past the smooth behavior of Side A. Note that the Reynolds number changes rapidly during that time, reducing roughly more than half from 10 million to 4 million.

Figures 67 - 69 provide the descent transition onset times inferred from the converted heat transfer traces for the surface thermocouples behind the LE-81 trip. The time at which each sensor reaches the smooth-wall turbulent heat transfer rates is consistent with previous results (both CL and LE-19). As mentioned previously, the thermocouple closest behind the LE-81 trip (MT-B-52-81F) was not working during flight. But from the remaining sensors, the most downstream (MT-B-95-81F) was the first to reach the calculated turbulent heating levels at 399.3s Fig. 69), followed quickly at 399.6s at MT-B-80-81F (Fig. 68). The next working sensor in the series, which is the one closest to the LE-81 trip (MT-B-70-81F), reaches turbulent heating levels at 400.7s (Fig. 67). Thus, for the LE-81 trip during descent, incipient transition would correspond to 399.3s, and effective transition would be 400.7s. Figures 68 & 69 provide comparisons to Side A and reveals LE-81 trip forces transition roughly 4s ahead of the smooth side.

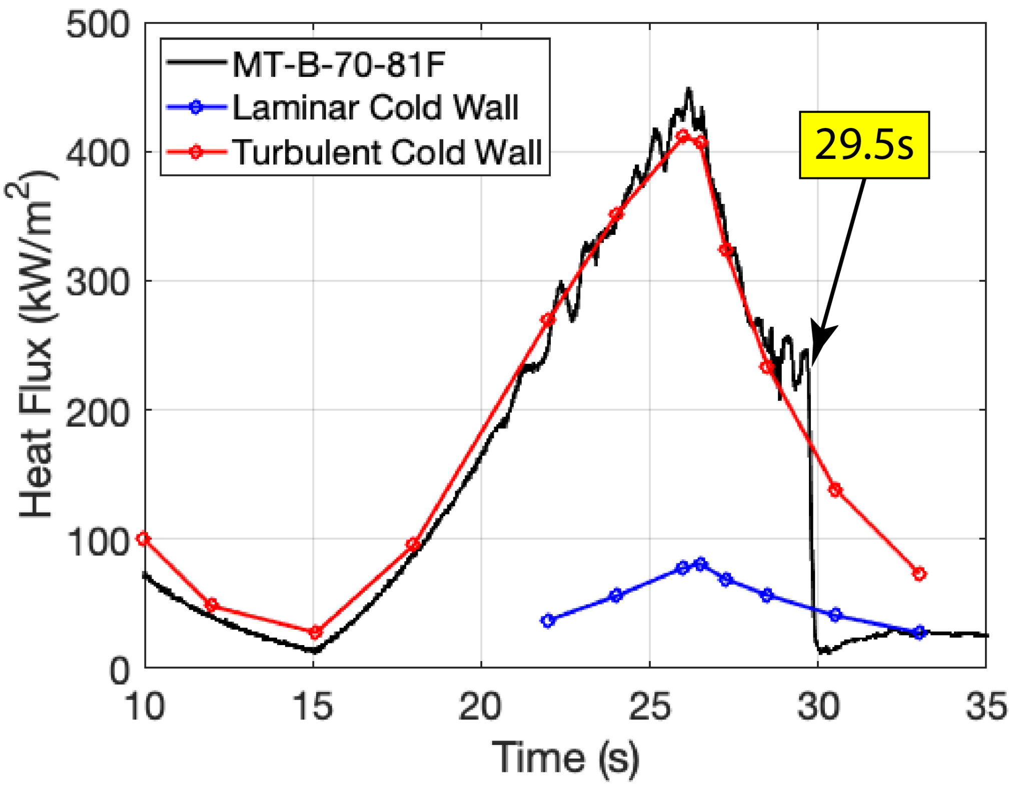

Figure 64. Calculated heat transfer during ascent from sensor MT-B-70-81

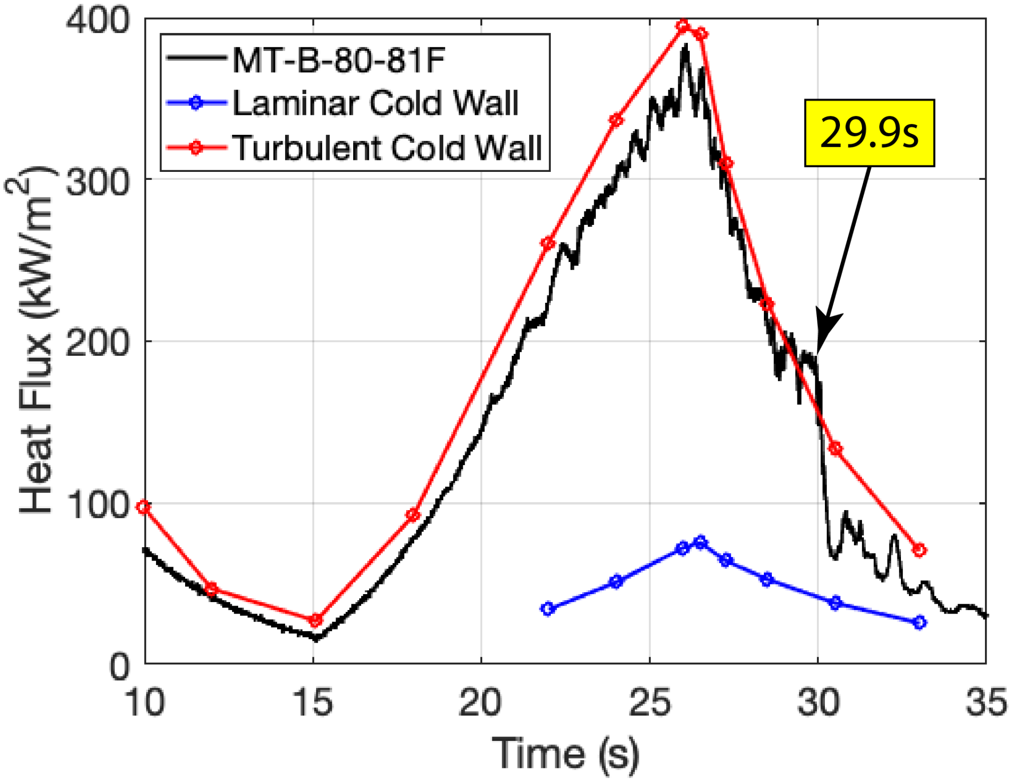

Figure 65. Calculated heat transfer during ascent from sensor MT-B-80-81

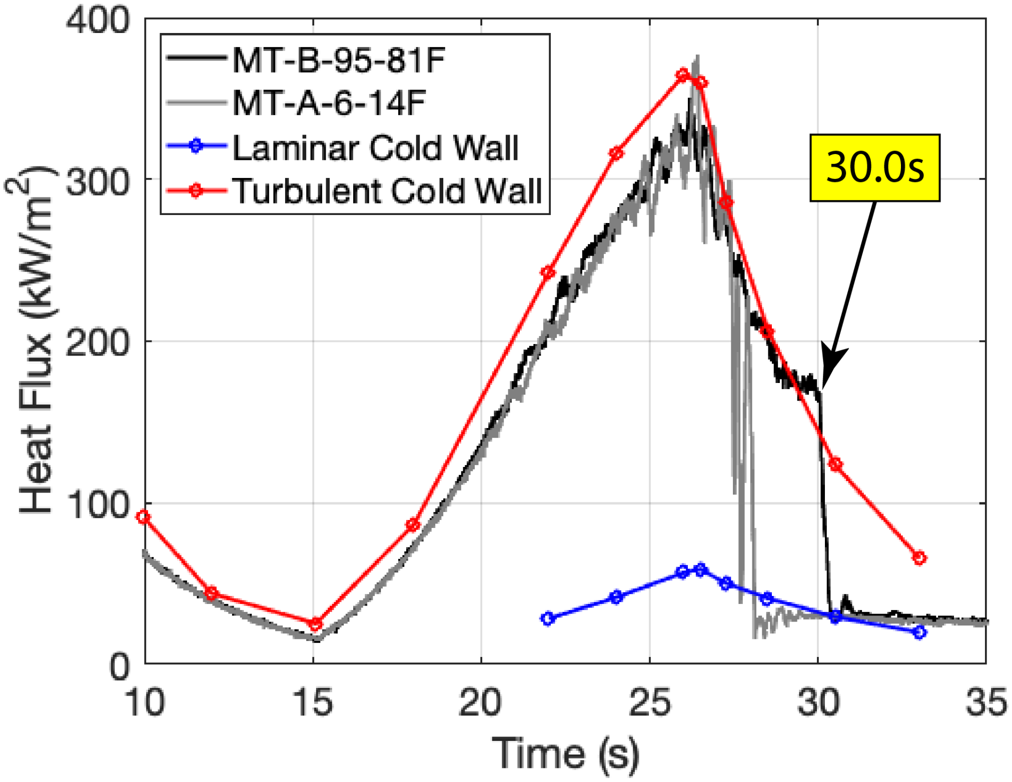

Figure 66. Calculated heat transfer during ascent from sensor MT-B-95-81

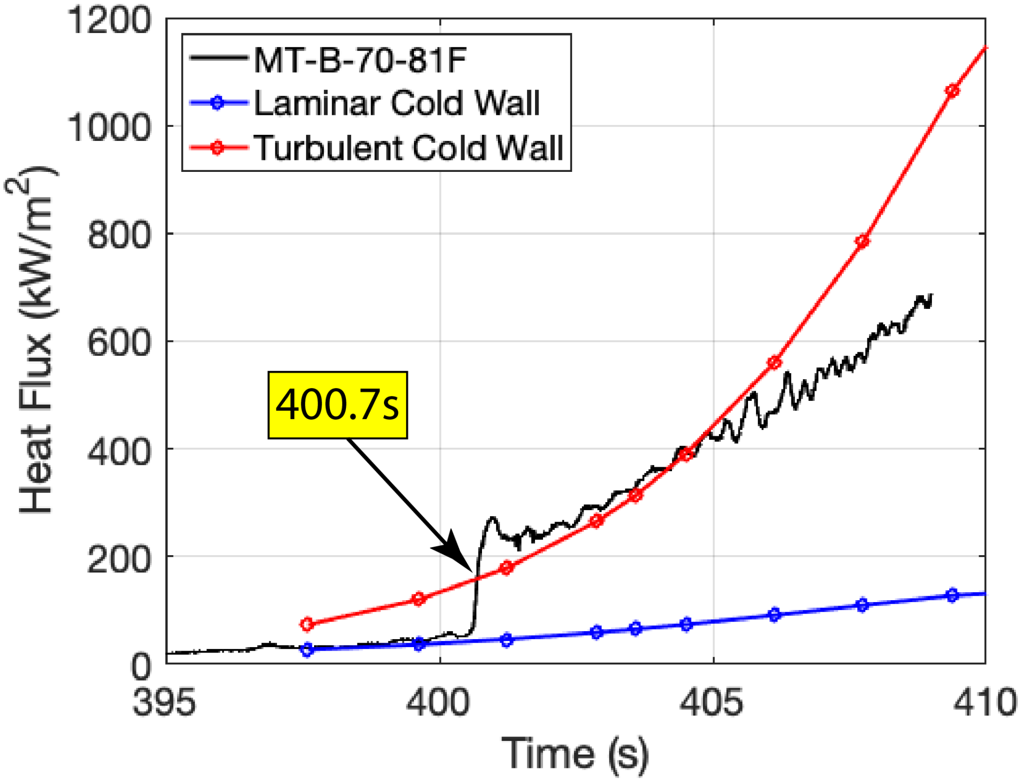

Figure 67. Calculated heat transfer during descent from sensor MT-B-70-81

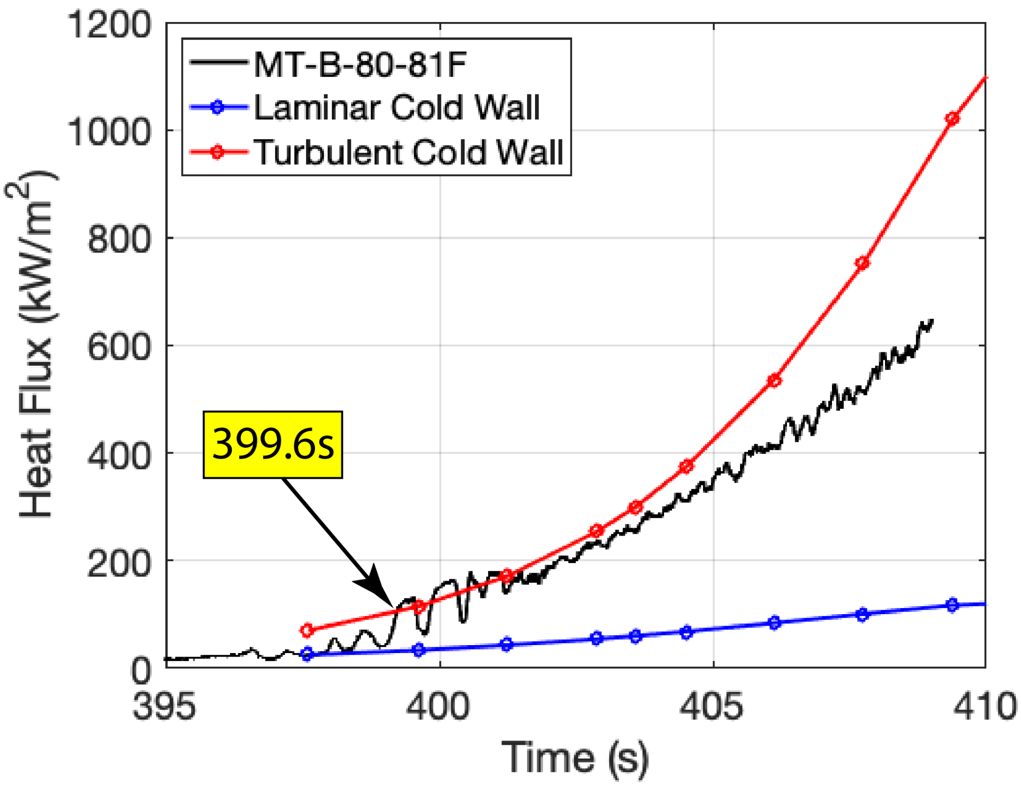

Figure 68. Calculated heat transfer during descent from sensor MT-B-80-81

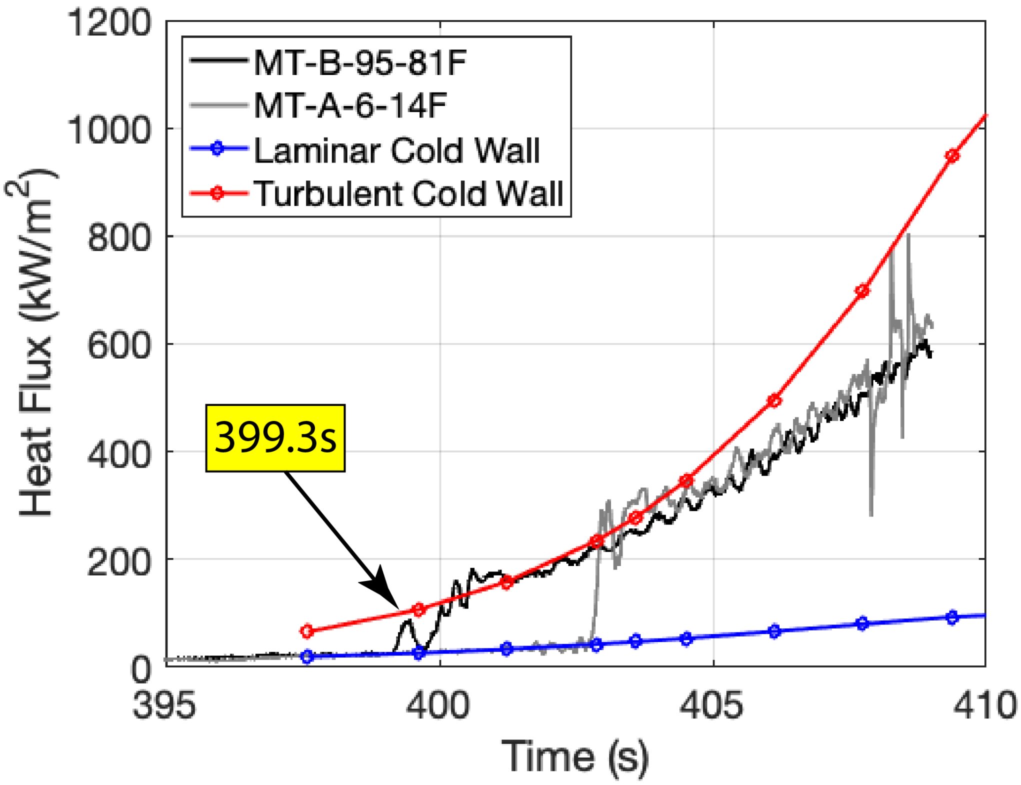

Figure 69. Calculated heat transfer during descent from sensor MT-B-95-81

Spanwise Array #1 Behind LE-81 Trip

Downstream of LE-81 are two spanwise arrays of thermocouples intended to look at the lateral spreading of the turbulent wedge. The first one is at lengthwise station of 80% down the body. Figure 28 provides a sketch showing five Side B thermocouples that are distributed in a spanwise array downstream of the starboard leading edge trip (LE-81), starting with MT-B-80-19 in the most inboard location (note the location error), followed by MT-B-80-72, MT-B-80-77, MT-B-80-81, MT-B-80-85, and MT-B-80-89 being most outboard. These six will be used to determine the lateral spreading of the turbulent wedge associated with the LE-81 trip during ascent and descent.

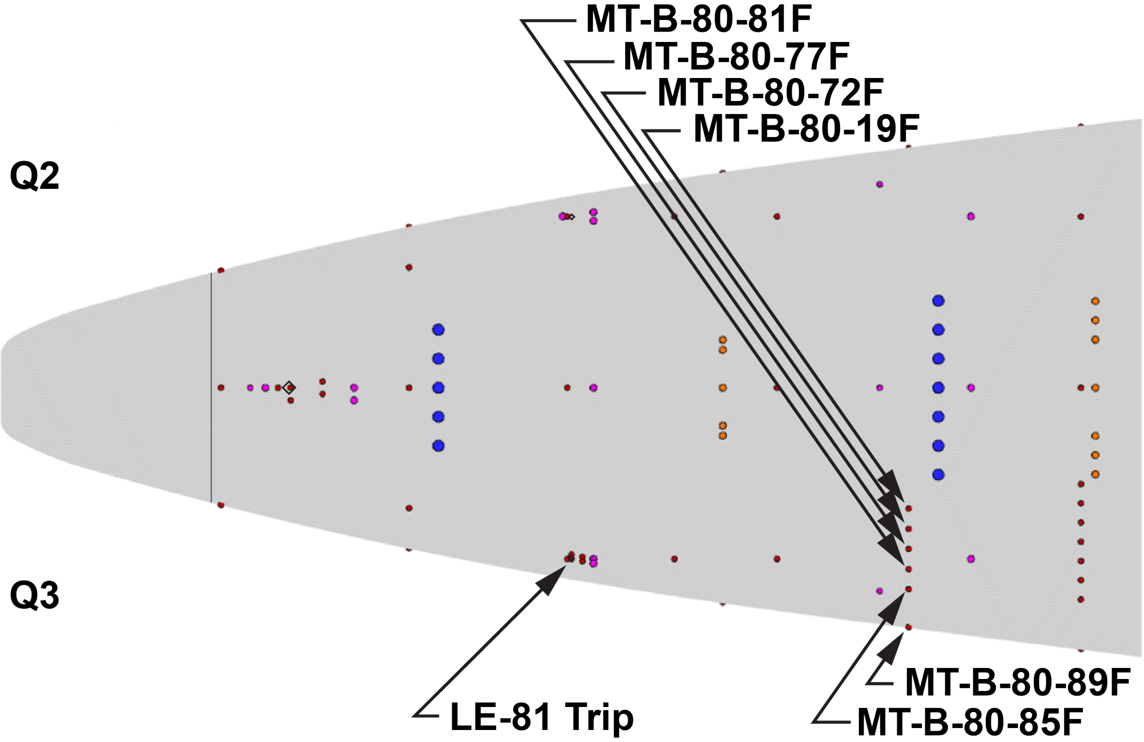

Figure 70. Lateral array of thermocouples at station 80 downstream of the Side B LE-81 trip

Figures 71 - 75 provide an assessment of the turbulent wedge spreading behind the LE-81 trip during ascent at this first station. The earliest onset time inferred from the measured heating occurs at the most inboard location with MT-B-80-19F at 27.8s (Fig. 71). This location does allow comparison to a corresponding Side A thermocouple, which shows a slightly later onset time (~1s). Moving outboard, the next two thermocouples, MT-B-80-72F (Fig. 72) and MT-B-80-77F (Fig. 73), are next to show onset, at 28.5s and 29.3s, respectively. Neither of these locations had a corresponding Side A sensor. The next two outboard sensors, MT-B-80-81F (shown previously in Fig. 65) and MT-B-80-85F (Fig. 74), indicate transition onset at 29.9s and 30.5s, respectively. These both had corresponding Side A sensors that show onset roughly 4 seconds earlier than Side B, indicating the influence of the trip. Thus, these two locations represent the likely disturbance path from the LE-81 trip, with the wedge growing laterally outward with time. Finally, MT-B-80-89 (Fig. 75), which is on the swept leading edge, indicates no transition onset during ascent, while the corresponding Side A sensor does indicate transition onset at 25.2s. This is a somewhat inconsistent result as, in general, Side A has been showing transition onset ahead of Side B. This inconsistency will be discussed in more detail near the end of Results and Discussion section. Since the LE is highly three-dimensional, the one-dimensional heat conduction analysis should not be expected to match perfectly with the computations.

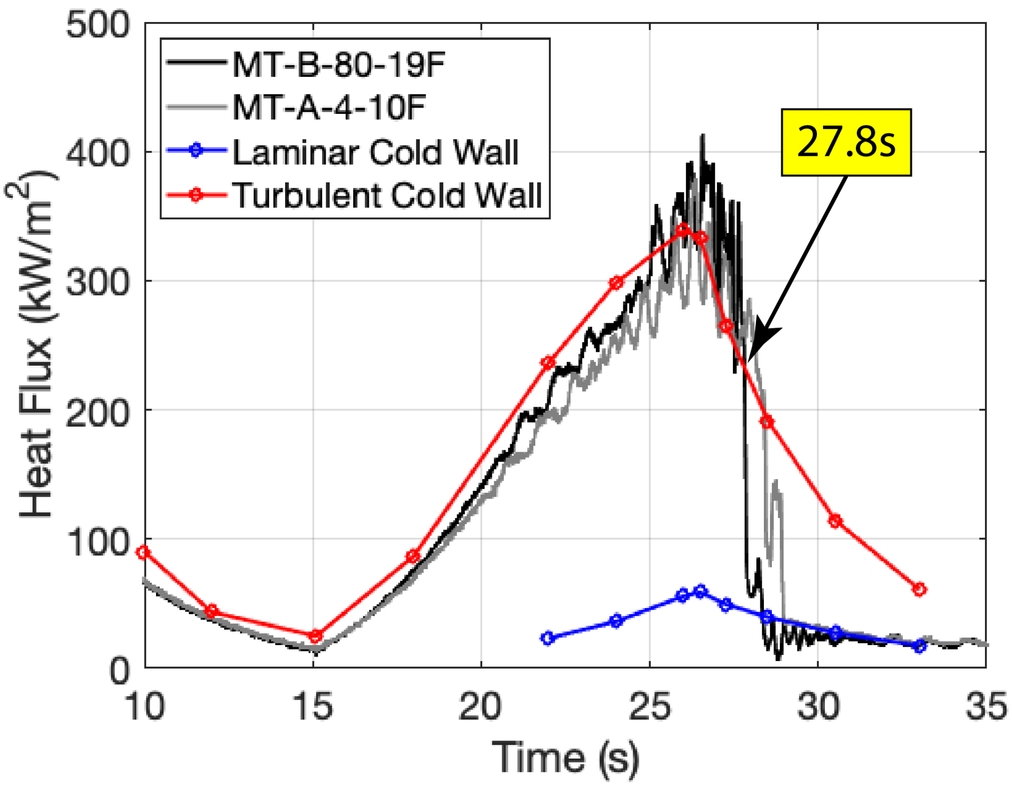

Figure 71. Calculated heat transfer during ascent from sensor MT-B-80-19

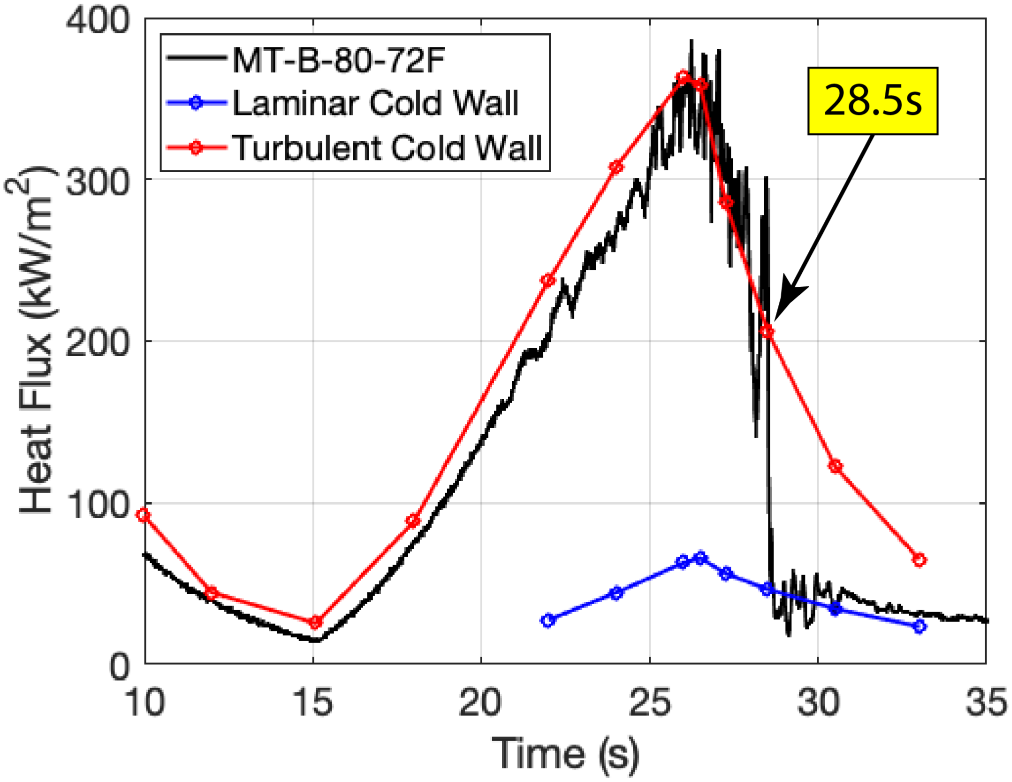

Figure 72. Calculated heat transfer during ascent from sensor MT-B-80-72

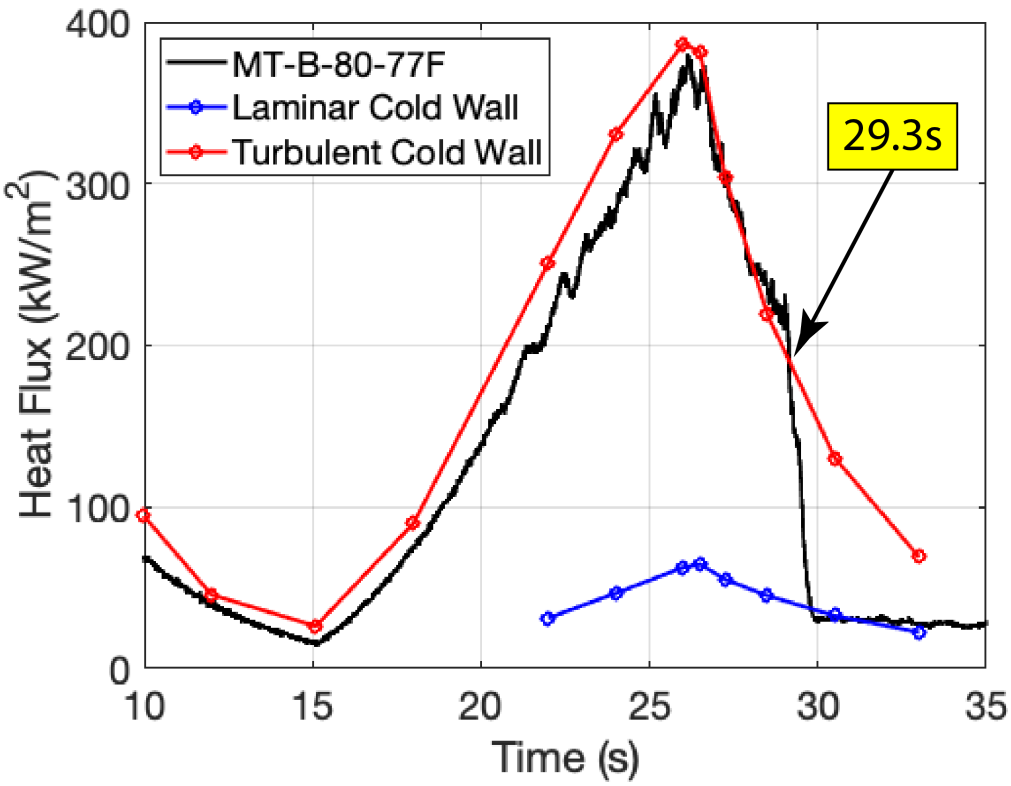

Figure 73. Calculated heat transfer during ascent from sensor MT-B-80-77

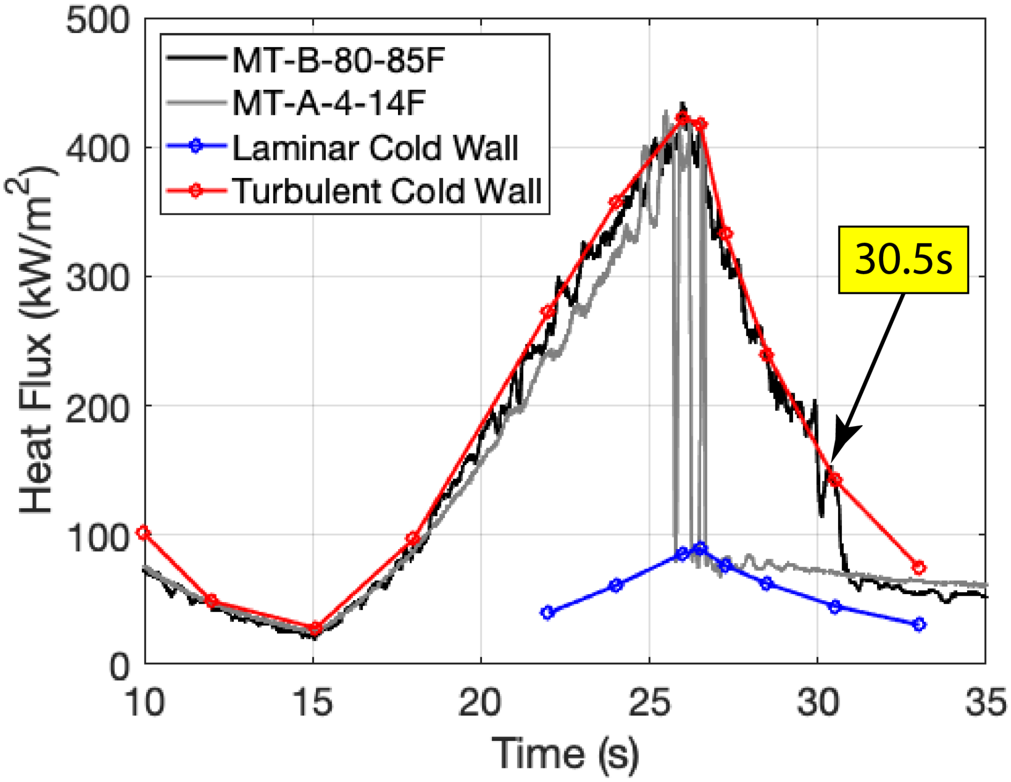

Figure 74. Calculated heat transfer during ascent from sensor MT-B-80-85

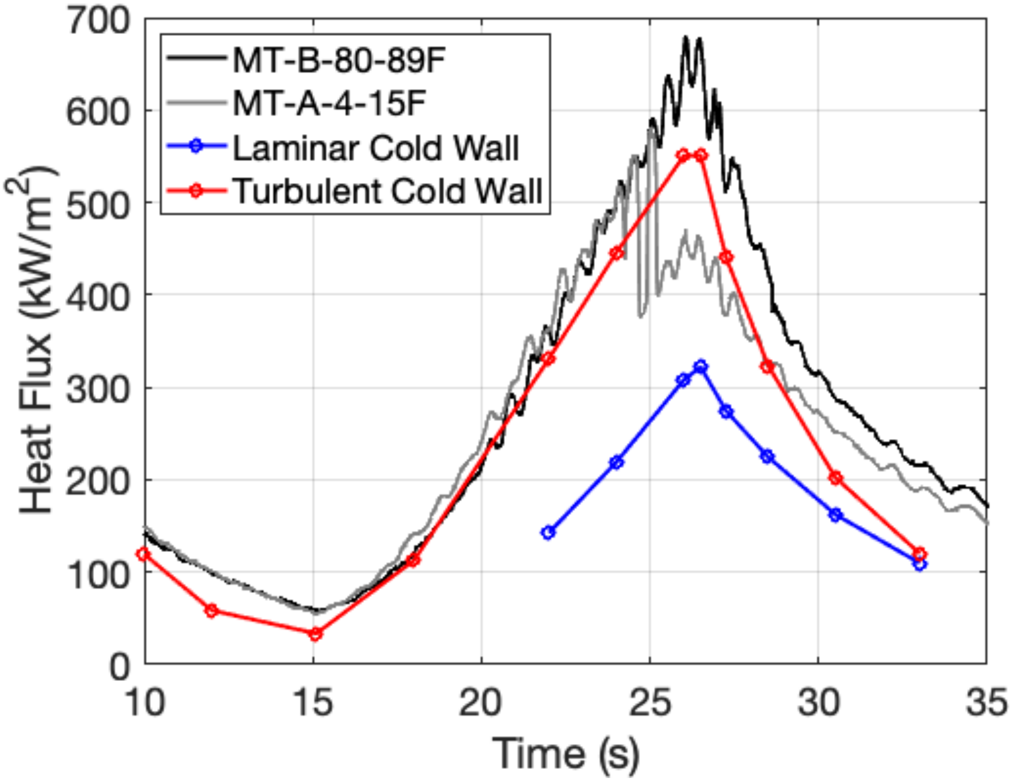

Figure 75. Calculated heat transfer during ascent from sensor MT-B-80-89

For this same station, an assessment of the turbulent wedge spreading behind the LE-81 trip during descent is provided in Figures 76 – 80. As expected, the trends are consistent even while the traces are starting off as initially laminar. The two outboard locations (that are not on the leading edge), MT-B-80-85F (Fig. 79) and MT-B-80-81F (Fig. 68), reach the smooth-wall turbulent heating predictions at identical times of 399.6s. The Side A results shown in these figures reveal transition onset about 4-5 seconds after Side B, an indication that these sensors are in the wake of the trip. The next two sensors moving inboard reveal transition onset times in progression with MT-B-80-77F (Fig. 78) indicating 400.9s and MT-B-80-72F (Fig. 77) showing 402.1s. These two locations do not have a corresponding Side A sensor. The most inboard sensor, MT-B-80-19F (Fig. 76), is the last to reach the predicted turbulent heating levels at 402.7s. The corresponding onset time from Side A is a little over a second ahead of Side B, which is consistent with the general observations of Q4 (Side A) having the earlier transition onset times. Finally, MT-B-80-89 (Fig. 80) on the swept leading edge provides a transition onset time of 402.9s, with the corresponding Side A sensor being roughly 3 seconds later. It is unclear as to why the swept LE on Side B stays turbulent throughout ascent while providing transition onset during descent. These last two points will be discussed again near the end of this section.

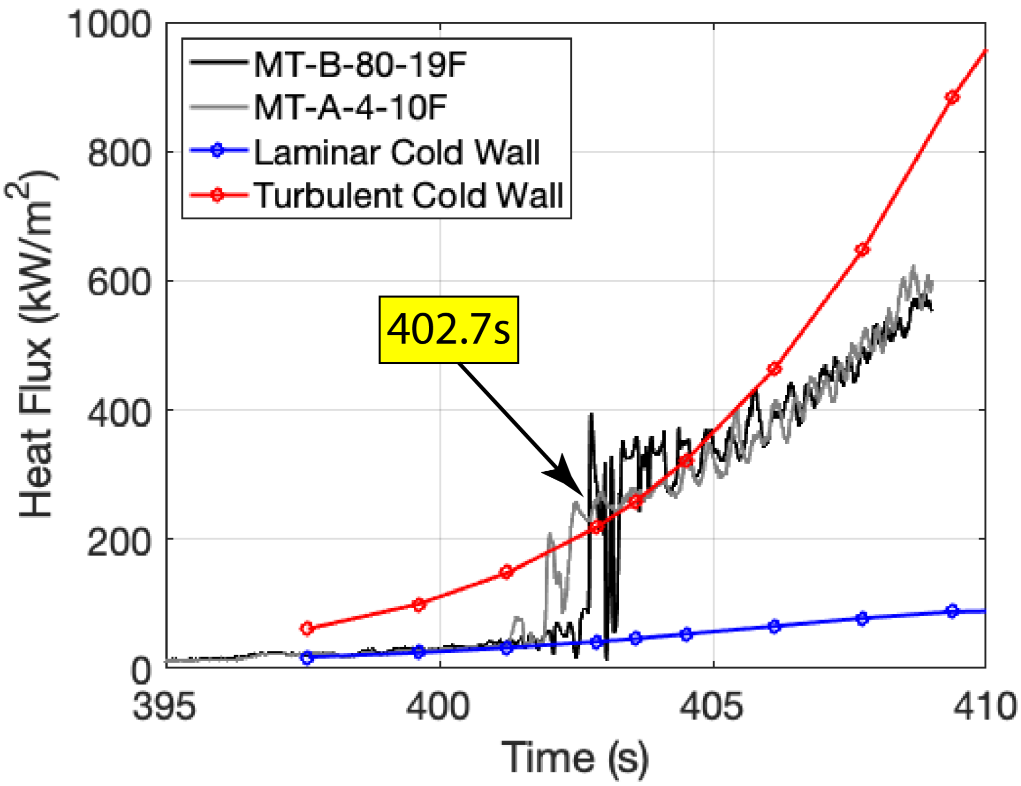

Figure 76. Calculated heat transfer during descent from sensor MT-B-80-19

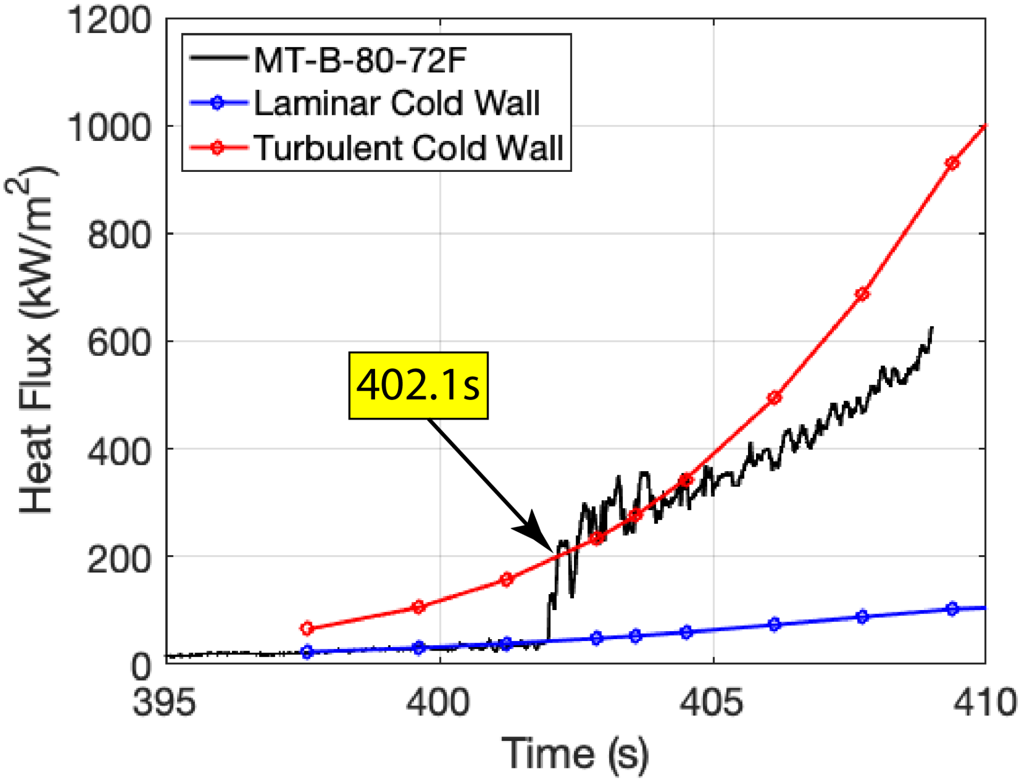

Figure 77. Calculated heat transfer during descent from sensor MT-B-80-72

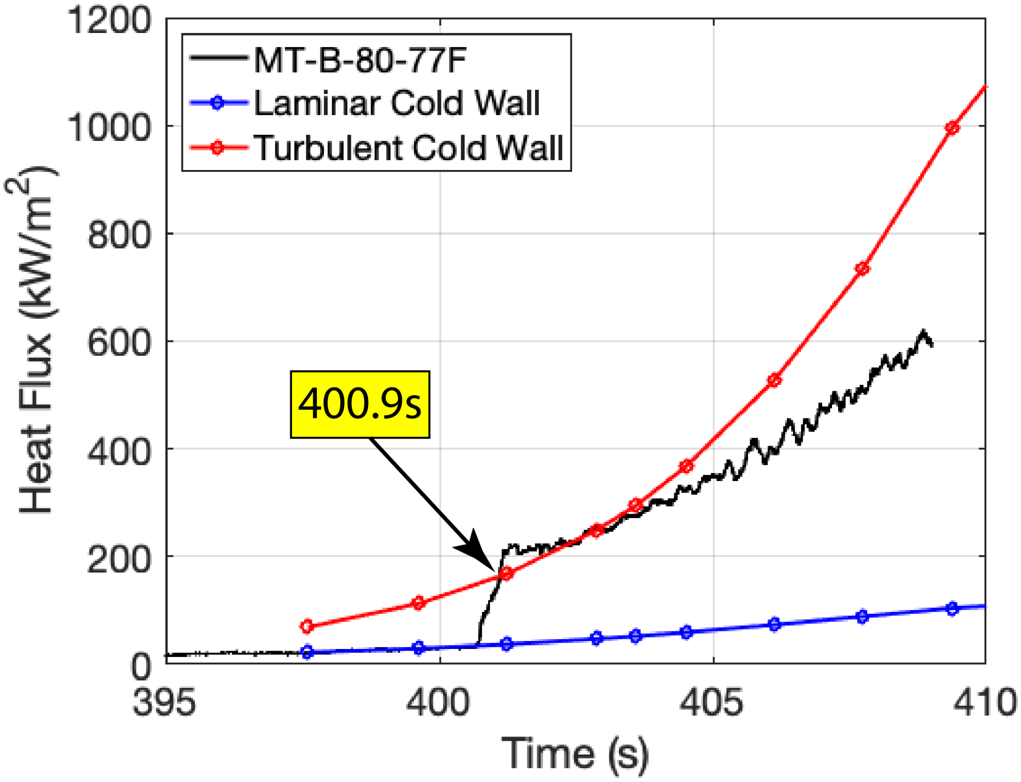

Figure 78. Calculated heat transfer during descent from sensor MT-B-80-77

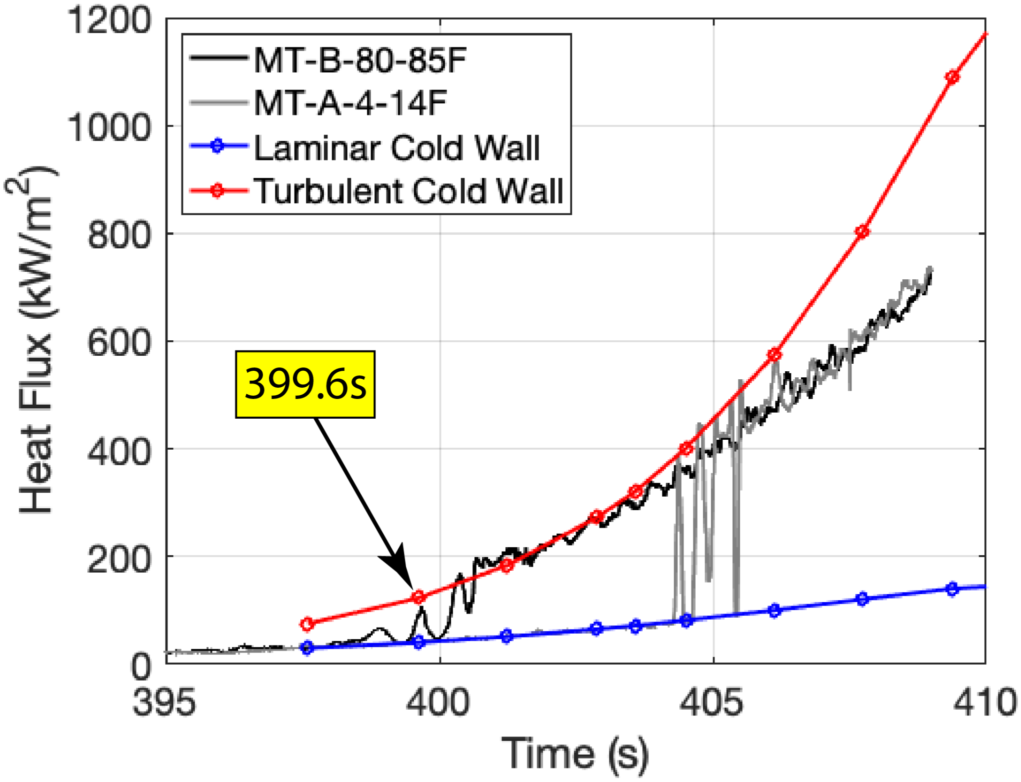

Figure 79. Calculated heat transfer during descent from sensor MT-B-80-85

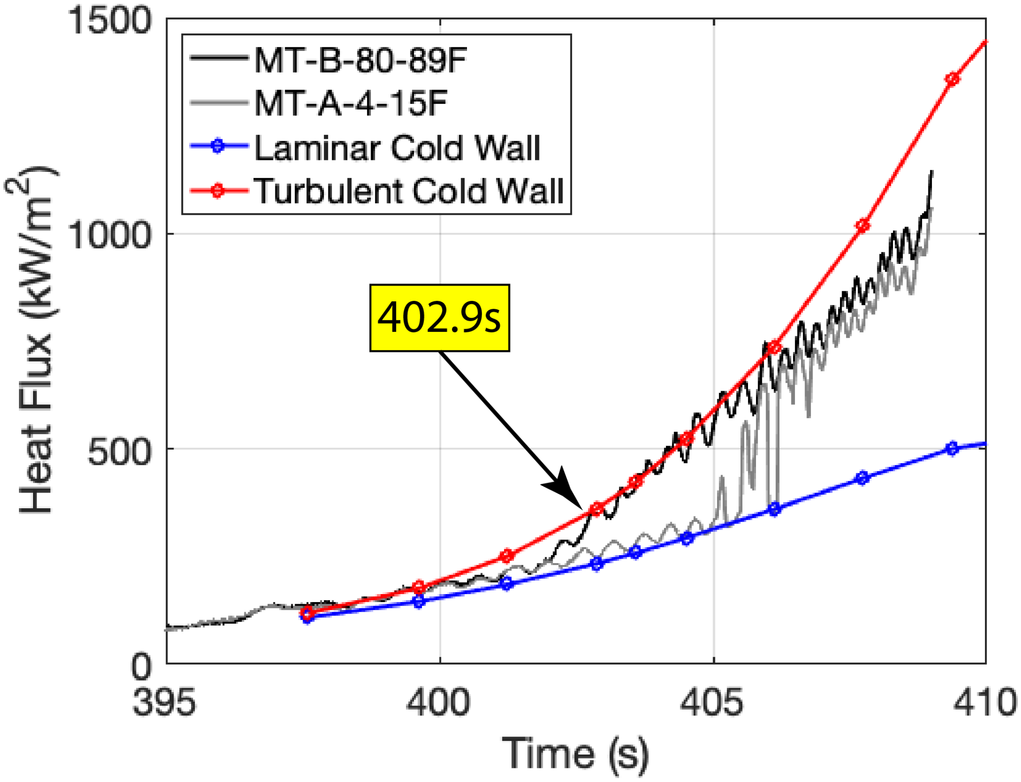

Figure 80. Calculated heat transfer during descent from sensor MT-B-80-89

Spanwise Array #2 Behind LE-81 Trip

Figure 81 provides a sketch showing seven Side B thermocouples that are distributed in the second spanwise array downstream of the LE-81 trip, starting with MT-B-95-68 in the most inboard location, progressing outboard with MT-B-95-71, MT-B-95-76, MT-B-95-79, MT-B-95-86, with MT-B-95-90 being most outboard. Note that MT-B-95-81 has already been captured as part of the lengthwise array (and shown in Figs. 66 & 69). These seven will be used to determine the lateral spreading of the turbulent wedge at the second spanwise array associated with the LE-81 trip during ascent and descent.

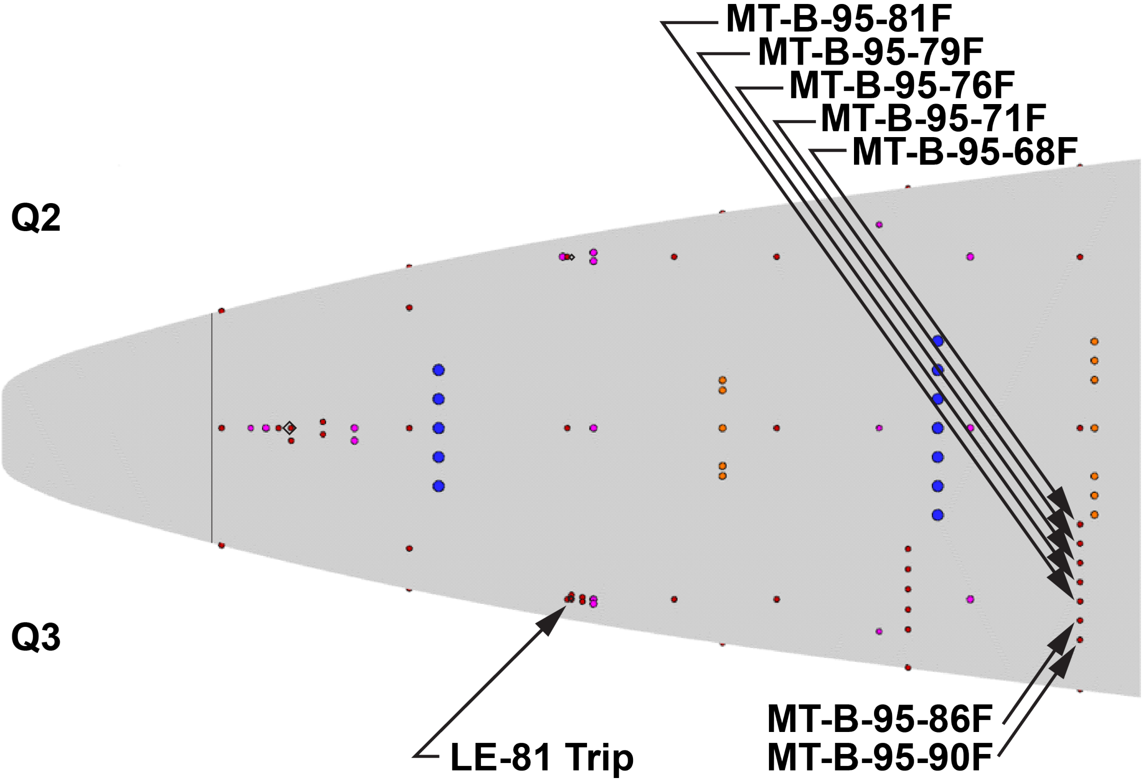

Figure 81. Lateral array of thermocouples at station 95 downstream of the Side B LE-81 trip

Figures 82 - 87 provide an assessment of turbulent wedge spreading during ascent at the second spanwise array (which is 95% lengthwise down the vehicle) behind LE-81. Consistent with the forward spanwise array, the most inboard location MT-B-95-68F (Fig. 82) departs from turbulent levels first at 27.6s. This location has a corresponding Side A sensor, which stays turbulent roughly 1s later. Moving outboard, MT-B-95-71F (Fig. 83) and MT-B-95-76 (Fig. 84) indicate transition onset in succession with 28.2s and 29.0s, respectively. In both cases, the Side A sensors indicate turbulence persisting nearly 1s later. Next, MT-B-95-79F (Fig. 85) indicates transition onset at 29.6s. For this location, the Side A onset time is now 1s earlier, which may suggest this Side B sensor is now being influenced by the turbulent wedge coming from LE-81 trip. The next sensor, which is MT-B-95-81 and is shown in Fig. 66, is similar with onset at 30.0s and the corresponding Side A sensor being about 2s earlier. The latest time of onset from this spanwise array is at MT-B-95-86F (Fig. 86) with onset at 32.3s, which has no corresponding sensor on Side A. The onset time for MT-B-95-90F (Fig. 87) is at 32.0s, with a corresponding Side A onset time being nearly 5 seconds earlier. Since MT-B-95-86F has the latest transition onset time during ascent, this likely indicates the wake disturbance path behind LE-81 tracking through this sensor location.

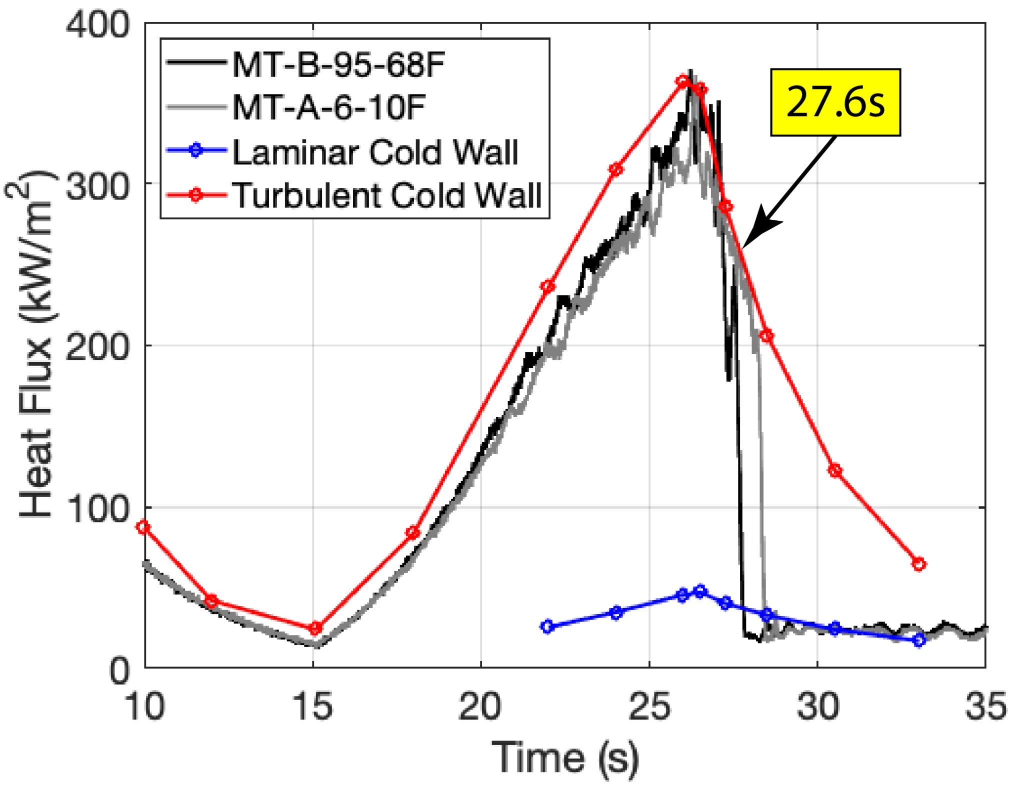

Figure 82. Calculated heat transfer during ascent from sensor MT-B-95-68

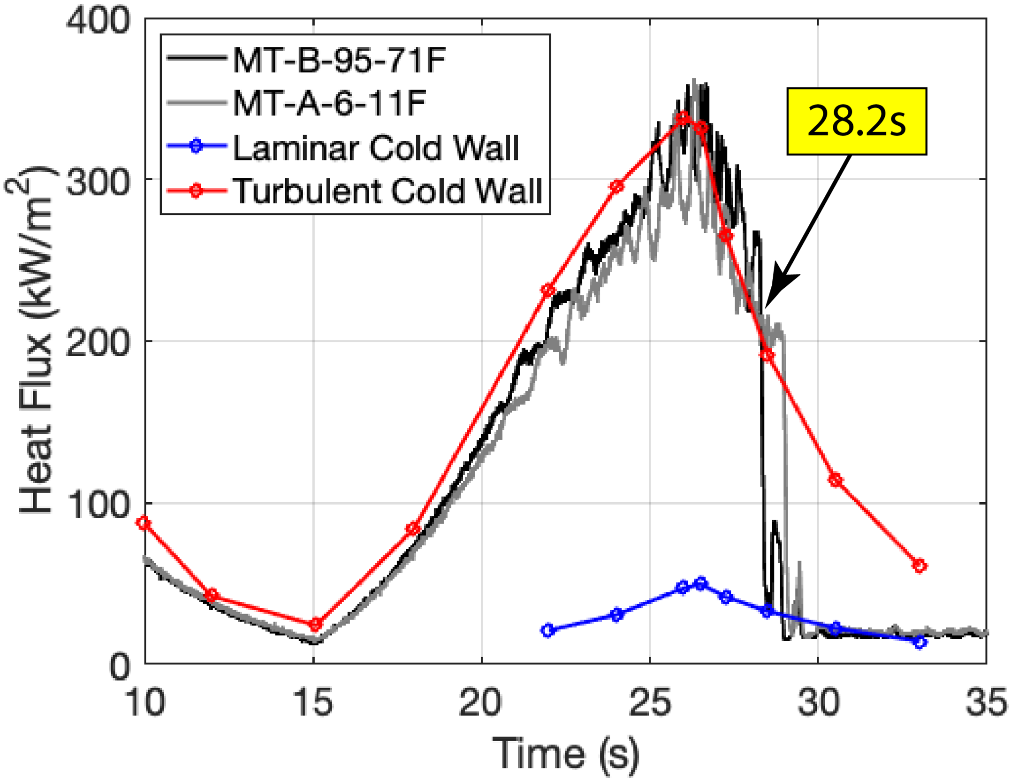

Figure 83. Calculated heat transfer during ascent from sensor MT-B-95-71

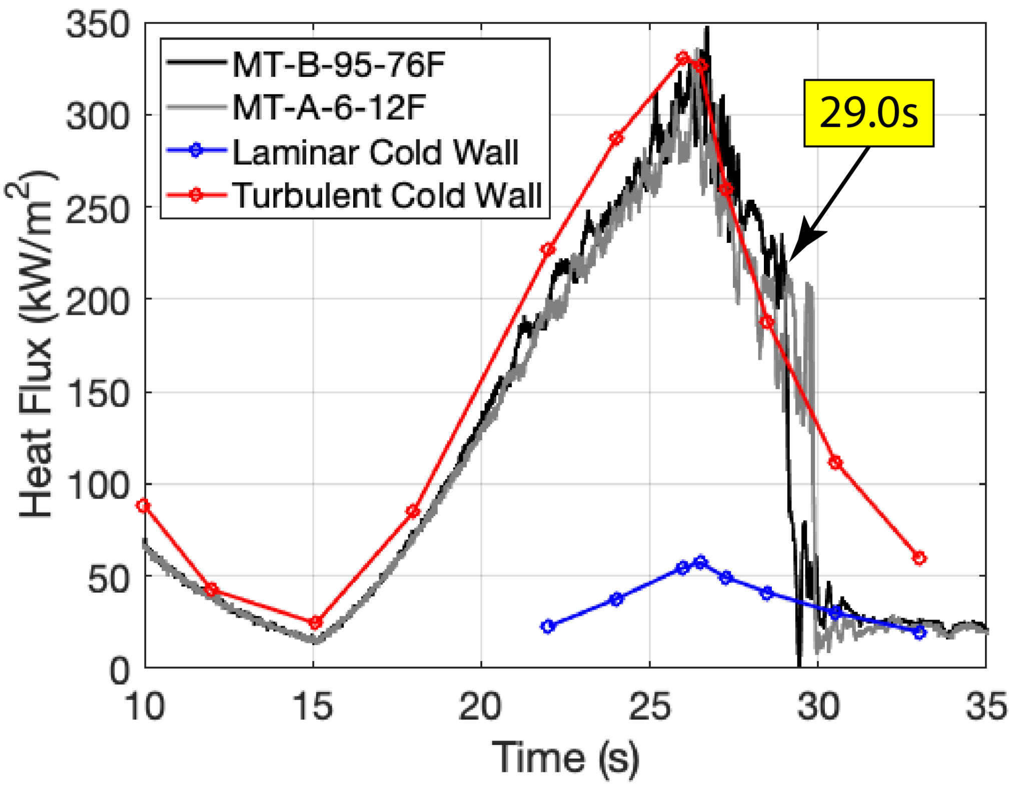

Figure 84. Calculated heat transfer during ascent from sensor MT-B-95-76

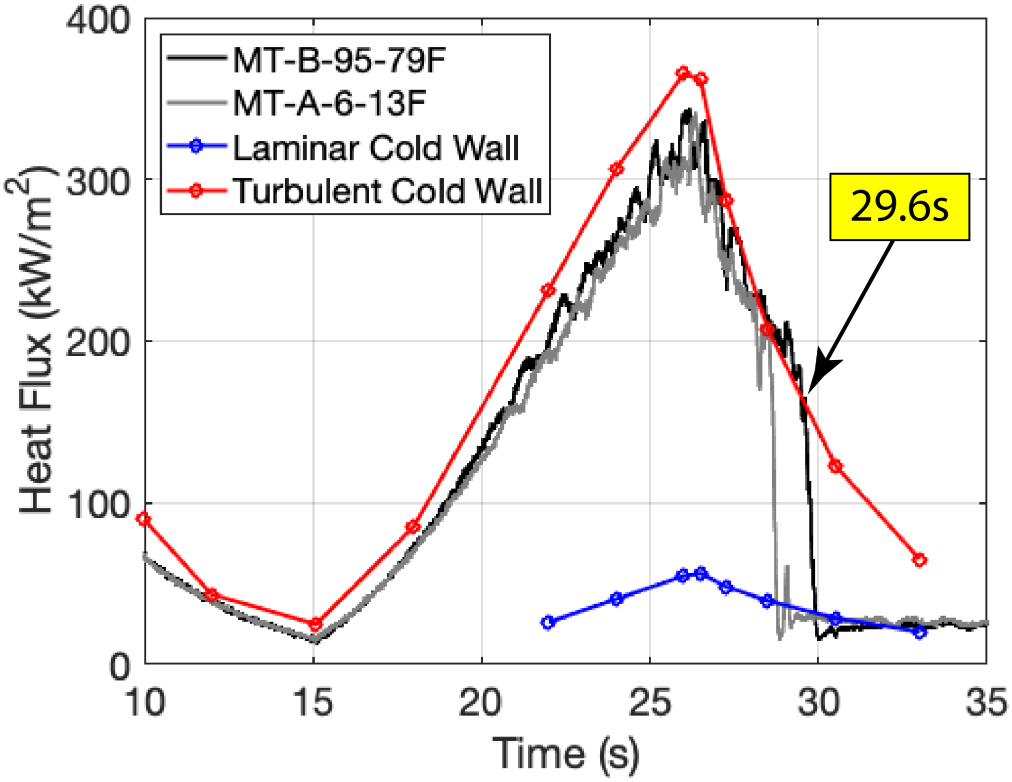

Figure 85. Calculated heat transfer during ascent from sensor MT-B-95-79

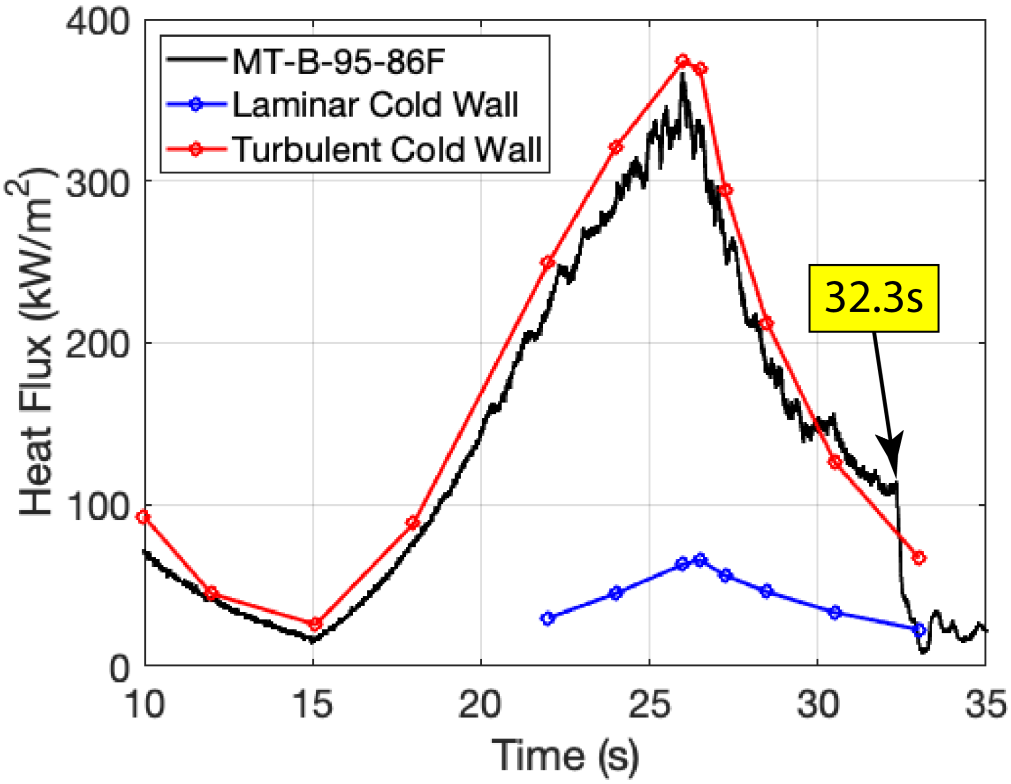

Figure 86. Calculated heat transfer during ascent from sensor MT-B-95-86

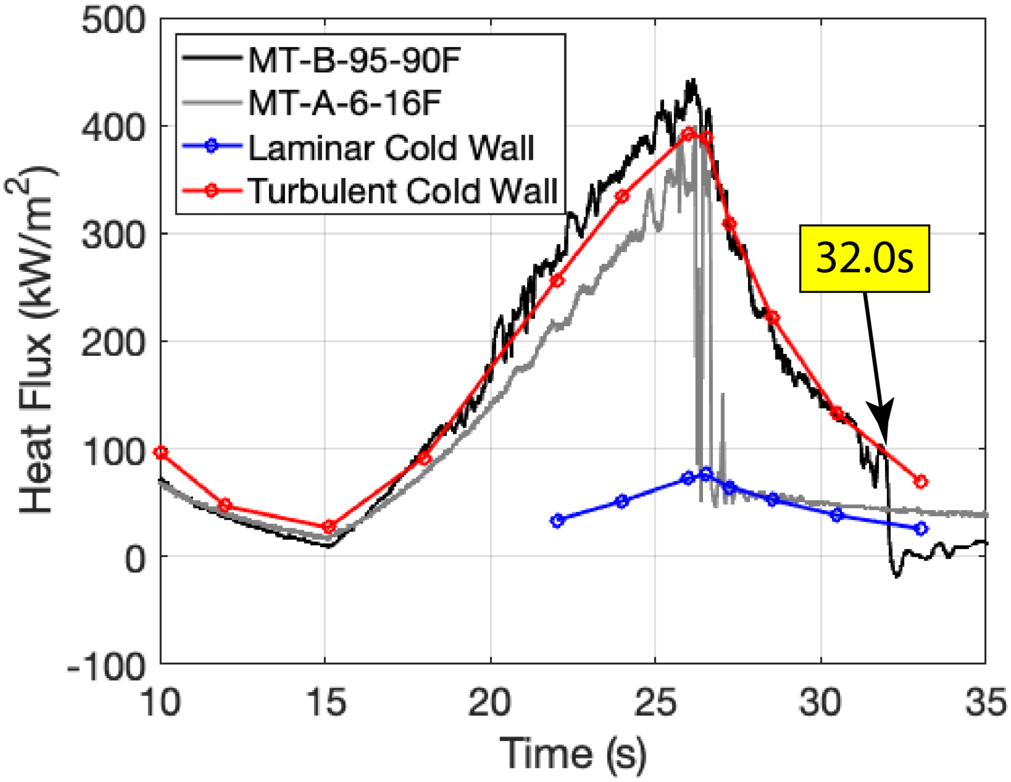

Figure 87. Calculated heat transfer during ascent from sensor MT-B-95-90

Figures 88 - 93 provide an assessment of wedge spreading during descent at the second spanwise array (which is 95% lengthwise down the vehicle) behind LE-81. Consistent with the forward spanwise array, the most inboard location MT-B-95-68F (Fig. 88) reaches the turbulent predictions last at 403.3s. This location has a corresponding Side A sensor, which indicates transition onset almost 1s earlier. Moving outboard, MT-B-95-71F (Fig. 89) indicates transition onset at 402.0s while MT-B-95-76 (Fig. 90) indicates transition onset next at 401.5s. In both cases, the Side A sensors indicate turbulence occurs less than 1s earlier. Next, MT-B-95-79F (Fig. 91) indicates transition onset at 400.8s. For this location, the Side A onset time is now more than a second later, which may suggest this Side B sensor is now being influenced by the turbulent wedge coming from LE-81. The next outboard sensor, which is MT-B-95-81 (shown in Fig. 69), indicates transition onset at 399.3s with the corresponding Side A sensor being about 3 seconds later. The earliest time of onset from this spanwise array is at MT-B-95-86F (Fig. 92) with transition onset at 398.0s, and there is no corresponding sensor on Side A. The onset time for MT-B-95-90F (Fig. 93) is at 398.8s. The corresponding Side A sensor for this location indicated transition ~6s later. With transition onset occurring the earliest at MT-B-95-86F, this is a likely indication of the wake disturbance path behind LE-81 tracking through this sensor location.

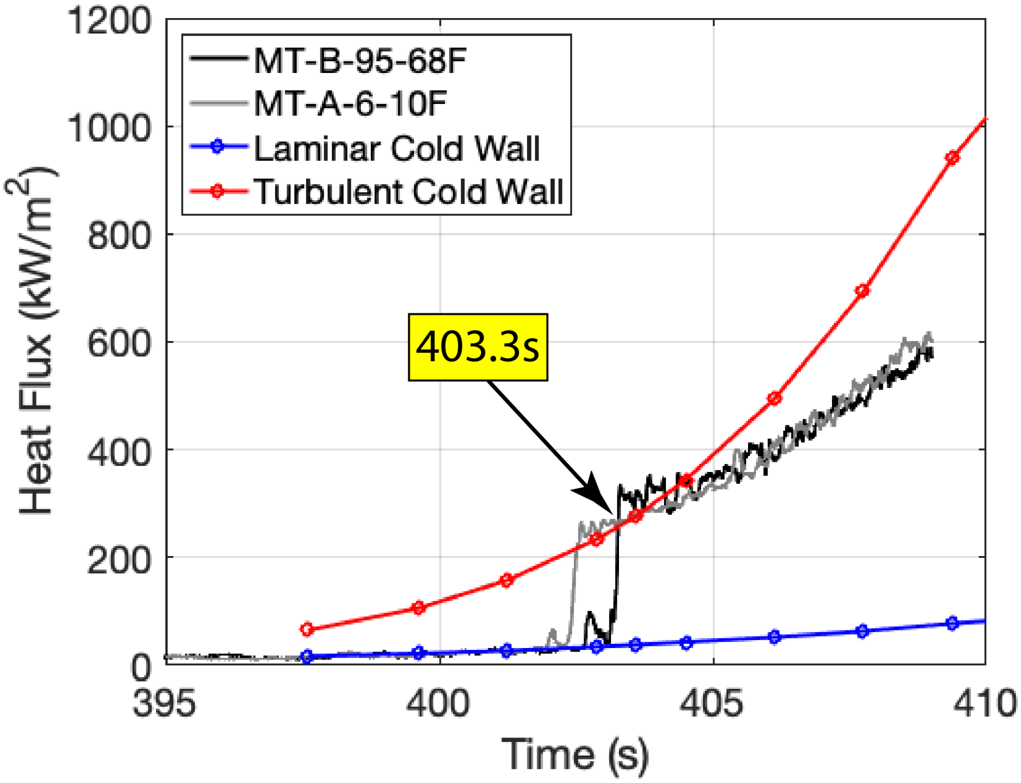

Figure 88. Calculated heat transfer during descent from sensor MT-B-95-68

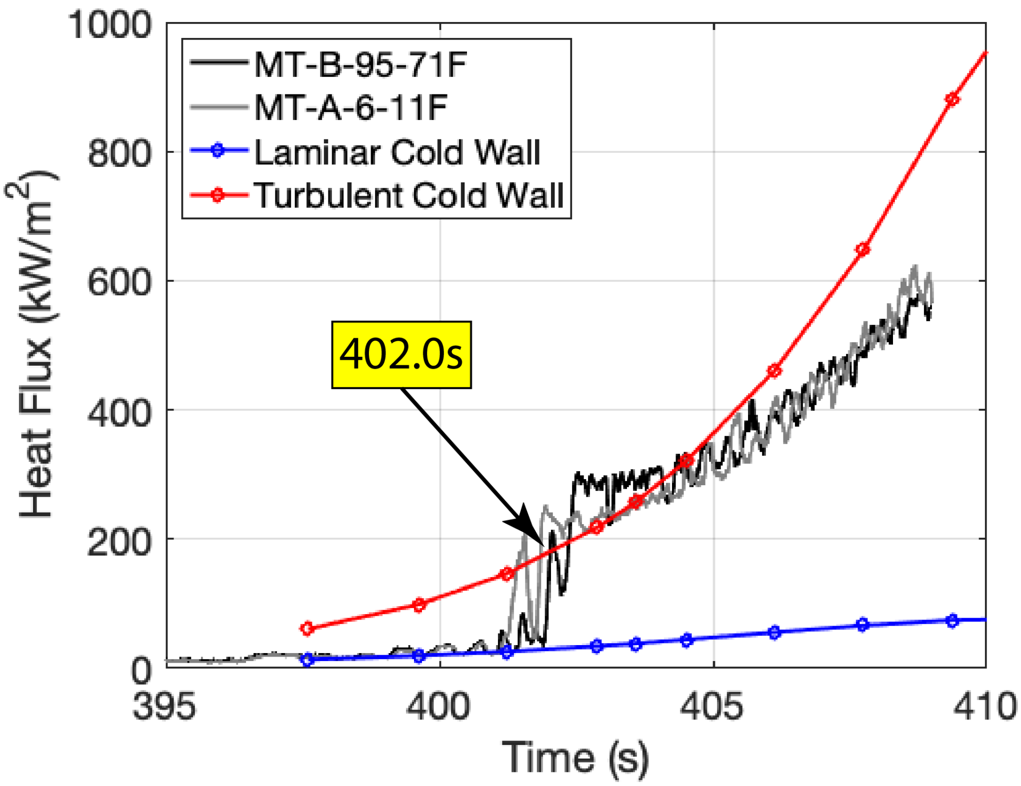

Figure 89. Calculated heat transfer during descent from sensor MT-B-95-71

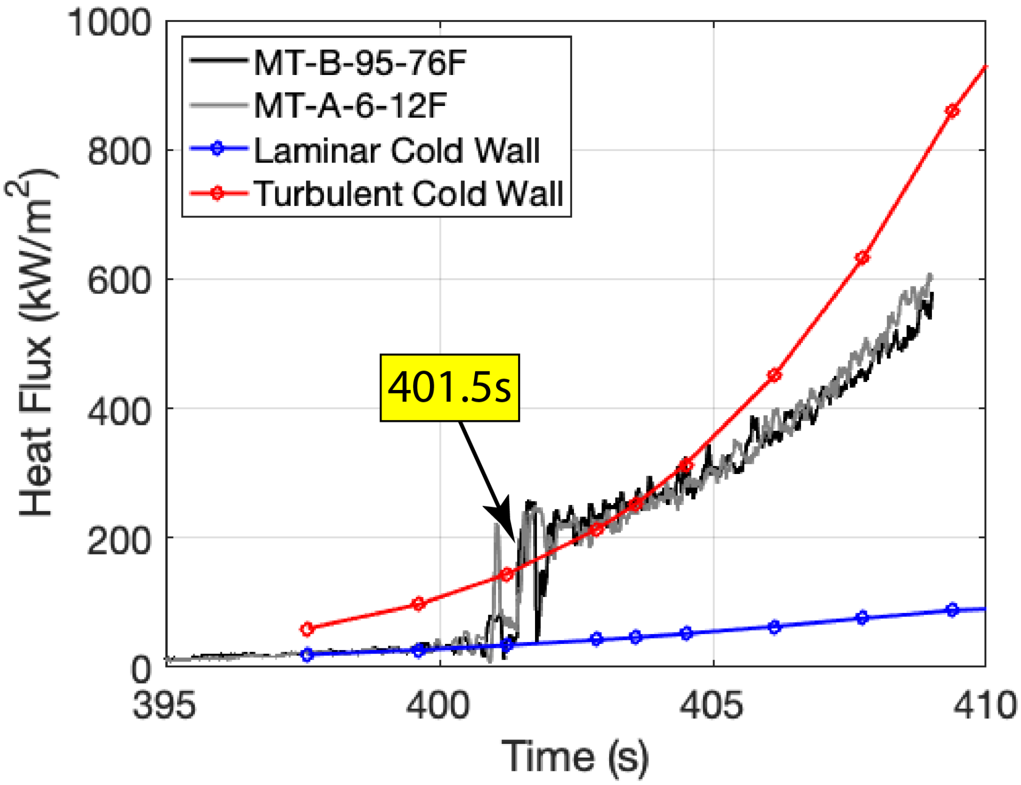

Figure 90. Calculated heat transfer during descent from sensor MT-B-95-76

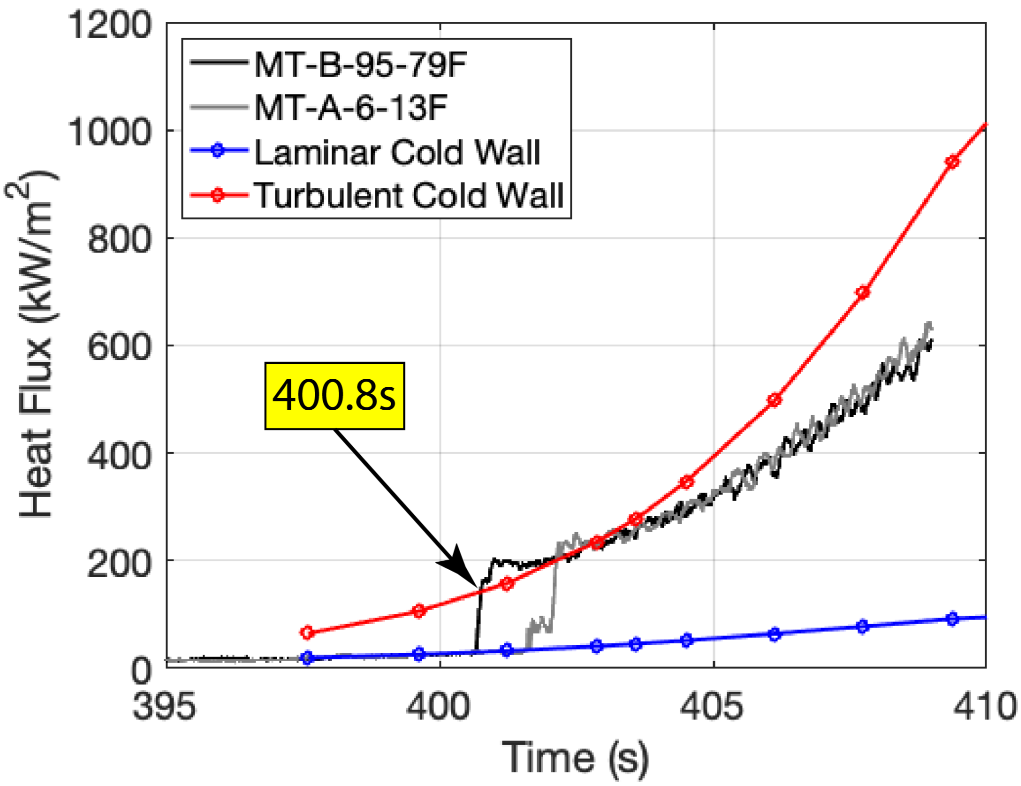

Figure 91. Calculated heat transfer during descent from sensor MT-B-95-79

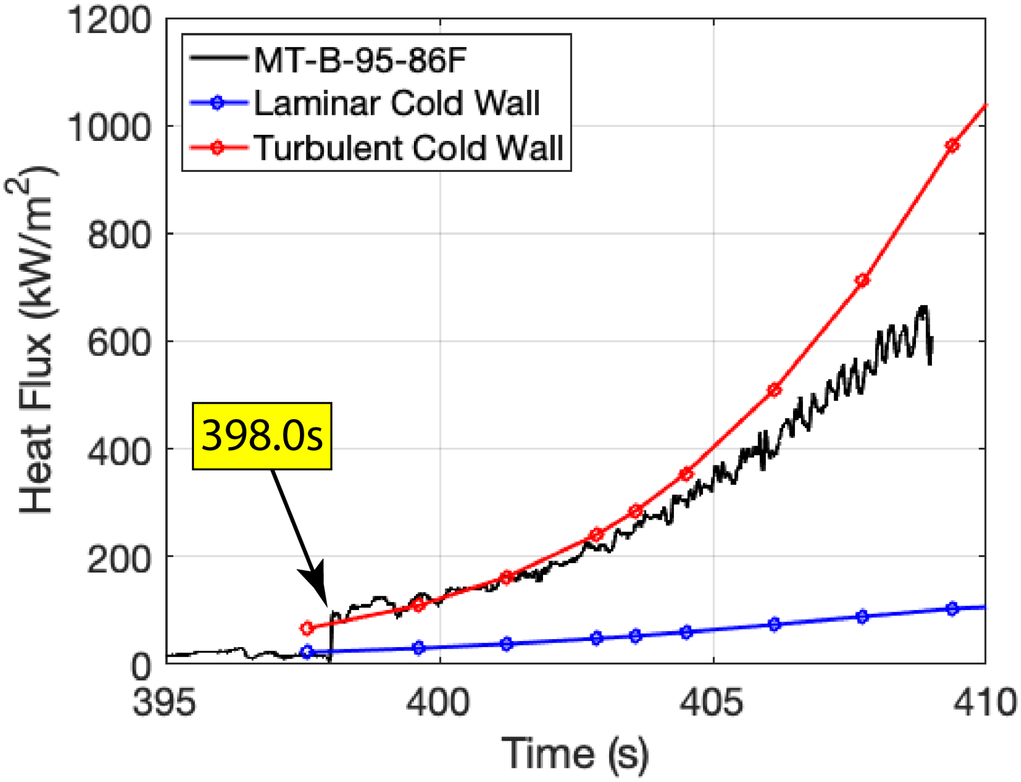

Figure 92. Calculated heat transfer during descent from sensor MT-B-95-86

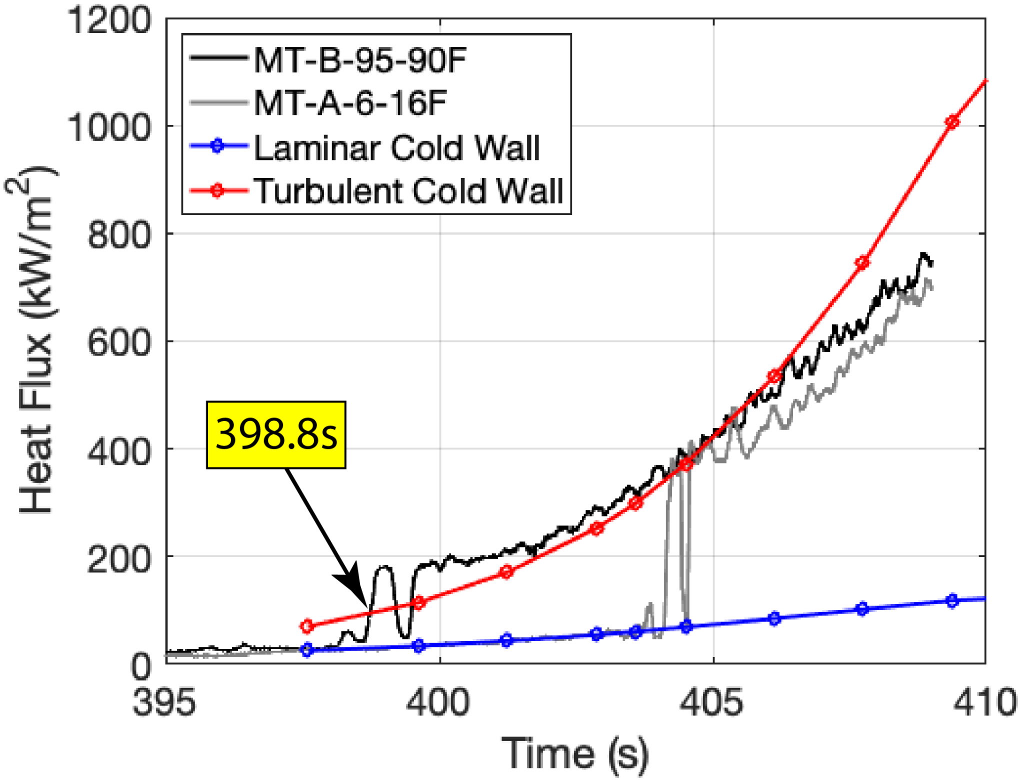

Figure 93. Calculated heat transfer during descent from sensor MT-B-95-90

Thermogage Results

There were 12 thermogage (TG) sensors allocated for Side B, which were split across two spanwise arrays directly behind the CL trip. These sensors provide a direct measurement of surface heating, however they also required frequent calibrations to reduce/minimize sensor drift. The data to be plotted from these sensors will, therefore, be presented as provided from the flight data output files, without computational predictions for reference. While considered a more qualitative dataset, in comparison to the previous results, the intent is still to derive transition times to further develop, and augment, the desired onset maps. For the heat transfer plots in this subsection, best efforts will be made to identify a similar "point of departure" from turbulence, even though there are no computations to assist the process. The data will instead be plotted together by groupings such that the onset times can be determined by association with the results from nearby sensors.

The stated range for the TG sensors is from 0 and 1000 W/cm^2. However, significant measurement drift was observed with many of them, which is a known weakness. Standard practice is to periodically re-zero the sensor output at set times during the mission. The original plan was to recalculate zero offsets just prior to launch and then near the end of the mission, however the output drift was still significant. Thus, for the results plotted herein, an additional re-zeroing was conducted near flight apogee, to separate the measurements between ascent and descent, in hopes of minimizing the drift. In some cases, trying to correct for sensor drift helped. In others it did not, as will be shown.

Spanwise Array #1 Behind CL Trip

Figure 94 provides a sketch showing five Side B thermogages that were distributed in the initial spanwise array, located 42% down the body with TG-B-42-38 and TG-B-42-46 on the Q2 side of the trip, TG-B-42-50 directly behind the CL trip, and TG-B-42-54 and TG-B-42-62 on the Q3 side. These five locations were chosen to help determine the lateral spreading behind the CL trip during ascent and descent.

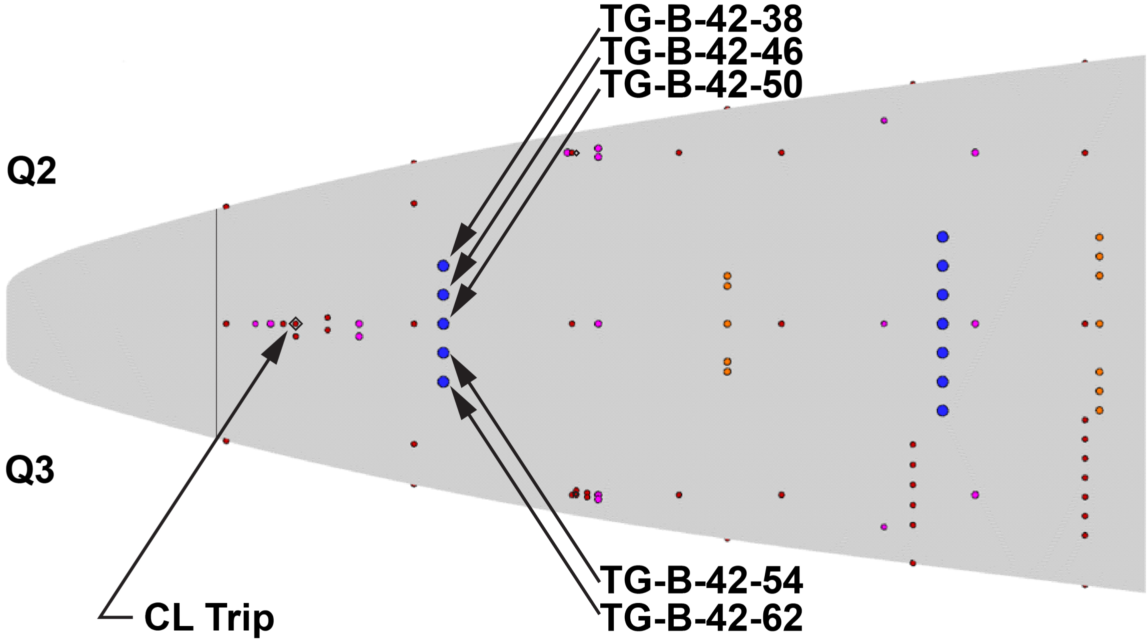

Figure 94. Lateral array of thermogages at station 42 downstream of the CL trip

Figure 95 provides the measured heat flux results from the station-42 thermogages during ascent. All five are plotted together in one figure to allow for easier comparison across the span. Unfortunately, with this grouping, various postflight attempts to correct for sensor drift did not help, as the traces are still significantly offset from each other. The spread in the sensor traces makes it difficult to determine transition onset times. Some, such as TG-B-42-46 and TG-B-42-54, look to have very similar trends, even resembling previous thermocouple traces. However, these traces are still offset significantly, even early in flight when heating is low. If these traces could be made to collapse on top of each other, then maybe transition onset times could be determined. Then, there are others, such as TG-B-42-38, TG-B-42-50, and TG-B-42-62, that do not show similar trends to any of other measurements, which support a conclusion that these could just be faulty sensors.

Similar observations are seen in the descent data for the thermogage sensors from the station 42 spanwise array, as shown in Fig. 96. Two of the traces (same ones noted above) appear to have similar trends to each other but with incorrect zero offsets, while the other three (again same ones noted above) appear to behave strangely. All attempts to re-zero the measurements have failed to clarify the transition time observations for this group of sensors. For this reason, times from this sensor array were not included in the final transition onset maps to come. However, the results are included here for documentation and completeness.

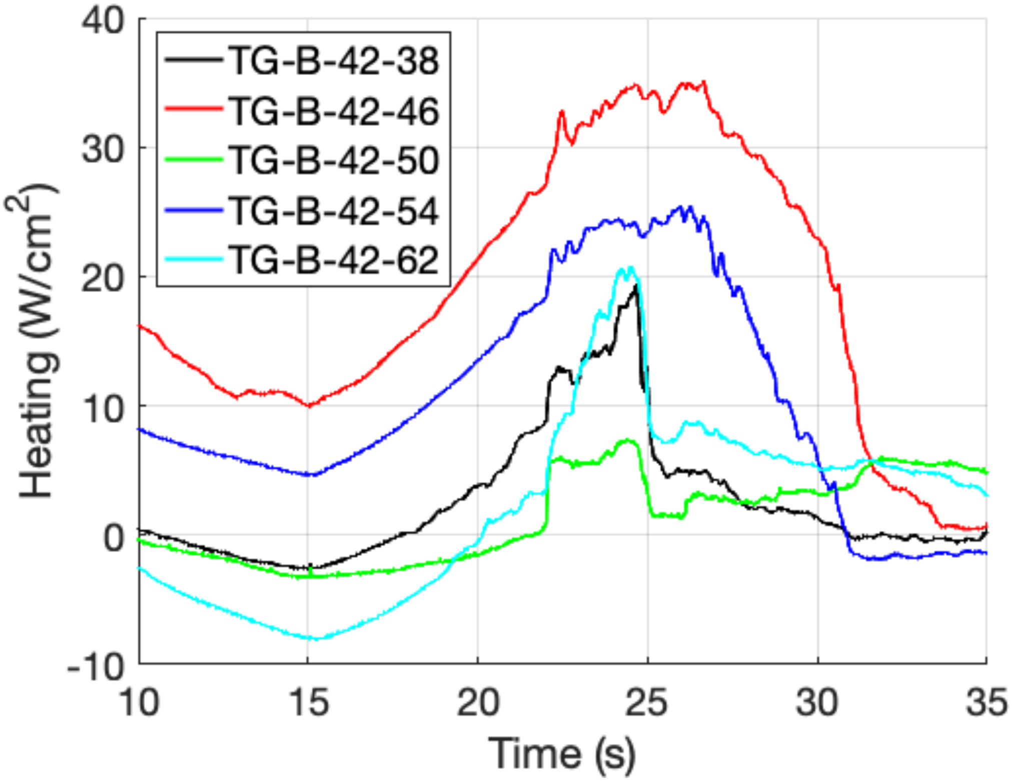

Figure 95. Measured heat transfer during ascent from station 42 sensor array

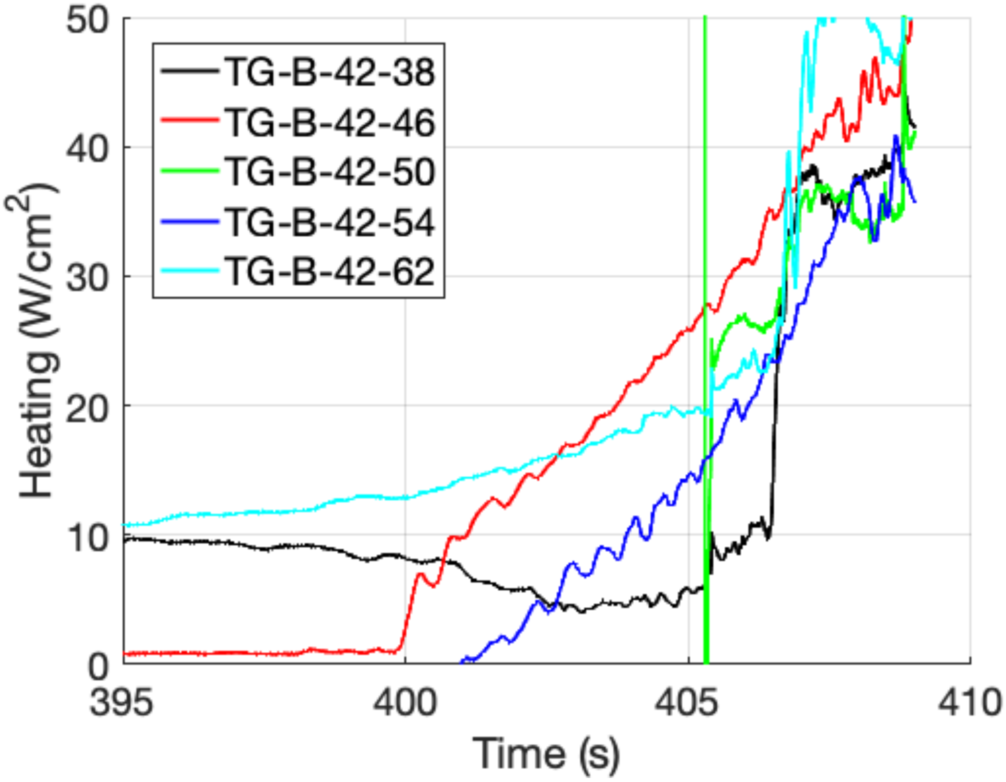

Figure 96. Measured heat transfer during descent from station 42 sensor array

Spanwise Array #2 Behind CL Trip

Figure 97 provides a sketch showing seven Side B thermogages that are distributed in a second spanwise array, at station 82, directly behind the CL trip, which starts with TG-B-82-38, TG-B-82-41, and TG-B-82-46 to the Q2 side of the trip, TG-B-82-50 directly behind the trip, and TG-B-82-54, TG-B-82-59, and TG-B-82-62 to the Q3 side. This lateral array was similarly intended for determination of turbulent spreading behind the CL trip during ascent and descent.

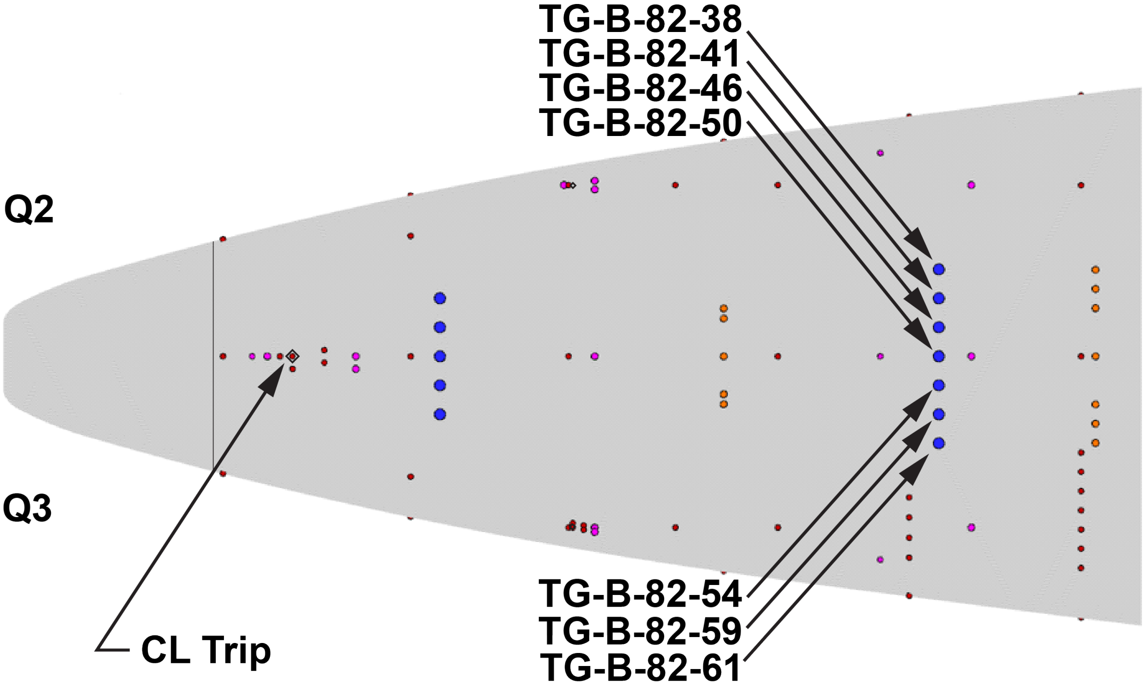

Figure 97. Lateral array of thermogages at station 82 downstream of the CL trip

Figure 98 provides the measured heat flux results from the station 82 sensor array during ascent. All seven TG sensors from this station are plotted together in one chart, to allow for easier comparison across the span. These results are better behaved than the previous grouping with most of the traces tracking close to each other, allowing identification of points of transition onset. The one exception is TG-B-82-61, which appears out of family from the rest, likely an unreliable or faulty sensor. All others track nearly in sync, initially, with systematic departures from the perceived turbulent heating levels: starting with TG-B-82-38, the most outboard sensor (with the other being unreliable) indicating transition onset at 27.2s; next TG-B-82-41 and TG-B-82-59, the next two inboard sensors, indicate onset at 28.3s; then TG-B-82-46 and TG-B-82-54, being the next inboard sensors, indicating transition at 31.0s; and finally the CL sensor, TG-B-82-50, indicating transition onset at 32.7s. In comparison to other nearby measurements along the vehicle centerline, a transition onset time of 32.7s aligns well with the thermocouple results, with MT-B-70-50 and MT-B-95-50 providing transition onset values of 31.6s and 33.1s, respectively.

Figure 99 provides the descent results from the station 82 measurements. The descent results are also similarly behaved, allowing for systematic determination of onset times that start with the centerline sensor, TG-B-82-50 at 398.3s, followed in succession by the next two outboard sensors, TG-B-82-46 and TG-B-82-54, at 399.4s, then TG-B-82-41 and TG-B-82-59 at 402.5s, and finally with TG-B-82-38 at 403.9s (TG-B-82-61 being faulty). In comparison to nearby thermocouples along vehicle centerline, the onset time of 398.3s falls in line with the measurements from MT-B-70-50 at 398.7s and MT-B-95-50 at 397.6s.

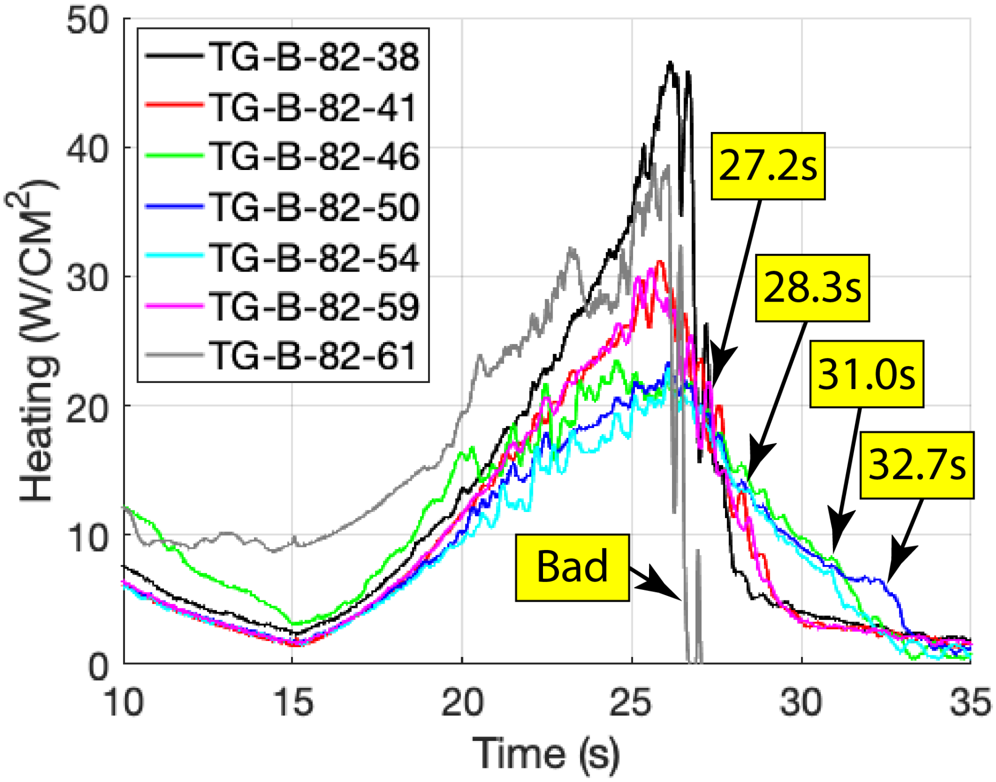

Figure 98. Measured heat transfer during ascent from station 82 sensor array

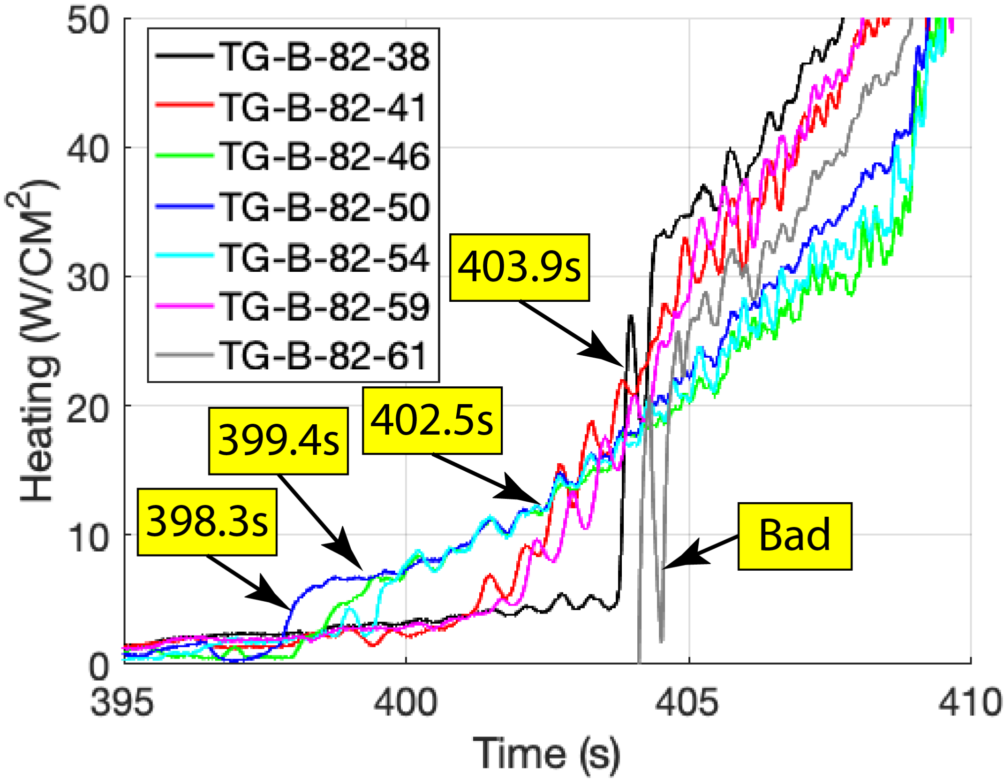

Figure 99. Measured heat transfer during descent from station 82 sensor array

Thin-Film Results

A total of 12 thin-film sensors were used on Side B of BOLT-2 in additional spanwise arrays behind the CL trip. These are proven sensors for use in hypersonic wind tunnels, including the high-enthalpy tunnel at CUBRC that reproduces true hypersonic flight conditions. However, these sensors have never been tried in flight before. They are fast response sensors that can provide surface temperatures, although in the tunnel they are typically used to pick up turbulent bursts. For now, with the lack of operational experience with these sensors in flight, they are considered qualitative. To convert surface temperature measurements to heat transfer, some assumption about the back face temperatures would be needed. During typical short duration runs within CUBRC, these sensors are analyzed using 1D heat conduction with no temperature rise on the back side of the sensors, which greatly simplifies the analysis.

These TF sensors are rated to measure surface temperatures in a range from 0 to 350°C. Some minor drift between sensors is possible, likely an indicator of the health of the sensing elements, as any erosion/damage to the circuit can result in a shift of the sensor output and ultimately to the failure of the sensor. When looking at temperature-time traces, the typical method for determining the time of transition onset is to find the inflection point, sometimes also called the "knee in the curve," that identifies when the surface heating switches between laminar and turbulent states. The present dataset represents the first experience of these sensors on a hypersonic flight vehicle.

Spanwise Array #3 Behind CL Trip

Figure 100 provides a sketch showing an array of five Side B thin-film sensors distributed spanwise at station 63 downstream of the CL trip, starting with TF-B-63-42 and TF-B-63-46 to the Q2 side of the trip, TF-B-63-50 directly behind the trip, and TF-B-63-54 and TF-B-63-58 to the Q3 side. These five were intended to support the analysis of the lateral spreading of the turbulent wedge behind the CL trip as a function of time during ascent and descent. The outboard locations from this array were symmetrically placed to catch the expected width of a fully turbulent wedge behind an effective CL trip.

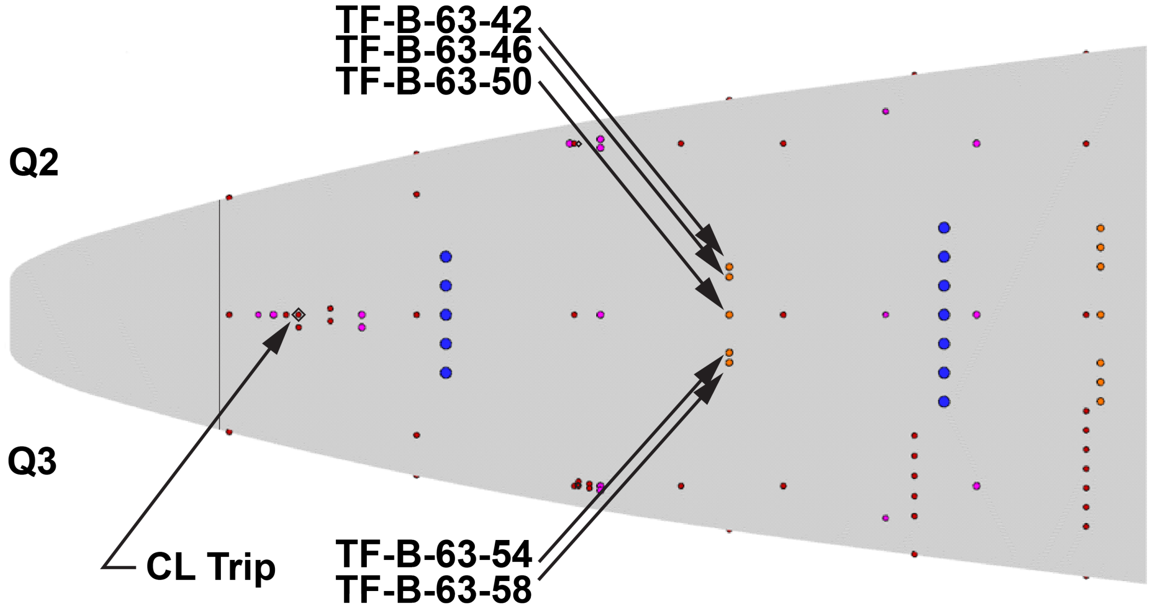

Figure 100. Lateral array of thin-film sensors at station 63 downstream of the CL trip

Figure 101 provides the measured surface temperatures from the station 63 spanwise thin-film array during ascent. The TF sensors are sensitive enough to capture maneuvering behavior (the small fluctuations seen in the plots are from minor alpha/beta variations), which does increase the subjectivity of identifying transition onset. In most cases, the inflection point identifying transition onset is obvious. In a few cases, the sinusoidal nature of the vehicle maneuvers masks the slope change. To improve inflection-point identification, thin straight lines, intended to remove the sinusoids, were added to each trace (in matching color) to aid interpretation of the transition onset times. When using the straight lines for guidance, the transition onset times during ascent are systematic with the outboard sensors (TF-B-63-42 and TF-B-63-58) indicating transition onset at 29.0s, and the sensor behind the CL trip (TF-B-63-50) indicating 30.8s. In comparison to the closest centerline sensors during ascent, an onset time of 30.8s from TF-B-63-50 is synchronous with MT-B-48-50 with an onset of 30.7s and MT-B-70-50 with a transition onset of 31.6s.

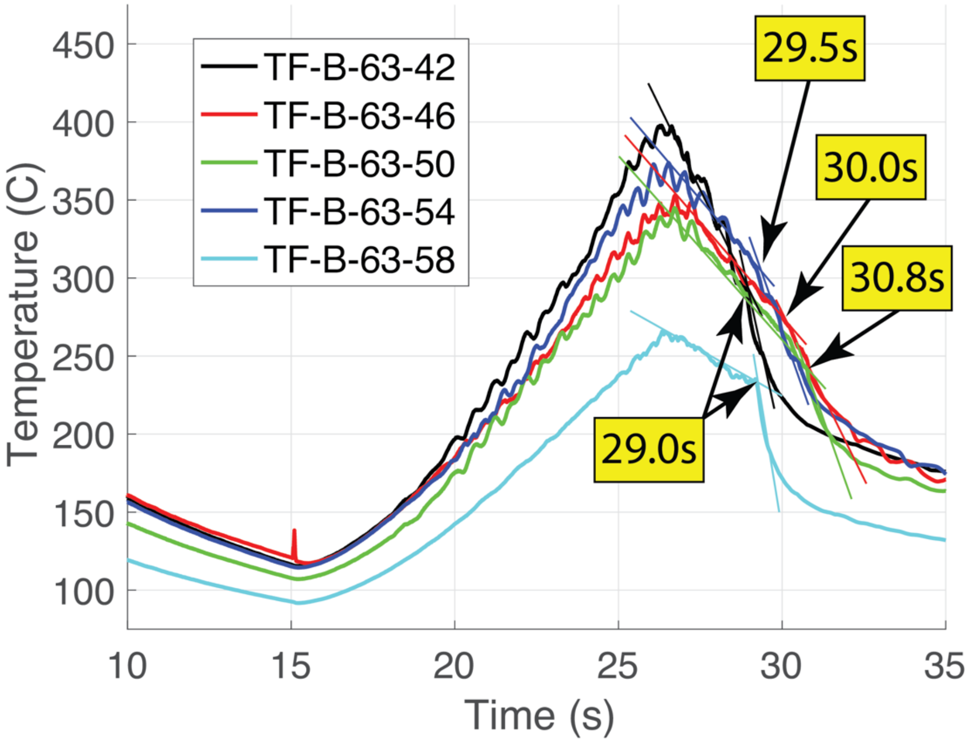

Figure 101. Measured surface temperatures during ascent from station 63 TF sensor array

Figure 102 provides the station 63 TF results during descent. Again, the same approach (as discussed above) was utilized with straight line approximations being used to filter out the sinusoidal behavior of the vehicle maneuvers, which provides for systematic observations of transition onset. Thus, during descent, the sensor in line with the CL trip (TF-B-63-50) is the first to observe transition onset at 399.4s. Moving outboard, sensors TF-B-63-46 and TF-B-63-54 indicate transition onset at 399.8s and 400.8s, respectively. The most outboard locations, with TF-B-63-42 and TF-B-63-58 provide the latest transition onset times (for this sensor array) with transition at 401.3s and 401.8s, respectively. In comparison to the closet centerline sensors, at transition onset time of 399.4s for TF-B-63-50 is slightly earlier than the observations of 399.7s at MT-B-48-50. This could be a case where a difference in sensitivity between the various sensor types, or the approach used to analyze the various data, results in a slight bias in the observed transition onset times.

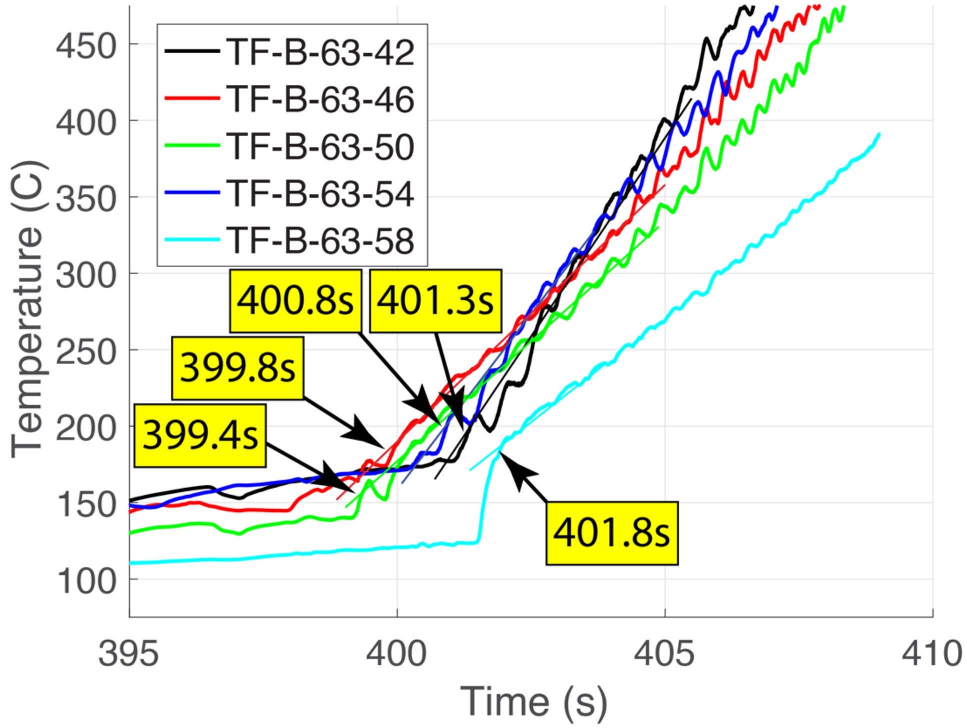

Figure 102. Measured surface temperatures during descent from station 63 TF sensor array

Spanwise Array #4 Behind CL Trip

Figure 103 provides a sketch showing an array of seven Side B thin-film sensors distributed spanwise at station 96 downstream of the CL trip, starting with TF-B-96-38, TF-B-96-42, TF-B-96-46 to the Q2 side of the CL trip, TF-B-96-50 directly behind, and TF-B-96-54, TF-B-96-58, and TF-B-96-64 to the Q3 side. This array was also intended to support the measurement of the turbulent wedge angle and spreading as a function of time. As such, the outboard locations from this array were also symmetrically placed to catch the expected width of a fully turbulent wedge behind an effective CL trip.

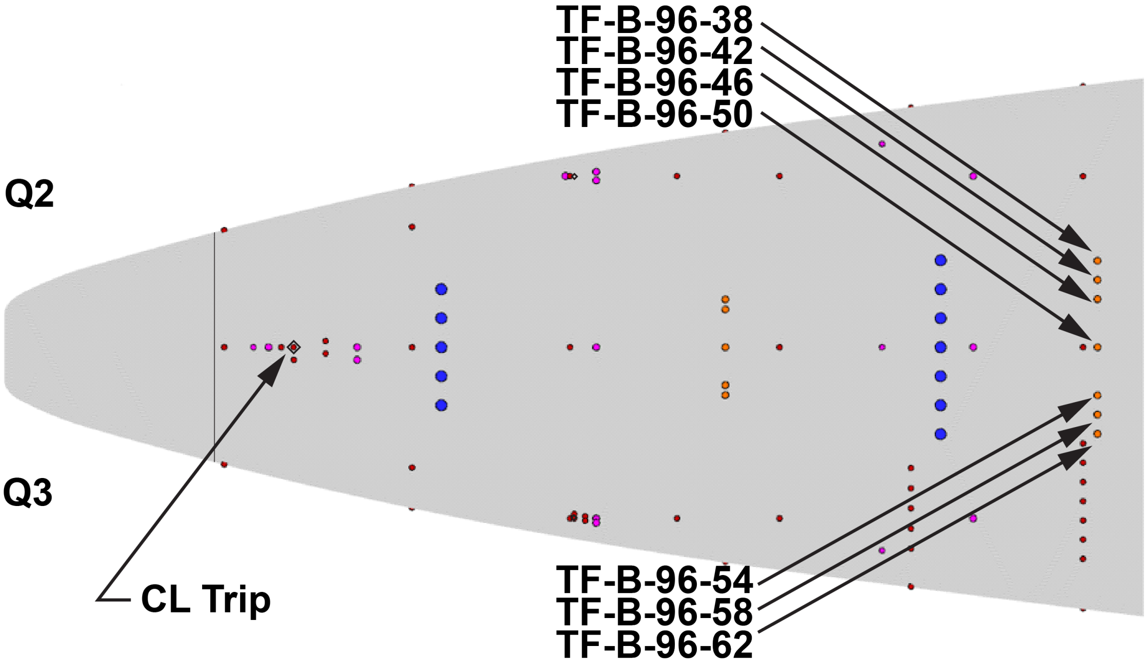

Figure 103. Lateral array of thin-film sensors at station 96 downstream of the CL trip

Figure 104 provides the measured surface temperatures from the station 96 thin-film array during ascent. Using the same analysis approach discussed in the previous section, the onset times during ascent are systematic with outboard sensors (TF-B-96-38, TF-B-96-42, TF-B-96-58, and TF-B-96-64) being the first to show transition onset at around 27s. The sensor directly behind the CL trip (TF-B-96-50) indicated transition onset last at 33.0s, roughly 5s later. One thin-film sensor in this array stopped working during ascent (TF-B-96-46), while its opposite (TF-B-96-54) indicated transition onset at 28.0s. In comparison to the closest centerline sensor during ascent, an onset time of 33.0s from TF-B-95-50 is almost identical with the result from MT-B-95-50 that had indicated transition onset at 33.1s. Similarly, the most outboard sensor, TF-B-96-62, indicated transition onset at 27.1s, while the closest thermocouple, MT-B-95-68, provided a transition onset time of 27.6s, which is consistent.

During descent, similar results were obtained with this TF array, as shown in Fig. 105. For instance, the sensor directly behind the CL trip (TF-B-96-50) was the first to indicate transition onset at 398.5s during descent. The closest thermocouple on centerline, MT-B-95-50, had indicated transition onset at 397.6s, which is slightly earlier. This is another case where there could be a slight bias in time based on the different sensor types. The rest of TF sensors had transition onset roughly 5s later than the centerline one, with transition onset times closer to 403s. Based on knowing that Side A had transition onset times during descent at roughly the same time, this could be an indication that these locations were all outside the influence of the turbulent wedge behind the CL trip. The closest (non-CL) sensor types on Side B were TF-B-96-62 with a transition onset time of 403.0s and MT-B-95-68 with transition onset of 403.3s, which is close, all things considered.

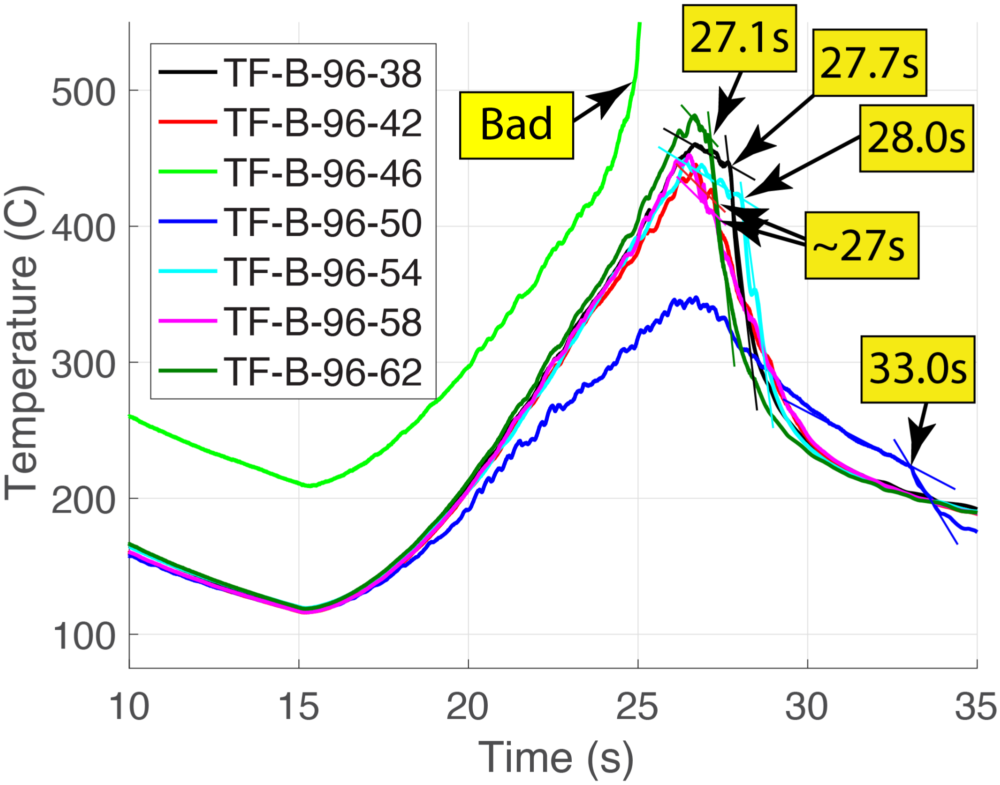

Figure 104. Measured surface temperatures during ascent from station 96 TF sensor array

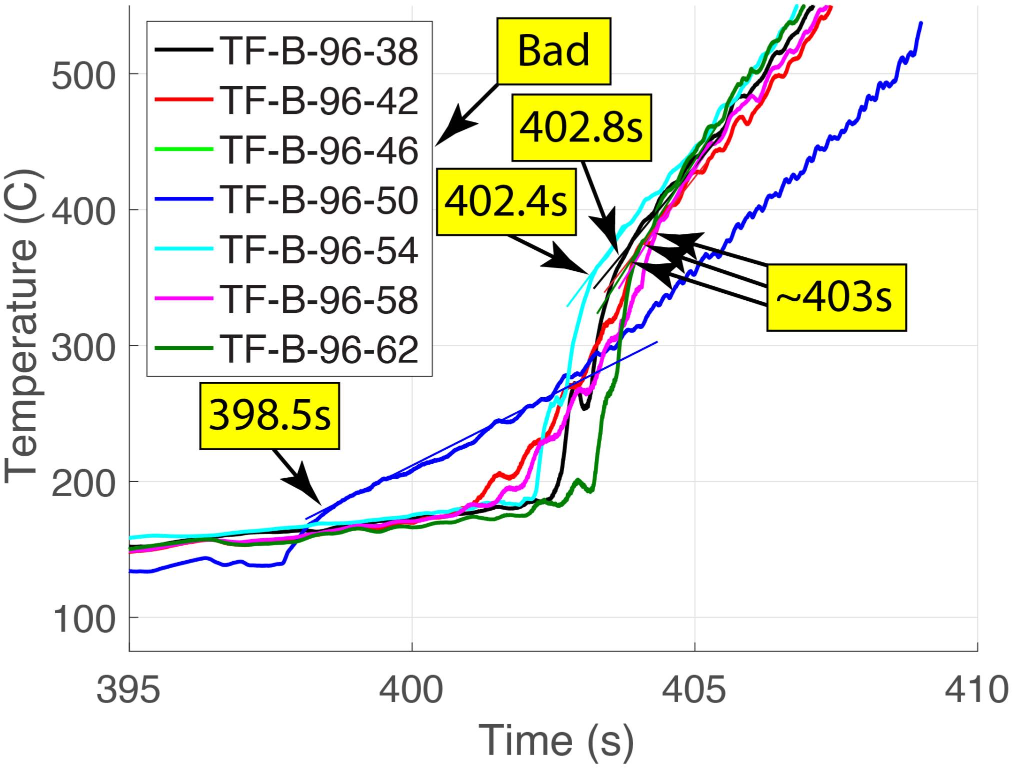

Figure 105. Measured surface temperatures during descent from station 96 TF sensor array

Pressure Data

The Side B pressure data are included in this report for completeness. However, since the focus here is primarily on trip performance, the measured results during the flight are presented as is, with no further in-depth analysis. Three different pressure sensors were used on BOLT-2 Side B. These include measurements of mean pressures, sampled at 400 Hz, as well as high-frequency measurements of pressure fluctuations, sampled at 57 kHz. Mean pressures were obtained with temperature-compensated Honeywell transducers rated to measure up to 15 psi. Fluctuating pressures were measured with both PCB and Kulite transducers that were AC coupled (mean filtered out) and rated to measure up to 20 kHz.

Mean Pressures

Figure 106 shows the locations of the four Side B mean pressure sensors, which were meant to be part of the FADS measurements. Typically, FADS are used to assess aerodynamic maneuvering (α/β changes in time) using sensors located systematically around the vehicle. There is an identical set of measurements on Side A (as captured in Table 5), as well as in the gutters. To date, there has been no attempt to update the BET based on an analysis of the FADS data. Factory calibrations were applied to each sensor during preflight checkouts and an inflight calibration procedure using ground and flight apogee as endpoints to remove any sensor drift in time. Measurement uncertainty for the static pressures is thought to be on the order of 1% of full scale.

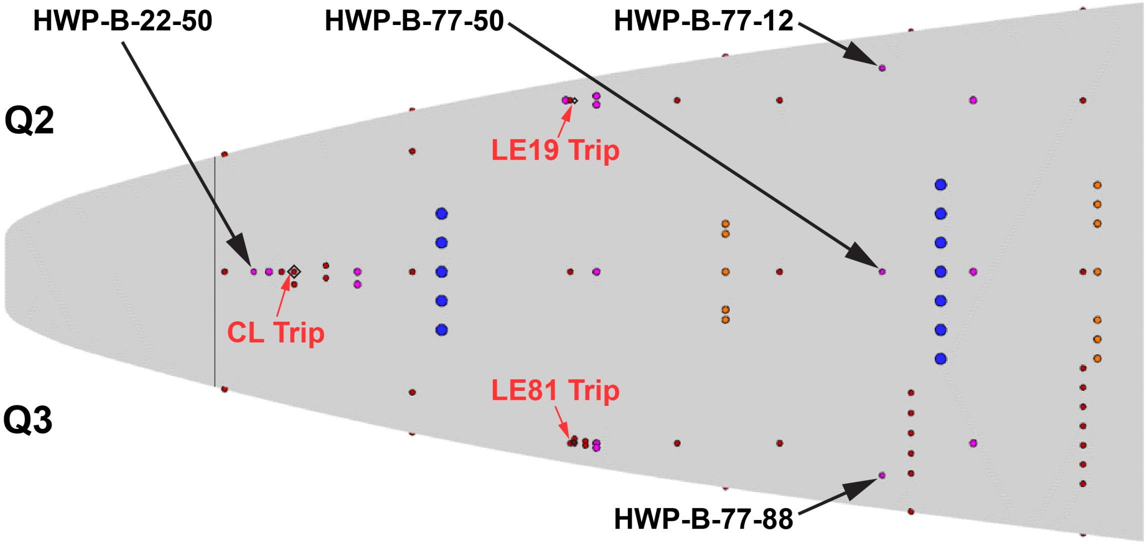

Figure 106. Sketch showing locations of the Side B mean pressure sensor locations.

Table 5. FADS sensor locations on the primary and secondary surfaces.

Side A FADS	X (m)	Y (m)	Z (m)	Side B FADS
HWP_A_1_01	0.2184	±0.0308	0	HWP_B_22_50
HWP_A_4_01	0.7706	±0.1106	0.1783	HWP_B_77_12
HWP_A_4_02	0.7706	±0.0973	0	HWP_B_77_50
HWP_A_4_03	0.7706	±0.1106	-0.1783	HWP_B_77_88

The mean surface pressures measured on Side B during the ascent and descent science windows are provided in Figs. 107 and 108, respectively. The Side A pressures (not shown) are nearly identical to these results, except 180° out of phase, indicating the effects of the minor alpha/beta changes (on the order of ±0.5° with both – see Fig. 7) during flight.

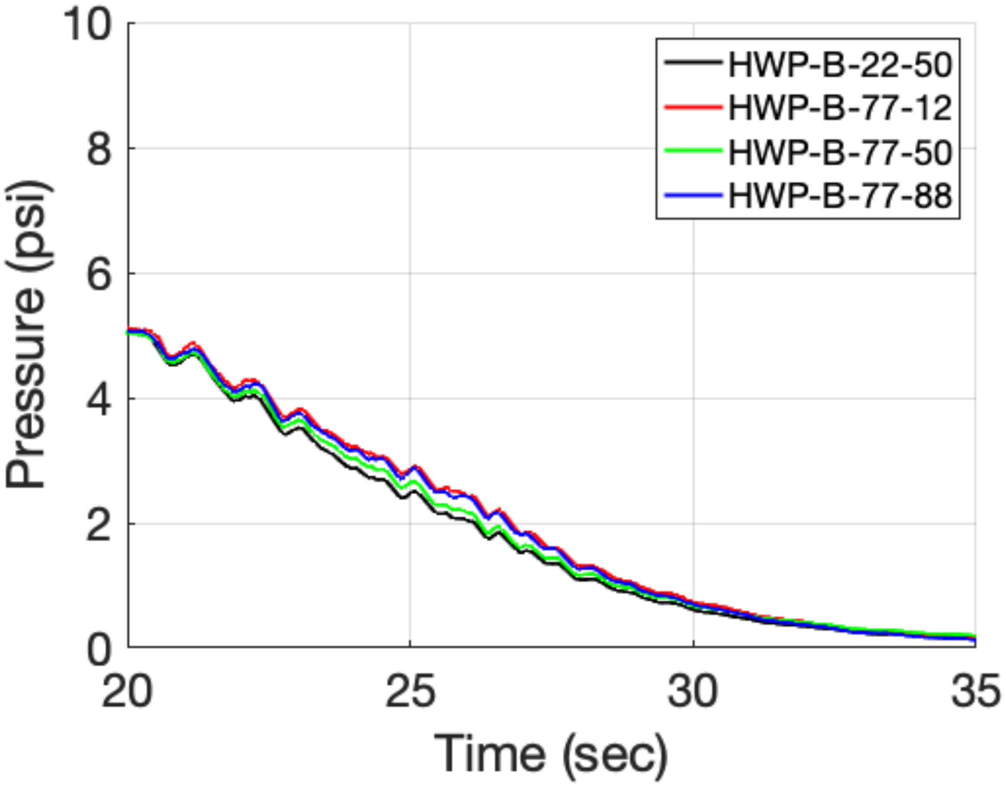

Figure 107. Measured surface pressures during ascent from FADS sensor array

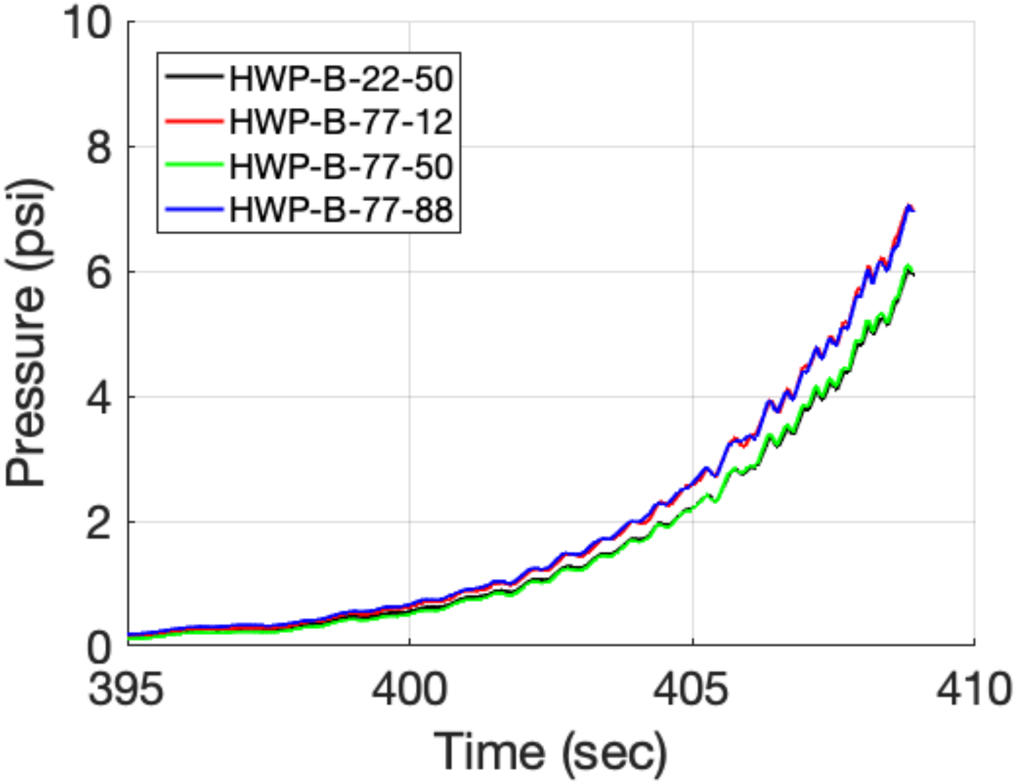

Figure 108. Measured surface pressures during descent from FADS sensor array

Fluctuating Pressures

Figure 109 provides a sketch of the 9 Side B sensor locations dedicated to fluctuating pressure measurements during the BOLT-2 flight. As shown in the figure, five of those locations are in line with the CL trip, two are in line with the LE19 trip, while the remaining two are in line with the LE81 trip. These are the specific sensors for which output files were recorded, however all PCB sensors (shown in grey font) flatlined very early in the launch sequence (prior to t=10s) and thus will not be shown. Only the three Kulite measurements (shown in black font) will be presented. There were an additional three sensors (KUL-RMS-B-42-18, KUL-RMS-B-42-82, and KUL-RMS-B-52-83) installed, but are not shown in the sketch as they were determined to be non-functional prior to launch.

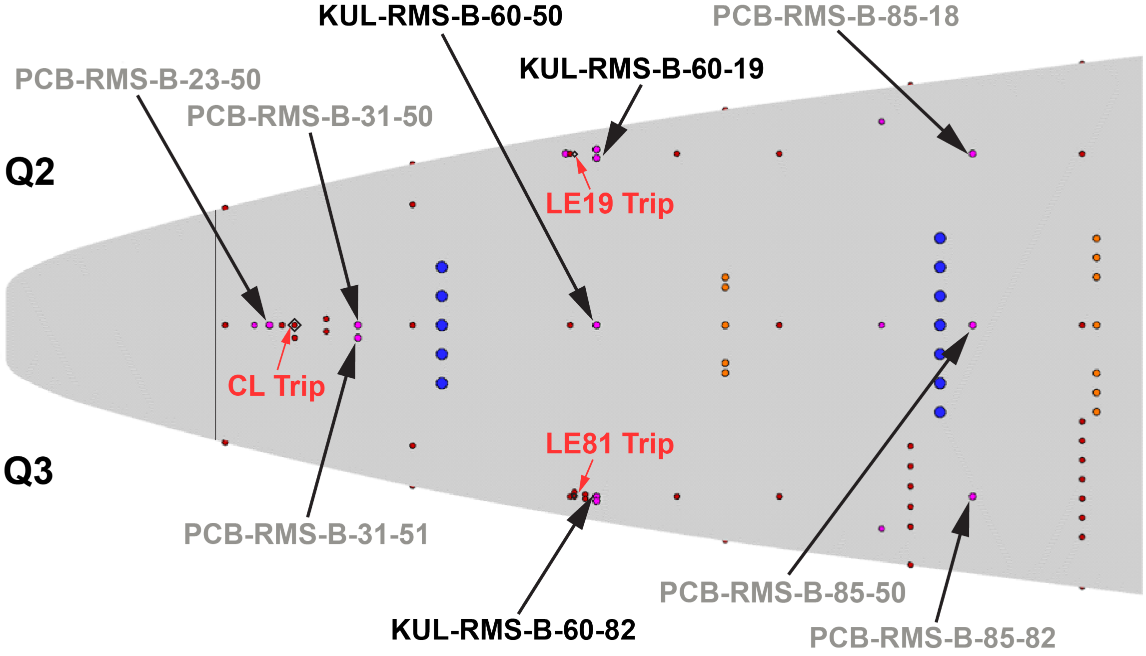

Figure 109. Sensors dedicated to measure fluctuating pressures on Side B.

The measured pressure fluctuations for KUL-RMS-B-60-50, which is behind the CL trip, are presented in Fig. 110 for both the ascent and descent test windows. There are some key points that can be seen in the fluctuating pressure data, such as the fluctuation levels when the rocket motor is burning, the turbulent boundary layer measurements just after motor burnout, and the much smaller fluctuations associated with a laminar boundary layer. For comparison, the transition onset times derived from the closest T/C location, which is the MT-B-48-50 sensor, were 30.7s and 399.3s for ascent and descent, respectively. Thus, the frequency content from KUL-RMS-B-60-50, just judging from the time the fluctuations are minimal, would seem to suggest an earlier observation of transition onset during ascent and a later time during descent. The reason for this discrepancy between the two sensor types is not presently known.

Figure 111 provides the pressure fluctuation measurements from KUL-RMS-B-60-19, which is just behind the LE19 trip on the Q2 side, during both ascent and descent. The resulting observations of key events are very consistent with the previous case, including the discrepancy in transition onset times between the different sensor types. For comparison, the transition onset times derived from the closest T/C location, which is MT-B-52-19, were 29.1s and 401.2s for ascent and descent, respectively.

Figure 112 provides the pressure fluctuation measurements from KUL-RMS-B-60-82, which is just behind the LE81 trip on the Q3 side, during both ascent and descent. Once again, the resulting observations of key events are very consistent with the previous two cases, including the discrepancy in transition onset times between the different sensor types. For comparison, the transition onset times derived from the closest T/C location, which is MT-B-70-81, were 29.5s and 400.7s for ascent and descent, respectively.

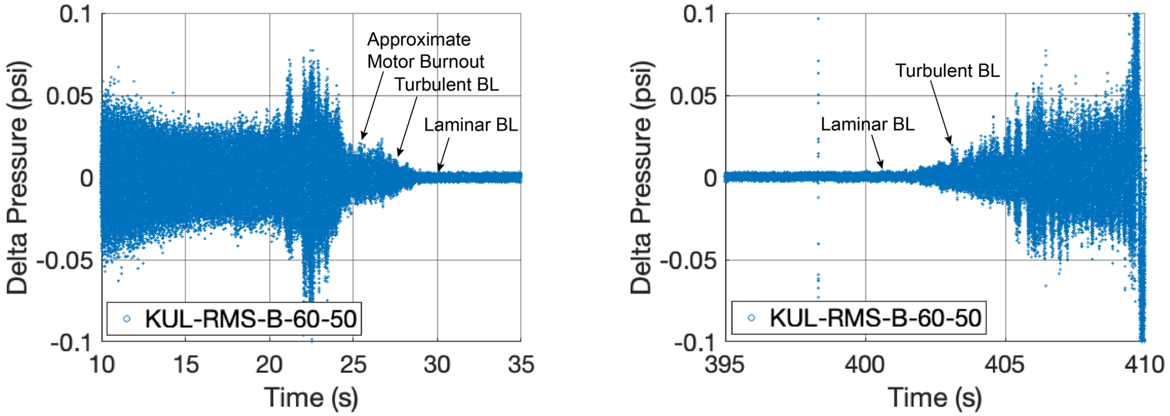

a) Ascent *b) Descent*

Figure 110. Fluctuating pressure measurements for KUL-RMS-B-60-50.

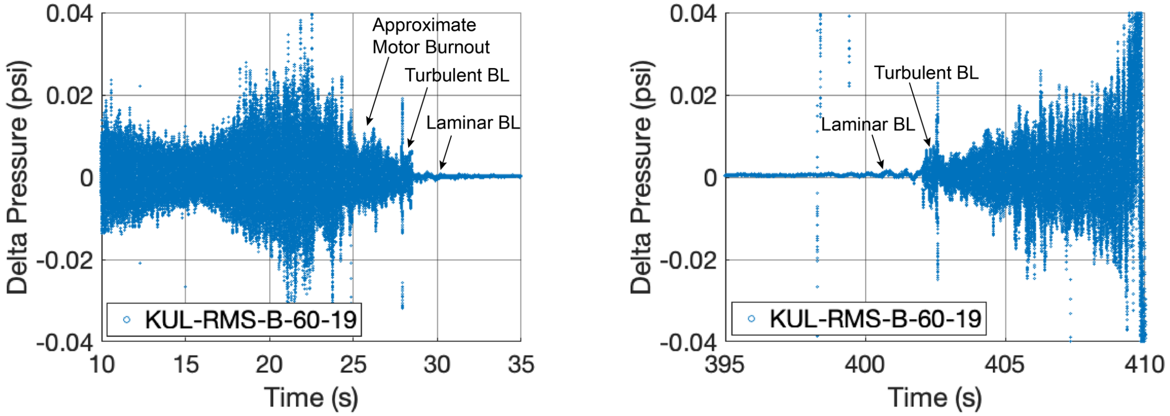

a) Ascent *b) Descent*

Figure 111. Fluctuating pressure measurements for KUL-RMS-B-60-19.

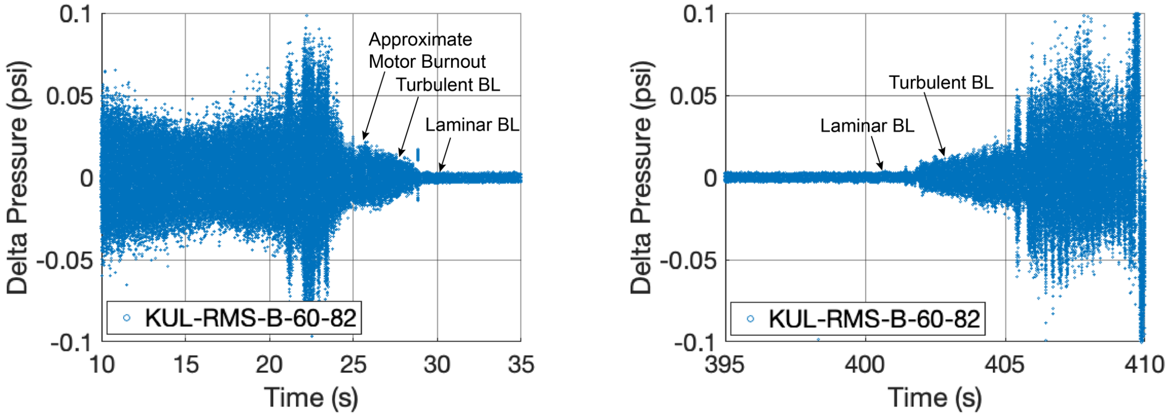

a) Ascent *b) Descent*

Figure 112. Fluctuating pressure measurements for KUL-RMS-B-60-82.

Transition Onset Maps

Comprehensive transition onset maps developed from the preceding discussion and analysis of the Side B flight data are presented in Fig. 113 and 114 for ascent and descent, respectively. For both maps, each sensor location is marked with one of four outcomes, all based on the previous sections: (1) the time of transition onset, (2) noted if bad, or if (3) laminar or (4) turbulent throughout the test window. Also included on these maps are red lines representing the progression of the turbulent wedges emanating from each trip, with the solid line indicating the initial disturbance path and eventual center of the wedge, and dashed lines for the extent of the turbulent spreading assuming a 3° half angle for a fully effective trip. From the lateral arrays, a straight line angled 3° away from the disturbance path starting at the trip seemed to best fit the data. That amount of turbulent spreading is consistent with previous observations captured by Fischer [25]. An initial observation of the onset times presented in Figs. 113 and 114 is that the trips behaved as intended, as all three trips forced transition onset at about the same time during both ascent and descent. Sizing the height and width of the trips based on a percentage of the local boundary layer thickness was a successful approach to obtain consistent transition behavior.

Aside from a few traces that had to be discounted due to faulty results, the consistency in observation of onset times across the various sensor types provides confidence with the results obtained during the BOLT-2 flight. Of the 38 Side B thermocouples, only two were considered suspect (~95% success rate). In contrast, half of the 12 thermogages on Side B provided unreliable results (~50% success rate). Finally, of the 12 Side B thin-films, only one was problematic (~92% success rate). Overall, of the sensors that were intended for monitoring BOLT-2 Side B boundary layer transition behavior, roughly 84% provided well-behaved and systematic onset times, with some consistency across the different sensor types.

During ascent, the trips were observed to be fully effective (defined as when transition onset is because of and as close to the trips as can be measured) at roughly 30s after liftoff. At this point in the trajectory, all other sensors outside of the dashed lines of the turbulent wedges are indicating the switch to laminar heating before this time, as shown in Fig. 113. And based on comparisons between the two sides (A to B), the trips promoted turbulent heating levels for roughly 5 seconds longer during ascent. The incipient condition (defined as when transition onset as far away from the trip as can be measured) was nearer to 33s on ascent. Due to symmetry with the observations from port to starboard, the turbulent wedge sketched behind the LE-19 trip is assumed.

During descent, the incipient condition (here, when transition onset is first observed behind the trip) was indicated at roughly 398s. The trips appear to be fully effective (in this case, when transition onset is observed directly behind the trip) at roughly 400s after liftoff, as all locations inside of the dashed lines of the turbulent wedges were measured to have turned turbulent before this time, as shown in Fig. 114. Comparisons between the sides (A to B) indicate that the trips induced turbulence roughly 5 seconds earlier than on the smooth side during descent. Again, due to symmetry with the measurements from port to starboard, the turbulent wedge sketched behind the LE-19 trip is assumed.

The transition onset maps of Figs. 113 and 114, developed based on time, can be hard to decipher, without spending some time studying them. An alternate presentation approach for this same data is shown in Fig. 115, which instead provides a series of “traffic-light” visualization plots (red/green dots representing the sensor locations, where green = laminar and red = turbulent) at select trajectory points during ascent and descent. Here, the focus is Reynolds number, instead of time, to synchronize the ascent and descent measurements to the design condition. As noted in [8], the BOLT-2 trips were sized based on a k/δ of 0.7 (the Hyper-X criteria) providing a “threshold for when onset would occur downstream of the trips” for Re of 2.5M. As can be seen in Fig. 115 transition onset is observed behind the trips by the design condition for both ascent and descent.

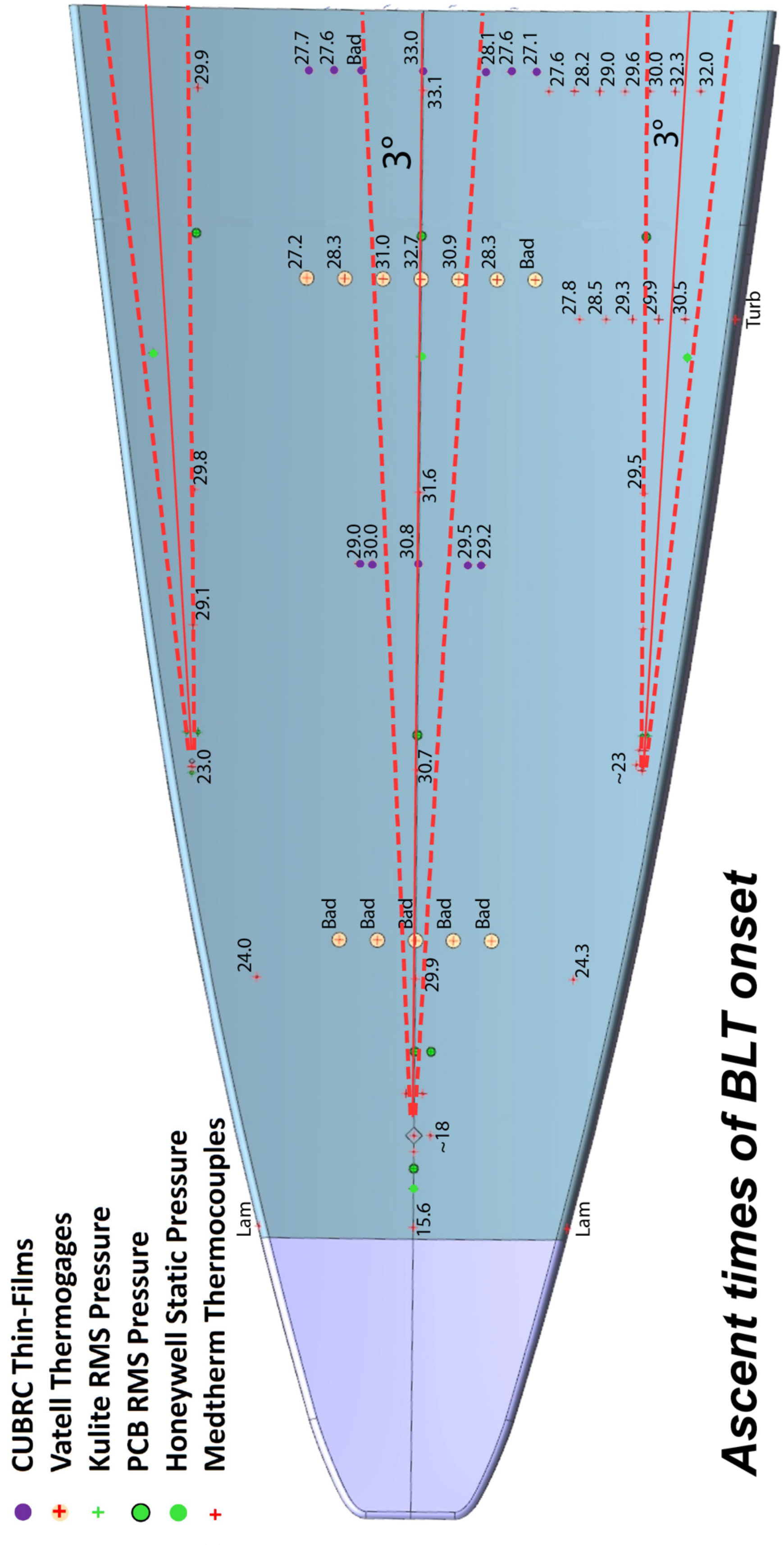

Figure 113. Transition onset map during ascent.

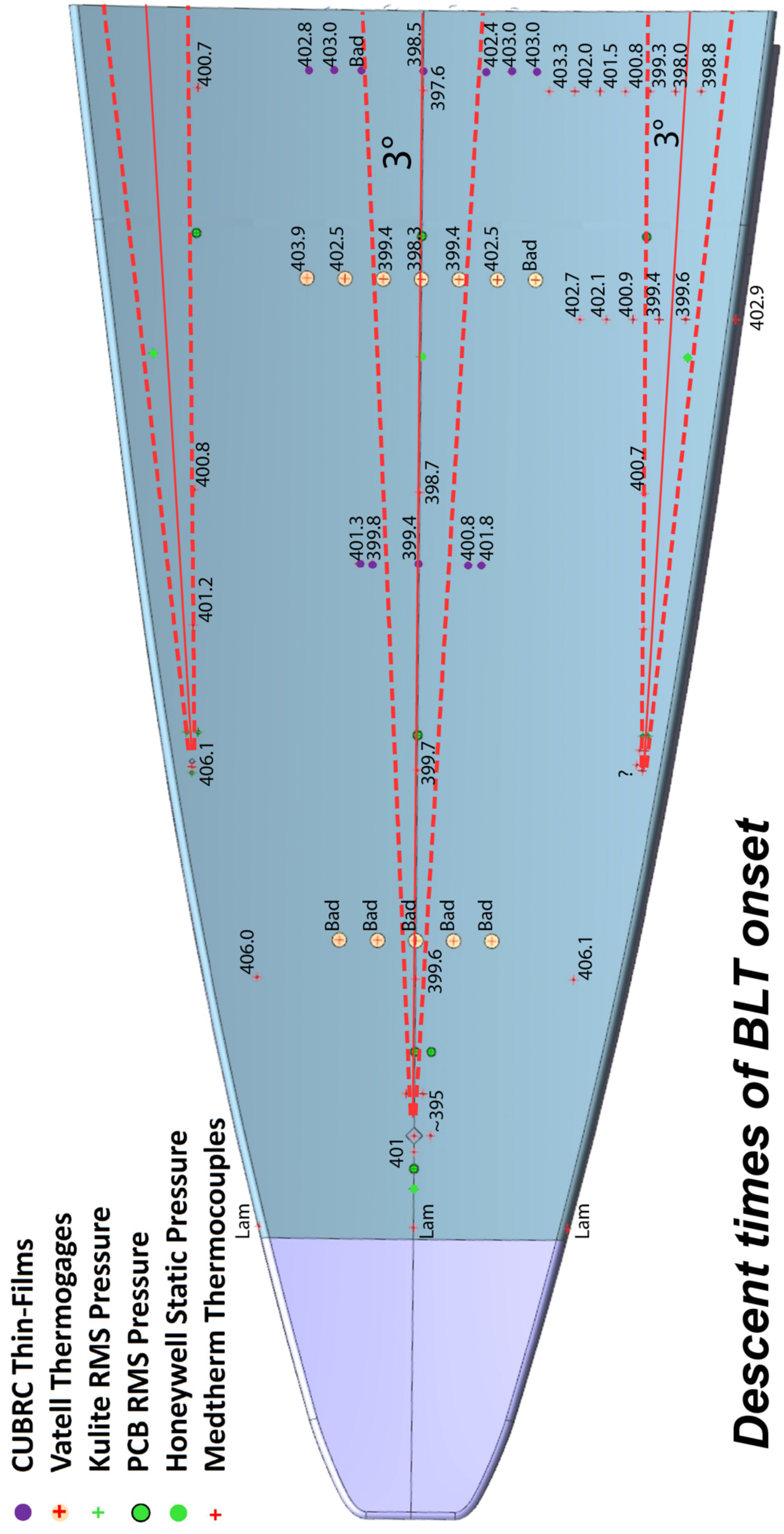

Figure 114. Transition onset map during descent.

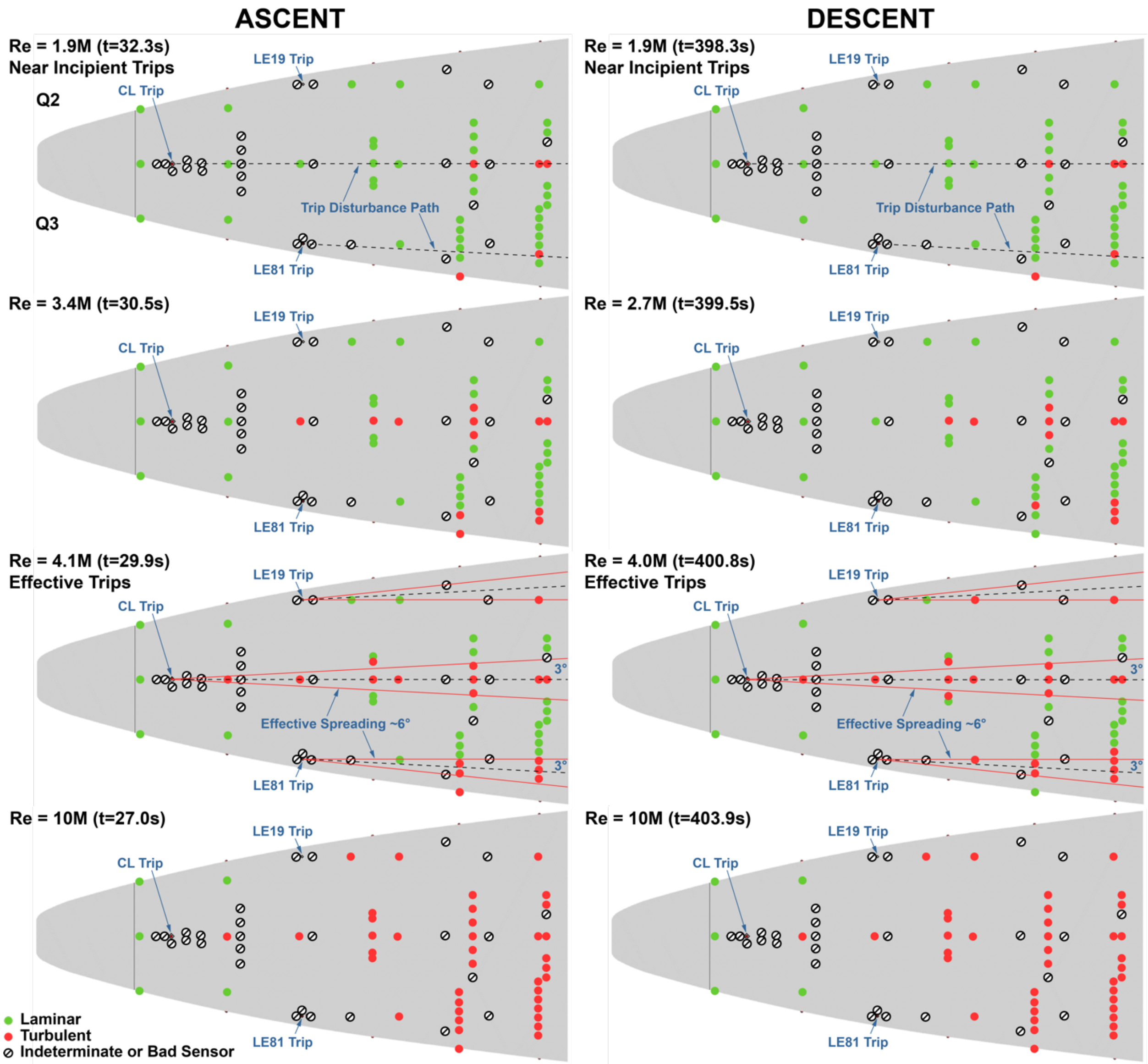

Figure 115. Transition behavior as function of Reynolds number during ascent and descent.

Thanks to BOLT-2 following a ballistic sounding rocket trajectory, Reynolds number changes rapidly: first decreasing with time during ascent, then increasing with time during descent. As shown in Fig. 115, the time required for Re to change from approximately 1M to 10M is within a few seconds (~5s). The incipient condition is captured in the initial cases shown, which represents the lowest Re at which most of the vehicle is laminar and the first hints of transition onset are seen towards the end of the body. For both ascent and descent, the incipient case was at Re=1.9M. Based on these initial sensors indicating transition, dashed straight lines were included connecting the trips to the initial red dot locations. Presumably, this straight line, which is labeled in the figure as the trip disturbance path, should also represent the rough direction of the surface streamlines behind the trips. Note that the disturbance path behind the LE81 trip is seen to have a slightly outboard trend, around ~3° from horizontal. At the next higher Re shown, the red turbulent dots are seen filling in along the path of the disturbance directly behind the trips. Eventually, as Re increases, all the sensor locations directly behind the trips indicate turbulence, while the rest of the vehicle is shown to still be laminar. This identifies the effective trip condition, which occurred at roughly Re=4.1M during ascent and descent. For these effective cases, additional straight red lines were included to represent the turbulent wedge spreading starting at each trip. These wedges start at the trips and angle away from the disturbance path with an additional 3° of turbulent spreading in both directions, which as mentioned previously is supportive of previous observations [25]. It is important to note that all Side B sensors within this effective wedge are indicating turbulence in contrast to any corresponding sensors on Side A, which would still be laminar. As the Reynolds number increases even further, shown in Fig. 115 for Re=10M, other sensors not within the effective wedge also start to fill in as turbulent, loosely in sync with observations of transition from Side A.

Based on the observations of incipient and effective cases mentioned above, flow conditions have been extracted from the trajectory file and presented in Table. 6. These conditions represent the flight trajectory points at which follow up computations could be used to extract boundary layer information appropriate for correlating trip performance, especially for assessing the scaling that was originally done between wind tunnel and flight. This step will be left for a subsequent report.

Table 6. Flow conditions corresponding to incipient and effective BOLT-2 Side B trips

Trip Case	Time (s)	M_∞	Re_L (x10^6)	Alt. (km)	Vel. (km/s)	Rho (kg/m^3)
Ascent - Incipient	32.3	5.93	1.93	30.14	1.77	0.0158
Ascent - Effective	29.9	6.21	4.13	25.98	1.79	0.0316
Descent - Incipient	398.3	5.88	1.87	30.28	1.75	0.0154
Descent - Effective	400.8	6.11	4.04	26.01	1.76	0.0315

Review of Step Effects

A final review of observations of nose-joint step effects in the BOLT-2 flight data seems appropriate, especially considering the recent successful BOLT flight (BOLT-1B) intended to explore the influence of steps on the boundary layer transition process with the Side B experiment. In the BOLT-2 data presented herein, there were noticeable differences detected between the sides that could be attributed to step effects. The earliest onset of natural transition, when discounting all Side B sensors influenced by the trips, was typically observed at a lower Reynolds number on Q4 of Side A (based on a delta observed in the trajectory file due to a time difference of a second or more). The pre-flight measurements of joint steps were reported in [17]. Measurements were taken around the periphery of the nose joint, as shown in Fig. 116, which is based on the vantage point of looking aft on the vehicle. Moving in a clockwise direction on the figure, the key locations for the two sides (neglecting the gutters) are Q4-D, Q4-C, Q4-B, Q1/4-A, Q1-B, Q1-C, and Q1-D for Side A, and Q2-D, Q2-C, Q2-B, Q2/3-A, Q3-B, Q3-C, and Q3-D for Side B. At each of these key locations, the preflight step measurements are captured in Tables 7 and 8 for Sides A and B, respectively. The noted maximum values listed in Table 2 of [17] were captured here, with the exception of the D locations, where only the results shown to the body-side of Figs. 12-18 of [17] were reflected. This was to remove undue bias from some extreme values captured in the gutter regions that could skew interpretation of the results. The thermal growth during flight was predicted in [23], which is also reflected in the tables based on the distribution of thermal growth across the span from Fig. 23 of [23], which reported that "a perfectly flush nose-to-body joint at launch" would see at the end of descent "a maximum aft-facing differential thermal expansion of 79 μm." The pre-flight measurements are combined with the thermal growth estimates (by summation) for the bottom row, which is the expected step sizes around the periphery of the side A & B nose-joints at the end of descent. Note, in the tables, a positive value identifies forward facing, or FF, steps, while negative implies rearward facing (RF) steps. The largest expected nose-joint step size (highlighted in yellow) was predicted for Q4 near the LE where the BL would be the thinnest. This region, location C (at the LE), would then be expected to be most sensitive to step effects.

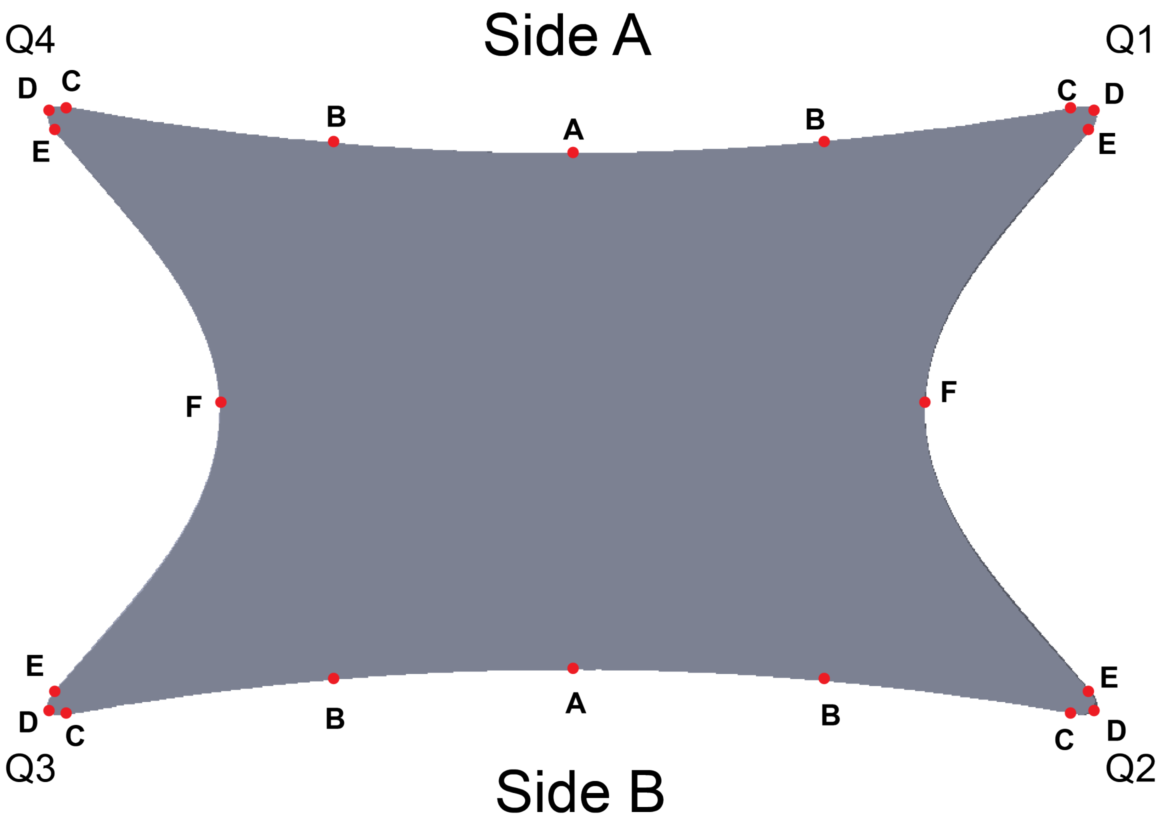

Figure 116. Locations where molds taken to provide detailed step data prior to flight.

Table 7. Expected thermal growth for Side A by end of descent.

Side A	Q4-D	Q4-C	Q4-B	Q1/4-A	Q1-B	Q1-C	Q1-D
Pre-flight (µm)	-5	-63.7	-66.4	-21.6	31.7	27.1	10
Thermal Growth (µm)	-79	-60	-15	-5	-15	-60	-79
Total (µm)	-84	-123.7	-81.4	-26.6	16.7	-32.9	-69

Positive = FF step

Table 8. Expected thermal growth for Side B by end of descent.

Side B	Q3-D	Q3-C	Q3-B	Q2/3-A	Q2-B	Q2-C	Q2-D
Pre-flight (µm)	20	85.1	64.1	56	17.6	-18.4	-5
Thermal Growth (µm)	-79	-60	-15	-5	-15	-60	-79
Total (µm)	-59	25.1	49.1	51	2.6	-78.4	-84

Positive = FF step

The tables above represent the end of descent, which indicates the largest nose-joint step was on Q4 of Side A with an expected RF step of -123.7 µm (0.0049”). However, Side A Q4 also reflected early transition onset during the ascent portion of flight. Expected thermal growth during ascent only was estimated to be approximately two-thirds of the end of descent value. Thus, by end of ascent, the Q4-C location would still have been a RF step over 100 µm (0.0039”) tall, still the outlier of the group. It might be noteworthy to point out that BL thickness variation across the body, from the center region to the LE, is at least on the order of 3 to 1 (just based on the trip size variation from CL to LE). Thus, the nose-joint step in the center region (locations A or B) would likely have to be over 3 times larger than near the LE (locations C or D) for the same level of tripping effectiveness.

Supplemental photos of the Side A and B steps, taken with a magnifying lens at the marker locations noted in Fig. 116, are presented in Appendix D. While originally intended for extraction of dimensional data, these preflight zoom photos are uncalibrated and intended here as visual evidence as to the relative size and direction of the steps around the body. Text boxes attached to each photo provide the measurements derived from the scan data [17], which reflect the values captured in the above tables. The photos provide supporting information of the scan data as a starting basis for the thermal growth analysis above.

While the anomalous Q4 behavior of Side A can be generally attributed to the larger RF step near the LE at location C, there are two other aspects to the data that are harder to explain. The first one has to do with the measured behavior along the LE at MT-B-80-89 (Q3) in comparison to MT-A-4-15 (Q4), which shows Q3 staying turbulent during the entire ascent test window and then showing transition onset later than Side A during descent. This might suggest Side B being rougher than Side A, which is not supported by the tables above. One possible explanation is that the LE of Q3 could be picking up some contamination from the gutter region. The tables above do not reflect anything from the gutter regions based on the assumption that the main body measurements should not be influenced by the gutters. But, perhaps, that is a faulty assumption. The molds and scans of [17] do indicate that location E of Q3 had a large RF step, with a maximum value of -115.8 μm (0.0046”). With thermal effects, that step would presumably grow taller in time. The corresponding location on Q4 is a FF step of 53.2 μm (0.0021”) that would then shrink due to thermal effects. That might explain the LE differences between the sides. One result that cannot be explained away, however, is the measurements on CL just behind the joint, shown by the comparison of MT-B-19-50 to MT-A-1-3. Figure 20 shows Side B to have transition onset roughly 2s later than Side A during ascent. During descent, neither showed transition onset, unfortunately. If we just assess the CL based on the preflight measurements, since the difference was seen early in flight likely before thermal effects would have changed the steps much, then Side B would have been a 56 μm (0.0022”) FF step, while Side A would have been a -21.6 50 μm (0.0008”) RF step. It is much harder to connect the dots here and provide a rational explanation for this anomaly. This was just after 2nd stage ignition and the angle of attack during this time was generally with Side A to windward by a small amount (~1 deg or less). Perhaps computational analysis of stability mechanisms with small variations in vehicle attitude could shed some light on this particular result. Aside from this one anomaly, the rest of the Side B data are well-behaved and systematic in their relation to the various known roughness sites.

Concluding Remarks

The successful BOLT-2 flight provided a wealth of discrete-roughness boundary-layer transition data, which is the focus of the present analysis and document. Side B of BOLT-2 was specifically designed to compare three boundary layer trips, that were scaled based on consideration of the local boundary layer thickness, to trip at the same time based on data from a previous wind tunnel campaign. The flight sensor layout for Side B was designed to capture the movement of transition behind these three trips. There were two separate science windows during flight, one each on ascent and descent. Comprehensive success was selected preflight to be based on controlling the vehicle attitude (alpha/beta) to better than ±2 deg, which was achieved throughout both science windows. From the present in-depth review of the BOLT-2 Side B flight data, several observations and lessons learned can be made:

- A roll rate under ±1 Hz was desired and achieved during flight for both test windows, which greatly simplified interpretation of the flight data.
- The Side B instrumentation worked well, providing valuable insight into the performance of the trips, with an overall measurement success rate of 84%.
- Top surface thermocouples were more than sufficient to back out surface heating for most locations, which is a lesson learned applied to the next BOLT mission.
- The sensor layout, which was somewhat limited based on budget, was sufficient for indication of both the forward movement of transition onset as well as the lateral spreading behind the trips.
- The BL trips performed per expectations, with all three indicating incipient and effective conditions at nearly same conditions during ascent and descent.

  - During ascent, all trips were incipient at 32.3 seconds into flight (M_∞= 5.93 and Re_L = 1.93 million) and effective at 29.9 seconds (M_∞= 6.21 and Re_L = 4.13 million).
  - During descent, all trips were incipient at 398.3 seconds into flight (M_∞= 5.88 and Re_L = 1.87 million) and effective at 400.8 seconds (M_∞= 6.11 and Re_L = 4.04 million).
- The consistency in transition onset measurements between the 3 locations provides confidence in both the data obtained and the methodology/approach used to select and scale the original ground-based data to flight.
- While not the original intent of the BOLT-2 mission, the flight data did point to possible step effects due to asymmetries observed between the sides, although further analysis is still needed to factor in any influence of the small alpha and beta changes during the key observation points.
- Considering the sensitivity seen with relatively small step heights in the present dataset, the ability to conduct real time measurements of the nose-joint step growth and change during flight, as opposed to relying solely upon postflight analysis, could provide valuable insight for the aerothermodynamic flight testing community.

References

---

[1] Wheaton, B.M., Butler, C. S., McKiernan, G. R., and Berridge, D.C., “Initial Results from the BOLT Flight Experiment,” AIAA Paper 2022-0345. https://doi.org/10.2514/6.2022-0345

[2] Morreale, B. J., Swinny, E., Kostak, H., Bowersox, R. D., White, E. B., Dufrene, A. T., and Wadhams, T. P., “Boundary Layer Turbulence Flight Experiment in Memory of Mike Holden: Pre-Flight Mission Design,” AIAA Paper 2023-0477.

[3] Wirth, J., Morreale, B. J., Kostak, H., Bowersox, R. D., Dufrene, A. T., Portoni, P. and Wadhams, T. P., “Boundary Layer Turbulence Flight Experiment in Memory of Mike Holden: Side A Flight Data,” AIAA paper 2023-0682.

[4] Dolvin, D. J., “Hypersonic International Flight Research and Experimentation,” AIAA Paper 2008-2581.

[5] Johnston, Z. M., Hemiti, M., S., and Candler, G. V., “Modal Analysis of Instabilities in the BoLT-2 Flowfield,” AIAA Paper 2022-0348.

[6] Wheaton, B.M., Berridge, D.C., Wolf, T.D., Stevens, R.T., and McGrath, B.E., “Boundary Layer Transition (BOLT) Flight Experiment Overview,” AIAA Paper 2018-2892.

[7] Berry, S. A., Wheaton, B. M., and Chynoweth, B. C., “Secondary Side Considerations for BOLT Flight Experiment,” AIAA Paper 2020-1559. https://doi.org/10.2514/6.2020-1559

[8] Berry, S. A., Semper, M. T., Riha, A. K., Mullen, C. D., Reed, H. L., Dufrene, A., Fasel, H. F., “Development of the BOLT-2 Roughness Experiment for Flight,” AIAA Paper 2022-0347. https://doi.org/10.2514/6.2022-0347

[9] Semper, M. T. and Cummings, R. M., “Hypersonic Trip Development for BOLT-II,” AIAA Paper 2022-0349. https://doi.org/10.2514/6.2022-0349

[10] Berry, S. A., Mason, M. L., Greene, F., King, R., Rieken, E., Basore, K., “LaRC Aerothermodynamic Ground Tests in Support of BOLT Flight Experiment,” AIAA Paper 2019-0091. https://doi.org/10.2514/6.2019-0091

[11] Berry, S. A., Auslender, A. H., Dilley, A. D., and Calleja, J. F., “Hypersonic Boundary Layer Trip Development for Hyper-X,” Journal of Spacecraft and Rockets, Vol. 38, No. 6, 2001, pp. 853-864.

[12] Berry, S. A., Daryabeigi, K., Wurster, K., and Bittner, R., “Boundary Layer Transition on X-43A,” Journal of Spacecraft and Rockets, Vol. 47, No. 6, 2010, pp. 922-934.

---

[13] Berry, S. A., Bouslog, S. A., Brauckmann, G. J., and Caram, J. M., “Shuttle Orbiter Experimental Boundary-Layer Transition Results with Isolated Roughness,” Journal of Spacecraft and Rockets, Vol. 35, No. 3, 1998, pp. 241-248.

[14] Kimmel, R. L., Adamczak, D., Paull, A., Paull, R., Shannon, J., Pietsch, R., Frost, M., and Alesi, H., “HIFiRE-1 Ascent-Phase Boundary-Layer Transition, Journal of Spacecraft and Rockets, Vol. 52, No. 1, 2015, pp. 217-230.

[15] Berry, S. A., Chen, F. J., Wilder, M. C., and Reda, D. C., “Boundary Layer Transition Experiments in Support of the Hypersonics Program,” AIAA Paper 2007-4266. https://doi.org/10.2514/6.2007-4266

[16] Dufrene, A. T., Portoni, P. P., Maclean, M., Wadhams, T., Kostak-Teplicek, H., Bowersox, R. D., “Boundary Layer Turbulence Flight Experiment in Memory of Mike Holden: Vehicle Design, Instrumentation, and Ground Test Results,” AIAA Paper 2023-0478.

[17] Leidy, A., “BOLT II Forebody Surface Measurement Analysis,” NASA TM-20230000169, Jan 2023.

[18] Vidal, R. J. "Model Instrumentation Techniques for Heat Transfer and Force Measurements in a Hypersonic Shock Tunnel." Cornell Aeronautical Laboratory Report AD-917-A-1, 1956.

[19] Dobbins, T. J., ArchMiller, M. C., Horak, E. H., Taylor, L. N., Van Kerkhove, J. J., and Wiebold, M. D., “Atmospheric Measurements with the HALAS LiDAR System supporting the BOLT II Flight Test,” AIAA Paper 2023-0479.

[20] 46.027/Holden Impact Anomaly Investigation Report, Wallops Flight Facility, April 5, 2024. (Limited distribution report/please contact Jim Lanzi/WFF with questions)

[21] Cook, W. J., and Felderman, E. J., “Reduction of Data from Thin-Film Heat-Transfer Gages: A Concise Numerical Technique,” AIAA Journal, Vol. 4, No. 3, 1966, pp. 561–562. doi:10.2514/3.3486.

[22] Cook, W. J., “Determination of Heat-Transfer Rates from Transient Surface Temperature Measurements,” AIAA Journal, Vol. 8, No. 7, 1970, pp. 1366–1368. doi:10.2514/3.5909.

[23] Wheaton, B.M. and Dufrene, A. T., “Thermal and Structural Analysis of BOLT-2: The Holden Mission,” AIAA Paper 2023-0685.

[24] Berry, S. A. and Wheaton, B.M., “BOLT II Roughness Side Flight Results,” AIAA Paper 2023-0684.

[25] Fischer, M. C., “Spreading of a Turbulent Disturbance,” AIAA J. Vol. 10, No. 7, 1972, pp. 957-959.

Fully assembled 2nd stage launch stack [Source: AFRL]

Front view of BOLT-2 showing difference between the two sides [Source: AFRL]

Side view of BOLT-2 showing one of the gutters [Source: AFRL]

Launch stack being carted to launch pad [Source: AFRL]

BOLT-2 launch team [Source: NASA]

BOLT-2 launch on March 21st at 7:12pm [Source: NASA]

Side A – note handling blocks indicating port & starboard [Source: AFRL]
Yellow tape covers various sensors during pre-flight handling

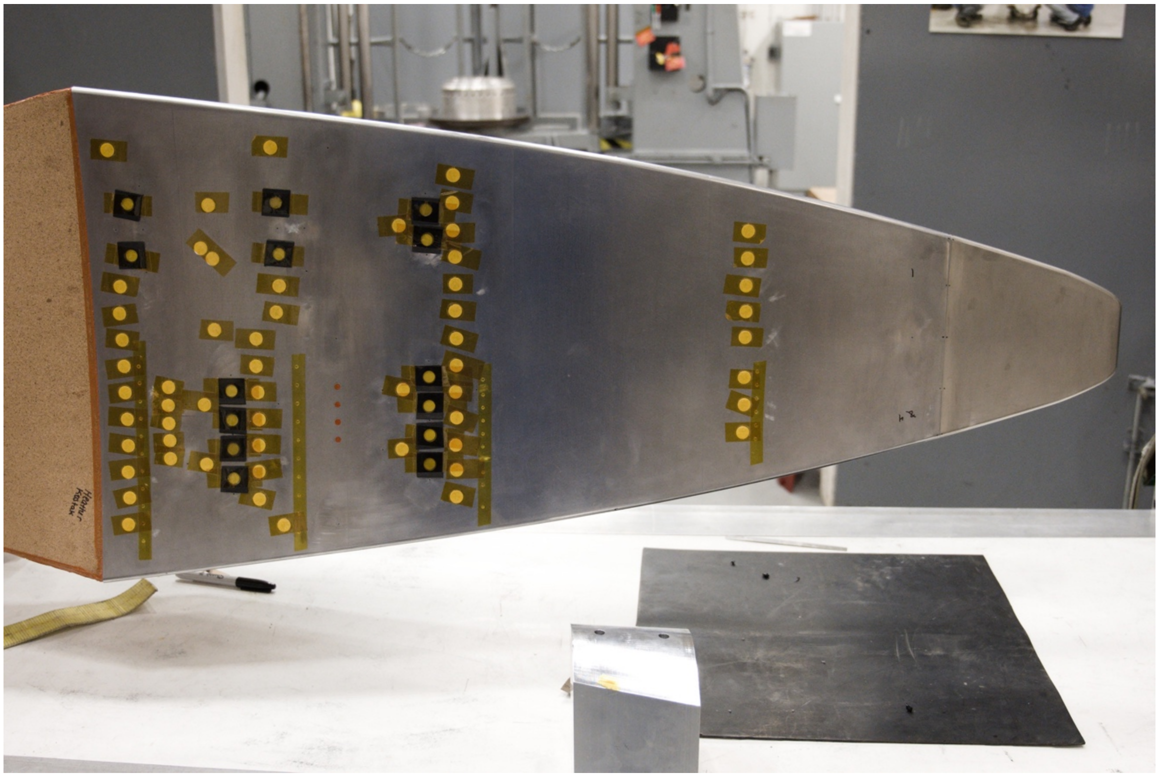

Different view of Side A – note Q1 (port) & Q4 (starboard) markings near step [Source: AFRL]

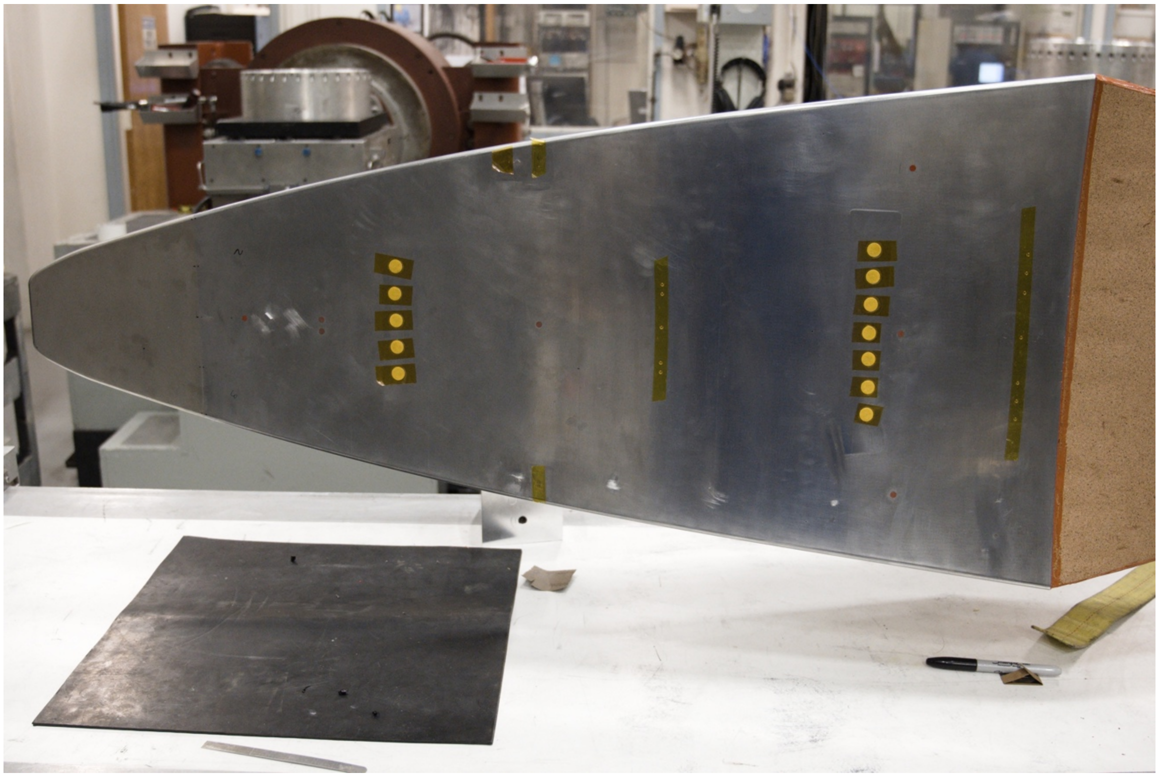

Side B – note markings near step identifying Q2 & Q3 [Source: AFRL]

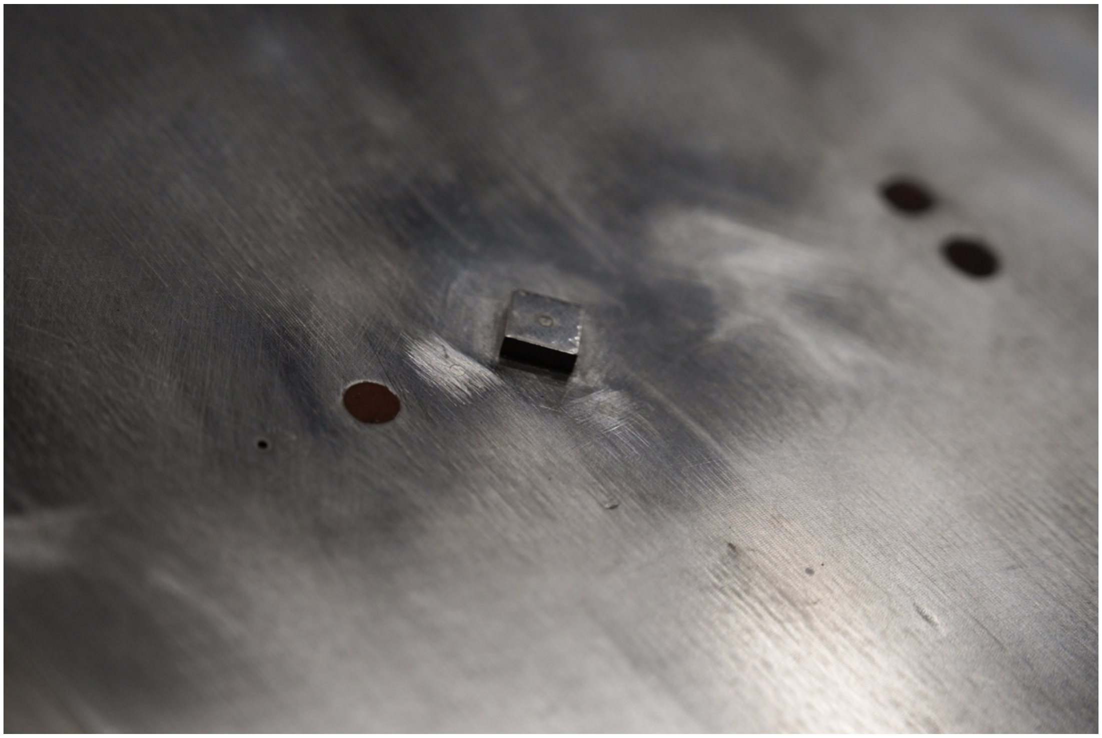

Closeup photo of CL Trip, view from the side [Source: AFRL]

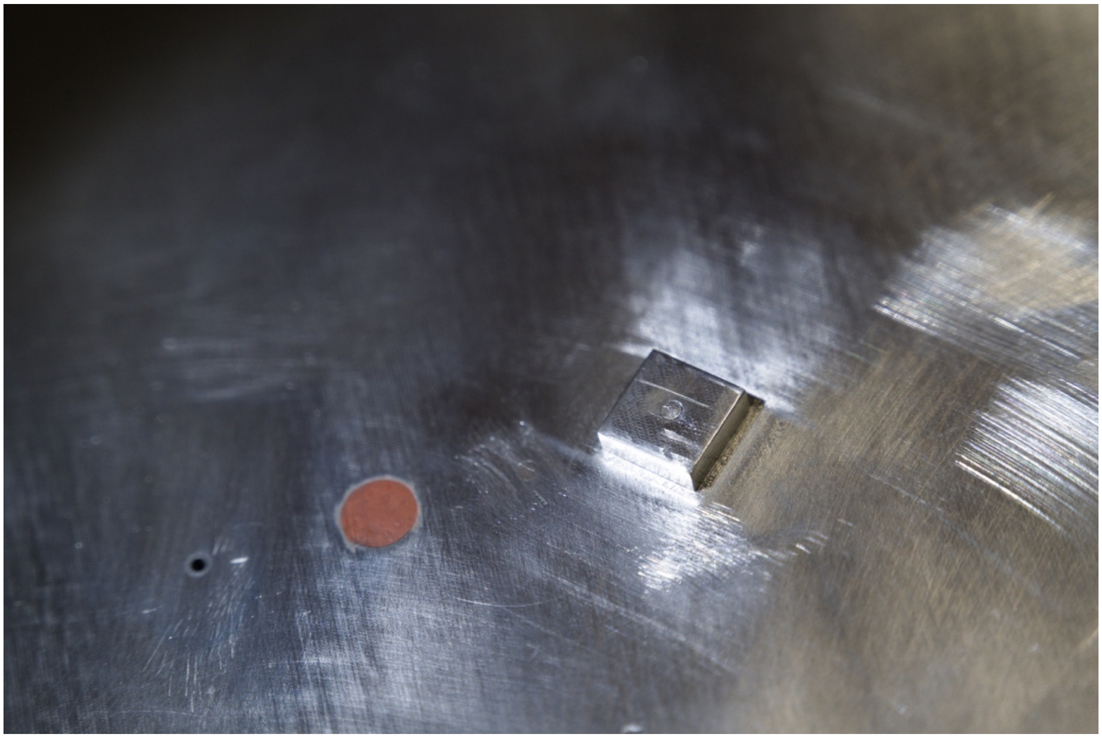

Closeup photo of CL Trip, similar view from the side [Source: AFRL]

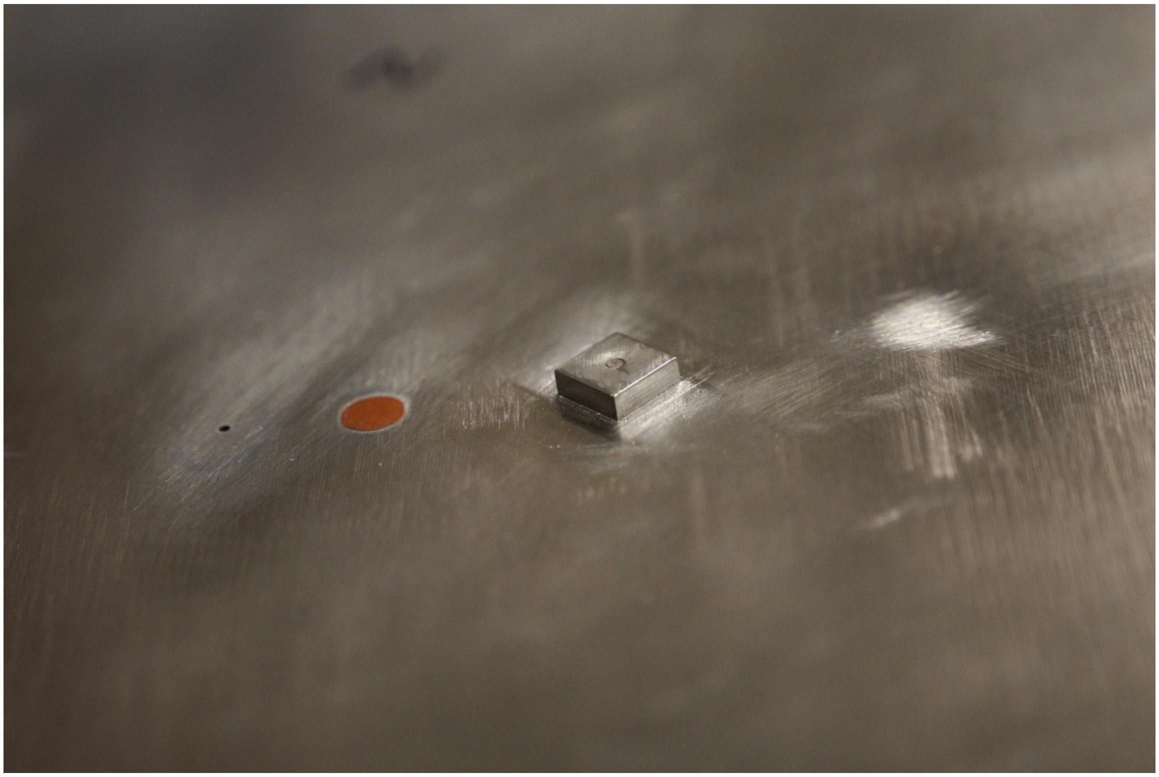

Closeup photo of CL Trip, another view from the side [Source: AFRL]

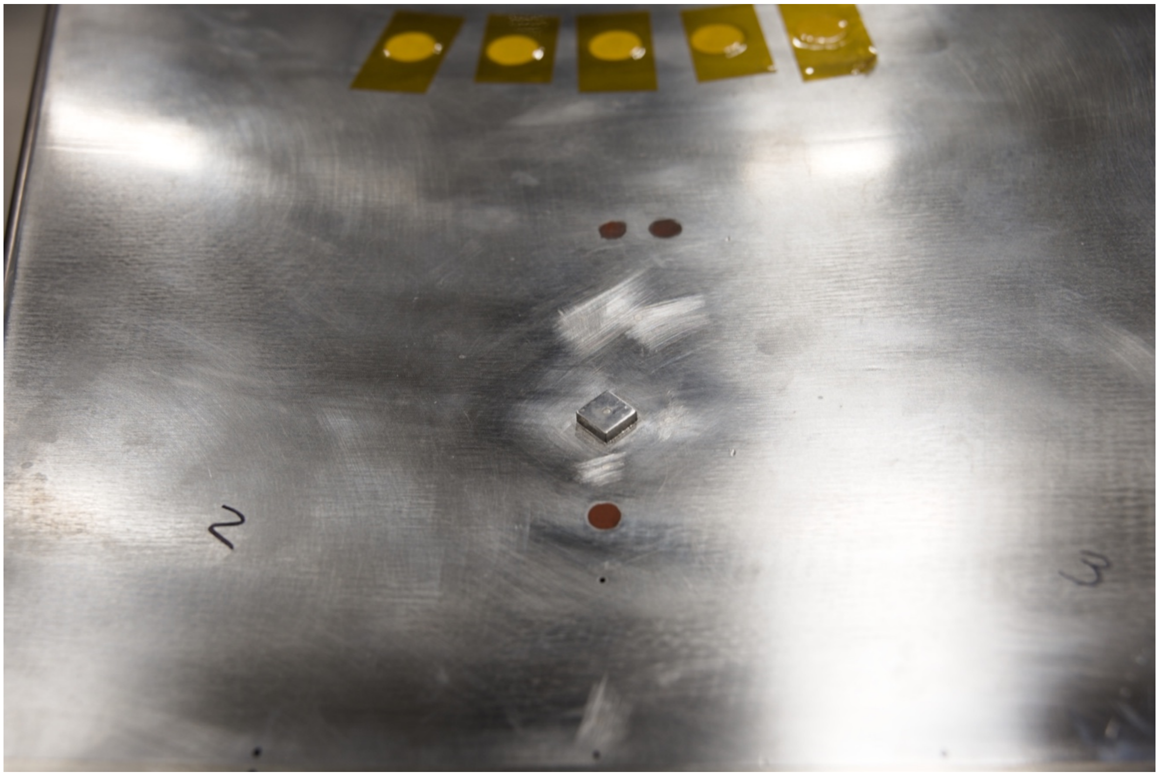

Closeup photo of CL Trip, view from in front [Source: AFRL]

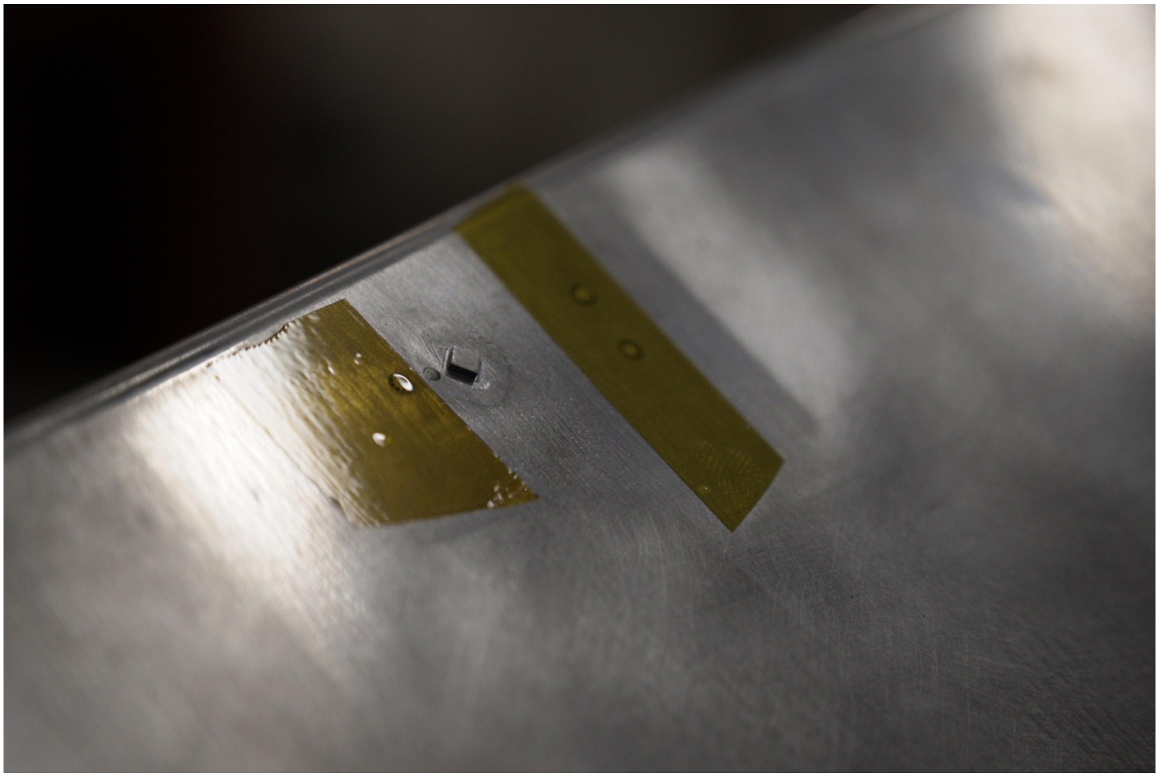

Closeup photo of LE-19 Trip [Source: AFRL]

Closeup photo of LE-19 Trip [Source: AFRL]

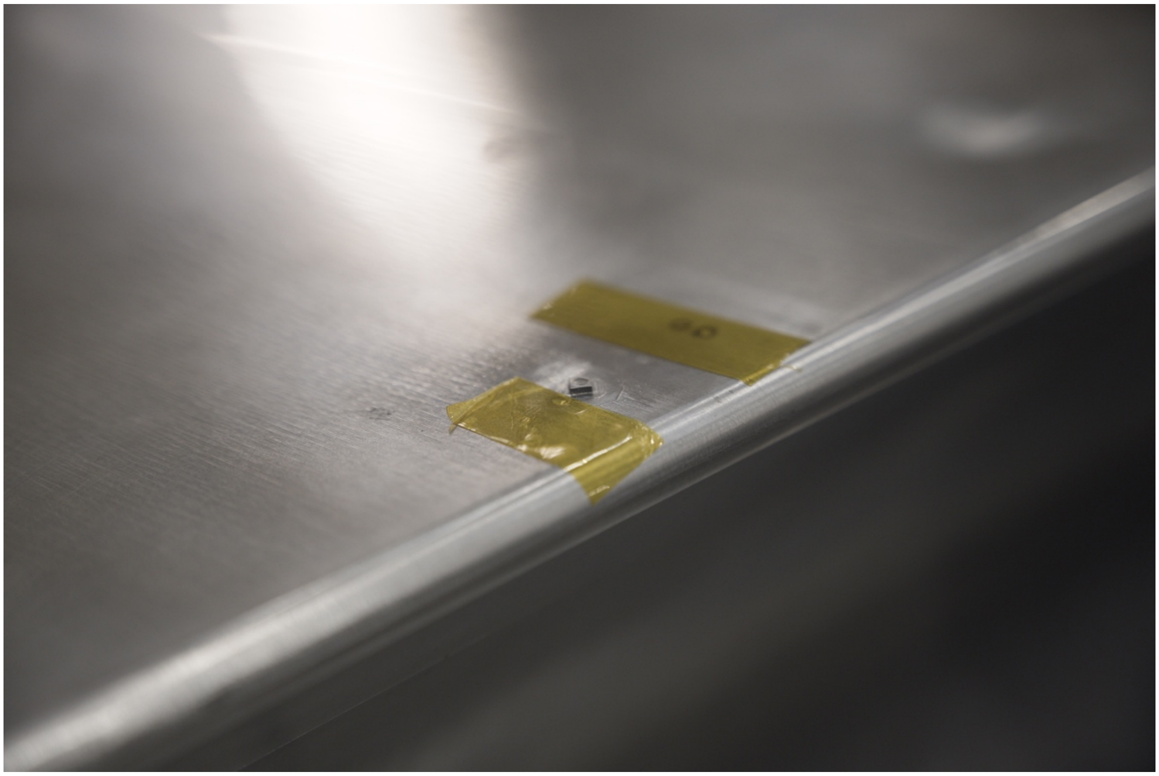

Closeup photo of LE-81 Trip, view form the side [Source: AFRL]

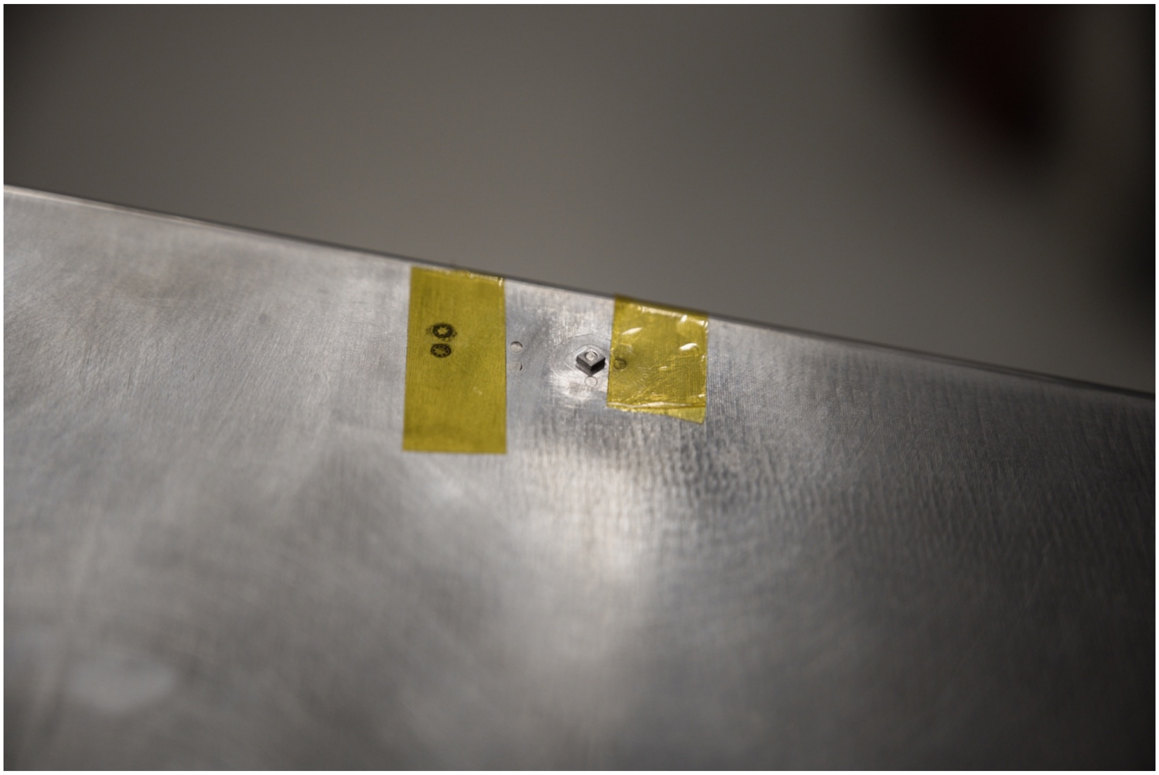

Closeup photo of LE-81 Trip, view from the other side [Source: AFRL]

Closeup photo of LE-81 Trip, view from in front [Source: AFRL]

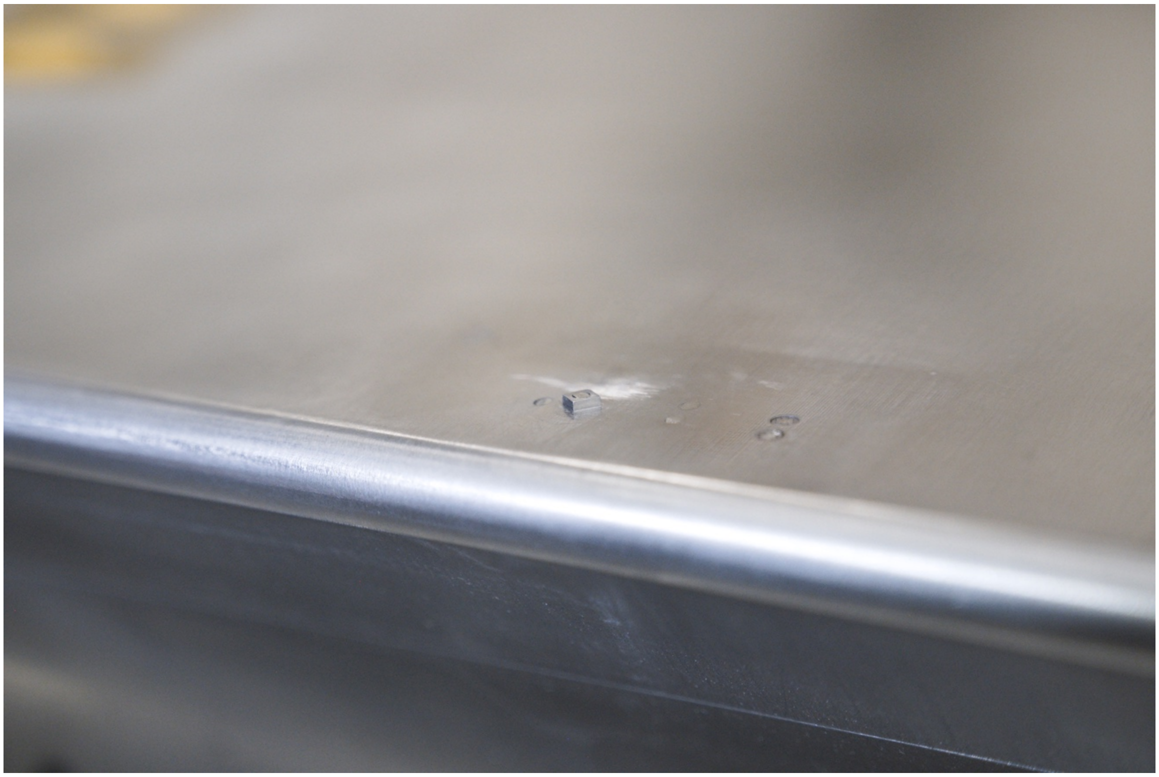

Closeup photo of LE-81 Trip, different view from the side [Source: AFRL]

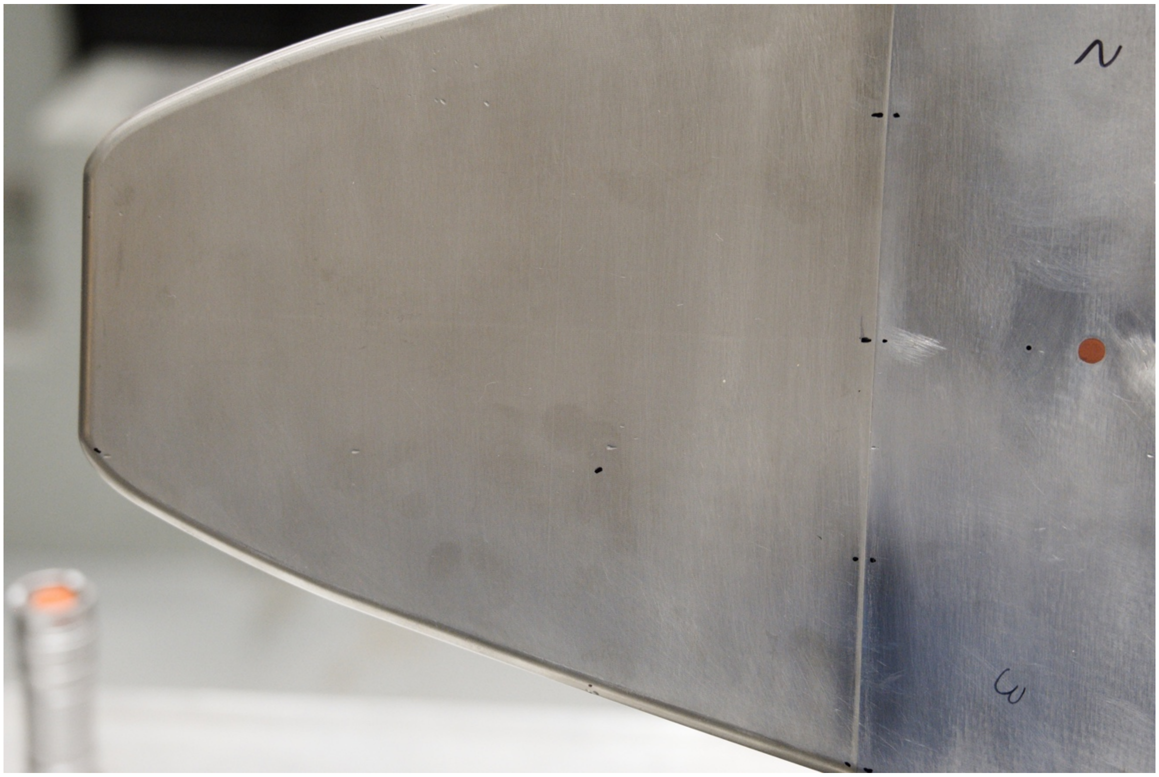

Close up of Side B nose, showing small damage/defect sites [Source: AFRL]

Close up of Side B nose, showing small damage/defect sites [Source: AFRL]

Close up of Side B nose, showing small damage sites [Source: AFRL]

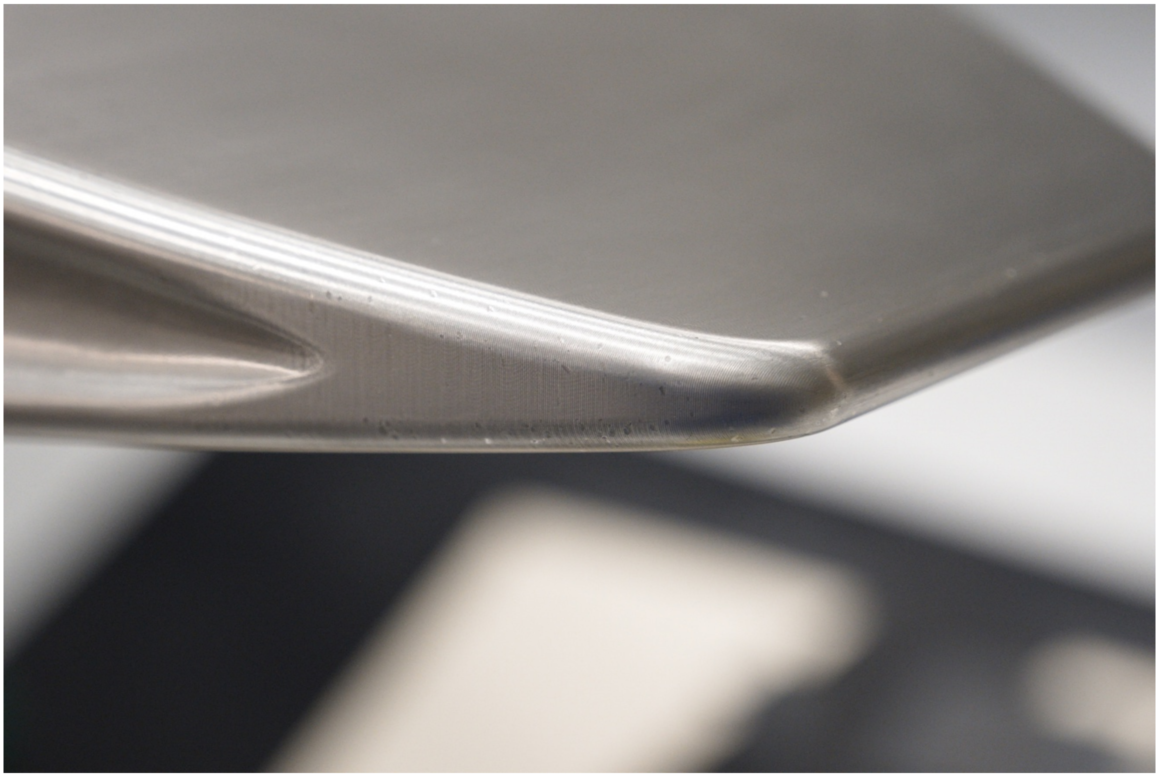

Details of the Q2 nose corner [Source: AFRL]

Details of the Q3 nose corner [Source: AFRL]

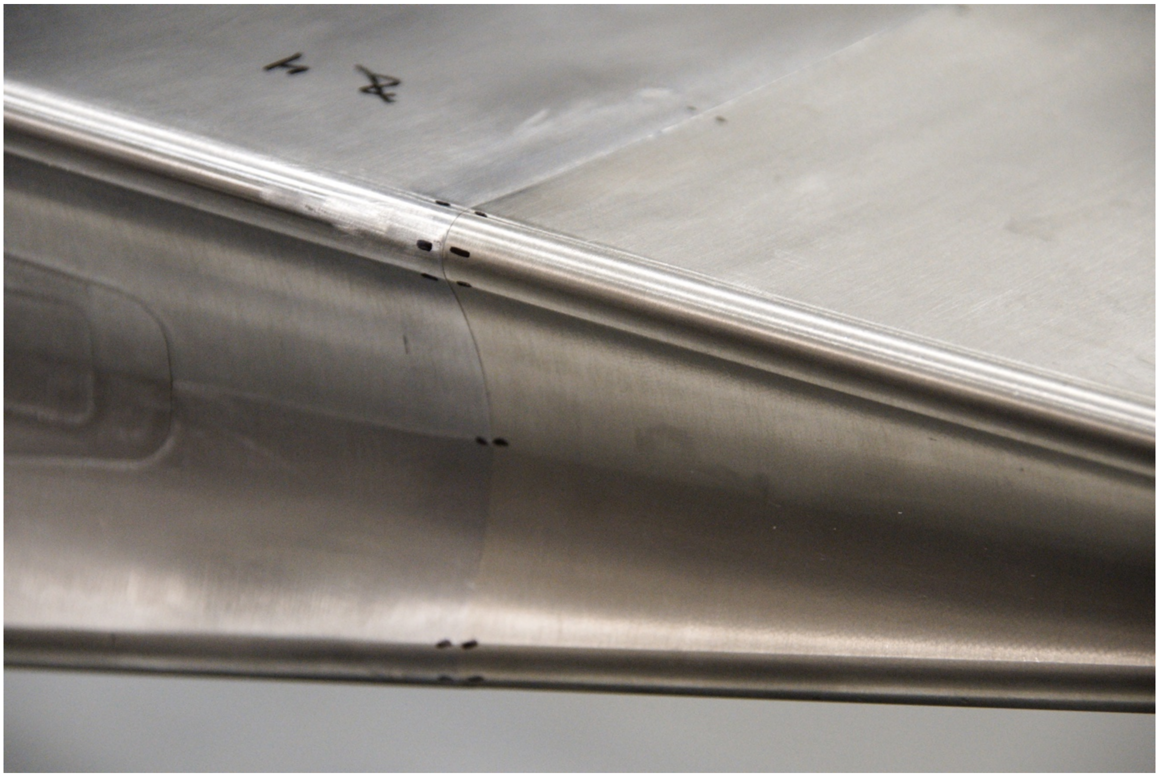

Details of the Q4 nose-step, showing marks where molds taken [Source: AFRL]

Appendix B – Side B sensor details

Table A. Side B thermocouples and locations.

Channel Name	x (m)	y (m)	z (m)	Type	Units	Min Range	Max Range
MT_B_19_28F	0.1930	-0.0288	0.1026	Medtherm TCS-061-EE-0.XX-20-10607	C	10	662
MT_B_19_50F	0.1930	-0.0277	0.0000	Medtherm TCS-061-EE-0.XX-20-10607	C	10	662
MT_B_19_72F	0.1930	-0.0288	-0.1026	Medtherm TCS-061-EE-0.XX-20-10607	C	10	662
MT_B_23_50F	0.2431	-0.0337	0.0000	Medtherm TCS-061-EE-0.XX-20-10607	C	10	662
MT_B_25_50F	0.2539	-0.0377	0.0000	Medtherm TCS-061-EE-0.XX-20-10607	C	10	662
MT_B_25_54F	0.2542	-0.0352	-0.0111	Medtherm TCS-061-EE-0.XX-20-10607	C	10	662
MT_B_28_49F	0.2820	-0.0385	0.0055	Medtherm TCS-061-EE-0.XX-20-10607	C	10	662
MT_B_28_51F	0.2820	-0.0385	-0.0055	Medtherm TCS-061-EE-0.XX-20-10607	C	10	662
MT_B_36_28F	0.3579	-0.0525	0.1055	Medtherm TCS-061-EE-0.XX-20-10607	C	10	662
MT_B_36_50F	0.3579	-0.0476	0.0000	Medtherm TCS-061-EE-0.XX-20-10607	C	10	662
MT_B_36_72F	0.3579	-0.0525	-0.1055	Medtherm TCS-061-EE-0.XX-20-10607	C	10	662
MT_B_48_19F	0.4966	-0.0736	0.1501	Medtherm TCS-061-EE-0.XX-20-10607	C	10	662
MT_B_48_50F	0.4966	-0.0643	0.0000	Medtherm TCS-061-EE-0.XX-20-10607	C	10	662
MT_B_48_81F	0.4966	-0.0736	-0.1501	Medtherm TCS-061-EE-0.XX-20-10607	C	10	662
MT_B_50_79F	0.5003	-0.0750	-0.1500	Medtherm TCS-061-EE-0.XX-20-10607	C	10	662
MT_B_50_81F	0.5004	-0.0737	-0.1463	Medtherm TCS-061-EE-0.XX-20-10607	C	10	662
MT_B_51_80F	0.5100	-0.0750	-0.1482	Medtherm TCS-061-EE-0.XX-20-10607	C	10	662
MT_B_51_81F	0.5100	-0.0755	-0.1520	Medtherm TCS-061-EE-0.XX-20-10607	C	10	662
MT_B_52_19F	0.5904	-0.0850	0.1501	Medtherm TCS-061-EE-0.XX-20-10607	C	10	662
MT_B_52_81F	0.5904	-0.0850	-0.1501	Medtherm TCS-061-EE-0.XX-20-10607	C	10	662
MT_B_70_19F	0.6805	-0.0958	0.1501	Medtherm TCS-061-EE-0.XX-20-10607	C	10	662
MT_B_70_50F	0.6805	-0.0865	0.0000	Medtherm TCS-061-EE-0.XX-20-10607	C	10	662
MT_B_70_81F	0.6805	-0.0958	-0.1501	Medtherm TCS-061-EE-0.XX-20-10607	C	10	662
MT_B_80_19F	0.7960	-0.1051	-0.1060	Medtherm TCS-061-TT-0.XX-20-10607	C	10	662
MT_B_80_72F	0.7960	-0.1068	-0.1236	Medtherm TCS-061-EE-0.XX-20-10607	C	10	662
MT_B_80_77F	0.7960	-0.1088	-0.1413	Medtherm TCS-061-EE-0.XX-20-10607	C	10	662
MT_B_80_81F	0.7960	-0.1110	-0.1590	Medtherm TCS-061-EE-0.XX-20-10607	C	10	662
MT_B_80_85F	0.7960	-0.1134	-0.1766	Medtherm TCS-061-EE-0.XX-20-10607	C	10	662
MT_B_80_89F	0.7960	-0.1155	-0.2099	Medtherm TCS-061-EE-0.XX-20-10607	C	10	662
MT_B_95_19F	0.9470	-0.1281	0.1500	Medtherm TCS-061-EE-0.XX-20-10607	C	10	662
MT_B_95_50F	0.9470	-0.1186	0.0000	Medtherm TCS-061-EE-0.XX-20-10607	C	10	662
MT_B_95_68F	0.9470	-0.1216	-0.0844	Medtherm TCS-061-EE-0.XX-20-10607	C	10	662
MT_B_95_71F	0.9470	-0.1229	-0.1012	Medtherm TCS-061-EE-0.XX-20-10607	C	10	662
MT_B_95_76F	0.9470	-0.1245	-0.1181	Medtherm TCS-061-EE-0.XX-20-10607	C	10	662
MT_B_95_79F	0.9470	-0.1263	-0.1350	Medtherm TCS-061-EE-0.XX-20-10607	C	10	662
MT_B_95_81F	0.9470	-0.1283	-0.1519	Medtherm TCS-061-EE-0.XX-20-10607	C	10	662
MT_B_95_86F	0.9470	-0.1306	-0.1687	Medtherm TCS-061-EE-0.XX-20-10607	C	10	662
MT_B_95_90F	0.9470	-0.1332	-0.1856	Medtherm TCS-061-EE-0.XX-20-10607	C	10	662

Table B. Side B thermogauges and locations.

Channel Name	x (m)	y (m)	z (m)	Type	Units	Min Range	Max Range
TG_B_42_38	0.3836	-0.0520	0.0508	Vatell TG-2000	w/cm^2	0	1000
TG_B_42_46	0.3836	-0.0510	0.0254	Vatell TG-2000	w/cm^2	0	1000
TG_B_42_50	0.3836	-0.0507	0.0000	Vatell TG-2000	w/cm^2	0	1000
TG_B_42_54	0.3836	-0.0510	-0.0254	Vatell TG-2000	w/cm^2	0	1000
TG_B_42_62	0.3836	-0.0520	-0.0508	Vatell TG-2000	w/cm^2	0	1000
TG_B_82_38	0.8220	-0.1060	0.0762	Vatell TG-2000	w/cm^2	0	1000
TG_B_82_41	0.8220	-0.1046	0.0508	Vatell TG-2000	w/cm^2	0	1000
TG_B_82_46	0.8220	-0.1038	0.0254	Vatell TG-2000	w/cm^2	0	1000
TG_B_82_50	0.8220	-0.1035	0.0000	Vatell TG-2000	w/cm^2	0	1000
TG_B_82_54	0.8220	-0.1038	-0.0254	Vatell TG-2000	w/cm^2	0	1000
TG_B_82_59	0.8220	-0.1046	-0.0508	Vatell TG-2000	w/cm^2	0	1000
TG_B_82_61	0.8220	-0.1060	-0.0762	Vatell TG-2000	w/cm^2	0	1000

Table C. Side B thin-films and locations.

Channel Name	x (m)	y (m)	z (m)	Type	Units	Min Range	Max Range
TF_B_63_42	0.6330	-0.0816	0.0419	CUBRC Thin films	F	0	977
TF_B_63_46	0.6330	0.0813	0.0332	CUBRC Thin films	F	0	977
TF_B_63_50	0.6330	0.0808	0.0000	CUBRC Thin films	F	0	977
TF_B_63_54	0.6330	0.0813	-0.0332	CUBRC Thin films	F	0	977
TF_B_63_58	0.6330	-0.0816	-0.0419	CUBRC Thin films	F	0	977
TF_B_96_38	0.9597	-0.1225	0.0759	CUBRC Thin films	F	0	977
TF_B_96_42	0.9597	-0.1216	0.0591	CUBRC Thin films	F	0	977
TF_B_96_46	0.9597	-0.1209	0.0422	CUBRC Thin films	F	0	977
TF_B_96_50	0.9597	0.1201	0.0000	CUBRC Thin films	F	0	977
TF_B_96_54	0.9597	0.1209	-0.0422	CUBRC Thin films	F	0	977
TF_B_96_58	0.9597	0.1216	-0.0591	CUBRC Thin films	F	0	977
TF_B_96_62	0.9597	0.1225	-0.0759	CUBRC Thin films	F	0	977

Table D. Side B mean pressures and locations.

Channel Name	x (m)	y (m)	z (m)	Type	Units	Min Range	Max Range
HWP_B_22_50	0.2186	-0.0308	0.0000	Honeywell 19C	psi	0	15
HWP_B_77_12	0.7706	-0.1106	0.1783	Honeywell 19C	psi	0	15
HWP_B_77_50	0.7706	-0.0973	0.0000	Honeywell 19C	psi	0	15
HWP_B_77_88	0.7706	-0.1106	-0.1783	Honeywell 19C	psi	0	15

Table E. Side B fluctuating pressures and locations.

Channel Name	x (m)	y (m)	z (m)	Type	Units	Min Range	Max Range
KUL_RMS_B_42_18	0.4927	-0.0732	0.1501	Kulite XCE-093-5psid	psi	0	7000
KUL_RMS_B_42_82	0.5196	-0.0769	0.1539	Kulite XCE-093-5psid	psi	0	7000
KUL_RMS_B_60_19	0.5196	-0.0760	0.1463	Kulite XCE-093-5psid	psi	0	20000
KUL_RMS_B_60_50	0.5196	-0.0764	-0.1501	Kulite XCE-093-5psid	psi	0	7000
KUL_RMS_B_60_82	0.5196	-0.0769	-0.1540	Kulite XCE-093-5psid	psi	0	7000
PCB_RMS_B_23_50	0.2318	0.0324	0.0000	PCB 112B05	psi	0	20000
PCB_RMS_B_31_50	0.3097	-0.0418	0.0000	PCB 112B05	psi	0	20000
PCB_RMS_B_31_51	0.3097	-0.0419	-0.0111	PCB 112B05	psi	0	20000
PCB_RMS_B_52_83	0.5196	-0.0671	0.0000	PCB 112B05	psi	0	20000
PCB_RMS_B_85_18	0.8506	-0.1165	0.1501	PCB 112B05	psi	0	20000
PCB_RMS_B_85_50	0.8506	-0.1070	0.0000	PCB 112B05	psi	0	20000
PCB_RMS_B_85_82	0.8506	-0.1165	-0.1501	PCB 112B05	psi	0	20000

Description of Flow Around Diamond Trip

As a visual aid in supporting discussion in the main body of this report, the following image is provided of the surface streamlines (as observed using an oil-flow technique) formed around a diamond shaped trip protruding from the surface in a hypersonic boundary layer. Flow in this image is moving from left to right revealing a horseshoe vortex rollup pattern that is produced on a flat surface, in this case at Mach 10. This image was acquired by the first author years ago but never published. The first line of oil accumulation that forms a distinctive “C” around the trip is the outline of the initial vortex rollup induced by this obstruction to the boundary layer. The higher momentum fluid at the top of the boundary layer is initially turned downwards by the obstruction, which then leads to the start of the vortex rollup. In the cross plane through the diagonal of the diamond trip, the vortex is moving in a clockwise direction (see sketch side view). Thus, at the front base of the trip, the streamlines are moving upstream (right to left) at the surface, terminating at a point of low momentum or surface shear (the oil accumulation line) where the two opposing flows stagnate. This main or primary vortex then wraps around the trip, with the streamlines at the surface moving away from the trip. Just downstream of the widest point of the diamond trip, the primary vortex is seen to continue far past the trip but is quickly joined by a secondary vortex that is rotating in a direction counter to the primary vortex. Thus, there are two pairs of counter rotating vortices behind the trip, one at the top and one at the bottom of the diamond. The white lines of oil accumulation represent the zones of low shear, while higher shear regions are seen in between from the counter rotating vortices scrubbing the oil away. Thus, lines of high shear are seen in this oil flow image as the locus of points where the streamlines are moving in dissimilar directions. These high shear lines form near the widest point of the trip and are seen to angle inboard behind the trip slightly towards each other.

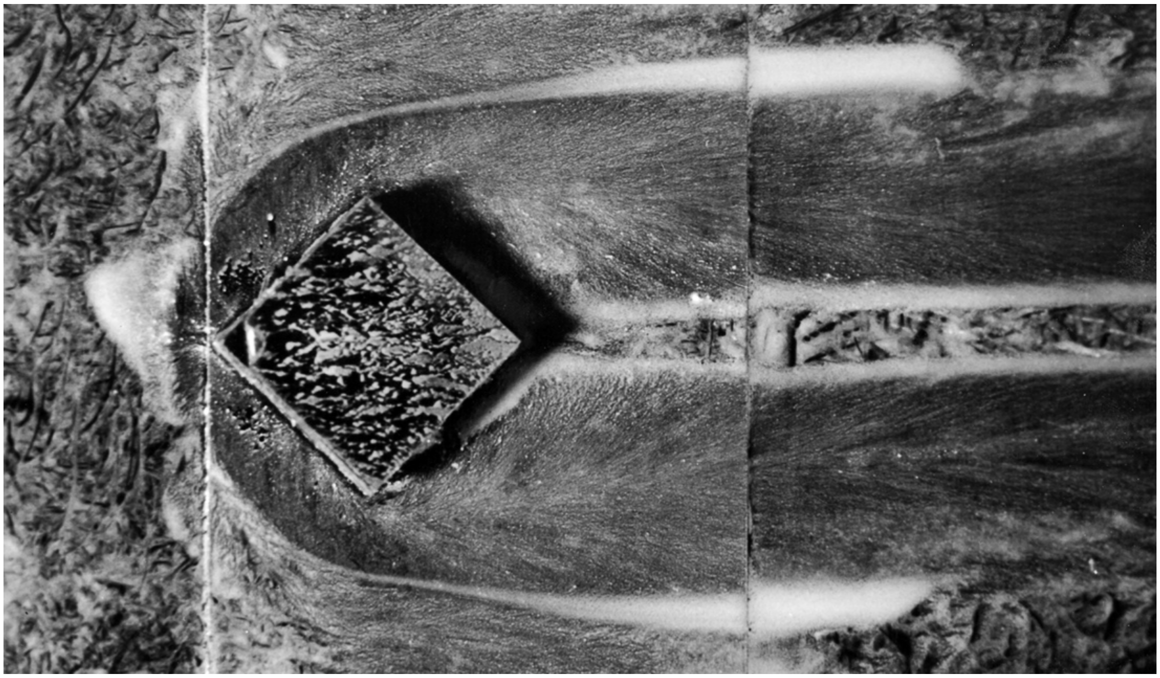

Oil-flow image showing surface streamlines around diamond trip

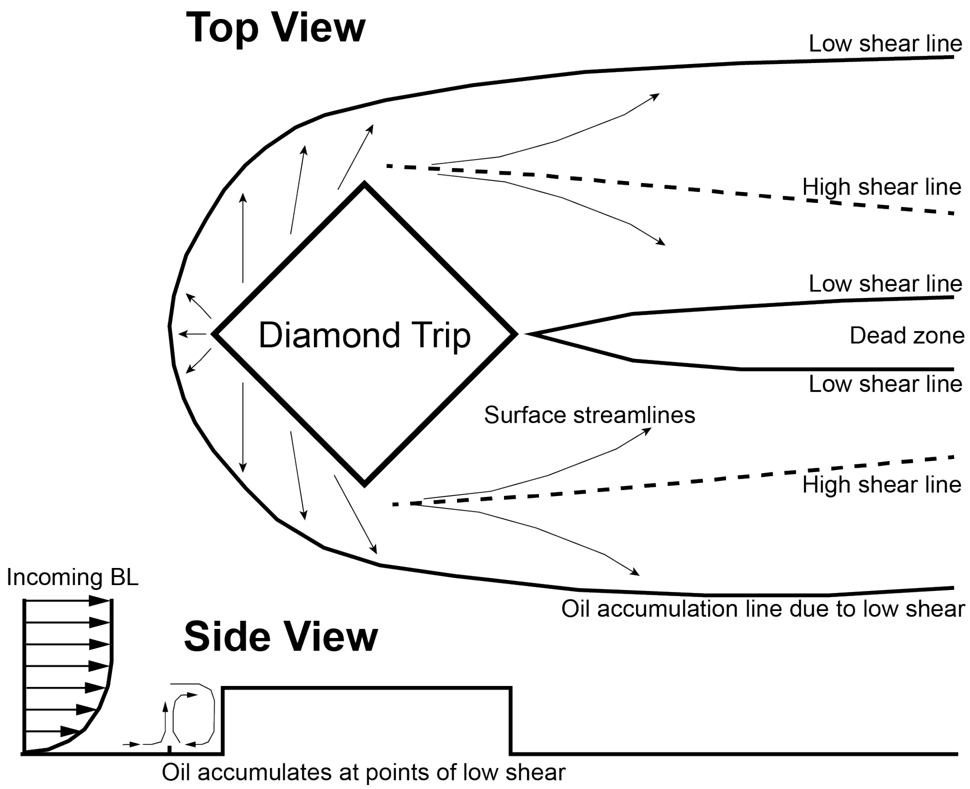

Sketch of streamlines inferred from oil flow image

This image and sketch represent the expected local flow structure surrounding the BOLT-2 trips in flight. And it provides context for any observations captured by the thermocouples nearest the trips. There are sensors in front of and to the side of two of the three BOLT-2 trips. There were also sensors placed on top of those trips, mainly to capture the temperatures that the trips might experience. Finally, there were two additional sensors placed downstream on either side of the trip centerline roughly located along the expected high-shear lines of the counter rotating vortex pairs. While informative, this image, only shows the flow structure at a single condition. Whereas, during flight, conditions would be rapidly changing as the Mach and Reynolds number vary. Thus, the relative size of this horseshoe-shaped structure, and the corresponding locations of lines of low or high shear, should change as the boundary layer develops and/or changes state (laminar or turbulent). One would expect that the size of the primary vortex structure, or horseshoe, would be larger when the incoming boundary layer is laminar, based on the knowledge that laminar separation zones are generally larger than when turbulent. Computations could be used to confirm or refute this expectation.

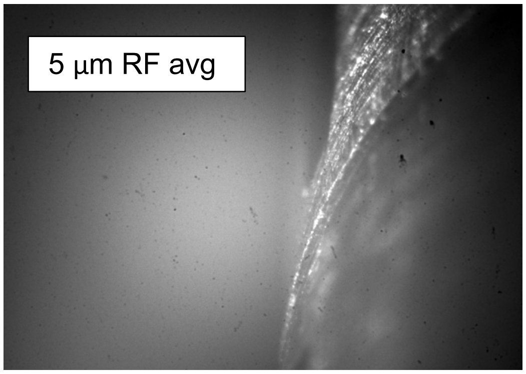

Close-up of Q4-D showing a RF step.

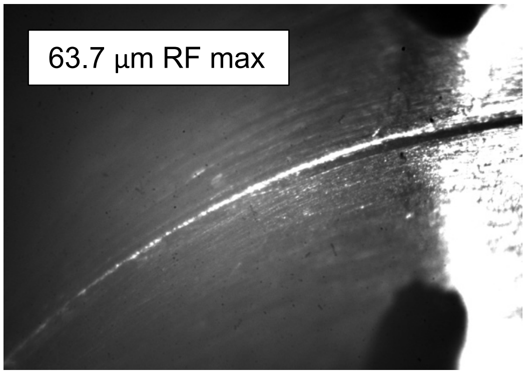

Close-up of Q4-C showing a RF step.

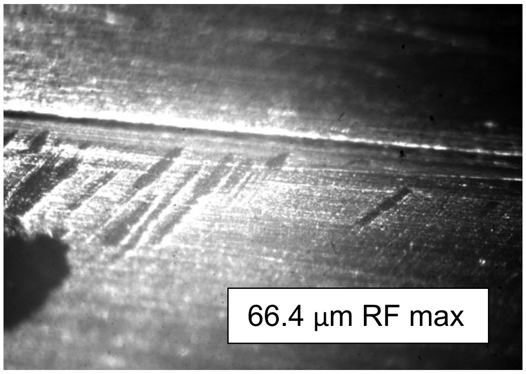

Close-up of Q4-B showing a RF step.

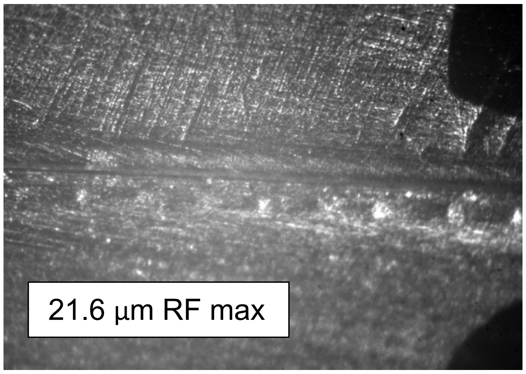

Close-up of Q1/4-A showing small RF step.

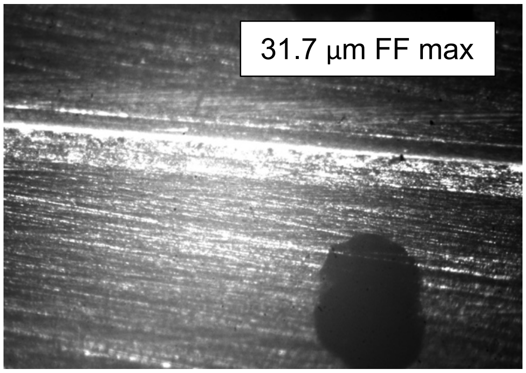

Close-up of Q1-B showing a FF step.

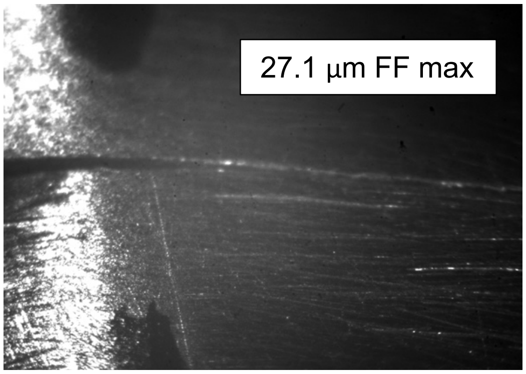

Close-up of Q1-C showing a FF step.

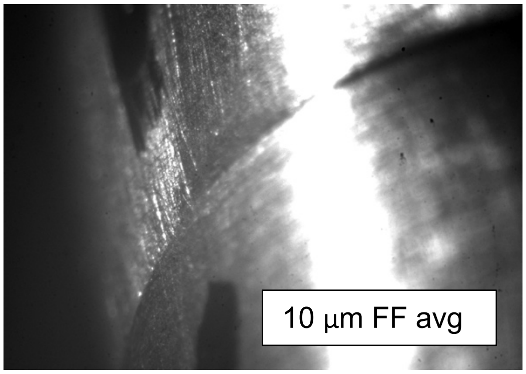

Close-up of Q1-D showing a FF step to the right of the marker.

This page represents Side A

Notes:
FF steps = camera view is aft
RF steps = camera view is forward
Text box on photo is from mold scan data
Photos uncalibrated, not same magnification, intended for guidance only
For all photos on this page [Source: NASA]

Appendix D – Close up photos of nose-joint steps on both sides

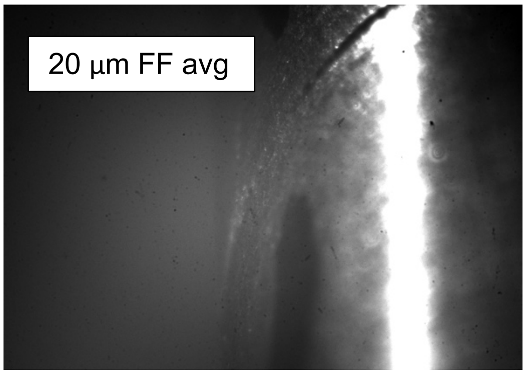

Close-up of Q3-D showing FF step.

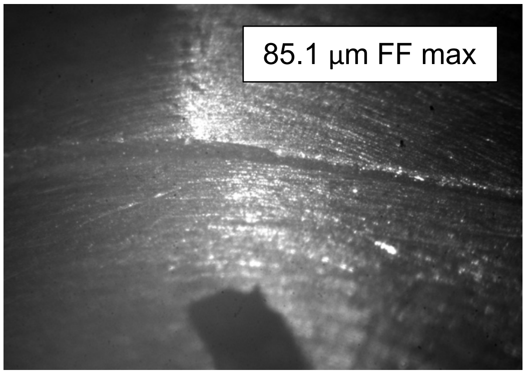

Close-up of Q3-C showing FF step.

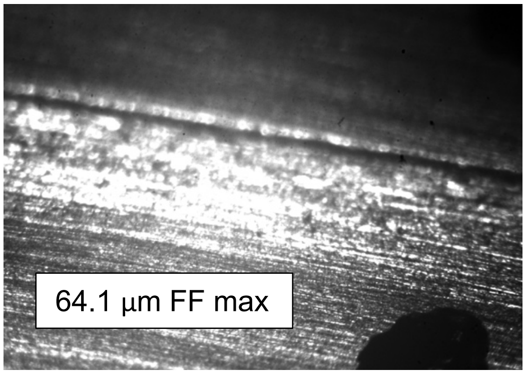

Close-up of Q3-B showing FF step.

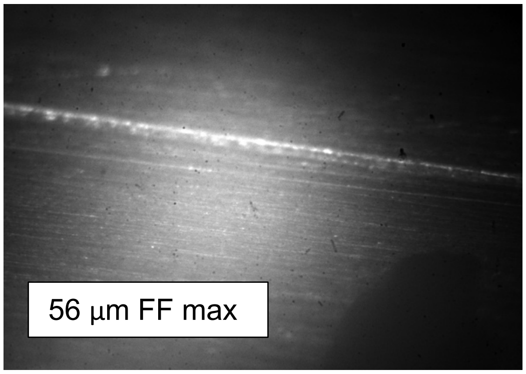

Close-up of Q2/3-A showing FF step.

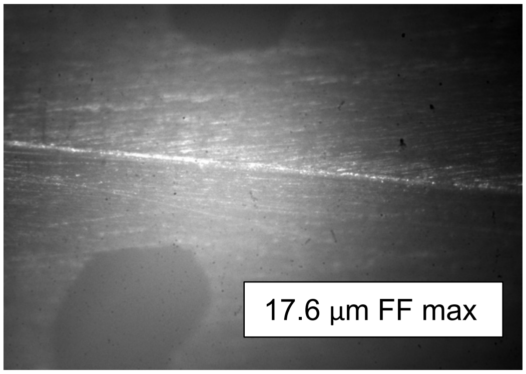

Close-up of Q2-B showing FF step.

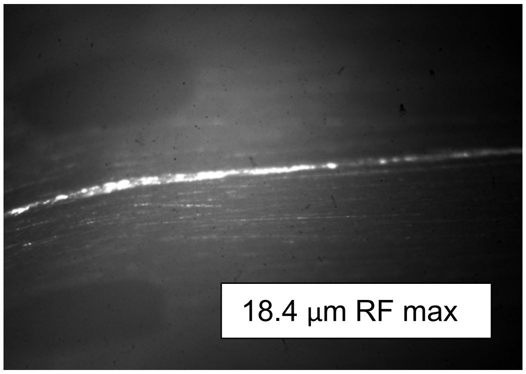

Close-up of Q2-C showing a RF step.

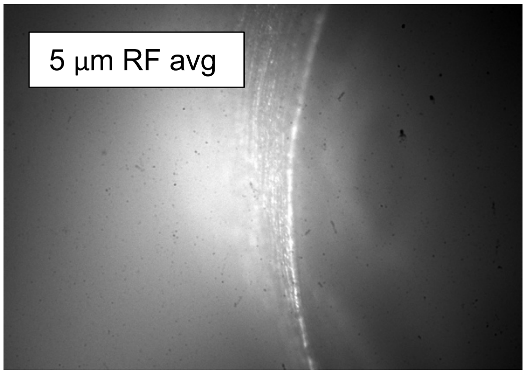

Close-up of Q2-D showing RF step.

This page represents Side B

Notes:
FF steps = camera view is aft
RF steps = camera view is forward
Text box on photo is from mold scan data
Photos uncalibrated, not same magnification,
intended for guidance only
For all photos on this page [Source: NASA]